

**Department of Mechanical Engineering**

**Investigation of the Production and Mechanical Properties of Porous Beta  
Titanium Alloy Compacts Prepared by Powder Metallurgy Processes for  
Biomedical Applications**

**Aris Widy Nugroho**

**This thesis is presented for the degree of  
Doctor of Philosophy  
of  
Curtin University of Technology**

**April 2013**

## Declaration

To the best of my knowledge and belief this thesis contain no materials previously published by any other person except where due acknowledgment has been made.

This thesis contains no material, which has been accepted for the award of any other degree or diploma in any university.

Signature : .....

Date : .....

## Publications

Some of the work presented in this thesis has been published in the following:

Journal :

Nugroho, Aris, Garry Leadbeater, and Ian J. Davies, 2010, Processing of a porous titanium alloy from elemental powders using a solid state isothermal foaming technique. *Journal of Materials Science: Materials in Medicine* 21 (12):3103-3107.

Conference Proceedings:

Nugroho, Aris, Garry Leadbeater, and Ian J. Davies, 2010, Processing and properties of porous Ti-Nb-Ta-Zr alloy for biomedical applications using the powder metallurgy route, *in Proceeding of 6th Australasian Congress on Applied Mechanics (ACAM 6)*, 12-15 December 2010, Perth, Australia, 1226

## Acknowledgements

I would like to express my gratitude to my supervisor, Dr Garry Leadbeater for his encouragement and valuable guidance during the course of this work. I thank him also for his patience and his endless effort in reviewing and polishing the draft of this thesis. I would also like to thank to my co supervisor Dr Ian J. Davies for his support and his advice in laboratory works and analysis and publication work. Thanks also go to Dr Rodney Enwistle for chairing my thesis committee.

The financial support provided by Asian Development Bank through Technological and Professional Skilled Development Project (TPSDP) of Muhammadiyah University of Yogyakarta, Indonesia, Directorate General for Higher Education, Department of Education Indonesia and my institution Muhammadiyah University of Yogyakarta during the course of this PhD project is greatly acknowledged.

I also wish to thank the Australian Nuclear Science and Technology Organization (ANSTO), Sydney for carrying out the HIP-ing and foaming procedures. Thanks also go to Australian Synchrotron facility in Melbourne for assisting in the phase identification. My earnest thanks also go to all members of the Mechanical Engineering Laboratory and Applied Physics Department Laboratory, *i.e.* David Courier, Dereck Oxley, Michael Elliss, Karen Haynes, Graeme Watson, John Murray, Rob Cutter, Elaine Miller, William Richard, and Ross William for their assistance during my research.

To all my colleagues in postgraduate study in Department of Mechanical Engineering and Department of Applied Physic, especially Mark Rank, Sudarisman and Julie, I would like to thanks for the support and sincere friendship. Thanks also go to all my colleagues in Mechanical Engineering Department, Muhammadiyah University of Yogyakarta for their support during my study.

Finally, I would like to thank my parents for their everlasting support and prayers, my father and mother-in-law for looking after my family during the first two years of my study. I would

especially like to thank my wife, Rumiwati, my children; Hasna and Navi for their everlasting love, understanding and support during my study.

## Abstract

Titanium and its alloys are known to be widely used for biomedical applications due to their biocompatibility, and excellent corrosion resistance. The introduction of porosity into the metals may reduce the stiffness to match that of bone and allow the completion of bone ingrowth into the porosity of the implant leading to improvement in implant fixation. Porous metals are recognised in demonstrating considerable advantages in a wide variety of applications due to their low density and novel physical, mechanical, thermal, electrical and acoustic properties. These materials have already exhibited potential for lightweight structures, thermal management, energy absorption and more recently for biomedical applications. The present study was carried out to develop porous titanium alloys from elemental powders, *i.e.* titanium, niobium, tantalum and zirconium using a powder metallurgy method based on the argon filled pore expansion technique. This technique utilises highly pressurised argon pores created by the hot isostatic pressing of metal powders, in the presence of argon gas followed by expansion of the pressurised argon at high temperature. The objectives of the research are : (i) to investigate a novel procedure on developing porous beta ( $\beta$ ) titanium alloys from elemental powders (titanium, niobium, tantalum and zirconium) based on the expansion of the pressurised argon bubble technique, (ii) to determine the effect of foaming parameters on the microstructure, phase transformation and resulting porosity of the porous alloys, (iii) to determine the compressive elastic modulus and compressive strength of the porous alloy.

The powder form of starting materials, *i.e.* titanium, niobium, tantalum and zirconium in angular shape with the size and purity of the elemental powders being  $<44\mu\text{m}$  and  $>99.5\%$ , respectively, were weighed to attain a nominal composition of Ti-29Nb-13Ta-4.5Zr, and were then blended in a roller mixer. Following this, the blended powder was placed into stainless steel cans. Each can was subsequently evacuated and then backfilled with 0.34, 0.48, 0.68 and 0.86 MPa of argon gas and sealed. Afterwards, the pressurised cans were hot isostatic pressed (HIP-ed) at  $1100^{\circ}\text{C}$  under 100 MPa of argon pressure for 4 hours followed by furnace cooling. Cubic specimens each of approximate nominal dimensions of 10 x 10 x 10 mm were sectioned from the HIP-ed billet using wire electrical discharge machining (WEDM). The cube specimens were then foamed in an argon flushed graphite element

vacuum furnace at 1100°, 1225° and 1350°C for 10 hours. Following this, the foamed specimens were prepared for microstructural analysis and examined using optical microscopy and scanning electron microscopy. The fraction of porosity was determined using digital image analysis using open source software (ImageJ). Phase identification within the specimens was carried out using X-ray diffraction (XRD) and/or Synchrotron Radiation Diffraction (SRD). Hardness values were obtained by using a microvickers hardness tester. Open-circuit potential (OCP) and potentiodynamic polarisation measurements were performed to evaluate their corrosion behaviour. Compression tests were carried out using standard mechanical testing equipment, in which the specimen strain was measured using two clip gauges attached to the platen surfaces in contact with the specimen.

The experimental results are summarised as follows. A novel procedure using elemental powders in the argon filled pore expansion technique to produce porous  $\beta$  titanium alloy has been developed. Hardness, corrosion potential ( $E_{\text{corr}}$ ) and corrosion current density ( $i_{\text{corr}}$ ) values of the developed titanium alloy were in the range of 340–474 HV, 445 mV to -321 mV and 0.322 A/cm<sup>2</sup> to 1.51 A/cm<sup>2</sup> respectively which is comparable to those of Ti-6Al-4V or commercially pure (CP) Ti. Regarding the porous structure, although the resulting porosities are comparable with that obtained using existing techniques, the elastic modulus was found to be lower and the compressive strength slightly lower than that of alpha-beta ( $\alpha+\beta$ ) titanium alloys. The porosity level was found to reach approximately 17.8% at a temperature of 1100°C for 20 hours. Foaming at higher temperatures resulted in the development of  $\alpha$  phase. At 1225°C the  $\alpha$  phase areas became larger and at 1350°C the  $\alpha$  phase continued to grow by forming  $\alpha$  platelets within the  $\beta$  phase matrix. Pore morphology of the samples foamed at 1225°C remained discrete with few coalesced pores and a porosity level of 37.1% was achieved. Foaming at 1350°C resulted in the pores growing considerably larger with multiple pores sometimes having become interconnected with porosity levels and pore size reaching approximately 40.2% and 200  $\mu\text{m}$ , respectively. The elastic modulus and compressive yield strengths of the three sets of foamed samples were all found to decrease with the increase of porosity. However, an increase in modulus and yield strength was the trend with increasing foaming temperature. The experimental results indicate that porous  $\beta$  titanium alloys can be produced using elemental powders in the argon filled pore expansion technique, and these materials exhibit properties inclusive of those required for biomedical applications.

## Abbreviations and Symbols

ASTM	American Society for Testing and Materials
BE-SEM	Backscattered Electron - Scanning Electron Microscope
bcc	Body Centered Cubic
CEP	Creep Expansion Process
CF	Carbon Fibre
CIP	Cold Isostatic Press
CP	Commercially Pure
CS	Combustion Synthesis
CVD	Chemical Vapour Deposition
ECAP	Equal Channel Angular Processing
EDM	Electrical Discharge Machining
EDS	Energy Dispersive X-ray Spectroscopy
GF	Glass Fibre
HA	Hydroxyapatite
hcp	Hexagonal Close Packed
HDPE	High Density Polyethylene
HIP	Hot Isostatic Press
HP	Hot Press
HR-SRS	High Resolution Synchrotron Radiation Source
KF	Kevlar Fibre
LDH	Lactate dehydrogenase
PA	Polyacetal
PEEK	Polyethyletherketone
PGA	Polyglycolic-acid
PMMA	Polymethylmethacrylate
PPEP	Pressurised Pore Expansion Processes
PREP	Plasma Rotating Electrode Processing
OM	Optical Microscope
OCP	Open-circuit potential
PS	Polysulfone

PSP	Powder Sintering Processes
PTFE	Polytetrafluoroethylene
PU	Polyurethane
SCE	Saturated Calomel Electrode
SE-SEM	Secondary Electron Scanning Electron Microscope
SEP	Superplastic Expansion Process
SEM	Scanning Electron Microscope
SHS	Self propagating High temperature Synthesis
SR	Silicone Rubber
SRD	Synchrotron Radiation Diffraction
STQ	Solution Treatment and Quench
SS	Stainless Steel
TCP	Tricalcium Phosphate
TZP	Tetragonal Zirconia Polycrystal
UHMWPE	Ultra High Molecular Weight Polyethylene
WEDM	Wire Electrical Discharge Machining
XRD	X-Ray Diffraction

## List of Symbols

$\text{Å}$	Angstrom
C	Proportion constant
E	Young's elastic modulus
$E_{\text{corr}}$	Corrosion potential
f	Pore volume fraction
$i_{\text{corr}}$	Corrosion current density
mm	Millimetre
m, n	Exponent factor
nm	Nanometre
$\alpha$	Hcp titanium phase, coefficient
$\alpha'$	Hcp martensite titanium phase

$\alpha''$	Orthorhombic martensite titanium phase
$\beta$	Bcc titanium phase, coefficient
$\sigma$	Stress
$\rho$	Density
$\mu\text{m}$	Micrometre
$\omega$	Simple hexagonal titanium phase

### **Subscripts**

ath	Athermal
i	Inclusion materials
iso	Isothermal
pl	Plateau
s	Fully solid
ys	Yield

### **Superscript**

*	Porous materials
---	------------------

## Table of contents

Declaration.....	ii
Publications.....	iii
Acknowledgements.....	iv
Abstract.....	vi
Abbreviations and Symbols .....	viii
Table of contents.....	xi
List of Tables .....	xiv
List of Figures.....	xv
Chapter 1 Introduction .....	1
1.1 Research Background .....	1
1.2 Research Objectives.....	5
1.3 Significance.....	5
1.4 Structure of Thesis .....	6
Chapter 2 Literature Review .....	7
2.1 Introduction.....	7
2.2 Biomaterials for biomedical applications .....	7
2.3 Biomaterials for orthopaedic applications .....	12
2.3.1 Biomaterials considerations for orthopaedic applications .....	12
2.3.1.1 Biological compatibility.....	13
2.3.1.2 Biomechanical compatibility .....	18
2.3.1.3 Corrosion and wear resistance .....	19
2.3.1.4 Osseointegration .....	21
2.3.2 Material systems in biomedical applications .....	21
2.3.2.1 Metallic biomedical materials .....	21
2.3.2.2 Polymeric biomedical materials.....	30
2.3.2.3 Ceramic biomedical materials.....	34
2.3.2.4 Composite biomedical materials.....	36
2.4 Titanium and titanium alloys for biomedical applications .....	38
2.4.1 Metallurgical aspects .....	38
2.4.2 Biocompatibility, thermomechanical processing and mechanical properties of titanium and its alloys.....	44
2.4.3 Corrosion behaviour of titanium alloys .....	59

2.5	Porous materials in biomedical applications.....	61
2.6	Fabrication techniques of porous titanium.....	65
2.6.1	Sintering of powder compact techniques.....	66
2.6.2	Space holder techniques.....	68
2.6.3	Wire space holder .....	71
2.6.4	Gel casting methods.....	72
2.6.5	Fugitive scaffold methods.....	73
2.6.6	Freeze casting method.....	74
2.6.7	Pressurised pore expansion with argon or hydrogen gas method.....	75
2.7	Synopsis of other methods .....	78
2.8	Mechanical behaviour of porous structures .....	79
2.9	Summary .....	82
Chapter 3 Experimental Procedure .....		85
3.1	Introduction.....	85
3.2	Alloy fabrication .....	86
3.2.1	Powder mixing .....	87
3.2.2	Pressurised argon gas infusion.....	88
3.2.3	The HIP-ing process .....	90
3.2.4	Sectioning samples.....	92
3.2.5	Pressurised pore expansion – the foaming process.....	95
3.3	Characterisation .....	96
3.3.1	X-ray diffraction (XRD) analysis .....	97
3.3.2	Synchrotron radiation diffraction (SRD) analysis .....	99
3.3.3	Microstructural examination and EDS analysis.....	100
3.3.4	Porosity and pore size distribution determination .....	102
3.4	Electrochemical corrosion assesment .....	104
3.5	Mechanical properties assessment .....	105
3.5.1	Hardness testing .....	105
3.5.2	Compressive testing .....	106
Chapter 4 Results and Discussion.....		108
4.1	Introduction.....	108
4.2	Raw material evaluation .....	108
4.3	As HIP-ed characterisation .....	112
4.3.1	Microstructure and phase evaluation .....	112

4.3.2	Initial porosity and pore size distribution .....	117
4.4	As foamed characterisation.....	121
4.4.1	Microstructure and phase identification.....	121
4.4.1.1	Microstructure and phase identification of specimens foamed at 1100°C ...	121
4.4.1.2	Microstructure and phase identification of specimens foamed at 1150°C ...	125
4.4.1.3	Microstructure and phase identification of specimens foamed at 1225°C ...	127
4.4.1.4	Microstructure and phase identification of specimens foamed at 1350°C ...	130
4.4.2	Porosity, pore morphology and pore distribution .....	133
4.4.3	Electrochemical corrosion assesment .....	147
4.4.4	Mechanical properties assessment .....	150
4.4.4.1	Hardness testing .....	150
4.4.4.2	Compressive testing .....	151
4.5	Summary .....	161
Chapter 5 Conclusions and Recommendations.....		165
5.1	Conclusions.....	165
5.2	Recommendations for future work .....	167
References.....		169
Appendices.....		202

## List of Tables

Table 2.1 : Application of biomaterials in medical applications [70] (p.3).....	11
Table 2.2 : Classification of biomaterials based on their interaction with surrounding tissue. Adapted from [69, 94].....	14
Table 2.3 : Mechanical properties of various biomaterials. Adapted from [68, 112, 117-120] .....	18
Table 2.4 : Composition of 316 L Stainless Steel (ASTM, F139-86, 1992) .....	25
Table 2.5 : Mechanical properties of 316L for implants (ASTM, F139-86, 1992).....	25
Table 2.6 : Chemical composition of cobalt alloys (ASTM, F75-87; F90-87; F562 -84, F563. 1992) .....	27
Table 2.7 : Mechanical properties of cobalt alloys (ASTM, F75-87; F90-87; F562 -84, 1992) .....	27
Table 2.8 : Biomedical application of polymeric biomaterials. Table compiled from [174-176] .....	31
Table 2.9 : Summary of physical properties of the unalloyed metals used in this work, <i>i.e.</i> titanium, niobium, tantalum and zirconium .....	40
Table 2.10 : Mechanical properties of selected titanium and its alloys for biomedical application. Adapted from [69, 139, 227].....	41
Table 2.11 : Specification chemistry limit for commercially pure (CP), $\alpha+\beta$ and metastable $\beta$ type titanium alloys. Adapted from [248] and [249] .....	46
Table 3.1 : Powder composition used for the alloy .....	87
Table 3.2 : HIP-ing settings .....	92
Table 3.3 : The WEDM setting conditions for cutting the titanium alloy specimens: .....	94
Table 3.4 : The schedule of the foaming process in the vacuum furnace .....	96
Table 3.5 : Operating condition for quantitative analysis using EDS on a Zeiss Evo 40XVP SEM .....	102
Table 4.1 : Pore volume fraction of the specimens foamed at various foaming temperatures and backfill pressures for 10 hours and for 2 x 10 hours .....	135
Table 4.2 : Main electrochemical parameter in Hank's solution at 37°C for 10 hours and for 2 x 10 hours .....	149
Table 4.3 : The elastic modulus of the fabricated porous titanium alloys foamed at 1100°C, 1225°C and 1350°C .....	156

## List of Figures

Figure 2.1 : Classification of biomaterials. Adapted from [62] and[64] .....	8
Figure 2.2 : Global biomaterials market by product, 2009. Redrawn from [83] .....	12
Figure 2.3 : Cytotoxicity of pure metal : only relative growth rate of L-929 cell for Mo (a), Relationship between polarisation resistance and biocompatibility of pure metals, Co-Cr alloy, stainless steels SUS 316L, SUS 304L (b) [110] .....	17
Figure 2.4 : Percentage of metal allergy caused by each metal element. Redrawn from[112].....	17
Figure 2.5 : Comparison of elastic moduli of metallic biomedical materials. Redrawn and compiled from [69, 139, 140]. Shadings in bars represent ranges .....	23
Figure 2.6 : Fracture toughness of biomedical titanium alloys. Redrawn from [139]. Shadings in bars represent ranges.....	23
Figure 2.7 : Fatigue longitudinal strength at $10^7$ cycles of biomedical stainless steel, cobalt alloys, titanium and its alloys, and cortical bone. Data without notation of rotating bending are those obtained from uniaxial fatigue tests. Redrawn and compiled from [39, 139, 141]. Shadings in bars represent ranges.....	24
Figure 2.8 : Schematic diagram of influence of alloying elements on phase diagram of titanium alloys [216] (p.22) .....	39
Figure 2.9 : Pseudo-binary schematic phase diagram of $\alpha$ , $\alpha+\beta$ and $\beta$ titanium alloy [216]...	42
Figure 2.10 : A schematic TTT diagram for $\beta$ phase transformation in titanium alloy with $\beta$ stabilising elements [219].....	44
Figure 2.11 : Change in Young's modulus as a function of Nb, Ta, Zr content in Ti- $X_1$ Nb-10Ta-5Zr, Ti-30Nb- $X_2$ Ta-5Zr, Ti-30Nb-10Ta- $X_3$ Zr respectively. Adapted from [240] .....	58
Figure 2.12 : Schematic compressive stress-strain diagram for foams illustrating the three regimes of linear elasticity, plateau and densification.....	79
Figure 2.13 : A cubic model for (a) open-cell, (b) closed-cell [362] (p.185 and p.194) .....	80
Figure 2.14 : Young's modulus values of porous metals fabricated from various techniques vary inversely with pore volume fraction. The filled symbols represent the elastic modulus determined by compression test, the open symbols denote the moduli determined from ultrasonic testing (US) while the lines show the model developed by Ashby-Gibson or Zhao <i>et al.</i> (redrawn from [360] and [50]).....	82
Figure 3.1 : Outline of the experimental work.....	85
Figure 3.2 : Schematic diagram of solid state processing to fabricate porous titanium foam based on expansion of pressurised gas bubbles.....	86
Figure 3.3 : The elemental powder packaging supplied by CERAC.....	88

Figure 3.4 : HIP canister design (a) Shop drawing of HIP canister and (b) assembled canister showing weld locations .....	89
Figure 3.5 : Diagram of typical trial run HIP-ing cycle, with smooth line and jagged line showing cycle set up and actual cycle data respectively .....	91
Figure 3.6 : A WEDM, a FANUC ROBOCUT $\alpha$ -OiD machine used in this work (left), basic feature of WEDM process (right) [389] .....	94
Figure 3.7 : Typical WEDM-ed specimens of a (a) HIP-ed canister and (b) foamed specimen .....	95
Figure 3.8 : The specimen positioned on the sample holder for XRD examination.....	98
Figure 3.9 : Powder diffraction data (pure titanium) of a small region $2\theta$ showing the gap in the first histogram (ti_p1).....	100
Figure 3.10 : Photo micrograph of the calibration bar captured under 10x optical magnification .....	103
Figure 3.11 : Series of steps of digital image analysis using the ImageJ software (same magnification for (a), (b) and (c)).....	104
Figure 3.12 : Clip gauge calibration, (a) Linear displacement of the clip gauge was measured by a Mitutoyo external micrometer, (b) Calibration curves.....	106
Figure 3.13 : Schematic diagram of compressive test set up.....	107
Figure 4.1 : Backscattered electron image of powder morphologies used for the alloy (a) titanium, (b) niobium, (c) tantalum, (d) zirconium.....	109
Figure 4.2 : EDS spectra of elemental powders (a) titanium, (b) niobium, (c) tantalum, (d) zirconium .....	109
Figure 4.3 : Backscattered scanning electron micrograph of the mixed powder (a) and corresponding energy spectra from EDS measurement (b).....	110
Figure 4.4 : Diffraction patterns of samples of the mixed powder obtained from (a) x-ray diffractometer, (b) synchrotron radiation source .....	111
Figure 4.5 : Secondary image SEM micrograph of a typical wire electrical discharge machined workpiece surface texture .....	112
Figure 4.6 : Energy Dispersive Spectrometry analysis of the WEDM-ed surface .....	113
Figure 4.7 : X-ray diffraction plots of the densified Ti-Nb-Ta-Zr powder (a) by hot isostatic pressing in argon (1100°C/4hrs/100 MPa), (b) by hot isostatic pressing in argon (1000°C/2 hrs/100 MPa). .....	114
Figure 4.8 : Synchrotron radiation diffraction plots of the densified Ti-Nb-Ta-Zr powder (a) by hot isostatic pressing in argon (1100°C/4hrs/100 MPa), (b) by hot isostatic pressing in argon (1000°C/2 hrs/100 MPa). .....	115
Figure 4.9 : Backscattered scanning electron micrographs of etched titanium alloy specimens following HIP-ing in argon: (a) 1000°C/2 hrs/100 MPa.....	116
Figure 4.10 : Backscattered scanning electron micrographs of etched titanium alloy specimens following HIP-ing in argon 1100°C/4 hrs/100 MPa).....	117
Figure 4.11 : Initial porosity from HIP-ing procedures with various argon backfill pressures .....	118

Figure 4.12 : Optical microscope image showing pore section in cylindrical form .....	119
Figure 4.13 : Pore size distribution for each of the four argon backfill pressure groups.....	120
Figure 4.14: X-ray diffraction patterns of the foamed titanium alloy at 1100°C with an argon backfill pressure of (a) 0.34 MPa, (b) 0.86 MPa, both foamed for 10 hrs, and (c) 0.68MPa foamed for 2 x 10 hrs. ....	121
Figure 4.15: Back scattered electron image of a titanium alloy specimen foamed at 1100°C for 10 hours showing a black spot representing a pore, a smaller dark area which represents $\alpha$ phase, and light grey area corresponding to $\beta$ phase. Insert, backscattered electron image of an etched specimen presenting dark area with Widmanstatten structure. ....	123
Figure 4.16: Backscattered electron image of titanium alloy specimen foamed at 1100°C/0.68MPa/ 2 x 10 hours.....	124
Figure 4.17: Composition analysis of titanium alloy specimens foamed at 1100°C for 10 hours using EDS. (a) spectra of small dark area, (b) spectra of light grey area, (c) low resolution backscattered image where data were taken, and (d) chemical composition of the alloy at different points shown in (c). ....	125
Figure 4.18 : X-ray diffraction patterns of a foamed specimen at 1150°C with argon backfill pressure of 0.48 MPa.....	126
Figure 4.19 : Backscattered scanning electron micrograph of the titanium alloy specimen foamed in vacuum furnace at 1150°C showing incomplete dissolution of tantalum particles (arrow; brighter areas).....	127
Figure 4.20: X-ray diffraction patterns of the foamed Ti-Nb-Ta-Zr powder at 1225°C with argon backfill pressure of (a) 0.34 MPa, (b) 0.86 MPa (both held for 10 hrs), (c) 0.68 MPa foamed for 2 x 10 hrs.....	128
Figure 4.21: Backscattered electron image of titanium alloy specimen foamed at 1225°C for 10 hours.....	129
Figure 4.22: Composition analysis of titanium alloy specimens foamed at 1225°C for 10 hours using EDS, (a) spectra of small dark area, (b) spectra of light grey area, (c) low resolution backscattered image where data were taken, and (d) chemical composition of the alloy at different points shown in (c). ....	130
Figure 4.23: X-ray diffraction patterns of the foamed titanium alloy powder at 1350°C with argon backfill pressure of (a) 0.34 MPa, (b) 0.86 MPa (foamed for 10 hrs), (c) 0.48 MPa (foamed for 2 x 10 hrs).....	131
Figure 4.24: Composition analysis of titanium alloy specimens foamed at 1350°C for 10 hours using EDS. (a) spectra of small dark area, (b) spectra of light grey area, (c)low resolution backscattered image where data were taken, and (d) chemical composition of the alloy at different points shown in (c). ....	132
Figure 4.25 : Backscattered electron image of thr titanium alloy specimen foamed at 1350°C for 10 hours.....	133
Figure 4.26 : Image of titanium alloy specimen isothermally foamed at 1350°C (a) and (b), 1225°C (c) and polished HIP-ed billet (d). ....	134
Figure 4.27 : Porosity level achieved for the porous titanium alloys (a) foamed for 10 hours and (b) foamed for 2 x 10 hours .....	135

Figure 4.28 : Secondary electron micrograph showing pore morphology of a specimen foamed at 1100°C/0.68 MPa/10 hours (Porosity of 10.2%).	136
Figure 4.29 : Secondary electron micrograph showing pore morphology of a specimen foamed at 1225°C/0.68 MPa/10 hours with porosity level of 21.6%	137
Figure 4.30 : Secondary electron micrograph showing pore morphology of a specimen foamed at 1350°C/0.86 MPa/10 hours (38.7%).	138
Figure 4.31 : Optical micrograph of a specimen close to the centre, showing the early stage of pore coalescence during isothermal foaming at 1350°C/0.86MPa/10 hours. Arrows indicate protrusion	139
Figure 4.32 : Optical micrograph of the region close to the surface with larger pore size under foaming conditions of 1350°C/0.86MPa/10 hours.	140
Figure 4.33 : Optical micrograph of the region close to the surface of a typical specimen foamed at 1225°C/0.68 MPa/10 hours showing a relatively uniform pore expansion (porosity level of 26.7%)	141
Figure 4.34 : Secondary electron micrograph showing pore morphology of a specimen foamed at 1350°C/0.68 MPa/2 x10 hours (porosity level of 40.2%).	142
Figure 4.35 : A typical pore size distribution of samples foamed at (a) 1100°C/0.86 MPa/10 hours with a porosity level of 11.3%, (b) at 1225°C/0.86 MPa/10 hours with a porosity level of 37.1%.(c) at 1350°C/0.86 MPa/10 hours with a porosity level of 38.7% (d) 1350°C/0.68 MPa/ 2 x 10 hours with a porosity level of 40.2%.	143
Figure 4.36 : Plot of as HIP-ed porosity corresponding to as foamed porosity at 10 hours foaming holding time t for various argon backfill pressures and foaming temperatures.	145
Figure 4.37: The open circuit electrode potential (OCP) as a function of time of the specimens foamed at 1100°C, 1225°C and 1350°C in Hank’s solution at 37°C	147
Figure 4.38: Potentiodynamic polarisation curve for specimen foamed at 1100°C, 1225°C and 1350°C in Hank’s solution at 37°C	148
Figure 4.39: (a) Hardness values of specimen foamed at 1100°C, 1225°C and 1350°C, (b) optical image micrograph of Vickers indentation on specimen foamed at 1100°C	150
Figure 4.40: Typical compression stress-strain curves for the specimens foamed at different temperatures: (a & b) 1100°C, (c & d) 1225°C, and (e & f) 1350°C..	152
Figure 4.41: Pictures showing typical deformation of the foamed samples, (a) undeformed (upper image) and deformed (lower image) sample foamed at 1100°C, (b) deformed sample foamed at 1225°C-bottom and V shape of the compressed sample (upper image), (c) deformed sample foamed at 1350°C....	153
Figure 4.42: Secondary electron micrographs showing a typical surface fracture of specimen foamed at (a) 1100°C (b) 1225°C (c) 1350°C. Backscattered electron micrograph of a cross section of fractured specimen foamed 1350°C (d) showing the fracture path propagating between pores crossing the phases.	155

Figure 4.43 : Influence of pore volume fraction on the elastic modulus of foamed samples at 1350°C, 1225°C and 1100°C.....	156
Figure 4.44 : Influence of relative density on Young's modulus of foamed samples at 1350°C, 1225°C and 1100°C. $R^2$ is coefficient of determination. ....	157
Figure 4.45 : Plot of relative Young's modulus versus relative density of foamed samples at 1350°C, 1225°C and 1100°C.....	158
Figure 4.46 : Plot of yield strength versus relative density of samples foamed at 1350°C, 1225°C and 1100°C .....	160

# Chapter 1

## Introduction

### 1.1 Research Background

The global burden of musculoskeletal disorders, causing severe pain and physical disability affecting millions of people around the world, is estimated to have increased by 25% over the past decade [1, 2]. In Australia, it has been reported that more than 31% of the population (6 million people) experienced musculoskeletal problems during the 2004-2005 period [3]. The costs related to arthritis and musculoskeletal problems were estimated at \$4 billion AUD, which accounted for 7.5% of the allocated health system expenditure. During 2005-2006, according to the Australian Institute for Health and Welfare, 44,446 total knee and hip joint replacements were undertaken with a major diagnosis of disease of the musculoskeletal system (mainly coming from osteoarthritis) [4] (p.214). Unfortunately, the prevalence of musculoskeletal problems is predicted to increase year by year due to population growth, particularly in the overweight and elderly age groups. Based on those statistical figures, it is considered very important that the development of new skeletal tissue engineering materials for bone repair or reconstruction be carried out intensively. Accordingly, the research described in this thesis explores the development of titanium alloys for biomedical implant material applications.

Metallic biomaterials have been used mainly for fabrication of medical devices because they are reliable from view point of mechanical performance. This trend is expected to continue. Further, stainless steel, cobalt alloys and titanium and its alloys are mainly used in the fabrication of metallic biomaterials [5]. Due to their excellent biocompatibility, high specific strength and excellent corrosion resistance [6-8] the research and development of titanium system biomaterials is being carried out intensively in the field of metallic biomaterials. Amongst these Ti-6Al-4V (Grade 5) and CP titanium are currently the most widely employed materials for biomedical applications [9]. However, a number of concerns associated with the use of titanium and its alloys as implant materials still exist. Alloying elements of the titanium alloys

are the first concern. Nickel and chromium are well known as metal allergens [10]. Vanadium has been confirmed as causing cytotoxic [11] and adverse tissue reactions [12] whilst aluminium is associated with potential neurological disorders [13]. Hence, aluminium- and vanadium-free titanium alloys are being explored as implant materials. The use of  $\beta$  stabilising elements, such as niobium, tantalum and zirconium has been reported to result in alloys with excellent biocompatibility [14] [15]. Furthermore, these alloying elements would also be expected to enhance strength and decrease the elastic modulus of the resulting alloys [16]. In light of the above information, titanium alloys containing niobium, tantalum, zirconium, molybdenum have been proposed as implant materials.

Although titanium alloys are known as biocompatible materials, they are not fully accepted by the human body. Titanium, as with other materials, initiates a foreign body reaction, *i.e.* the body isolates itself from an implant by implant encapsulation in a thin collagenous sac [18]. The encapsulation may cause a weak bone implant interface leading to loosening of the implant and subsequent fixation failure [19]. In the case of titanium, the encapsulation still occurs, albeit with a thinner encapsulation layer (100-200 Å) in comparison with other materials (*e.g.* 50  $\mu\text{m}$ ) [18]. The use of porous structures which are expected to be osteoconductive, allows the bone cell to adhere, proliferate and form an extracellular matrix on its surface and in the pores. It should also be able to induce bone formation through biomolecular signaling and reducing progenitor cell (osteoinductive). Furthermore, it needs to form blood vessels around the implant within weeks of implantation to support nutrients, oxygen and waste transport [17] leading to the generation of a strong bone-implant bond. Lincks *et al.* [20] pointed out that the degree of roughness and the composition of implanted titanium alloys may significantly contribute to the properties of adherent cells. Yang *et al.* [21] stated that the regeneration of specific tissues on the porous implant materials is affected by the pore size and porosity of the implant. Another study suggested that the optimal porosity for implant materials is in the range of 20-50% [22]. Interconnected porosity where the pore size diameter should be at least 100  $\mu\text{m}$  for successful dissolution of essential nutrients and oxygen for survivalibility has also been reported [23]. According to Murphy *et al.* [24] pore sizes in the range of 200-350  $\mu\text{m}$  are found to be optimum for bone tissue ingrowth. From

the literature study, there is still controversy over definite agreement on the pore size for bone ingrowth [25-34] This also indicates that metals, with ostensibly low bioactivity and containing no calcium and phosphorus, can meet one of the requirements, if they have a specific porous structure, they can demonstrate the behaviour of an osteoinductive material.

The discrepancy of mechanical properties between human bones and the implant titanium alloys is another concern. The Young's modulus of implanted materials, such as CP Ti or Ti-6Al-4V (102-115 GPa) is much higher than that of compact or cortical bone (10-40 GPa [8, 35]). When the implants are significantly stiffer than the adjacent bone, internal loads will mainly be supported by the implant that now is "shielding" the bone from carrying the normal mechanical stress. This stress shielding effect alters the normal stress stimuli for bone growth. In accordance with Wolff's law, the reduction of bone stress relative to the natural situation causes bone to adapt itself by its mass in a process of resorption around the implant. Over a long period, this may result in micromotion, and could further damage the interfacing bone layer and anchorage performances subsequent to possible implant loosening and failure of the implantation, leading to inflammation and extreme pain. Accordingly,  $\beta$  titanium alloys containing the less potentially harmful elements than aluminium and vanadium have been proposed as implant materials due to their elastic modulus, which is lower than that of Ti-6Al-4V. Among those, Ti-Zr-Nb-Ta alloys have commonly been explored for biomedical applications [36-43].

$\beta$  titanium alloys containing elements which exhibit good biocompatibility are known to have low elastic modulus with the lowest modulus value being reported so far of 55 GPa [44]; however, they are still stiffer than cortical bone. Some research work aimed at reducing the stiffness has been carried out [35, 45-50]. It is established that introducing pores to the materials will decrease the values of Young's modulus [45]. Both porous pure titanium and porous titanium alloys are preferred to be fabricated by solid state routes such as sintering of compact powder processes, space holder techniques, a pressurised pore expansion process, etc., rather than the melting route, due to the high reactivity and high melting point (1670°C) of pure titanium.

The process of sintering of powder compacts is the simplest technique. The original pores in the powder dictate the shape, size and volume fraction of the pores in the final titanium foam (this term is used interchangeably herein with porous material). However, these processes do not permit easy control of the level of pore connectivity to each other and to the surface. This method is based on partial sintering of loose titanium powder into a porous body, with porosity in the range of 5-50% and low strength at higher porosity. Oh *et al.* [35] applied sintering to pure titanium under variable conditions such as sintering temperature, sintering pressure and powder size variations. The results showed that the elastic modulus and bending strength of porous CP titanium are similar to those of human cortical bone at a porosity content of approximately 30%. However, the yield strength obtained at 0.2% offset of the porous CP titanium is lower than the yield strength of the bone. A different approach by Queheillalt *et al.* [51] employed hollow titanium powder or spheres to increase porosity. Another approach consisted of generating larger pores around which titanium powders were afterwards completely sintered as struts or walls, using gas such as carbon dioxide as a blowing agent, a polymer as a binder [52, 53], carbamide and ammonium hydrogen carbonate as a particle spacer [45, 52-55] or polyurethane foam as a fugitive scaffold [56]. No information was reported on contamination levels for titanium porous materials for either the particle spacer foaming or for fugitive scaffold foaming, but such contamination was found for gaseous polymer foaming [52].

The use of inert gas, such as argon, to promote porosity due to the expansion of pressurised argon bubbles within a metal matrix at elevated temperature was first introduced by Kearns *et al.* [57]. The amount and morphology of the porosity can be controlled by the foaming parameters such as backfill pressure, foaming temperature or foaming time. This technique has led to development of porous pure titanium [58] and titanium alloys based on prealloyed starting powder [50, 57, 59]. For instance, Kearns *et al.* [57] reported that porous Ti-6Al-4V containing porosity of up to 40% has been developed at a foaming temperature of 1240°C. Another study on porous Ti-6Al-4V carried out by Ashworth [59] reported that when the degrees of porosity are in the range 25-40%, the material stiffness effectively decreases by up to 50%. CP titanium foaming at lower temperatures (960°C) resulted in a porosity of 27% with the elastic modulus being 60 GPa [58]. The elastic moduli were still found to be

higher to that of compact bone. In addition, the use of prealloyed powder containing elements of lower biocompatibility has implications on materials availability and production costs, complexity of the manufacturing process and the biocompatibility. Alternatively, the use of elemental powder as starting materials is a much simpler and more flexible route. Whilst critical concerns have been raised from the use of elemental powders regarding whether alloying can be accomplished under the conditions required to fabricate highly porous titanium alloys, the use of biocompatible elemental powders, *i.e.* titanium, niobium, tantalum and zirconium, as starting materials is expected to enhance the strength and to decrease the elastic modulus of the resulting porous titanium alloys. So far, such a study has not been found in the literature. Therefore, the current study on the development of a porous titanium alloy from the elemental powders as starting materials based on the expansion of pressurised argon bubbles technique has been undertaken.

## **1.2 Research Objectives**

The objectives of the present research are as follows:

- (1) To develop porous  $\beta$  titanium alloys from elemental powders (titanium, niobium, tantalum and zirconium) based on the expansion of pressurised argon bubble technique.
- (2) To determine the effect of foaming parameters on the microstructure, phase transformation and resulting porosity of the porous alloys.
- (3) To determine the compressive elastic modulus and compressive strength of the porous alloy.

## **1.3 Significance**

This research is aimed at contributing to the manufacture of porous  $\beta$  titanium alloys using biocompatible elemental powders as starting materials which potentially offers a much simpler and more flexible route in comparison with the existing technique using prealloyed powder. The study also seeks to establish a significant advance in the design and understanding of porous  $\beta$  titanium alloys with the prospect of developing mechanical properties commensurate with those of bone. Therefore, the

stress shielding that can result in the failure of some implants, due to a mismatch of stiffness between bone and the implanted materials can be reduced.

## **1.4 Structure of Thesis**

The studies reported in this thesis were focused on the microstructural design, characterisation, and the measurement of the physical and mechanical properties of the porous titanium alloys fabricated from elemental starting powders using a powder metallurgy process. This thesis is separated into 5 chapters as follows:

- Chapter 1. Introduction. This chapter presents the background to the research topic, the objectives, the statement of significance and the structure of thesis.
- Chapter 2. Literature Review. The chapter reviews the literature of the theoretical background related to the research topic. This chapter describes synthetic biomaterials for biomedical applications, with solid and porous structures of titanium and its alloys being reviewed in detail.
- Chapter 3. In chapter 3 the experimental procedures conducted in this work are described. For example, the experimental procedure started with powder preparation, powder consolidation and the foaming process, followed by characterisation and the evaluation (assessment) of material properties.
- Chapter 4. The results of the research are presented and discussed in this chapter, which is notionally divided into three stages addressing the microstructural analysis and characterisation of the HIP-ed materials, foamed materials and the mechanical properties of the foamed materials.
- Chapter 5. Conclusions drawn from this study and the recommended future work to be carried out are presented in this chapter. Some selected information required during the study can be found in the appendices.

# **Chapter 2**

## **Literature Review**

### **2.1 Introduction**

This chapter describes the theoretical background associated with the research topic and involves the use of biomaterials for biomedical applications, including titanium and its alloys in porous form and their fabrication. The most common problem that restricts the use of implanted metallic materials is their lack of biocompatibility, exhibiting characteristics such as low bioactivity and a mismatch of mechanical properties with the body tissues. This study presents an overview on both. Both powder sintering processes (PSP) and pressurised pore expansion processes (PPEP) were employed to manufacture the porous structure of the materials and accordingly reviews on these topics were also undertaken.

### **2.2 Biomaterials for biomedical applications**

Biomaterials were first defined as “non-viable materials used in a medical device, intended to interact with biological systems” [60]. Black [61] (p.1) broadened the definition to materials of natural or man-made origin that are used to direct, supplement or replace the function of living tissues in the human body. Biomaterials can be broadly classified into two groups, namely biological biomaterials and synthetic biomedical materials. Whilst biological materials can be further classified into soft tissues and hard tissues, synthetic biomedical materials are further classified as (a) metallic, (b) polymeric, (c) ceramic and (d) composite biomedical materials [62, 63], as depicted in Figure 2.1. Hereafter, the term “biomaterials” will be used to refer to synthetic biomedical materials.

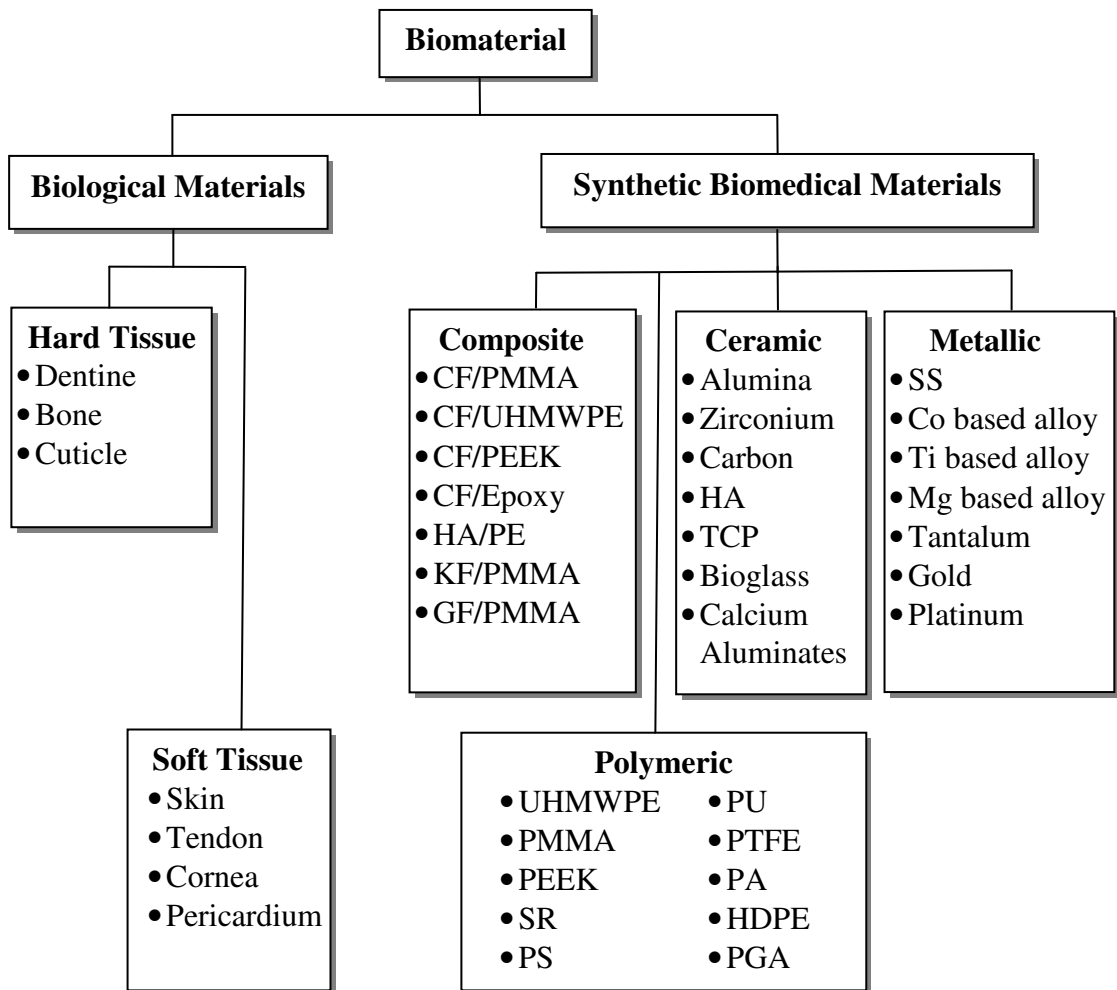


**Figure 2.1** : Classification of biomaterials. Adapted from [62] and [64]

A complementary term, biocompatibility, is defined as the ability of a material to perform in a specific application with an appropriate host response [65]. According to Ramakrishna *et al.* [64], the co-author, Wintermatel and Mayer have previously proposed that the term biocompatibility can be expanded to include surface and structural compatibility. Surface compatibility is linked to the suitability of the implant surface into the host tissue, including chemical, biological, physical and morphological surface properties of the implant. Structural compatibility is the suitability of the mechanical properties of the implant when used with the host tissue, *e.g.* strength, fatigue, elastic modulus, hardness, etc. In line with this, Peters *et al.* [66] described biocompatibility using two aspects. First is the absence of a cytotoxic effect, which implies that there is no harmful effect caused by the material. Second is

the aspect of functionality which assumes the absence of impairment of cellular function, and the materials can match the mechanical, chemical and physical requirements of the host tissue. Today, the term biocompatibility is commonly used as a qualitative term describing how the body tissue reacts with the biomaterials and the impact of the implant on the body [67-69].

Historically, biomaterials have been used far back into ancient civilizations, as summarised from a number of references [70] (p.1), [71], [72] and [73] (pp.2.3-2.4), for aesthetic purposes, medical treatment and the improvement of health care. Metallic biomaterials were used in orthopaedic procedures for the first time around 700 BC during the ancient Greek period by the Etruscan (the precursors of the Romans) in Etruria. Other examples of early biomaterials include wooden teeth and glass eyes that were found in Egyptian mummies. Golden wires were believed to have been used for fracture treatment by the Father of Medicine, Hippocrates (460-377 BC). More than 2000 years ago the Roman, Chinese, Aztec and Egyptian civilizations also used gold in dentistry treatment. A copper and wooden leg has been found in Cappy, Italy, which has been dated to 300 BC. Following the invention of metal production technologies, such as iron casting in 1620, records of gold, iron and bronze being used in medical devices for laceration sutures have been found.

In the 19th century, steel materials were employed as bone plates and screws to fix fractures. As carbon steel corrodes easily in human the body, subsequently it was replaced by nickel-plated steel and vanadium steel. Due to insufficient corrosion resistance and also adverse tissue reaction, those metals were then replaced by stainless steel for orthopaedic applications. By the early 1930's stainless steels, which were invented and developed in the early 1900's, were generally available and utilised successfully as implant materials in the surgical field, followed by the introduction of cobalt-chromium-molybdenum alloys, for example Vitallium<sup>®</sup>. Titanium and titanium alloys were introduced by the 1940's. Lately titanium alloys gradually are getting more attention among the three main metallic biomedical materials used in orthopaedic applications [74]. NiTi shape memory alloys were a major innovation due to their specific mechanical behaviour, and were introduced in the 1960's [75].

The first report of a bioceramic to fill bone defects was published in 1892 [76]. Of the ceramic biomaterials, alumina and zirconia are the most common due to their high strength and wear resistance. In the early 1970's, Hench *et al.* [77] demonstrated a new biomaterial, Bioglass®, which was able to spontaneously bond to living bone. During that time, tricalcium phosphate, which shows absorption characteristics, was also developed.

Although synthetic polymers were discovered at the end of the 19<sup>th</sup> century, in biomedical applications polymeric materials, *e.g.* PMMA, were only introduced in dentistry in 1937 and in contemporary orthopaedics as bone cement in the 1950's [78]. These types of biomaterials have seen increased applications over the last twenty years. For example, medical grade silicone elastomers have been widely used in small joint replacements, introduced for the first time in the mid-1960s. Currently, a large number of polymers [64], as shown in Figure 2.1 and Table 2.1 are also used in biomedical applications. In more recent years, polymer/ceramic composite materials reinforced with ceramic particles or fibres such as CF/PMMA, CF/PEEK, CF/UHMWPE, etc. have also been developed for biomedical applications.

Currently, biomaterials such as metals, polymers and ceramics are used extensively for biomedical applications in a large number of implant forms (sutures, bone plates, joint replacements, ligaments, heart valves, dental implants, etc.) and medical device forms (pacemakers, biosensors, artificial health, blood tubes, etc.) with the examples being shown in Table 2.1.

**Table 2.1** : Application of biomaterials in medical applications [70] (p.3)

<b>Application</b>	<b>Types of Biomaterials</b>
Skeletal system Joint replacement (hip, knee) Bone plate for fracture fixation Bone cement Bony defect repair Artificial tendon and ligament Dental implant for tooth fixation	Titanium, Ti-Al-V, SS, ceramic, UHMWPE, SS, Co-Cr alloy PMMA HA Teflon, Dacron Titanium, alumina, calcium phosphate
Cardiovascular system Blood vessel prostheses Heart valve Catheter	Dacron, Teflon, polyurethane Reprocessed tissue, SS, carbon Silicone rubber, Teflon, polyurethane
Organ Artificial heart Skin repair template Artificial kidney (hemodialyzer) Heart-Lung machine Breast augmentation or reconstruction Maxillofacial reconstruction Penile implant	Polyurethane Silicone-collagen composite Cellulose, polyacrylonitrile Silicone rubber Silicone gel Calcium phosphate [76] Silicone tubing[79]
Senses Cochlear replacement Intraocular lens Contact lens Corneal Bandage	Platinum electrodes PMMA, silicone rubber, hydrogel Silicone acrylate Collagen, hydrogel
General surgery [80] Sutures  Blood substitutes	Catgut, Silk, Nylon 66, Steel, polyglycol acid, polybutyleneterephalate, [81](p.358) Fluosol [81](p.295)

The estimated world market for all devices incorporating biomaterials including diagnostic and therapeutic equipment was \$115.4 billion in 2008. Within this industry, the world market for biomaterials is estimated at around \$25.5 billion for the same year [82] with the composition of the biomaterials market products as shown in Figure 2.2. The figure shows that the orthopaedic biomaterials segment is the dominant one for biomaterials with 38% market share, closely followed by cardiovascular biomaterials with 37% market share. The ageing population in developing and developed countries may contribute to the growth of these markets.

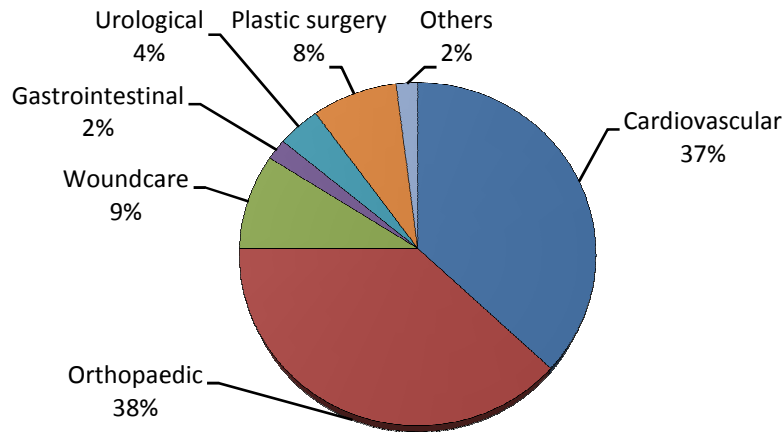


**Figure 2.2 :** Global biomaterials market by product, 2009. Redrawn from [83]

## 2.3 Biomaterials for orthopaedic applications

Bone and joint degenerative and inflammatory problems affect millions of people worldwide. Around half of these chronic diseases are found in people over 50 years old in developed countries, and this number is predicted to increase due to the doubling in number of aged people by 2020 [84]. There are other needs in addition to these diseases; surgery is often needed for hard tissue replacement (*e.g.* total hip replacement) due to deterioration of the bone-joint, and numerous other musculoskeletal problems such as osteoporosis, lower back pain, bone fractures, etc., also requiring treatment using permanent, temporary or degradable materials. In order to overcome these problems, materials are required that meet certain functions for orthopaedic applications which can also be safely placed (implanted) into the human body.

### 2.3.1 Biomaterials considerations for orthopaedic applications

Since biomaterials are implanted into the human body, they will interact with biological entities. Body response to the materials and vice versa becomes a critical factor for accomplishing the biomaterial functionality. An extensive research effort towards understanding the interaction between the materials and the host tissue has been attempted and reported [24, 85-91] in order to obtain biomaterials that serve

longer *in situ* without adverse reaction. Biomaterials, therefore, should have specific properties that can be tailored to meet the requirement of a particular application without causing an unacceptable degree of harm in the body as described below.

### **2.3.1.1 Biological compatibility**

Biological compatibility, commonly known as biocompatibility, is a descriptive term which indicates the ability of materials to interact with living tissue. Biocompatibility of a scaffold is described as its ability to support normal cellular activity including the molecular signaling system without any local and systematic toxic effect to the host tissue [92]. The materials implanted into the body are expected to be highly non-toxic and non-cytotoxic to avoid damage to cell or alteration of cellular membranes, and materials must not inhibit enzymatic metabolic processes [93], and should not result in any allergic or inflammation reactions. This performance is determined by two factors; the host response induced by the materials; and the materials degradation in the living tissue environment. When foreign materials are placed into the body, it naturally responds using its defense mechanisms. The foreign materials will be digested by cells by means of releasing chemicals and enzymes to dissolve and later absorb them. If the materials cannot be digested, the material will be isolated from the surrounding tissue by fibrous tissue encapsulation. Tissue reaction around a metallic implant can be classified into two categories, according to the tissue thickness; a minor reaction (*e.g.* titanium alloys, stainless steel, Co-Cr alloys) and a severe reaction (*e.g.* Fe, Co, Cr, Ni, Mo, V, Mn, Incoloy<sup>®</sup>) [8]. Based on the body's response to implanted biomaterials, with the exception of the material being non-toxic, biomaterials can be classified into [69] biotolerant, bioinert, bioactive, bioresorbable materials and inductive materials as shown in Table 2.2.

**Table 2.2 :** Classification of biomaterials based on their interaction with surrounding tissue.  
Adapted from [69, 94]

Classification	Response	Example	Effect
Biotolerant materials	Formation of connective tissue membran, fibrous tissue, osteochondroma fragments.	316 L steel, Co-Cr based alloys, PTFE, PMMA ,	Distance osteointegration, Rejection of implant leading to implant failure
Bioinert materials	Formation of connective very thin tissue.	Ta, Pt, AuTi, Ti alloys, C, Alumina [95], Zirconia [95]	Contact osteointegration, Rejection of implant leading to implant failure
Bioactive materials	Formation of bony tissue around the implant materials and strongly integrated with the implant surface	Bioglass <sup>®</sup> , HA, Glass Ceravital <sup>®</sup> [95], Ceramic A-W <sup>®</sup> [95]	Acceptance of the implant leading to the success of the implantation
Bioreorbable materials	Replaced by autologous tissue	Polylactic acid, polyglycolic polymer, processed bone graft, composites of all tissue extract or protein and structural support system, Sintered $\beta$ -TCP [95], Calcite [95]	Acceptance of the implant leading to the success of the implantation
Inductive materials	Induce bone formation when implanted at heterotopic sites	Porous HA Porous TiO <sub>2</sub> , Porous Ti chemically treated Porous Poly-HEMA [96]	Acceptance of the implant leading to the success of the implantation

A prolonged inflammation or even death of the surrounding tissue may occur if the implanted material is toxic. The attachment of biotolerant or bioinert materials into living tissue may stimulate dense fibrous tissues with different levels of thickness to encapsulate the materials, resulting in a weakness in interfacial strength between the material and the tissue [97]. This allows micromotion, and there is evidence that too

much relative motion between implant and host tissue leads to thickening of the fibrous connective tissue. Burke *et al.* [98] have shown that micromotion with a larger displacement (75  $\mu\text{m}$ ) induced fibrous tissue ingrowth instead of woven bone tissue, as shown in a smaller displacement (40  $\mu\text{m}$ ). This accommodation of larger micromotion of implants can lead to associated fretting-fatigue corrosion failure of implants. Bioactive materials offer high integration to host tissue mainly in the hard tissue replacement [19, 99, 100]. The materials are able to stimulate tissue regeneration by inducing the formation of a carbonated hydroxyapatite (CHA) bone-like layer on their surface after implantation [97, 101].

Besides the chemical composition of the material, the geometry and macrostructural properties have been found to play an important role. In the case of macrostructure, the importance of porosity, bone formation has never been observed on a dense sintered ceramic, that does not degrade *in vivo*, whereas a ceramic with the same chemical composition, but containing pores, induced bone formation [102, 103]. In the case of inductive materials, the importance of pores inside bone graft substitutes is related to the invasion of the material by blood vessels, that bring along nutrients and oxygen sustaining the metabolism of cells, that may have capacity to differentiate into osteoblasts (mononucleate cells that are responsible for bone formation), inside the scaffold [104]; the property is known as osteoinduction.

Kulkarni *et al.* [105, 106] introduced the concept of bioresorbable materials in the 1960's. This property is another importance factor for scaffolds in tissue regeneration [92]. An ideal scaffold should also be able to degrade with time *in vivo*, preferably at a controlled resorption rate and eventually creating space for the new bone tissue to grow [95]. The degradation behaviour of the scaffold should vary based on the application. These materials have been employed in many orthopaedic applications, such as cartilage, bone substitution or repair of bone fracture.

Biomaterials may degrade into ions and debris, since the human body is a very aggressive environment, with the pH of body fluids in various tissues being varied in the range of 1 to 9, and inducing various applied stresses including static and repetitive stresses [64]. In this regard, these degradation products have to be highly biocompatible to minimize any adverse tissue reactions. It is well noted that some

biomaterials release substances with potentially harmful local and systemic effects. Consequently, non-toxic elements should be chosen as alloying elements for biomedical applications. For example, when biomedical devices such as artificial hips or knee joints are placed in a physiological environment, *i.e.* the human body, they may release metallic, ceramic and polymeric debris into surrounding tissue. The toxicity of the released particles can be classified into two types; chemical, caused by the release of soluble ions and monomers; and mechanical, such as insoluble particles produced by mechanical stimulation.

Ti-6Al-4V is the most extensively used implant metallic material. However, for vanadium, which is considered to be an essential element in the body, its high solubility can raise its levels in the living body to a toxic range [107, 108]. Ceramic biomaterials may release particulate debris instead of soluble metal ions. It has been reported that the cytotoxicity levels of ceramic particles (*e.g.* TiO<sub>2</sub>, Al<sub>2</sub>O<sub>3</sub>, ZrO<sub>2</sub>, Si<sub>3</sub>N<sub>4</sub> and SiC) is lower than that of metal ions [109]. Figure 2.3 shows examples of cytotoxicity of the various pure element metals represented by the relative growth rate of L-929 cells and their coefficient of fibroblastic outgrowth as shown in Figure 2.3(a) (toxicity is indicated by lower growth rate of L-929 cell), whereas the data on corrosion resistance and biocompatibility of pure metals and alloys and representative biocompatibility is shown by Figure 2.3(b).

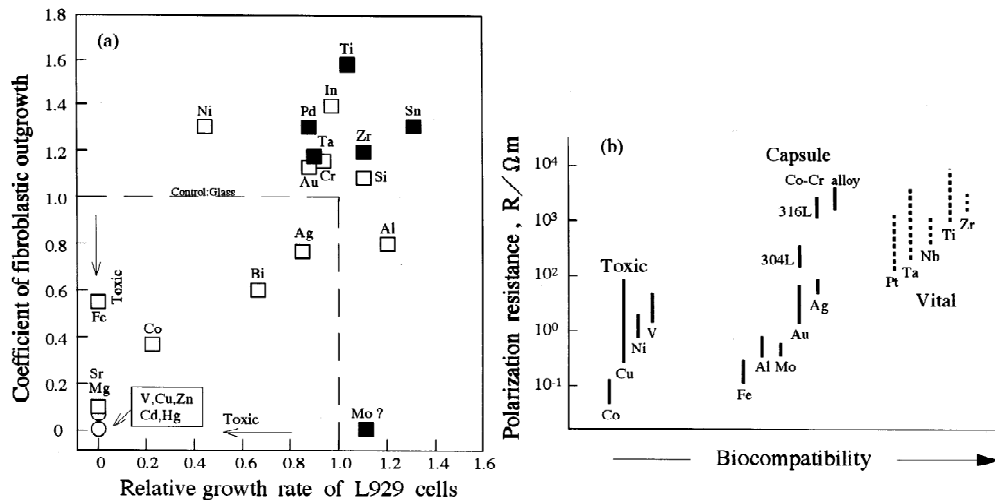


**Figure 2.3 :** Cytotoxicity of pure metals: only relative growth rate of L-929 cells for Mo (a), Relationship between polarisation resistance and biocompatibility of pure metals, Co-Cr alloy, stainless steels SUS 316L and SUS 304L (b) [110]

Another consideration in the selection of materials for biomedical applications is metal allergies due to skin penetration and keratin binding of metallic ions (*e.g.* Ni, Cr, Co) which can be released from the alloy through sweat and other body fluids [10]. Figure 2.4 shows the percentage of metal allergies caused by each metallic element. For example, it can be seen that cobalt and nickel are found to be the second most serious metal allergen. Noting that although cobalt ions or debris are allergenic, cobalt alloys are excellent in fatigue and corrosion resistance [111].

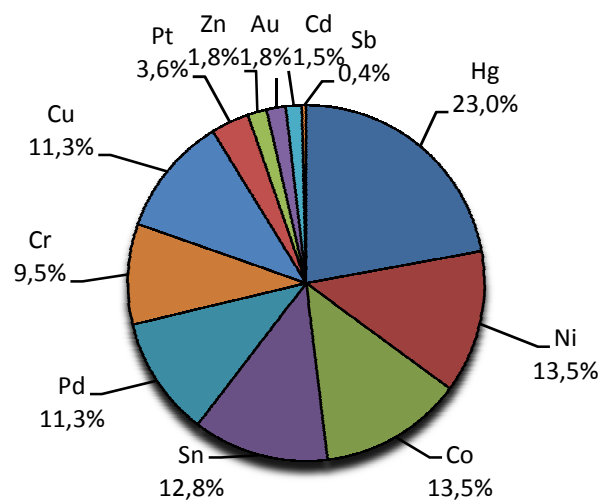


**Figure 2.4 :** Percentage of metal allergies caused by each metal element. Redrawn from [112]

### 2.3.1.2 Biomechanical compatibility

Biomechanical compatibility, especially for hard tissue replacement, is an important characteristic of biomaterials. This compatibility refers to the appropriate mechanical properties of the biomaterials related to the host tissue, mainly as follows; strength, elastic modulus and fracture toughness, as shown in Table 2.3. The resistance of the materials to repetitive and fluctuating stresses or strains, known as fatigue strength, also determines the long term success of the materials exposed to cyclic load. For example, fatigue failure has been reported in dental implants [113] and hip prostheses [114-116]. Fatigue may also contribute to the release harmful debris through fretting-fatigue.

**Table 2.3 :** Mechanical properties of various biomaterials. Adapted from [68, 112, 117-120]

Material	Density (g/cc)	Compressive strength (MPa)	Elastic Modulus (GPa)	Toughness (MPa m <sup>1/2</sup> )	Tensile strength (MPa) <sup>(c)</sup>
Human Bone Cancellous Bone Cortical Bone	1.8-2.1	4-12 130-180	0.02-0.5 10-40 <sup>(g)</sup>	3-6	10-20 82-114
Metals					
Ti and Ti Alloys	4.4-4.5	590-1117	55-117	55-115	900-1172
Co-Cr-Mo Alloys	8.3-9.2	450-1896	200-253	100	400-1030
Stainless Steel	7.9-8.1	170-310	189-205	50-200	515-620
Magnesium	3.1	65-100	41-45	15-40	
Polymers					
HDPE	0.94-0.96	25	1-2	-	27 <sup>(a)</sup>
UHMWPE	0.41-0.49	28	1	20	38-48 <sup>(d)</sup>
PTFE	2.1-2.2 <sup>(b)</sup>	30-60 <sup>(b)</sup>	0.3-0.7 <sup>(b)</sup>		15-40 <sup>(b)</sup>
PMMA	1.12-1.2 <sup>(e)</sup>	45-107 <sup>(e)</sup>	0.8-1.3 <sup>(e)</sup>	1.8-3.3 <sup>(e)</sup>	38-80 <sup>(e)</sup>
Ceramics					
Zirconia	6.1	2000	220	9	800-1500
Alumina	3.98	4000-5000	380-420	3-5	282-551
Bioglas	2.7	1000	75	-	
HAP	3.1	600	73-117	0.7	38-48
AW glass Ceramic	-	1080	118	1.9-2	
Composites (f)					
CF/PMMA			55		772
CF/Polysulfone			76		938
CF/Epoxy Stycast			30		535
CF/Epoxy Hysol			24		207

**Noted:** <sup>(a)</sup> [61] p.252, <sup>(b)</sup> p.288, <sup>(c)</sup> [121] p.6-4, <sup>(d)</sup> [122], <sup>(e)</sup> [61] p.288-289, <sup>(f)</sup> [61] p.260, <sup>(g)</sup> [8]

Biomaterials are expected to possess adequate strength and fracture toughness to avoid implant fracture due to static or dynamically applied loads. Ceramic materials show higher strength but lower toughness. Polymeric materials tend to be too flexible and too weak to meet the mechanical properties in orthopaedic applications. Metallic and composite materials offer excellent strength and toughness, yet a relatively higher elastic modulus than that of bone. In hard tissue replacement, some implanted material is expected to have a Young's modulus commensurate to that of bone. For example, in long bones, *e.g.* the femur, two distinct morphological types of bone are present, *i.e.* cortical (compact) bone and cancellous or trabecular (spongy) bone. As shown in Table 2.3, the elastic modulus of the cortical bone is in the range of 10-40 GPa depending on the type and the measurement direction [8, 61]. Finite element simulations also suggest that joint replacements may better simulate the femur in distributing stress if a lower modulus material is used [123, 124]. If an implanted material has an elastic modulus higher than that of bone, then the implant will bear more of the load. Thus, the bone is insufficiently loaded compared to the implant. The required stress (25-40 MPa [125]) that maintains the bone density is inhibited from being transferred to the bone. This phenomenon is called stress shielding or the stress protection effect. The effect stimulates bone resorption around the implant leading to increased bone porosity also known as bone atrophy [126], and further the failure of implant fixation occurs. Therefore, materials that typically exhibit combinations of high strength, toughness and a low elastic modulus close to that of bone are the main candidates for structural biomaterials, in order to avoid loosening of the implant and afford reliability for long term service.

### **2.3.1.3 Corrosion and wear resistance**

Corrosion in biomaterials is a complex phenomenon that depends on the geometric, metallurgical, mechanical and solution chemistry parameters [127]. Common electrochemical techniques being used to investigate the corrosion behaviour are; open-circuit potential, potentiodynamic polarisation and electrochemical impedance spectroscopy measurement. The corrosion resistance of biomaterials under biological conditions is assessed using those techniques in order to verify their low impact on the physiological medium. As the physiological solution (body fluid) is considered corrosive to metallic materials, the corrosion of a metallic implants may occur and affect the human body. Metallic implants used as surgical implants achieve passivity

by the development of a protective surface passive film. This film inhibits corrosion and keeps current flow and the release corrosion products at a very low level.

Investigation of corrosion behaviour of titanium alloy without vanadium, Ti-25Ta-25Nb alloy, in Ringer's solution has been carried out. The result shows a corrosion resistance higher than that of CP Ti [128]. The electrochemical behaviour of various titanium alloys (CP Ti, Ti-15Al, Ti-5Al-2.5Fe, Ti-6Al-4V-Ti-6Al-4Fe, Ti-6Al-4Nb, Ti-13.4Al-29Nb and Ti-13Nb-13Zr) have been studied in Hank's solution[129]. Potentiodynamic polarisation measurements indicated stable passive polarisation behaviour for all the alloys. Corrosion potential and corrosion current density measurements of the alloys were comparable one to another in the range of -379 mV to -606 mV and  $0,08 \mu\text{A}/\text{cm}^2$  to  $0,48 \mu\text{A}/\text{cm}^2$  respectively. Noble breakdown potentials and large passive ranges were also observed for all the alloys. The electrochemical behaviour of CP Ti and Ti-6Al-4V in Hank's solution at 37°C with no hysteresis loop and breakdown potential indicating excellent pitting and crevice resistance have been reported with  $E_{\text{corr}}$  values of -470 mV and -470 mV and  $i_{\text{corr}}$  values of  $5,72 \mu\text{A}/\text{cm}^2$  and  $2,76 \mu\text{A}/\text{cm}^2$ [130].

It has been established that porous metallic scaffolds meet the mechanical requirements of bone. In this regard, the corrosion behaviour of porous metal has also been investigated intensively. The influence of pore morphology on corrosion has been revealed that whilst in highly porous compacts with open, interconnected pore morphology the free flow of species resulted in a material with much higher resistance to pitting. In porous titanium with small, isolated pore size morphology, the  $E_{\text{corr}}$  value reduces with decreasing porosity due to ionic species being trapped and the supply of oxygen being exhausted [131]. Metal ion leaching also raises concerns in porous metallic scaffolds. In addition to releasing corrosion products (metal ions) which may be non-biocompatible, resulting in toxic or allergic reactions, it also may reduce the service period of the implant device [93]. Another factor that affects the service life of the device is the wear resistance of its components. Wear may shorten the life period of the implant device due to implant loosening, and wear debris is noted to cause several adverse reactions to the tissue in which they are deposited [132, 133]. Wear is commonly found in orthopaedic applications such as knee [133] and hip joint [132] prostheses. Therefore corrosion and wear resistance

are considered as important properties for prolonged service life of the materials in human body.

#### **2.3.1.4 Osseointegration**

Osseointegration is the anchorage of implants in the surrounding bone and, when effectively applied, significantly improves the long term behaviour of the implanted devices and decreases the risk of loosening and failure of the implant fixation. According to Braceras *et al.* [134], Branermark defined osseointegration as the direct connection between living bone and a load-carrying endosseous implant at the light microscopic level. Currently, this term can be simply accepted as a general term for intimate implant surface-to-bone contact [135]. The intimate attachment mechanism of surface implant materials to bone may take place by biomechanical bonding or biochemical bonding or a combination of both. Biochemical bonding may take place by using bioactive materials for implants or by coating the surface of an implant material with a bioactive material. Biomechanical bonding involves the ingrowth of bone into surfaces with irregularities, such as porous coatings or fully porous materials, which can provide mechanical interlocking between bone and the implant. In this regard, implant materials with appropriate surface chemistry, surface morphology, surface roughness, and surface topography play a crucial role in successful osseointegration [87, 88].

Additionally, biomaterials should also meet the following requirements; sterilisability – materials must be able to be sterilised without any degradation or formation of by-products; functionability – the ability of the materials to be shaped and applied to suit a specific function; and manufacturability – the ability of the materials to be appropriately manufactured for the specific components [62].

### **2.3.2 Material systems in biomedical applications**

#### **2.3.2.1 Metallic biomedical materials**

Metals are inorganic materials with a very orderly atomic arrangement and bonding characteristics leading to wide range of mechanical, thermal and electrical properties.

Excellent mechanical properties of metals allow them to be used in various medical applications [136], including hard tissue replacement, fixation devices, dental implants and active devices such as catheter guides, wire stents, orthodontic archwires and cochlea implants [137].

Metals such as iron, chromium, cobalt, niobium, nickel, molybdenum, tantalum and tungsten that are employed in the composition of alloys for the fabrication of implants can mostly be tolerated in limited amounts (below 0,01 mM [138]). A concern arising from most metallic implants is their biocompatibility; that is, metals can be corroded in physiological solution. This corrosion leads to deterioration of the implant, which will weaken it and release the corrosion products that potentially cause harmful effects. Metallic materials that have been used, presented in chronological order of introduction, are stainless steel, cobalt based alloys, titanium based alloys and shape memory alloys. A summary of the mechanical properties of metallic biomaterials including elastic modulus, fatigue strength, and fracture toughness can be seen in Figure 2.5, Figure 2.6 and Figure 2.7.

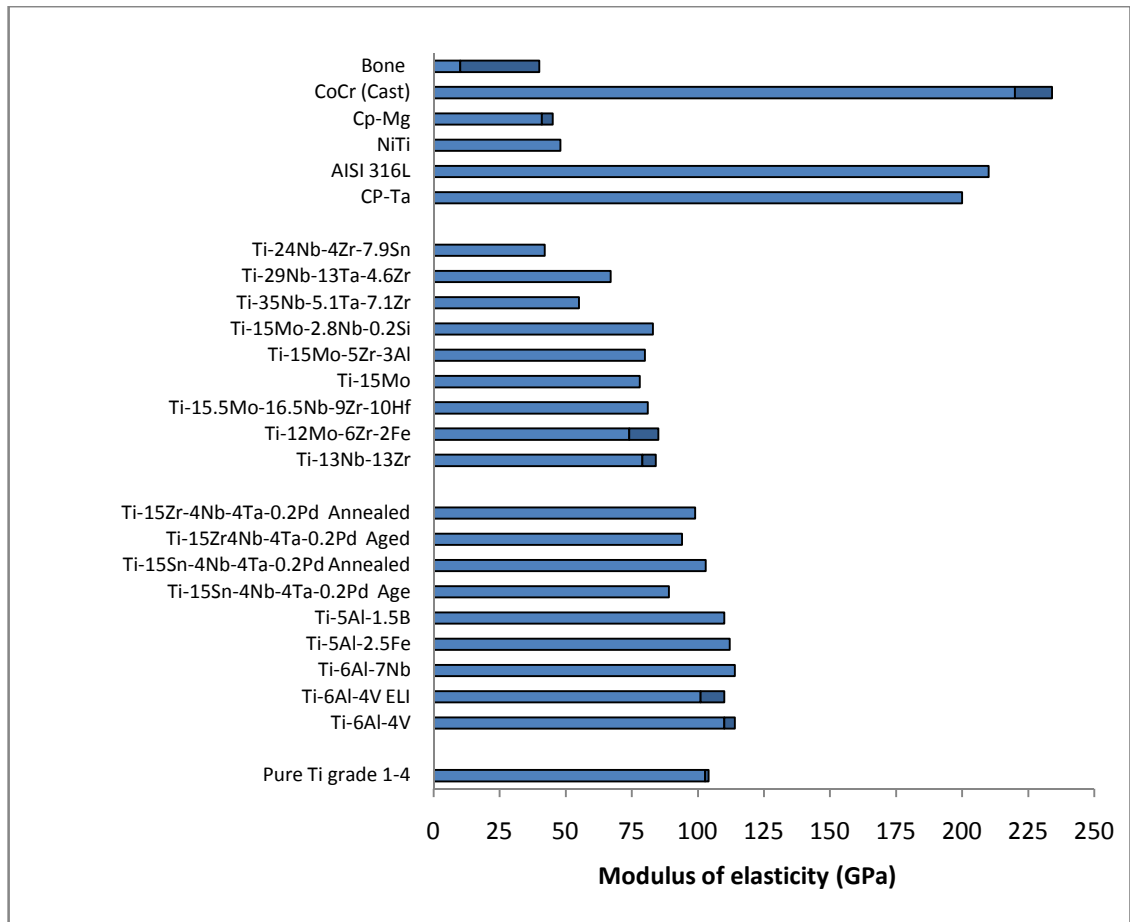


**Figure 2.5 :** Comparison of elastic moduli of metallic biomedical materials. Redrawn and compiled from [69, 139, 140]. Shadings in bars represent ranges (minimum and maximum).

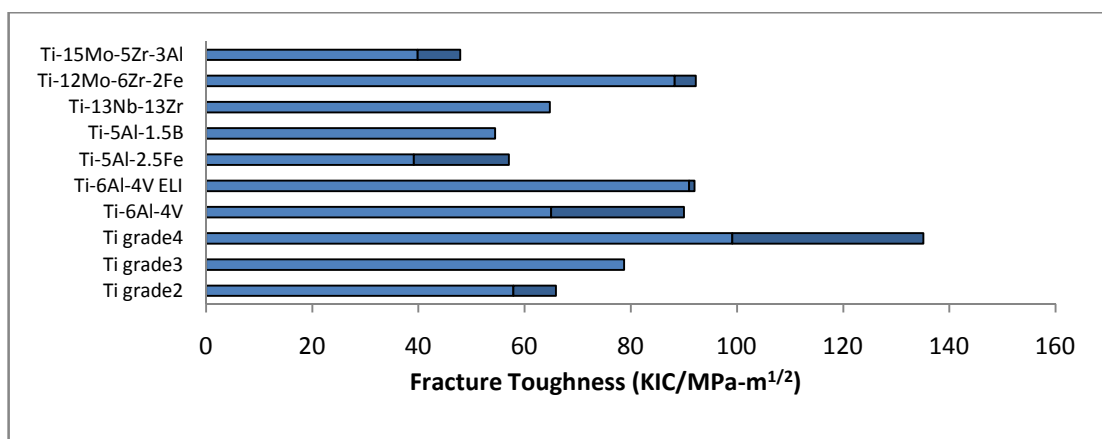


**Figure 2.6 :** Fracture toughness of biomedical titanium alloys. Redrawn from [139]. Shadings in bars represent ranges (minimum and maximum).

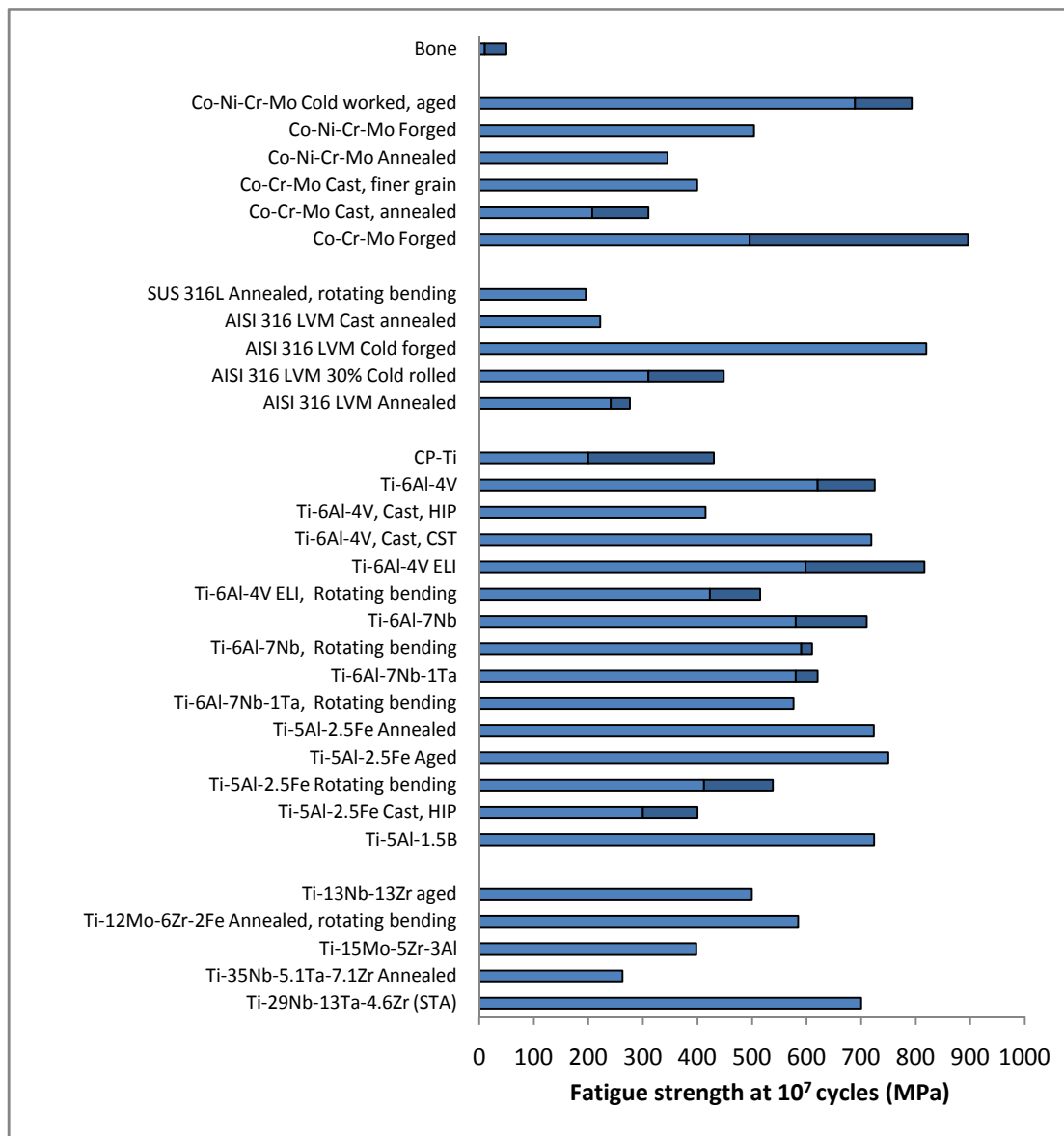


**Figure 2.7 :** Fatigue longitudinal strength at  $10^7$  cycles of biomedical stainless steel, cobalt alloys, titanium and its alloys, and cortical bone. Data without notation of rotating bending are those obtained from uniaxial fatigue tests. Redrawn and compiled from [39, 139, 141]. Shadings in bars represent ranges (minimum and maximum).

### Stainless steel

Vanadium steel was the first metal alloy to be utilised as a biomaterial, but it is not longer to be used due to inadequate corrosion resistance. It was replaced by stainless steel type 18-8 (AISI type 302) which is higher in corrosion resistance than vanadium steel. To improve the corrosion resistance the addition of a small percentage of molybdenum was introduced (type 18-8sMo). This type later became

known as SS 316. The carbon content of this type was then reduced from 0.08%wt to 0.03%wt for better corrosion resistance to chloride solutions and sensitisation (grain boundary precipitation of chromium carbides in a critical temperature range leading to reduced corrosion resistance [142]). This stainless steel, known as SS 316L, is an austenitic stainless steel commonly used in traumatological temporary devices such as fracture plates, screws, hip nails [137] and defibrillator casings [67], due to its relatively low cost, availability and ease of processing. The composition of 316L stainless steel with austenite stabilising elements such as nickel and manganese, and other minor elements is shown in

Table 2.4 while its mechanical properties are shown in Table 2.5. Other grades of stainless steel such as type 304, 316 and martensitic stainless steels, e.g. 17-7PH, 420 and 431 are employed to a lesser extent in other surgical implant applications, such as surgical sutures, microvascular clips and for neurosurgical uses [143]. .

**Table 2.4 :** Composition of 316L (ASTM, F139-86, 1992)

Elements	Composition (%wt)
Carbon	0.03 max
Manganese	2.00 max
Phosphorus	0.03 max
Sulphur	0.03 max
Silicon	0.75 max
Chromium	17.00-19.00
Nickel	12.00-14.00
Molybdenum	2.00-4.00

**Table 2.5 :** Mechanical properties of SS 316L for implants (ASTM, F139-86, 1992)

Condition	Ultimate Tensile Strength, min (MPa)	Yield Strength, min (MPa)	Elongation min(%)
Annealed	485	175	40
Cold Worked	860	690	12

The wear resistance of austenitic stainless steel is rather poor in comparison to other steel alloys. Due to high friction and a large number of wear debris particles that are produced, these metals are not used in metal-on-metal applications.

Common stainless steels contain significant amounts of nickel that may corrode inside the body under certain conditions. In highly stressed and low oxygen regions such as the contact under the screws of bone fracture plates [137], corrosion products can lead to potentially adverse effects such as allergies [10]. Considering the potential danger of nickel and the wide application of stainless steel for medical application, the development of nickel-free stainless steel is a great of importance.

At present, a large number of austenitic nickel-free/ultra-low-nickel stainless steels are used in medicine. The steels are readily available in the market, such as BioDur 108 alloy [144], 216 L[145], P588 [146]. The nickel-free/ultra-low-nickel stainless steels have a high chromium content (over 20%) where nickel is substituted by manganese, carbon and nitrogen [75, 147-149]. The purpose of nitrogen addition is to increase the corrosion resistance and strength. Increasing manganese, while at the same time reducing nickel, has been found to be conducive to the resistance to stress corrosion cracking in boiling  $MgCl_2$  [150]. Although manganese is widely used as a substitute for nickel in high-nitrogen nickel-free stainless steel, its use may hinder production of fine steel foil and wires. To overcome this problem Niinomi *et al.* [151] and Kuroda *et al.* [152] developed a nickel and manganese-free austenitic stainless steel which used ferritic stainless steel as a starting material. Because of the shallow depths that are penetrable by nitrogen atoms, this process allows the production of small devices and thin-walled parts with a maximum thickness or diameter of 4 mm. The strength of the developed stainless steel is higher than that of SS 316L, yet the elongation to fracture is lower.

### **Cobalt alloys**

Cobalt alloys have been used for manufacturing parts of medical devices, for example, the heads of artificial hip joints. There are four groups of cobalt alloys in the ASTM list that are recommended for medical applications, namely; (1) cast CoCrMo alloy (ASTM F75, Vitallium<sup>®</sup>), (2) wrought CoCrW<sub>Ni</sub> alloy (ASTM F90), (3) wrought CoNiCrMo alloy (ASTM F562) and (4) wrought CoNiCrMoWFe alloy (ASTM F563) [137]. The composition of each alloy is shown in Table 2.6. However, only two groups of the cobalt alloys are employed extensively, *i.e.* (1) the cast CoCrMo alloys and (2) the wrought CoNiCrMo alloys. The former has been used in

dentistry for many decades, and in making artificial joint hip prostheses, instead of stainless steel due to its better wear resistance [153] [154, 155]. The latter one is used for the stems of prostheses for heavily loaded joints such as the knee and hip [156], due to its high fatigue and ultimate tensile strength ( see Table 2.7).

**Table 2.6 :** Chemical composition of cobalt alloys (ASTM, F75-87; F90-87; F562 -84, F563. 1992)

	<b>CoCrMo (F75)</b>		<b>CoCrWNi (F90)</b>		<b>CoNiCrMo (F562)</b>		<b>CoNiCrMoWFe (F563)</b>	
	Min	Max	Min	Max	Min	Max	Min	Max
Cr	27.0	30.0	19.0	21.0	19.0	21.0	18.00	22.00
Mo	5.0	7.0			9.0	10.5	3.00	4.00
Ni		2.5	9.0	11.0	33.0	37.0	15.00	25.00
Fe		0.75		3.0		1.0	4.00	6.00
C		0.35	0.05	0.15		0.0025		0.05
Si		1.00		1.00		0.15		0.50
Mn		1.00		2.00		0.15		1.00
W			14.0	16.0			3.00	4.00
P						0.015		
S						0.010		0.10
Ti						1.0	0.5	3.50
Co	Balance	Balance	Balance	Balance	Balance	Balance	Balance	Balance

**Table 2.7 :** Mechanical properties of cobalt alloys (ASTM, F75-87; F90-87; F562 -84, 1992)

<b>Property</b>	<b>CoCrMo (F75)</b>	<b>CoCrWNi (F90)</b>	<b>CoNiCrMo(F562)</b>	
			Solution Annealed	Cold worked Aged
Tensile Strength (MPa)	655	860	793-1000	1793 min
Yield strength (MPa)	450	310	240-655	1585
Elongation (%)	8	10	50.0	8.0
Reduction area(%)Cr	8		65.0	35.0
Fatigue Strength (MPa)	310			

Cobalt based alloys are highly resistant to corrosion even in a chloride environment due to spontaneous formation of passive oxide layer within the human body environment [156-160]. These materials have superior mechanical properties such as

high resistance to fatigue and cracking caused by corrosion, and good wear resistance. They also exhibit a level of toughness with a minimum 8% ductility (elongation). The modulus of elasticity of cobalt alloys has been found to be higher than those of other implant materials (220-234 GPa) and the elastic modulus does not significantly change with the change of tensile strength. This is much higher than that of cortical bone, which may imply the occurrence of the stress shielding effect. Elements such as nickel, chrome and cobalt are indicated to be released from the stainless steel and cobalt chrome alloys due to corrosion in the human body [43, 161]. The thermal treatments used to Co-Cr-Mo alloys can modify the microstructure of the alloy and develop changes to the electrochemical and mechanical properties of the materials [159].

### **Titanium alloys**

Pure titanium and titanium alloys, especially Ti-6Al-4V, are widely used for biomedical applications due to their excellent properties such as high corrosion resistance, low elastic modulus, high strength-weight ratio and high biocompatibility with living tissue. The characteristics of titanium and titanium alloys will be discussed later in Section 2.4.

### **Others metals and alloys**

There are several other materials that can be utilised for biomedical applications such as the nickel-titanium alloy known as Nitinol<sup>®</sup>, zirconium alloys, tantalum, magnesium, amalgams and the noble metals (the gold, silver and platinum group).

The equiatomic Ni-Ti alloy (Nitinol<sup>®</sup>) is employed currently in orthopaedic, dental and cardiovascular applications [162]. One of the important properties of this material is shape memory, allowing the materials to return to the originally preset shape after deformation due a thermoelastic martensitic transformation. These materials are also reported to have good corrosion resistance due to a passive surface layer (TiO<sub>2</sub>) and have good biocompatibility according to short term *in vivo* tests [163, 164]. However, long term use of these materials, with the consequences of even minor nickel ion release as has been discussed earlier, may raise some concern related to their application.

Zirconium, is a highly reactive metal and will form a dense cohesive surface oxide layer ( $ZrO_2$ ) spontaneously on exposure to an oxygen-containing environment. In addition to the resulting corrosion protection,  $ZrO_2$  is very hard and can be used to produce good wear resistant surfaces. The stability of the oxides is increased by aging under potentiostatic conditions and can be decreased by the presence of chloride ions in the electrolyte during the anodization process [165]. Zr-alloys, for example Zr-Nb alloys, are used for making orthopaedic components that are primarily intended for compressive loading and resisting wear, such as for femoral hip implant and knee implant components [143, 166].

Tantalum is inert in bodily fluids, is very biocompatible and exhibits a very high resistance to corrosion. In porous structures, porous tantalum is used as a bone augmentation template [167]. However, due to its high stiffness (190 GPa) and its high density ( $16.6 \text{ g/cm}^3$ ) it is limited to a number of applications, such as wire surgical sutures [168] and as a radioisotope for bladder tumor detection [137].

Magnesium has been investigated as a biomedical material for applications in cardiovascular and orthopaedic fields, due to its specific advantages. In addition to its light density ( $1.7 \text{ g/cm}^3$ ), the metal has low mechanical properties and relatively low corrosion resistance in comparison to other metallic biomaterials. Interestingly, the corrosion products of magnesium are non-toxic and are excreted from the body quickly, leading to magnesium becoming a potential biodegradable metal [169].

Noble metals and platinum group elements such as platinum, iridium, palladium, ruthenium, osmium and rhodium are inert, biocompatible and not subject to corrosion reactions, yet their mechanical properties are not suitable for load bearing applications. As a result these metals are used in limited numbers of biomedical applications, such as in dentistry, as electrodes in stimulation and for sensing purposes in pacemaker tips [170].

Dental amalgams are formed by adding mercury to dental amalgam alloys. The alloys contain silver, copper, and tin with some minor element additions through the

amalgamation process. Dental amalgam alloys are available in powder form. Subsequent mixing of these alloy powders with liquid mercury results in a number of intermetallic compounds being formed. During the reaction the partially reacted powder can be manipulated to fill the tooth cavity. Its passivation products protect against further corrosion and act as a sealant at the amalgam/tooth interface. Easy *in situ* formability to the desired shape is the advantage of this type of material [143].

### **2.3.2.2 Polymeric biomedical materials**

Polymers are long-chain molecules composed of covalently bonded repeating units named monomers connecting together to form a common backbone [67]. Chain length is commonly determined by molecular weight, which is a product of the number of repeat units and the molecular weight of the individual monomer. Polymers form the largest category of diverse biomaterials. They can be classified into two groups [171] (p.490), *i.e.* (1) natural polymers such as DNA, enzyme starches, cellulose and collagen, and (2) synthetic polymers such as polyvinyl chloride (PVC), polyethylene (PE), polyurethane (PU), *etc.* as shown in Table 2.8. Those synthetic polymers are considered “biocompatible” [172]. They are also considered “biostable” in the human body and have found widespread applications in the medical field, ranging from PTFE vascular grafts to UHMWPE acetabular cups [70, 173]. According to their repeating units, the arrangement of polymer chains is classified into linear, branched, crosslinked and network structures. Further, when crosslinked or in the form of interconnected networks of molecule chains, polymers can be classified as (a) crystalline, if they have long range order, and (b) amorphous if they lack such order.

**Table 2.8 :** Biomedical application of polymeric biomaterials. Table compiled from [174-176]

Synthetic polymer	Applications
Polyvinylchloride (PVC)	Blood and solution bags, surgical packaging, IV infusion sets, dialysis devices, cardiac catheters, bottles, connectors and cannulas, artificial limbs, artificial hearts
Polyethylene (PE)	Pharmaceutical bottles, nonwoven fabric, catheter, pouch, flexible containers, orthopaedic implants
Polypropylene (PP)	Disposable syringe, blood oxygenator membrane, suture, nonwoven fabric, artificial vascular grafts
Polymethylmethacrylate( PMMA)	Blood pumps and reservoirs, membrane for blood dialyzer, implantable ocular lens, bone cement, artificial teeth, bone prostheses, cranial bone replacement
Polystyrene (PS)	Tissue culture flasks, roller bottles and water filters
Polyethyleneterephthalate (PET)	Implantable suture, mesh, artificial vascular graft, heart valve
Polytetrafluoroethylene (PTFE)	Catheters, artificial vascular grafts, retinal detachment, femoral stem
Polyurethane (PU)	Film, tubing, artificial heart pump materials, balloons, heart valve prostheses, coating for blood compatibility
Polyamide (nylon)	Packaging film, catheters, suture and mould parts
Silicone rubber	Hydrocephalus shunt, catheter, membrane for oxygenator, artificial skin, plastic surgery implant, artificial hearts, drug release system, ear prostheses, finger joint repair, tracheal prostheses, bladder prostheses, intestine patch, heart pacemaker leads, tendon
Polyester * polycatic acid, polyglycolic acid polycaprolactone, polyhydroxy butyrate, polyhydroxyvalerate	Vascular graft prostheses, fixation device for tissue, hernia repair, patches for heart, bladder, arteries, sutures, controlled release and tissue engineering,
UHMWPE	Acetabulum in total hip prostheses, artificial knee prostheses
Polycarbonates*	Membrane of oxygenator, hemodialyzer, plasmapheresis membrane
Polyanhydrides*	Controlled delivery of anticancer agent
Hydrogels	Controlled drug release, tissue regeneration scaffolds, cell and DNA encapsulation, contact lens, wound healing dressing, biosensor

• Note : \* Biodegradable polymer [175] (p.106)

With respect to their mechanical behaviour with rising temperature, polymers can be divided into two general categories: thermoplastics and thermosets. Thermoplastic

polymers are solid polymers that can be reshaped by increasing the temperature above their glass transition temperature ( $T_g$ ), and include nylon, polyethylene, polyurethane, polysulfone, polyacetal, etc. The glass transition temperature is a very important factor for polymers, representing the transition temperature of a polymer from viscous to solid. The polymer is rubbery above this temperature and gradually decreases in viscosity until the melting temperature is reached. In contrast, thermoset polymers cannot be reshaped after they are crosslinked, and include examples such as vulcanised rubber, used in prostheses and selected cardiovascular catheters. This material is relatively hard and is not able to be softened by increasing the temperature. Increasing temperatures can cause chemical decomposition of the materials without remelting [171] (p.507). Elastomeric materials for biomedical application are a special subset belonging to both thermoplastic and thermosets and, depending on the conditions, can be classed as either a thermoset or thermoplastic in nature. For example polyurethane and thermoplastic vulcanisates are included as thermoplastic elastomers, while silicone and natural rubber are categorised as crosslinked/thermoset elastomers [177]. The elastomeric materials are commonly used in peripheral intravenous and central venous catheters.

Polymers are used in a wide variety of biomedical applications such as in cardiovascular devices (*e.g.* vascular graft), membranes in extracorporeal bioactive membranes for controlling release delivery systems, suture and adhesives, reconstructive and orthopaedic implants, ophthalmic devices, dental restoratives, disposable equipment and degradable plastic products [172] (p.270).

Synthetic polymers can be further sub-divided into biodegradable types and non biodegradable types [174] (p.15). The biodegradable polymers are used as implant materials, which are gradually replaced by regenerating tissue *in vivo*, breaking down into biocompatible products and subsequently metabolised or eliminated from the body by hydrolytic and enzymatic degradation [174] (p.15). For example, poly(lactic acid), poly(glycol-acid) poly(lactide-coglycolide), are categorised as synthetic biodegradable polymers [175] (p.66), whereas collagen, chitin and starch are classified as natural biodegradable polymers [67].

Another useful category of polymeric biomaterials is hydrogels. Hydrogels are water swollen, cross-linked networks of hydrophilic polymer chain structures produced by the simple reaction of one or more monomers or by association bonds such as hydrogen bonds and strong Van der Waals interactions between chains [178]. Hydrogels have important properties such as *in situ* formability, responsive swelling and biodegradable natural tissue-like properties, and can be crosslinked by heat and radiation [174] (p.16). Hydrogels have been developed for medical and pharmaceutical applications, such as controlled drug release, tissue regeneration scaffolds, cell and DNA encapsulation, contact lenses, wound healing dressing and biosensors [174] (p.17). The biomedical applications of polymeric biomaterials are summarised in Table 2.8.

The use of polymers has, however, limitations as the mechanical properties of polymers (exhibiting low elastic modulus and low strength) do not meet the mechanical requirements for load bearing orthopaedic applications. The hydrophilic characteristic of some polymers, the absorption of liquids and swelling, and the release of undesired products such as monomers, fillers, and plasticisers has restricted their use, depending on the application. Another important consideration when choosing polymers for medical applications is that sterilisation processes may affect the polymer properties [176] (p.66). Common techniques for sterilising medical devices such as dry heat, autoclaving, radiation and ethylene oxide gas, may potentially deteriorate or oxidise the polymer due to the lower thermal and chemical stability of polymers compared to other materials such as metals and ceramics. For example, dry heat sterilisation requires temperatures between 160-190°C, which is above the transition temperature ( $T_g$ ) or the melting temperature of many polymers such as polyethylene and PMMA. Steam sterilisation (autoclaving) is performed under steam pressure at lower temperatures (~130°C), yet there are potential side reactions between water vapor and some polymers such as PVC, polyacetals, LDPE and polyamides. The use of radiation sterilisation by using the isotope  $^{60}\text{Co}$  has the potential of changing properties through dissociation or cross-linking of the polymer chain. Chemical treatments with such as ethylene and propylene oxide gas or phenolic and hypochloride solutions are commonly used for sterilisation, since this treatment is performed at low temperatures and most polymers are relatively inert in these treatments.

### 2.3.2.3 Ceramic biomedical materials

Ceramics are inorganic, non-metallic materials which exhibit relatively high level in compressive strength, inertness, wear resistance and resistance to degradation in corrosive environments, all of which make the ceramic useful for biomedical applications[67]. Ceramics include metallic oxides, carbides, silicates and various refractory hydrides, sulfides and selenides [179] (p.8). Other characteristics are (1) high melting points, (2) a low conductivity of electricity and (3) low thermal conductivity [180] (p.22). These properties are due to the chemical bonding within the ceramics. The first use of ceramics in biomedical applications was as plaster of Paris as a casting material [76]. In recent years, newer types of ceramics have been developed and have been increasingly used in biomedical applications due to their strength and inertness [181, 182]. According to the tissue response there are three types of bioceramic as follows: (1) bioinert, (2) bioactive or surface reactive ceramics and (3) biodegradable or reabsorbable bioceramics.

Bioinert ceramics are biocompatible materials that maintain their physical and mechanical properties while in the host. The bioinert ceramic does not induce a biological response and is non-carcinogenic in the body; the body usually forms a thin fibrous tissue to encapsulate the ceramic due to immunoreactions [95]. If the bioinert devices are implanted with a very tight mechanical fit and the in-service load is compressive, the implantations are very successful. On the other hand, when the implants are loaded allowing micromotion between the implant and the tissue, the fibrous tissues thicken to several hundred micrometers thick, leading to quick implant loosening [183] (p.74). Examples of the bioinert ceramics include aluminium oxide (alumina,  $Al_2O_3$ ), zirconium oxide (zirconia,  $ZrO_2$ ), silicon nitrides, calcium aluminates, and pyrolytic carbon [180] (p.23). In considering ceramics for use in orthopaedic applications in which a porous ceramic is employed for promoting bone ingrowth, concern has been raised about the effect of aging in the body environment, due to a possible decrease in mechanical properties. Frakes *et al.* [184] evaluated porous alumina with a theoretical density of approximately 65% for changes in strength by *in vivo* aging in rabbits and *in vitro* aging using deionised water and bovine blood. The conclusion of this work indicates that porous alumina exhibits a decrease in strength, flexure strength and static fatigue strength, depending on the

medium employed. A similar finding was also presented by Kerner *et al.* [185], who evaluated the changes in strength of a 72% theoretical density calcia-stabilised zirconia for *in vitro* (Ringer's solution) and *in vivo* (rabbits) aging. Using calcium aluminates for testing changes in strength due to aging *in vitro* (Ringer's solution) and *in vivo* (rabbits), Schnittgrund *et al.* [186] also found similar decreases in strength. On the other hand, fully dense alumina [187] and commercial zirconia [188] show no reduction in flexural strength after aging in Ringer's solution. Bioinert ceramics are commonly employed as structural supports and are popular in orthopaedic applications such as femoral heads and the components of total and partial hips. Non-structural support applications include sterilisation devices, ventilation tubes, drug delivery systems and repairing diseased heart valves and blood vessels [177] (p.15, p27).

Common techniques to improve the interfacial attachment of implant material involve the use of bioactive ceramic materials. Bioactive ceramics have the ability to chemically bond with adjacent tissue upon implantation in the host. The bioactive ceramics include Bioglass<sup>®</sup>; bioactive glass ceramics such as Ceravita<sup>®</sup>, A-W glass ceramics<sup>®</sup> or machinable glass ceramics; and dense hydroxyapatites such as Durapatite<sup>®</sup> or Calcitite<sup>®</sup> [183] (p.75). The bioactive glass ceramics (Bioglass<sup>®</sup> and Ceravital<sup>®</sup>) are mainly composed of SiO<sub>2</sub>, CaO, Na<sub>2</sub>O and P<sub>2</sub>O<sub>5</sub>. The simultaneous formation of calcium phosphate and a SiO<sub>2</sub>-rich film layer on the surface are attributed to the bonding of the ceramic glass to bone/host tissue [180] (p.39). These bioactive ceramics are available in bulk or in the form of a coating on other materials for interfacial bonding with adjacent tissues [179] (p.8). Examples of the use of this bioactive ceramic are as bone plate screws, as replacements of middle ear ossicles, for coating of metal prostheses, in reconstruction for dental defects and in replacing subperiosteal teeth.

Bioabsorbable materials offer gradual degradation over time and potential complete replacement by endogenous tissue resulting in normal, functional bone when used in orthopaedic applications. Materials classified as bioabsorbable ceramics include calcium phosphate, hydroxyapatite, calcium sulphate dehydrate (plaster of Paris), Tricalcium Phosphate (TCP), Zinc-Calcium-Phosphorous Oxide (ZCAP) [189], Zinc-Sulphate-Calcium Phosphate (ZSCAP) [190], and Ferric-Calcium-Phosphorus

Oxide (FECAP) [191]. The rate of degradation and of osteoid formation is variable depending on the material type. A typical reduction in the mechanical properties of the materials during the absorption process, resulting in a decrease in loading capacity over the integration, has been noted [67]. Bioabsorbable ceramics have been used in orthopaedic applications such as repairing bone damage, repairing maxillofacial and dental defects, repairing spinal and lumbo-sacral vertebrae, filling space in bone fixation devices and diseased bone loss, and as a drug delivery device [180] (p.29).

Although ceramics have many advantages as discussed above, they also have disadvantages due to their brittleness, high elastic modulus and high specific modulus, low fracture toughness, lack of resilience, relatively high density and low mechanical reliability [192] (pp.177-193) and [171] (pp.451-452).

#### **2.3.2.4 Composite biomedical materials**

Composites refer to a material composed of two or more distinct constituent biomaterials, namely, the reinforcement (inclusive materials) and matrix, macroscopically combined resulting in specific and advanced characteristics and properties [193] (p.1) and [194] (p.214). Within the mixture constituents can still be identified, with each constituent and interface separating the constituents being an important factor for transferring force. The main advantage of the composite materials compared with the other homogeneous materials such as metals, ceramics and polymers, is that their biological, mechanical and physical properties can be tailored to meet the requirements of specific application. The properties of composite materials are determined by several factors, *i.e.* geometry, orientation and the volume fraction of the inclusive material, and also the interface between the constituents. Composites can be classified according to the matrix materials used such as metal matrix composites, ceramic matrix composites and polymer matrix composites. Most composites used in biomedical applications are polymer matrix composites [195] (p.9.3). There are two main types of composite material based on reinforcement shape, namely particulate composites and fibrous composites [196] (p.4)

A particulate composite is a composite material in which, the inclusions take the form of particles. These composites tend to be more isotropic, *i.e.* the same properties in any directions, rather than anisotropic. Examples of the particulate composites are; bone particles impregnated in PMMA cement, used to improve the fatigue life and stiffness [197], and the inclusion of silica particles into rubber in catheters and gloves to improve their strength [198] (p.83). Cellular solids or porous materials are particulate composites using air as the inclusive phase [198] (p.87) and constitute a special class of particulate composites. The presence of voids or pores will reduce the stiffness of the materials. This porous structure is acceptable and desirable for some purposes such as thermal insulation, filtering, lightweight structures, shock absorbance and for encouraging tissue ingrowth in biomedical applications. This type of material will be discussed in Section 2.5.

Fibrous composites, otherwise known as fibre-reinforced composites, are composite materials consisting of fibres embedded into a matrix. A fibre is characterised by its length being much greater than its cross sectional dimensions. The main reinforcement materials that have been used in biomedical composites are carbon fibres, polymer fibres, ceramic fibres and glass fibres [199] (p.94). Mostly, composites in biomedical applications are aimed at hard tissue application such as bone repairing, joint replacement and dental application. For example, carbon fibre (CF) has been incorporated in various non-biodegradable polymer matrices for bone plate including CF/epoxy [200, 201], CF/PMMA, CF/PP, CF/PS, CF/PE, CF/PEEK [64]. The CF/PEEK composite has shown promise in strength [202] and biocompatibility [203], although toxic effects of the monomer in an uncured epoxy composite remain a concern [203, 204]. Carbon fibres are also embedded in biodegradable polymers for bone plates, in order to improve their mechanical properties, resulting in partially absorbable composites such as CF/PLA, although rapid loss of mechanical properties due to delamination has been reported [205]. Faster bone bonding in composite CF/C stems compared to high stiffness conventional implants due to the lower elastic modulus has been reported. It has also been found that the stems were stable and exhibited high static and fatigue strength [206]. A hip prosthesis fabricated with CF/epoxy by laminating 120 layers of unidirectional plies and stacking sequences has been introduced by Chang *et al.* [207]. Composite biomaterials offer an alternative to overcome many drawbacks of

the homogenous biomaterials. However, clinical reports revealed that most clinical applications such as hip arthroplasties have failed due to composite failure [208], poor implant design [209] or as a result of accumulation of wear debris due to increased implant-bone interface stress [210]. Inadequate manufacturing methods producing poor quality CF/PEEK bone plates is still a major challenge [211]. Although there are many theoretical advantages of less rigid plate fixation of long bones, fracture of fixation plates made of carbon fibre-reinforced polymer did not result in clinical success. Some issues related to biocompatibility [203, 204] and mechanical properties [205] of the composites have been noted.

## **2.4 Titanium and titanium alloys for biomedical applications**

### **2.4.1 Metallurgical aspects**

Titanium ranks as the fourth of the most plentiful of the structural metals and the ninth most abundant element in the earth's crust, and is found as rutile and ilmenite deposits [212]. The largest deposit of rutile is found in Australia (50%) followed by South Africa and India with 18% and 16%, respectively, and major deposits of ilmenite are found in China (30%), Australia (17%), India (13%), Brazil (10%) and South Africa (10%) [213]. Titanium was first discovered in 1791 by W. Gregor, an English mineralogist, as isolated black sand now known as ilmenite. In 1932, significant quantities of pure titanium were produced by W.J. Kroll, whose name is given to the means of extracting titanium (Kroll Process). It became commercially available and was patented in 1938. However, titanium processing from metal ore is an expensive process due to its high reactivity with oxygen, leading to an instantaneous formation of an oxide surface layer which is highly passive in nature [214]

Titanium is a hard, silvery-grey metallic element with a melting point of 1670°C. At room temperature, titanium has a hexagonal unit cell of the  $\alpha$  phase, with values of the lattice parameters  $a$  (0.295 nm) and  $c$  (0.468 nm). Pure titanium undergoes an allotropic transformation at 882.5°C [215] (p.2), altering from  $\alpha$  phase with hexagonal close-packed (hcp) crystal structure below the allotropic temperature to  $\beta$  phase with body-centered cubic (bcc) crystal structure above the temperature, and

this remains stable up to the melting point. The existence of the two phases with different crystal structures, *i.e.* hcp and bcc and the corresponding allotropic transformation temperatures are very important for the many varieties of microstructure, and further, properties in titanium. Since titanium is a transition metal having an incomplete electron shell, it allows the development of solid solutions with a number of substitutionally dissolved elements; hence the exact allotropic temperature for alloys is determined by the additional alloying elements [215]. Based on their influence on the allotropic temperature, alloying elements of titanium are classified into  $\alpha$  stabilisers,  $\beta$  stabilisers and neutrals (Figure 2.8). The alloys possess a high specific strength, with strengths similar to that of steels, whilst the densities are approximately 60% of that of steel.

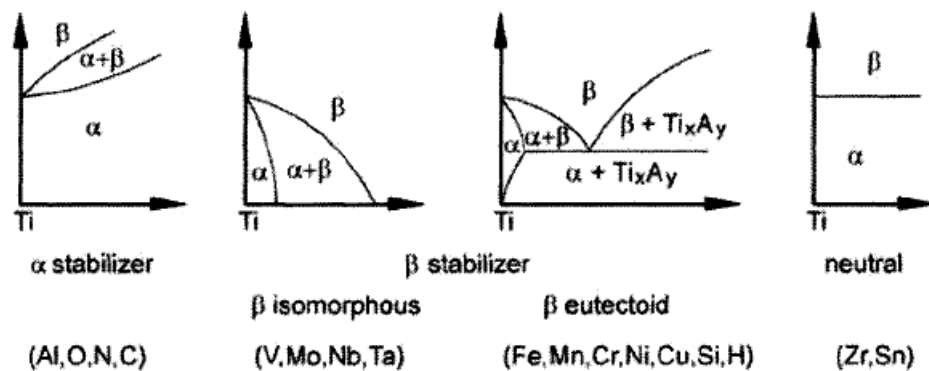


**Figure 2.8** : Schematic diagram of influence of alloying elements on phase diagram of titanium alloys [216] (p.22)

Alloying elements leading to an increase in the phase transformation temperature, generally non-transition metals such as aluminium, oxygen, nitrogen and carbon, are categorised as  $\alpha$  stabiliser elements. On the other hand, elements dissolved in titanium which decrease the allotropic transformation temperature are known as  $\beta$  stabilisers, and generally comprise the transition metals and noble metals [215, 217]. The  $\beta$  stabiliser elements are divided into  $\beta$  isomorphous elements (*e.g.* vanadium, niobium, molybdenum, and tantalum) and  $\beta$  eutectoid-forming elements (*e.g.* iron, manganese, chromium, nickel, copper, silicon, hydrogen). Neutral elements produce no significant change in the transformation temperature (*e.g.* tin,

zirconium) [217]. However, investigations carried out by Geetha *et al.* [218] and Tang *et al.* [219] have demonstrated that the addition of zirconium stabilises the  $\beta$  phase in tertiary Ti-Zr-Nb, systems. In addition,  $\omega$  phase (simple hexagonal titanium phase) formation in high  $\beta$  stabilised alloys is also delayed, leading to a decrease in the elastic modulus. Some of the basic physical properties of the unalloyed titanium and the alloying elements, *e.g.* niobium, tantalum and zirconium are presented in Table 2.9.

**Table 2.9 :** Summary of physical properties of the unalloyed metals used in this work, *i.e.* titanium, niobium, tantalum and zirconium

Property	Titanium (Ti)[119]	Niobium (Nb)[220]	Tantalum (Ta)[220]	Zirconium (Zr)[220]
Atomic number	22	41	73	40
Atomic weight	47.867	92.906	180.948	91.224
Allotropic transformation temperature (°C)	882.5	-	-	863
Lattice structure [221]	$\leq 882^\circ\text{C}$ Alpha : hcp, c(Å) : 4.6826 a (Å) : 2.9505 $\geq 882^\circ\text{C}$ Beta : bcc, , a(Å) : 3.3065	Beta : bcc a (Å) : 3.3066	Beta : bcc a(Å) : 3.3058	$\leq 863^\circ\text{C}$ Alpha : hcp, c (Å) : 5.1475 a (Å) : 3.2316 $\geq 863^\circ\text{C}$ Beta : bcc, a(Å) : 3.6090
Density (20°C) (g/cm <sup>3</sup> )	4.51	8.57	16.65	6.51
Coefficient of thermal expansion, $\alpha$ , at 20°C(K <sup>-1</sup> )	$8.4 \times 10^{-6}$	$7.07 \times 10^{-6}$ *	$6.6 \times 10^{-6}$	$5.7 \times 10^{-6}$
Thermal conductivity (W/(m.K))	19.2	53.7	57.5	22.7
Melting temperature (°C)	1668	2468	2996	1857
Young's modulus, E, (GPa)	100-145[222] 3	104.9[223]	185.7[224]	98[225]
Yield strength, $\sigma_{ys}$ , (MPa)	140[222] <sup>3</sup>	105 <sup>1</sup> [223]	170 <sup>1</sup> [224]	276[226]
Ultimate tensile strength, $\sigma_u$ , (MPa)	235[222] <sup>3</sup>	195 <sup>1</sup> [223]	285 <sup>1</sup> [224]	379[226]
		585 <sup>2</sup> [223]	650 <sup>2</sup> [224]	

Noted : <sup>1</sup> Annealed , <sup>2</sup> Cold worked , <sup>3</sup> Reference [222] (p. 20)

According to the nature of their microstructure at room temperature titanium alloys are generally classified into  $\alpha$  alloys,  $\alpha+\beta$  alloys and  $\beta$  alloys as shown in Table 2.10, with further subdivision into near- $\alpha$  alloys and metastable  $\beta$  alloys [215] (pp. 2-

4). The  $\alpha$  type titanium alloys are mainly fabricated from commercially pure titanium, and alloyed with  $\alpha$  stabilising elements singly or in combination, resulting in microstructures of  $\alpha$  phase at room temperature. The  $\alpha$  type titanium alloy is characterised by the lack of a heat treatment response, since it consists entirely of  $\alpha$  phase or only a small amount of the metastable  $\beta$  phase remaining (2-5 vol%) after cooling from high temperatures [216] (p.31). The alloys show acceptable strength, good toughness, high creep resistance, good weldability due to their heat treatment insensitivities, poor forgeability particularly at temperatures below the beta transus, and due to the absence of a ductile-brittle transition, they are suitable for cryogenic applications [215] (p3).

**Table 2.10 :** Mechanical properties of selected titanium and its alloys for biomedical application. Adapted from [69, 139, 227]

Materials	Standard	Tensile strength (MPa)	Elastic Modulus (GPa)	Elongation (%)
$\alpha$ type				
Pure Ti grade 1	ASTM F67	240	102.7	24
Pure Ti grade 2	ASTM F67	345	102.7	20
Pure Ti grade 3	ASTM F67	450	103.4	18
Pure Ti grade 4	ASTM F67	550	104.1	15
$\alpha+\beta$ type				
Ti-6Al-4V	ASTM F1472	895-930	110-114	6-10
Ti-6Al-4V ELI	ASTM F136	860-965	101-112	10-15
Ti-6Al-7Nb	ASTM F1295	900-1050	114	8.1-15
Ti-5Al-2.5Fe	ISO 5832-10	1020	112	15
$\beta$ type				
Ti-12Mo-6Zr-2Fe	ASTM F1813	1060-1100	74-85	18-22
Ti-15Mo	ASTM F2066	874	78	21
Ti-15Mo-5Zr-3Al	ISO 5832-14	852-1100	80	18-25
Ti-15Mo-2.8Nb-0.2Si	-	979-999	83	16-18
Ti-15Mo-3Nb-0.3O(21SRx)	-	1020	82	N/A
Ti-13Nb-13Zr	ASTM F1713	973-1037	79-84	10-16
Ti-35.3Nb-5.1Ta-7.1Zr	F-04.12.23	547.1	55	19
Ti-35Nb-5Ta-7Zr-0.4O	-	1010	66	N/A
Ti-29Nb-13Ta-4.6Zr	-	911	67-80	13.2
WQ			63[74]	
WQ Aged			97[74]	
WQ+CW			62[74]	
Ti-25Ta	-	560	64[228]	20
Ti-24Nb-4Zr-7.9Sn [228]	-	800-1200	33-42	5

The  $\alpha+\beta$  type titanium alloys have compositions with a high enough amount of  $\alpha$  and  $\beta$  stabiliser to result in a mixture of  $\alpha$  and  $\beta$  phases at room temperature. Due to the existence of both phases, the alloys exhibit higher strength and toughness than the  $\alpha$  type alloys. Alloys which contain in equilibrium a volume fraction of  $\beta$  phase less than 10% are often known as near- $\alpha$  alloys [216] (p.33), whereas alloys containing a higher  $\beta$  phase of about 10-30% are termed  $\alpha+\beta$  alloys [69]. Among the  $\alpha+\beta$  alloys, Ti-6Al-4V is the most commonly used and intensively developed and tested, especially in the aerospace industry [229] and as a biomaterial, mainly in orthopaedic implant devices [218]. The mechanical properties of the  $\alpha+\beta$  alloys are tailored by composition, thermal treatment and thermo-mechanical treatment conditions to adjust the microstructural and precipitational states of the  $\beta$  component.

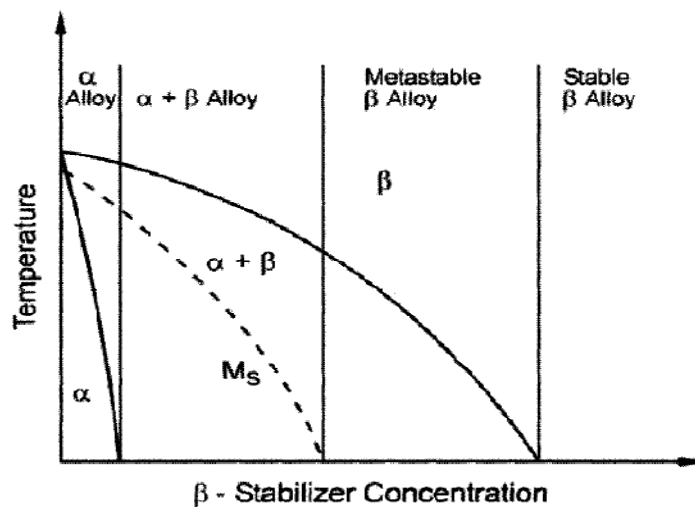


**Figure 2.9** : Pseudo-binary schematic phase diagram of  $\alpha$ ,  $\alpha+\beta$  and  $\beta$  titanium alloy [216]

As mentioned in Table 2.10, all alloys in the group of  $\beta$  alloys are classified as metastable  $\beta$  alloys because the presence of retained  $\beta$  phase is obtained by appropriate heat treatments, whereas stable  $\beta$  alloy located in the  $\beta$  single phase field (Figure 2.9) does not exist in commercial materials [216] (p33). The term “ $\beta$  type titanium alloys” used throughout this work thus refers to metastable  $\beta$  alloys. The  $\beta$  type titanium alloys are obtained by the addition of high amounts of  $\beta$  stabilising

elements. The additions allow a decrease in the  $\beta$  transus temperature and also enable a lowering of the martensite formation temperature (martensite start temperature,  $M_s$ ). Thus, the transformation from the elevated temperature  $\beta$  phase to  $\alpha$  phase will be constrained, allowing a number of metastable transformations to occur [230]. A single microstructure metastable  $\beta$  phase can be microscopically observed from elevated temperature  $\beta$  phase under the condition of solution-treatment followed by quenching (STQ) into ice water [231]. However, in general, elevated temperature  $\beta$  phase partially transforms into  $\omega$  phase and/or martensitic  $\alpha$  during the quenching processing, depending on cooling rate and alloy composition [219] as shown by Figure 2.10. Metastable  $\omega$  phase, with a simple hexagonal structure [232], can be formed either by quenching from the  $\beta$  field or during isothermal aging at intermediate temperatures after quenching [215]. The former is designated as  $\omega_{\text{ath}}$  phase and the later named as  $\omega_{\text{iso}}$  phase. Martensitic transformations may be found in one of two types of martensitic structures, hexagonal  $\alpha'$  martensite or orthorhombic  $\alpha''$  martensite [219]. The hexagonal  $\alpha'$  martensite is found if a titanium alloy with fewer  $\beta$  stabilising elements is rapidly by cooled to room temperature [233]. This hexagonal structure will distort and its hexagonal symmetry is lost. Orthorhombic  $\alpha''$  martensite will form instead with increasing  $\beta$  stabiliser content [234]. The martensitic  $\alpha$ , known as stress induced martensite, can also be produced from metastable  $\beta$  phase in a titanium alloy with low level  $\beta$  stabilising elements by using cold work processing at ambient temperature [235, 236].

The advantages of the  $\beta$  type titanium alloys are that they have high hardenability, excellent forgeability, can be deformed at low temperatures, exhibit high corrosion resistance [74], can be strengthened to high strength levels [237] [212] (p.31) and have a lower elastic modulus compared to  $\alpha$  titanium and  $\alpha+\beta$  titanium alloys [110]. The disadvantages of the alloys are higher density than that of  $\alpha+\beta$  alloys [238] (p.37). In this regard, the properties of titanium alloys are attributed to alloy composition, metallurgical processing conditions and the relative proportion of the phases/microstructure formed [217, 239-241].

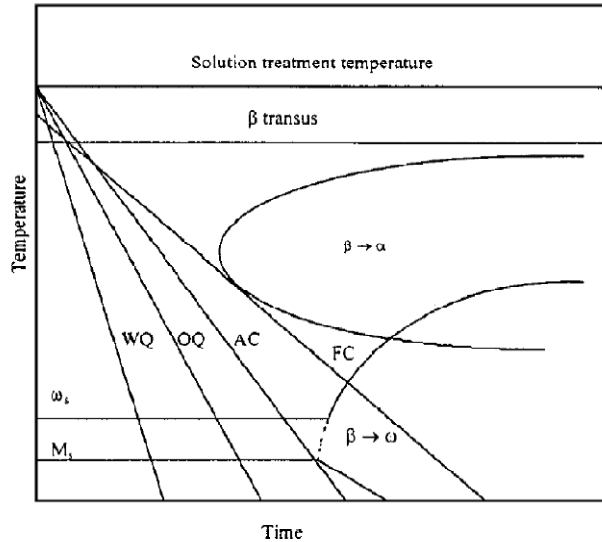


**Figure 2.10** : A schematic TTT diagram for  $\beta$  phase transformation in titanium alloy with  $\beta$  stabilising elements [219]

## 2.4.2 Biocompatibility, thermomechanical processing and mechanical properties of titanium and its alloys

Titanium and titanium alloys are considered as attractive materials for applications in aerospace [229, 242, 243], military [244], biomedical [74, 245], chemical, automotive, sports and many other industries [217] (pp.330-356). In biomedical applications, the use of titanium and its alloys is significant due to their remarkable properties, namely, good corrosion resistance [246], good biocompatibility [102, 210], high specific strength [102] and good biomechanical properties [112, 247], despite  $\alpha$ -Ti (CP Ti) and  $\alpha+\beta$  alloy (Ti-6Al-4V and Ti-6Al-4V ELI) alloy originally being developed for aerospace applications [229, 243]. CP Ti grade 4 (ASTM F67) and Ti-6Al-4V ELI (ASTM F136) are the most utilised and representative titanium alloys for implant materials [218]. The mechanical strength of CP Ti is relatively low compared to the normal threshold considered for hard tissue replacement. Improvement in strength has been achieved by increasing the oxygen content. Accordingly, CP Ti is available in four grades with a doubling of oxygen content from 0.18% for CP Ti grade 1 to 0.4 % for CP Ti grade 4. The increase in strength is accompanied with a decrease in elongation at failure from 24% for CP Ti grade 1 to 15% for CP Ti grade 4 as shown in Table 2.10 and Table 2.11.

Strength enhancement of CP Ti grade 4 increases its use. An alternative method to strengthen CP Ti grade 2 using equal channel angular processing (ECAP) has been reported [208]. This method develops an ultra-fine grain structure that enhances the mechanical properties of the alloy, including hardness, ultimate tensile strength (increased by 140%), fatigue strength (increase by 100%) compared to coarse grained commercially pure titanium grade 2 [245]. With respect to mechanical properties, the  $\alpha$  and  $\alpha+\beta$  type titanium alloys exhibit much lower elastic moduli than those of conventional stainless steel and cobalt-based alloys. In addition, their strengths are very close to that of stainless steel, whereas their densities are ~45% less than that of steel

**Table 2.11** : Specification chemistry limit for commercially pure (CP),  $\alpha+\beta$  and metastable  $\beta$  type titanium alloys. Adapted from [248] and [249]

Materials	Standard	Fe max	O max	N max	C max	H max	Al	V	Mo	Sn	Nb	Ta	Zr	Ti
$\alpha$ type														
Pure Ti grade 1	ASTM F67	0.2	0.18	0.03	0.08	0.015								Bal
Pure Ti grade 2	ASTM F67	0.3	0.25	0.03	0.08	0.015								
Pure Ti grade 3	ASTM F67	0.3	0.35	0.05	0.08	0.015								
Pure Ti grade 4	ASTM F67	0.5	0.4	0.05	0.08	0.015								
$\alpha+\beta$ type														Bal
Ti-6Al-4V	ASTM F1472	0.3	0.2	0.05	0.08	0.015	5.5-6.75	3.5-4.5						Bal
Ti-6Al-4V ELI	ASTM F136	0.25	0.13	0.05	0.08	0.012	5.5-6.5	3.5-4.5						Bal
Ti-6Al-7Nb	ASTM F1295	0.25	0.2	0.05	0.08	0.009	5.5-6.5				6.5-7.5			Bal
Ti-5Al-2.5Fe	ISO 5832-10	2.0-3.0	0.2	0.05	0.08	0.015	4.5-5.5							Bal
$\beta$ type														Bal
Ti-12Mo-6Zr-2Fe	ASTM F1813	1.5-2.5	0.28	0.05	0.05	0.015			10.0-13.0				5.0-7.0	Bal
Ti-15Mo	ASTM F2066	0.1	0.2	0.05	0.1	0.015			14.0-16.0					Bal
Ti-15Mo-5Zr-3Al <sup>a</sup>	ISO 5832-14						3.8		15.0				5.0	Bal
Ti-13Nb-13Zr	ASTM F1713	0.25	0.15	0.005	0.008	0.012					12.5-14.0		12.5-14.0	Bal
Ti-35Nb-7Zr -5Ta	F-04.12.23	0.25	0.75	0.02	0.02	0.02					34.0-37.0	4.5-6.5	6.3-8.3	Bal
Ti-29Nb-13Ta-4.6Zr <sup>b</sup>		0.05	0.16	0.02	0.04	<0.02					29.2-30.2	11.6-12.4	4.3-4.8	Bal
Ti-25Ta <sup>c</sup>			0.082									25		
Ti-24Nb-4Zr-7.9Sn <sup>d</sup>			0.11		0.008	0.006				7.85	24.1		3.92	

**Notes :**

Superscripts <sup>a,b,c,d</sup> indicate experimental alloys

<sup>a</sup> [249], <sup>b</sup> [231, 250, 251], <sup>c</sup> [228], <sup>d</sup> [140]

Titanium and its alloys are also known to be relatively inert and have good corrosion resistance because of the surface oxide film. This oxide film is spontaneously formed in air as a thin, (5-10 nm thick [252]) titanium dioxide ( $\text{TiO}_2$ ) passivation layer, which is described as a stable crystalline form that is more closely related to ceramics than to metals in its interactions with surrounding tissue behaviour [253] (p.168). The surface oxide exhibits positive effects in host response and demonstrates an ability to react with mineral ions, water, protein and other constituents of biofluids and that these reactions in turn cause a remodeling of the surface [253] (p.86), [254, 255].

Although titanium and its alloys, principally Ti-6Al-4V, have excellent properties in terms of biocompatibility and corrosion resistance, the release of vanadium from the alloys raises a concern for long term performance. Vanadium has been noted to be toxic in the elemental state and as vanadium oxides [107, 108, 256]. Vanadium oxide is formed at the alloy surface due to passivation. This oxide is thermodynamically unstable compared to  $\text{TiO}_2$  and  $\text{Al}_2\text{O}_3$ , and passes into solution. In response to this finding, Ti-6Al-7Nb was developed to obtain an  $\alpha+\beta$  type titanium alloy without vanadium [257], and also to enhance the wear resistance [258]. This alloy also shows the same  $\alpha+\beta$  structure as Ti-6Al-4V and demonstrates equally good mechanical properties (Table 2.10) and corrosion resistance. Another vanadium-free titanium-based alloy, Ti-5Al-2.5 Fe [259], was also developed. This alloy, which is categorised as an  $\alpha+\beta$  alloy, shows a higher  $\beta$  phase content - more than 15%, than that of Ti-6Al-4V, and exhibits good wear resistance and corrosion resistance [259]. Ti-6Al-7Nb has been registered in both ASTM and ISO standardisation (F1295-92 and ISO 5832-11), while Ti-5Al-2.5Fe has been registered in ISO standardisation (ISO 5632-10) for biomedical applications. These alloys show that vanadium was successfully substituted by niobium and iron in Ti-6Al-4V. These alloys, however, contained aluminium of which the effects on the immune function are still a controversial. Some research has shown that aluminium suppressed the immune function [260, 261], but other studies observed the opposite results [262, 263].

The  $\alpha$  and  $\alpha+\beta$  type titanium alloys are also known to possess low shear strength and low wear resistance [8]. These negative properties imply that titanium and its alloys

tend to suffer wear when they are rubbed between themselves or with other metals [264]. The released wear debris may cause inflammatory reactions and implant loosening. Another concern is that the elastic moduli of the  $\alpha$  and  $\alpha+\beta$  type titanium alloys are still found to be much higher than that of cortical bone. This mismatch in the elastic modulus may eventually lead to bone resorption due to the stress shielding effect. This limitation has encouraged biomedical researchers to develop metallic implants with mechanical properties more closely matching those of human bone.

Young's modulus, one of the intrinsic properties of materials, is determined by the bonding force between atoms, which is in turn associated with the crystal structure and the distance between atoms (represented by the unit cell volume or lattice parameter [265]), which can be affected by heat treatment and alloying additions [16, 266, 267]. A comparison between the slip systems and crystal structures of the different phases of titanium has led to the conclusion that the bcc structure has a lower elastic modulus and is easier to plastically deform than the hcp structure [268] [214] (pp.4-5). In this regard, the Young's moduli of  $\beta$  type titanium alloys, which predominantly consist of  $\beta$  phase with bcc crystal structure, are known to be lower than those of  $\alpha$  or  $\alpha+\beta$  type titanium alloys. In addition,  $\beta$  type titanium alloys exhibit low temperature workability [74] and high strength [237] [212] (p.31). Therefore, the research and development of low stiffness  $\beta$  type titanium alloys for biomedical applications is attracting a great deal of interest [219, 240, 241, 265, 269].

In the development of titanium alloys for biomedical applications, the heat treatment process and the selection of alloying elements, in this case  $\beta$  stabilising elements, are known to be important factors. Not all elements with  $\beta$  stabilising properties in titanium alloys are suitable for biomedical applications. Corrosion and wear processes cause a release of these elements into the surrounding tissue that may harm the living body. In this regard, besides the alloying elements being selected as  $\beta$  stabilising elements [270] (p.9), if they are compatible in their pure form they have a greater potential to be used in alloy form, with issues such as good interaction with the neighbouring cells or tissues, non toxic and non cytotoxic, non allergenic and high polarisation resistance (corrosion resistance) [10, 271] being important factors.

As a result the elements niobium, tantalum and zirconium, known to possess low toxicity and good cell interaction [15] have been identified as the most biocompatible alloying elements in titanium, followed by molybdenum and tin [74]. In addition, Song *et al.*[16] who theoretically studied the effect of alloying elements on the strength and modulus of binary  $\beta$  type titanium alloys (Ti-M alloy, M = vanadium, chromium, manganese, iron, zirconium, molybdenum, tungsten and tantalum) using the discrete variational cluster method (DVM) as a fundamental approach, suggested that  $\beta$  stabilising elements, *e.g.* niobium, tantalum, zirconium and molybdenum can be added to decrease the elastic modulus of  $\beta$  type titanium alloys without sacrificing strength.

Subsequently  $\beta$  type titanium alloys with low elastic modulus values, based on the Ti-Mo system, have been developed in the recent past, including Ti-12Mo-6Zr-2Fe (TMZF<sup>®</sup>, Howmedica Osteonic Corp USA, standardized by ASTM F1813), [272], Ti-15Mo-5Zr-3Al (Kobe Steel Ltd, Japan) [42, 273, 274], Ti-15Mo-3Nb-3O (TIMETAL 21SRx)[275], and Ti-15Mo (ASTM F2066) [276]. These  $\beta$  type titanium alloys, however, still contain elements such as aluminium, iron and molybdenum. As previously noted, although it is still controversial, aluminium has been linked to suppression of the immune function [260, 261], whereas iron and molybdenum in elemental form have been related to severe tissue reactions in animal studies [277]. The metals, when implanted in the back muscles of rabbits for 24 weeks, show pseudo membrane encapsulation with thicknesses of up to 1.8 mm. It has also been reported that in vitro, molybdenum, chromium and nickel in soluble form may induce cell transformation[278]. In addition, the minimum values of elastic moduli of these alloys (Table 2.10) are still higher than that of bone.

Attempts to develop a lower elastic modulus titanium alloy whilst maintaining high strength have been carried out in recent times by nanostructure formation. A combination of a high strength nano/ultra fine grain structured matrix and low stiffness and good ductility of bcc structured dendrites of titanium-based alloys has been demonstrated by He *et al.* [279]. They developed Ti-Cu-Ni-Sn-Nb system alloy and reported that the elastic modulus and tensile strength of 40 GPa and of 1350 MPa, respectively have been achieved. Hao *et al.* [140, 280] developed

nanostructured metallic materials Ti-24Nb-4Zr-7.9Sn by forging and hot rolling. They revealed that the designed  $\beta$  type titanium alloy possesses the lowest elastic modulus (33-42 GPa) and tensile strength of 800-1200 MPa. Although a low elastic modulus has been attained the alloys still contain elements that are less safe for the human body for long term applications. Therefore, biomedical titanium alloys based on these  $\beta$  stabilised elements, *i.e.* titanium, niobium, tantalum and zirconium have been under extensive development.

The possible use of titanium binary alloys for biomedical materials such as titanium-zirconium [281], titanium-niobium [282-285] and titanium-tantalum [265] have been investigated. Since zirconium has similar chemical properties to titanium and has as a low neutron absorption rate, this material is often used in nuclear reactors [220]. It has notable properties with corrosion resistance and biocompatibility as good as those of titanium alloys. The titanium-zirconium system exhibits a complete solid solubility for both low temperature  $\alpha$  phase and high temperature  $\beta$  phase [286]. Hence it could be possible to design alloys that have biocompatibility and high corrosion resistance comparable to pure titanium, and superior mechanical properties to the Ti-6Al-4V. Kobayashi *et al.* [281] examined the mechanical properties of various compositions of titanium-zirconium binary alloys which were fabricated by arc melting followed by heat treatment and furnace cooling. The alloy comprising 50 mol% zirconium with the finest martensitic microstructure observed exhibited the highest values for hardness (almost 2.5 times as large as the pure material hardness) and strength (more than 900 MPa), whereas the elastic moduli of the other alloys were not reported. With this favourable comparison to Ti-6Al-4V, the titanium-zirconium based alloys could provide a base material for a biomedical alloy.

Niobium is a shiny, silvery metal, soft and ductile in pure form, with a bcc crystal structure. It has exceptional corrosion resistance, although slightly inferior to that of tantalum. Niobium also has a good interaction with cells, including proliferation, mitochondrial activity, cell morphology and the size of MC3T3-E1 cells and GM7373 cells after 7 days incubation in direct contact with polished slices of the metal, as reported by Eisenbarth *et al.* [15], yet is less well tolerated when implanted in bone than tantalum or pure titanium [287]. The effect of niobium content on the

phase constitution of the Ti-Nb alloy has been investigated [282, 284, 285]. Hon *et al.* [282] varied niobium contents between 14 and 40 mass% niobium. The mixture was then subsequently arc melted, homogenised, hot rolled and annealed, followed by furnace cooling. The experiment results show that the Ti-Nb alloy with 14% niobium reveal  $\alpha+\beta$  phases with  $\alpha$  phase being the dominant one. The authors also reported that the elastic modulus of the alloy is determined by the phase constitutions. The elastic modulus of the Ti-Nb alloy initially decreased with an increase of niobium content up 26% due to the decrease of  $\alpha$  phase, and then increased to a maximum at 34% niobium due to the existence of  $\omega$  phase. The alloy converts completely to  $\beta$  phase when niobium exceeds 34%, from which the elastic modulus then decreases with an increase of niobium content. As long as the application in implant materials and low stiffness are considered, Ti-Nb alloy with a high niobium content (above 36%) is preferable. For example, Ti-40Nb was found to possess an elastic modulus of 57 GPa. However, its strength (612 MPa) is not sufficiently high compared to that of the Ti-6Al-4V (825-869 MPa). Santos *et al.* [284], who also developed the Ti-Nb alloy, revealed a different microstructural result. They employed a powder metallurgy technique using blended elemental powders with a niobium composition of 35% as a starting material. The blended powder was subsequently prepressed, cold isostatically pressed (CIP) and sintered at high temperatures (up 1600°C) for 1 hour, followed by furnace cooling. The homogenous microstructure resulting from the slow cooling from the  $\beta$  field consisted of fine plate-like  $\alpha$  structures dispersed in a  $\beta$  matrix, which indicates that the alloy was likely to be an  $\alpha+\beta$  alloy. This indicates that hot working may promote the formation of  $\beta$  phase. An investigation on phase constitution of the alloy with variations of niobium contents after higher cooling rate through graphite mold casting by Lee *et al.* [285] revealed that only a hexagonal martensite  $\alpha'$  phase was observed within the alloys containing 15% or less niobium. When containing 17.5-25% niobium, the alloys mainly consisted of an orthorombic martensite  $\alpha''$  phase. Metastable  $\beta$  phase begins to be retained at 27.5% niobium. In the alloys containing 27.5-30% niobium, small amounts of  $\omega$  phase were detected. The equiaxed  $\beta$  phase is almost entirely retained at niobium contents higher than 30%. Of these niobium containing alloys, Ti-10Nb and Ti-27.5Nb were found to have the highest strength, the  $\beta$  dominated and the  $\alpha''$  dominated alloy exhibited the lowest moduli.

Tantalum, which has superior ductility coinciding with superior corrosion resistance [220] even in a highly acidic environment [288], has already been used in surgical procedures including vascular axes [289] and secretory canals [290]. Research which was carried out by Johanson, *et al.* 1990 [287] proved that tantalum is well tolerated in bone structures and encourages the absorption of protein. Tantalum implants have also showed good biocompatibility without a surrounding inflammatory response supported by histological studies of retrieved specimens [14]. Hacking *et al.* [291] reported that analysis of a retrieved subcutaneous tantalum specimen implanted in a dog revealed complete tissue ingrowth with concomitant presence of blood vessels at the tissue implant interface. In a study of cellular responses of osteoblast-like cells, a polished and textured tantalum disc compared to the response on other common orthopaedic metals, (titanium and cobalt-chromium alloys), and tissue cultured plastic, it was found that the cellular responses with respect to absolute cell number, number of cell divisions, or cell proliferation were similar [292]. The effect of tantalum content in quenched binary Ti-Ta alloys with tantalum contents varying from 10 to 80% in eight increments has been investigated. The dynamic Young's modulus first decreases with an increase in tantalum content, reaches a value of 69 GPa at 30%, then gradually increases to 88 GPa at 50% tantalum followed by a gradual decline to 67 GPa at 70% tantalum [265]. A further increase in tantalum content leads to an increase in the elastic modulus [265, 293]. These are due to the various formations of metastable phases  $\alpha'$ ,  $\alpha''$  and  $\beta$  and their grain size at each tantalum content after quenching. Whilst further detailed investigations found that Ti-25Ta shows the lowest Young's modulus (64 GPa) with the highest ratio of strength to elastic modulus ( $7.5 \times 10^{-3}$ ), the tensile strength exhibits a value (approximately 580 MPa) which does not meet the criteria of ideal metallic biomaterials (should be approximately 1000 MPa) [228].

Extensive work has also been carried out to develop titanium alloys in tertiary, and system alloys [8, 139, 219, 294], in order to obtain biomedical alloys with non-toxic elements, good interaction with surrounding tissue, low elastic modulus and appropriate mechanical properties, *i.e.* high yield, tensile and fatigue strength, that will prolong implant service lives. For example, Davidson and Kovacs [295] developed near- $\beta$  type titanium alloys Ti-13Nb-13Zr to address the issue of biocompatibility with the exclusive use of Nb and Zr. This alloy has been registered

in ASTM standardisation (F1713). A titanium alloy, Ti-35Nb-7Zr-5Ta, which was first developed as a Ti-Nb-Ta-Zr system alloy for biomedical applications, was developed in the United States [296, 297]. More recently, Niinomi's Group in Japan developed Ti-29Nb-13Ta-4.6Zr under the guidance of the d-electron alloy design method [110].

The effect of thermomechanical processing on the mechanical properties of Ti-13Nb-13Zr alloy has been reported by Mishra *et al.* [298]. The alloy was prepared by vacuum arc melting, hot rolled and heat treated with different cooling rates. Water quenching of Ti-13Nb-13Zr from above the  $\beta$  transus temperature (735°C) resulted in the formation of hcp martensite ( $\alpha'$ ). Air cooling from the  $\beta$  field was found to produce  $\alpha'$ ,  $\alpha''$  and  $\beta$  phases indicating that some of the  $\beta$  phase transformed to  $\alpha'$ , while the rest of the  $\beta$  transformed to  $\alpha+\beta$  phase. Both cooling conditions resulted in an alloy with a similar strength (703-798 MPa). The elastic modulus of the air cooled alloy was found to be higher than the water quenched one (81 GPa compared to 64-77 GPa). On subsequent aging, the microstructure of the alloy was observed to consist of aged hcp martensite ( $\alpha'$ ) and sub-microscopic bcc  $\beta$  precipitates. These led to an increase in strength (994 MPa) by dispersion strengthening mechanisms. In the solution treated followed by water quenched condition the strength of this alloy can be increased by cold working or diffusion hardening (Table 2.10). In contrast to the diffusion hardening, cold working (using standard rolling and swaging) reduced the elastic modulus and its elongation to 44-51 GPa and 10-15% respectively. Further study on the development of an equiaxed microstructure, which is recommended due to the best combination of mechanical properties in the  $\alpha+\beta$  titanium alloy [299], on Ti-13Nb-13Zr and later on two other tertiary alloys, Ti-20Nb-13Zr and Ti-20Nb-20Zr, was reported by Geetha *et al* [218] [300]. The alloys were hot rolled in the  $\alpha+\beta$  phase field and then subjected to various heat treatments. The selection of appropriate processing results in the formation of an equiaxed structure in all of the tertiary alloys. The alloys which have been solution treated above the  $\beta$  transus followed by water quenching containing a high quantity of  $\beta$  stabilising elements, Ti-20Nb-13Zr and Ti-20Nb-20Zr, show a number of metastable phases  $\alpha'$ ,  $\alpha''$  and  $\beta$  phase while Ti-13Nb-13Zr exhibits  $\alpha'$  phase only due to martensitic transformation wherein the  $\beta$  phase completely transformed into the  $\alpha'$  phase [218].

On the other hand, the enrichment of  $\beta$  phase (Ti-20Nb-20Zr), is found to suppress the occurrence of the martensitic phases resulting in  $\alpha$  and  $\beta$  phases formation, when solution treatment is carried out in the  $\alpha+\beta$  field. Quite interestingly, the low temperature aging of alloy Ti-20Nb-20Zr shows the presence of  $\omega$  phase in addition to  $\alpha$  and  $\beta$  phases, leading to an increase in elastic modulus and strength of the alloy.

Phase transformations of the low elastic modulus metastable  $\beta$  titanium alloys has been investigated by Tang *et al.* [219]. Ti-Nb-Ta-Zr alloys were arc melted, homogenised at 900°C for 96 hours and furnace cooled. The homogenised samples were then solution treated at 1000°C and cooled at various cooling rates. The experimental results revealed that phase transformations in solution treated and rapid cooled Ti-(13-35.5)Nb-(5-22)Ta-(4-7.2)Zr (wt%) lead to the formation of three phases, namely  $\alpha''$ ,  $\beta$  and  $\omega$ . The volume percentage of  $\alpha''$  was found to decrease with either an increase in the Nb+Ta content or a decrease in the cooling rate. The presence of zirconium in the range 4.1-4.6 wt% decreased the martensite start temperature. Hence  $\alpha''$  phase was suppressed at rapid and intermediate cooling rates and only  $\beta$  and  $\omega_{\text{ath}}$  phases were observed. When slow cooled, precipitation of  $\omega_{\text{iso}}$  occurred. The martensite start temperature was further lowered,  $\beta$  and  $\omega_{\text{iso}}$  phases being observed after furnace cooling.

An increase in zirconium content continuously increased the stability of the  $\beta$  phase and delayed the formation of  $\omega_{\text{iso}}$  phase, shifting the  $\beta \rightarrow \alpha$  transformation to longer time periods. The  $\beta \rightarrow \alpha$  transformation was also avoided at all cooling rates due to a lowering of the critical cooling rate. This work revealed that the dynamic elastic moduli of the air cooled Ti-Nb-Ta-Zr alloys was sensitive to the composition, a minima at a niobium/tantalum ratio of 12 and 5 at% zirconium being observed [219]. Of all the developed alloys, the alloy with the nominal composition of Ti-35.3Nb-5.1Ta-7.1Zr wt% air cooled was found to achieve the lowest elastic modulus of 55 GPa, with a strength of 547 MPa and a good fatigue strength [296], the alloy being denoted as Ti-35Nb-7Zr-5Ta. Based on this composition, Taddei *et al.* [301] developed the  $\beta$  type titanium alloy Ti-35Nb-7Zr-5Ta by a powder metallurgy method using elemental powders as starting materials. The blended elemental powders were cold isostatically pressed and sintered at various temperatures (900-

1700°C) followed by furnace cooling. Sintering below 1500°C resulted in  $\alpha + \beta$  phase, the microstructures reflecting the presence of  $\alpha$  titanium,  $\beta$  titanium and the bcc structure of tantalum and niobium, whilst zirconium could not be detected. Sintering at 1500°C and above resulted in the complete dissolution of the alloy elements in titanium matrix. The homogenous  $\beta$  phase was observed at room temperature after furnace cooling due to the high stability of the  $\beta$  phase.

Some studies previously reported that the increase in tensile strength due to oxygen content was accompanied by an increase in the elastic modulus (66 GPa) [296] and the high-cycle fatigue strength of the alloy when solution treated [302]. More recently, investigation to increase the strength of Ti-35Nb-7Zr-5Ta by artificial aging (duplex aging) and/or by increasing their oxygen content has been carried out [237] [303]. This investigation reported the phase transformations in a Ti-35Nb-7Zr-5Ta-(0.06-0.68)O alloy solution treated in  $\beta$  field and aged at various temperatures. They observed that increasing oxygen content suppresses  $\omega$  phases by oxygen occupying the interstitial sites within the metastable  $\beta$  and hindering the atomic displacement that is required for  $\omega$  formation. In addition, being a strong  $\alpha$  stabiliser, the increase of oxygen content also promotes faster kinetic fine  $\alpha$  phase precipitate formation [304]. The high yield strength of the alloy with 0.68% oxygen content was due to the existence of the fine  $\alpha$  precipitate only. Increasing aging (538-593°C) temperature with higher oxygen contents (0.46 or 0.68%), however, resulted in the coarsening of  $\alpha$  phase precipitates [303] and an increased inhomogeneity in  $\alpha$  phase precipitation. Precipitate free zones were observed along the prior  $\beta$  grain boundary. These zones served as favoured paths for early crack propagation and decrease in tensile ductility [303].

According to Kuroda *et al* [110], in the 1990's Niinomi's group developed new quaternary  $\beta$  type titanium alloys, Ti-Nb-Ta-Zr, Ti-Nb-Ta-Mo and Ti-Nb-Ta-Sn; systems based on the d-electron alloy design method. The basic mechanical properties of the new alloy designs, button ingot melted by tri-arc furnace and thermomechanically processed (homogenised, cold rolled, solution treated and aged at 673 K for 10.8 ks), were investigated. After the solution treatment process the newly designed alloys exhibited a low elastic modulus range (~45 to ~78 GPa) and

low in strength (less than 650 MPa) compared to the solution treated conventional  $\alpha+\beta$  type titanium alloys (~80 to ~115 GPa). In contrast to the conventional titanium alloys, in general the elastic moduli of the newly designed alloys increased considerably after aging (~47 to ~105 GPa). The elastic moduli of solution treated (ST) and solution treated followed by aging (STA) Ti-29Nb-13Ta-4.6Zr were found to be ~47 GPa and ~80 GPa, respectively; the alloy with the less 'safe' element Sn, Ti-29Nb-13Ta-2Sn alloy, in these conditions having elastic moduli of ~45 GPa and ~47 GPa.

More investigations into the details of the phase transformations during heat treatment of Ti-29Nb-13Ta-4.6Zr have been conducted [231, 239, 250, 305]. Solution treatment and water quenching (STQ) of this alloy from above the  $\beta$  transus temperature resulted in a mixture of orthorhombic martensite  $\alpha''$  and  $\beta$  phases [250], but air or furnace cooling led to a mixture of  $\omega$  and  $\beta$  phases [305]. The  $\beta$  transus temperature of this alloy was found to be of the order of 650°C [250]. Further investigation has revealed that the volume fraction of the martensite phase and  $\beta$  grain size determine the mechanical properties. For instance, elastic modulus and yield strength with values of 65 GPa and 250 MPa respectively were obtained by STQ at 850°C for 1 hour, with an average grain size of 50  $\mu\text{m}$  with some of the  $\beta$  phase transforming to  $\alpha''$  being observed. Reduction in grain size to 25  $\mu\text{m}$  and a reduction in volume fraction of the martensite phase was found for STQ at 750°C for 0.5 hour. These contributed to an increase in yield strength to 400 MPa without affecting the elastic modulus [239].

The strength of this particular alloy can be increased by aging, this being accompanied by an increase in the elastic modulus. For instance, for 48 hours of aging at 450°C, yield strengths as high as 1150 MPa and increases of elastic modulus values to 85 GPa have been achieved. The increase in strength and Young's modulus are due to the presence of  $\omega$  and/or  $\alpha$  phase precipitation. Whilst  $\omega$  phase precipitation was found when aging at temperatures below 450°C, a mixture of  $\omega$  and  $\alpha$  phases was observed when aging at higher temperatures and/or longer times. The upper limit of  $\omega_{\text{iso}}$  precipitation was found to be around 450°C [231]. Thus only  $\alpha$  phase precipitation was observed when aging at temperatures above 475°C [239].

It is clear that the basic mechanical properties of this alloy are sensitive to the microstructures generated by various heat treatments. An increase in strength is accompanied by an increase in the elastic modulus and decrease in the ductility for the ( $\alpha+\beta$ ), ( $\alpha+\beta+\omega$ ) and ( $\beta+\omega$ ) microstructures. It has been noted that the ( $\beta+\omega$ ) microstructure is not recommended for biomedical applications due to its high Young's modulus and poor ductility [239].

Powder metallurgy methods have also been employed to fabricate Ti-Nb-Ta-Zr quaternary alloys. In 2004, Sakaguchi *et al.* [240] systematically investigated the effect of alloying elements on the elastic modulus of Ti- $X_1$ Nb- $X_2$ Ta- $X_3$ Zr alloys ( $X_i$ : mass% composition of  $i$ ; niobium (1), tantalum (2), zirconium (3)). They independently varied the content of each alloying element in the Ti-Nb-Ta-Zr alloys and fabricated each alloy by the blended elemental powder metallurgy method. The mixed powders were cold isostatically pressed and sintered at 1300°C for 16 hours. Subsequently, the sintered alloys were forged, swaged at 950°C and heat treated at 950°C for 30 minutes followed by air cooling. Niobium content was varied from 0 to 40% by eight increments, tantalum was varied from 0 to 20% by five increments and zirconium content was varied from 0 to 10% by five increments. Young's modulus was measured using the free resonance method at room temperature. The experimental results showed that, in general, the addition of the alloying elements decreases the elastic modulus at certain content percentages, beyond which an increase in elastic modulus is observed (Figure 2.11).

This increase is due to  $\omega$  phase formation and precipitation of  $\alpha$  on aging. The tantalum content is very critical and has to be kept within a limited range because tantalum tends to increase the elastic modulus when added beyond a certain amount. Higher elastic moduli have been observed at 0%, which may be due to the existence of  $\omega$ -phase, and at 20% because of the tendency to behave as pure tantalum rather than the titanium alloys [241]. Ti-30Nb-10Ta-5Zr, which is a simplified chemical composition of Ti-29Nb-13Ta-4.6Zr, with only the  $\beta$  phase was found to have the lowest Young's modulus (66.9 GPa). They also reported that furnace cooling after heat treatment of Ti-Nb-Ta-Zr quaternary alloys (*i.e.* Ti-20Nb-10Ta-5Zr) induces precipitation of  $\alpha$  phase in  $\beta$  phase, whereas precipitation of  $\omega$  phase in  $\beta$  phase was

found after the air cooling process. The Young's modulus of the former is lower than that of the latter. It shows that the precipitation of the  $\omega$ -phase in  $\beta$  phase has a significant role compared to the precipitation of  $\alpha$ -phase in raising the Young's modulus in the quaternary alloys.

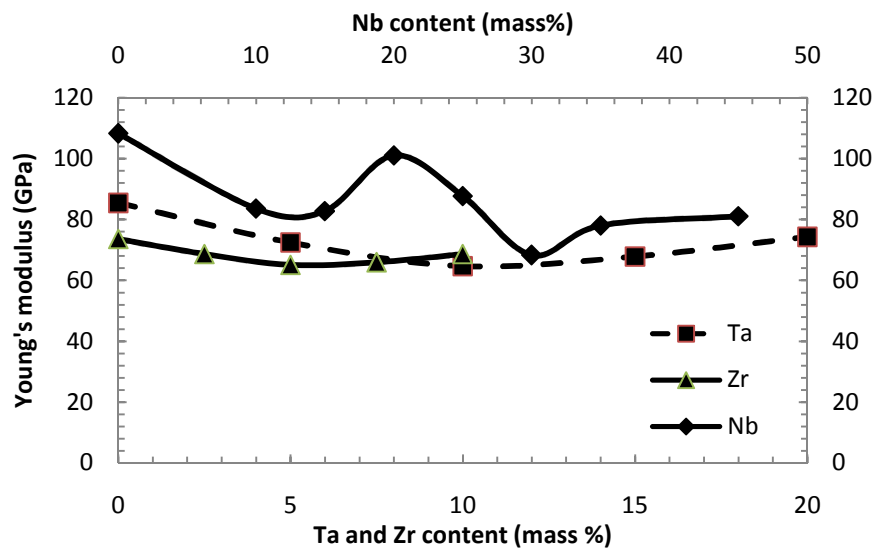


**Figure 2.11** : Change in Young's modulus as a function of Nb, Ta, and Zr content in Ti- $X_1$ Nb-10Ta-5Zr, Ti-30Nb- $X_2$ Ta-5Zr, and Ti-30Nb-10Ta- $X_3$ Zr respectively. Adapted from [240]

Further investigations by the Niinomi's research group revealed that the deformation behaviour of these alloys was determined by the niobium and tantalum content [241, 306]. The tensile properties of Ti-30Nb-XTa-5Zr alloy were found to change with a change of the deformation mechanism. The alloy with a tantalum content less than 10 mass% consisted of  $\beta$  and  $\omega$  phase and exhibited a stress-induced martensitic deformation mechanism, while above 20 mass% tantalum, the deformation was identified as slip. The tensile strength of Ti-XNb-10Ta-5Zr with a 20-35 mass% niobium content decreased with an increase in niobium content. The deformation mechanism of Ti-25Nb-10Ta-5Zr changed with variations in its microstructure. Interestingly, the behaviour of the loading-unloading stress-strain curve of air cooled Ti-20Nb-10Ta-5Zr and Ti-25Nb-10Ta-5Zr indicated shape memory effect behaviour, whereas the elastic deformation of Ti-30Nb-10Ta-5Zr was found to disobey Hooke's law.

### 2.4.3 Corrosion behaviour of titanium alloys

Corrosion is destructive attack on metallic materials when in contact with a chemical environment. Human body fluid pH in various tissues varies in the range from 1 to 9 [64] that may be considered an extremely corrosive environment for metallic materials, due to the presence of certain amount of NaCl and a series of acids [268]. For example, in normal conditions, the pH of normal blood and interstitial fluid are in the range of 7.35–7.45, however, it may decrease due to immune system response such as in case of infection or inflammation [307]. The presence of a high concentration of chlorides is also considered to accelerate corrosion of metallic implants that can lead to metal ion release. In addition, most metallic implants are subjected to a static loading or a low frequency cyclic loading. Whilst corrosion damage of the metallic biomaterials are found in many forms such as pitting, crevice, fatigue, fretting, wear and galvanic corrosion [93], the attack rate of general corrosion is very low because of the existence of spontaneous formation of passive surface layers on most metallic implants that are employed at the present time.

An advantage of titanium and its alloys is their superior corrosion resistance, which is due to the thermodynamically stable  $\text{TiO}_2$  film with, possibly, lower valence oxides such as  $\text{Ti}_2\text{O}_3$  and  $\text{TiO}$ , especially in the inner layers [6].  $\text{TiO}_2$  film is thinner but stronger than  $\text{CrO}_3$  film [308]. In addition, there are many other oxides that can form on the surface of various titanium alloys. For example, for Ti-6Al-4V,  $\text{Al}_2\text{O}_3$ ,  $\text{TiO}_2$  and  $\text{V}_2\text{O}_5$  are found in the oxide layer. Compared to  $\text{Al}_2\text{O}_3$  and  $\text{TiO}_2$ ,  $\text{V}_2\text{O}_5$  is thermodynamically unstable and dissolves into solution, but is generally eliminated from the body within 24 hours [257]. Titanium alloys containing niobium such as Ti-6Al-7Nb [257, 309] or Ti-Nb alloy [285] exhibited better corrosion resistance than Ti-6Al-4V, and this may be due to the existence of the more stable  $\text{Nb}_2\text{O}_5$  in the film which enhances passivation and also resistance to dissolution compared to  $\text{V}_2\text{O}_5$  formed on Ti-6Al-4V. The addition of niobium and zirconium into titanium also increases the corrosion resistance. Ti-13Nb-13Zr has been reported to possess a higher corrosion resistance than Ti-6Al-4V and Ti-6Al-7Nb in phosphate buffer solutions due to lower solubility of Nb and Zr in titanium than aluminium and vanadium and a higher inertness of their oxides ( $\text{Nb}_2\text{O}_5$  and  $\text{ZrO}_2$ ) than that of the oxides of aluminium and vanadium [310]. However, a change in pH of the phosphate buffer by addition of acid resulted in different corrosion behaviour. Ti-6Al-4V has

the more favourable corrosion resistance in comparison to Ti-13Nb-13Zr and Ti-6Al-7Nb for which the corrosion resistance is reduced in the presence of protein [311]. Khan *et al.* [310] also found that corrosion in protein solution reduced the hardness of the surface oxides of all the alloys.

Investigations on corrosion behaviour of titanium alloys containing tantalum also revealed that corrosion resistance of the binary Ti-Ta alloys increases with increasing tantalum content. The occurrence of an increase in the corrosion resistance is due to strengthening of the passive layer, TiO<sub>2</sub>, by the more stable Ta<sub>2</sub>O<sub>5</sub>. In addition, cytotoxicity level resistance as good as pure titanium and a higher wear resistance of the Ti-Ta alloys compared to that of Ti-6Al-4V have also been reported [312]. Okazaki and Gotoh [7] reported that the quaternary alloy, Ti-15Zr-4Nb-4Ta has better corrosion resistance than Ti-6Al-4V. The quantity of metals released in various solutions of the former is lower than that of the latter. The measurement of electrochemical activity of the alloy confirmed the potency of titanium, niobium, tantalum and zirconium to develop a highly protective passive layer. Okazaki *et al.* [313] also reported that passive films consisted of TiO<sub>2</sub>, ZrO<sub>2</sub>, Nb<sub>2</sub>O<sub>5</sub>, Ta<sub>2</sub>O<sub>5</sub> and Pd or PdO on the alloy Ti-15Zr-4Nb-4Ta-0.2Pd-0.2O-0.05N in calf serum.

The effect of heat treatment on the corrosion resistance on  $\alpha+\beta$  titanium alloy, Ti-6Al-7Nb, has been studied by Thair *et al.* [314]. An equiaxed structure resulted from solution treatment in  $\alpha+\beta$  field, and this showed better corrosion resistance as compared to the Widmanstätten structure (ST in  $\beta$  field). The compositional differences within the  $\alpha$ -phase in the Widmanstätten structure can lead to increased pitting corrosion tendency. They also reported that the alloy solution treated at 950°C and air cooled followed by aging at 550°C for 4 hours exhibited superior corrosion resistance in Ringer's solution (9 g/l NaCl, 0,43 g/l KCl, 0,2 g/l NaHCO<sub>3</sub>, 0,24 g/l CaCl<sub>2</sub>, pH = 7,4) due to the absence of selective dissolution of the phases. Ringer's solution was used due to its ion concentrations which are comparable to human blood plasma. In contrast to these, Rosa *et al.* [315] revealed results showing lower corrosion resistance of the alloy after hot working.

Though titanium and Ti-6Al-4V alloy possess excellent corrosion resistance, their application in sliding surface conditions remains limited due to low wear resistance and the possibility of vanadium release from the alloy. Tissue blackening around the titanium hip implants indicates the wear of titanium alloys. This may induce aseptic loosening during implantation [310, 311]. This has led to the development of vanadium free titanium alloys such as Ti-35Nb-7Zr-5Ta and Ti-29Nb-13Ta-4.6Zr. The passive surface layer containing Nb<sub>2</sub>O<sub>5</sub> in titanium alloys with a high content of niobium exhibits very good lubricating properties due to the ability of niobium to repassivate more quickly, and hence the passive film being more resilient than in the low niobium alloy [69].

A study on the corrosion behaviour of porous titanium [276] revealed that porous titanium shows more susceptibility to corrosion than solid titanium. It was also found that the corrosion resistance decreased with decreasing porosity, which was attributed to the small, isolated pore morphology that could trap ionic species of electrolyte and reduce the concentration of oxygen, resulting in a limitation for creating a corrosion resistant passive layer. Conversely, in highly porous compact with an open, interconnected pore morphology, resulted in materials with increased corrosion resistance to pitting.

## **2.5 Porous materials in biomedical applications**

Porous materials are defined as solids containing pores [316] (p.1). Based on the constituent synthetic materials, porous materials can be categorised into two types, *i.e.* porous metallic materials and porous non-metallic materials (*e.g.* ceramics and plastics). Geometrically, porous metals can further be classified into two main groups, namely closed-cell and open-cell structures. In an open-cell structure the individual cells are interconnected, whilst in a closed-cell structure, each cell is completely enclosed by a thin wall or metal matrix [317]. In porous metals, the existence of the pores within the metal matrix provides many beneficial properties such as low specific weight, high specific surface, high energy absorption, low heat conductivity (for closed-cell structures), high heat exchange and radiation ability, good permeability (for open-cell structure), good absorption of electromagnetic

waves, gas sensitivity, possibility of bone regeneration, resistance to heat, heat shock and so on. Porous metals have thus been used as functional and structural materials in a wide variety of applications. For example, they have been used to produce absorbing buffers, heat exchangers, hard tissue replacements, structures, etc. [318].

Fabrication of porous metals or metal foams has been commercially established over a number of years. In recent times, porous nickel, copper, zinc, bronze, steel, titanium and their alloys have become available, with porous aluminium being the most common of the porous metals. Porous nickel, INCO<sup>®</sup>, is applied as the electrode matrix in rechargeable batteries [319] (pp. 218-220). Porous stainless steels are known to be widely utilised as metallic filter materials and as metallic separator materials. For electromagnetic shielding, porous nickel and porous copper are available. Porous titanium, due to its superior properties in bulk form, such as high corrosion and temperature resistance, high specific strength and good biocompatibility, can be used as a new type of filtration and purification medium, and also in biomedical applications.

Although, as mentioned in section 2.4.1, considerable progress has been achieved in biomedical metallic implant biomaterials, the fixation of implants into the host bone remains a concern. Major problems concerning metallic implant materials in orthopaedic surgery are the mismatch of Young's modulus between the host bone and the implant materials, and a relatively low osseointegration. Concerning the mismatch of Young's modulus, once a metallic implant is placed in the intramedullary canal of bone, two important changes occur in the load transfer mechanism. First, the load is no longer transferred through the bone, but now involves the implant-bone interface. Second, the load which was earlier carried by the bone alone is now shared with the implant. The stress which is normally subjected to the bone is shielded by the stem, so that some bone will be lost due to bone resorption. The other problem related to low level of osseointegration results in a longer time period for implant fixation. The effect of stem stiffness on stress-related bone resorption has been investigated by Bobyn *et al.* [320]. Two modified porous-coated femoral implants with different stiffness (cobalt based alloys and titanium alloys) were implanted into eight dogs. After death, bone ingrowth and remodeling were quantified and compared between stem designs. This result showed that the femora with a lower

stiffness stem made of a titanium alloy revealed much less bone loss than that of the stiffer one. Numerical studies conducted by Yan, et al.,[321] also confirm that bone loss around the implant strongly depends on the value of the elastic modulus of the prosthesis. There will be a sharp drop of the volume of the bone with density loss if a cobalt–chrome implant is replaced by a porous titanium implant. The numerical results showed that both the bone volume with density loss and the bone density loss rate decreased linearly with the increase of the porosity. Titanium and its alloys have elastic modulus values that are much lower than that of the other types of metallic implant materials, but still higher than that of bone, thus resulting in the occurrence of stress shielding. A suggestion to overcome this problem may be the use of porous materials for the stem.

An early use of porous materials in biomedical applications was recorded in 1963 when Smith reported the development and use of porous ceramics in animal studies, substantial information concerning bone ingrowth being noted [322]. It did stimulate interest in further investigation into porous materials involving porous ceramic [25, 323-325], polymeric [26, 326, 327] and metallic materials [31, 328-330]. Kuboki *et al.* [331] have demonstrated the necessity of porosity in bone regeneration using a rat ectopic model and solid and porous particles of HA for bone morphogenetic protein (BMP) delivery; no new bone formed on the solid particles, while in the porous scaffolds direct osteogenesis occurred. The regeneration of specific tissues on the porous implant materials has been found to be dependent on the pore size and porosity of the implant [21]. Whilst the optimal porosity for implant materials is suggested in the range of 20-50% [22], the following studies for bone ingrowth into different porous implants suggest undefined pore size required for osseointegration. For example, Hulbert *et al.* [25] reveals that a pore size of 100  $\mu\text{m}$  of ceramic implant allows bone ingrowth, but osteon (the basic unit of structure of compact bone) formation requires pore sizes greater than 150  $\mu\text{m}$ . Klawiter *et al.* [326] examined bone ingrowth into porous high density polyethylene (PHDPE) with pore sizes as small as 40  $\mu\text{m}$ , while Spector *et al.* [26] showed bone growth with an average pore size of 450  $\mu\text{m}$  within similar materials. The effect of pore size on osseointegration of ceramic bone substitute *in vivo*, which were implanted into a critical-sized cranial defect in *Balb/c* mice has been studied by Klenke, et al. [332].

Twenty eight days after implantation, the volume of newly formed bone deposited within the implants increased as the pore size (40-280  $\mu\text{m}$ ) increased. The data demonstrated pore size to be a critical parameter governing the osseointegration process. For metal implant materials, Nilles *et al.* [27] demonstrated good bone attachment to stainless steel-void metal composites with an average pore size of 460  $\mu\text{m}$ , while Welsh *et al.* [28] and Cameron *et al.* [29] observed bone ingrowth into a porous surface of a cobalt based alloy consisting of multilayered powder particles with pores in the range of 50-100  $\mu\text{m}$ . Healing femoral defects in dogs has been demonstrated using implants with 50-60% porosity and 200-400 $\mu\text{m}$  pore size coating on titanium implants [333]. Itala *et al.* [30] found the formation of an osteonal bone structure in a perforated titanium triangle plate shape with pore sizes in the range of 50-125  $\mu\text{m}$  implanted in rabbit femurs. Assessment of bone ingrowth into porous scaffold using microtomography (micro-CT) showed that a strong enhancement of bone ingrowth is observed for pore diameters  $>100\mu\text{m}$  [334]. In addition, Bobyn *et al.* [31] showed pore sizes in the range of 50-400  $\mu\text{m}$  provided an optimum strength of fixation and bone ingrowth into a porous surface cobalt based alloy implant prepared by powder metallurgy techniques. An investigation using three different pores sizes in the range of 150-400  $\mu\text{m}$  (353, 218 and 178  $\mu\text{m}$ ) did not find significant differences in bone ingrowth rate during the cartilaginous period of bone ingrowth in Nitinol<sup>®</sup> implant materials [32]. When pore size was increased beyond 1mm, the tendency for the formation of fibrous tissue seemed to be increased [33]. Besides pore size, using three dimensional micro-CT based structural analyses of porous titanium implant pore connectivity also demonstrated an increase in bone and tissue growth [335]. Although previously published research works do not have a definite agreement on the pore size for bone ingrowth, most reports noted that pores size in the range 50-400 $\mu\text{m}$  may promote bone ingrowth to enhance osseointegration.

Although attempts to develop porous metals have been carried out since 1943, when Sosnik introduced pores by adding mercury to molten aluminium [336], the development of porous metals in biomedical applications was only carried out in the early 1970's. The use of porous polymeric materials and porous ceramics in biomedical applications has limitations due to their intrinsic properties. For example, the polymeric materials possess relatively low elastic moduli and strength properties,

whereas ceramic materials are known to possess intrinsic brittleness, making them unsuitable for load bearing substitute applications [337] [97]. This led to an increase research in porous metals, which have superior fracture and fatigue strengths but lower elastic moduli. It is especially interesting that the strength and the Young's modulus of the porous materials can be adjusted to match those of bone by variations of the porosity [45], thus reducing the stress shielding effect and avoiding bone resorption. Although the interaction between biomaterial implants and surrounding tissue is complicated, it can be explained briefly as follows. When an implant is surgically placed within bone there are numerous biological, physical, chemical, thermal, and other factors functioning that determine whether or not osseointegration will occur. The initial surgical procedure causes local tissue trauma and bleeding; this stimulates an acute inflammatory response in bone and the surrounding soft tissues [338, 339]. This leads to the ingress of proteins and cellular infiltrates composed primarily of polymorphonuclear leukocytes, macrophages, fibroblasts, and mesenchymal progenitor cells. The porous structure of the implant may facilitate this process. Growth factors such as fibroblast growth factor, other bone morphogenic proteins, vascular endothelial growth factor, and others stimulate the proliferation, differentiation, and maturation of osteoblast precursors [340]. Over subsequent weeks and months, the trabecular callus surrounding implants undergoing successful osseointegration remodels to form a more consolidated mature structure that can transmit load more effectively leading to improvements in implant fixation [341]. Vessel formation to facilitate vascularisation in porous ceramic material has been reported to occur with pore size more than 140  $\mu\text{m}$  [332]. Considerable progress has been obtained recently in the fabrication of porous metallic materials.

## **2.6 Fabrication techniques of porous titanium**

A number of techniques to fabricate porous titanium structures have been developed based on solid state techniques due to the relatively high melting point of titanium, reactivity at high temperature and its production costs. Recently, powder metallurgy (PM) technology has been employed in the various techniques of solid state foaming. The advantages of PM technology in biomedical materials fabrication can be described as follows [342] :

1. The ability to fabricate products by nearly waste-free net shape forming.
2. Accurate selection of chemical composition through the use of hard to machine or high melting point alloys to obtain a higher biocompatibility of implants.
3. Reduced chemical inhomogeneity as typically found in cast or some plastic formed materials, this improving the corrosion resistance.
4. The viability to obtain desirable porosity with the appropriate pore geometry.
5. The possibility to fabricate various composite materials comprising additions that improve biofunctionality.

This section discusses the solid state foaming fabrication techniques for porous titanium, with more specific details applied to the techniques used in this research project. The following paragraphs are brief illustrations of the processing techniques for porous titanium and its alloys.

### **2.6.1 Sintering of powder compact techniques**

This is the simplest technique used to fabricate porous titanium, based on partial densification during sintering of titanium powders. This technique generally involves the compacting, binding and sintering of the metal powders at high temperatures, allowing the powder particles to bond to each other with only small changes in the shape. The pore volume fraction is attributed to the particle size and to the extent of interconnectivity among the powder particles. Thus, this technique has limitations in the pore size and pore shape which can be produced, dictated by the powder size and powder shape. Moreover, those aspects have a major impact on the mechanical properties of the resulting materials, which are often found to be low in strength, brittle and poor in toughness and crack resistance [343]. Powder based on commercially pure titanium [35, 343], titanium alloys [47] [344] and nickel-titanium alloys [345] have been employed to develop both porous-coated [22] or fully porous biomedical materials. From the literature, [346] it can be found that maximum porosity achieved by spherical powder particles is 50% with highly non spherical pore shape.

Oh *et al.* [35] fabricated porous titanium compacts with porosities ranging from 5.0 to 37.1% using spherical unalloyed titanium powder as starting material, with and without applied pressure during sintering. Young's modulus and the compressive yield strength were found to decrease linearly with increasing porosity. In addition to the Young's modulus of the porous titanium with a porosity range of 32-36% being close to that of human cortical bone (20 GPa), the bending strength (115 MPa) was also close to the maximum of that of the bone (110-184 MPa). The compressive yield strength of Ti (61 MPa) porous compact, however, was found to be lower than that of the bone (104-121 MPa) [347].

A higher porosity of porous titanium material has been achieved by using a larger powder size (420-500  $\mu\text{m}$ ) as demonstrated by Asaoka *et al.*[343]. Double sintering to spherical titanium powder resulted in a porosity of 41.5% and the compressive strength of 182 MPa, whereas the elastic modulus was found to be low (5.2-5.5 GPa). Using coarse spherical commercially pure titanium fractions with powder size 180-1800 $\mu\text{m}$ , porosities between 30 and 60% have been achieved by Thieme *et al.* [22], the highest value being achieved with agglomerated powders. They also demonstrated that the addition of a fine-grained silicon powder as an additive accelerated sintering and improved the neck geometry. The bending strength and Young's modulus were measured to be from 5-190 MPa and 5-80 GPa respectively.

An attempt to increase the yield strength and porosity of powder compacts has been achieved by using titanium alloy powders with angular shapes as a starting material. Guden *et al.* [47] sintered compacted spherical and angular (100-200  $\mu\text{m}$ )  $\alpha+\beta$  type titanium prealloyed (Ti-6Al-4V) powder at 1200°C for 2 hours, achieving porosity in the range of 34-54%. The angularly shaped powder showed relatively higher porosity levels due to the higher probability of pore formation between particles of irregular shape. The elastic modulus of the porous titanium alloy was reported in the range of 0.5-7.0 GPa. Besides the compressive strength of sintered angular powder of ~50% porosity (~50 MPa) satisfying that of cancellous bone (3-20 MPa), the yield strength of the porous titanium alloy compacts with a porosity of 40-42% were close to that of human cortical bone (higher than 100 MPa). Another study carried out prior to this finding discovered that the sintering of similar powders of titanium alloy, Ti-6Al-4V,

at a lower temperature (1000°C) achieved a maximum compressive strength of 55 MPa which is lower than that of bone [348], even though it achieved a similar porosity range (41-55%). The investigations indicated that sintering at higher temperatures improved the mechanical properties of the porous titanium alloy without significantly sacrificing the porosity achieved.

Spherical  $\beta$  type titanium prealloyed powder (Ti-15Mo-5Zr-3Al) was subjected to sintering by hot pressing (HP) by Nomura *et al.* [344]. Powder sizes in the range of 300-500 $\mu$ m were used. The porosity of the sintered compact powder was reported to be higher than that of the sintered pure titanium previously reported by Oh *et al.* [35], showing higher creep resistance in the alloy. Some of the HP compacts were then solution treated and quenched (STQ). The STQ compact exhibited a slightly lower Young's modulus compared to the HP compact. Microstructural analysis revealed the presence of  $\alpha$  phase in the  $\beta$  phase within the HP compact, whereas only  $\beta$  phase was observed in STQ compact. In addition, the STQ compact having a porosity of about 26% showed a Young's modulus of 20 GPa, comparable to that of human bone, and exhibited superior strength (205 MPa) to the bone and the pure titanium compact.

### **2.6.2 Space holder techniques**

Another technique used to fabricate porous titanium for structural or biomedical applications is to use a space holder approach, consisting of solid materials which can be removed during the fabrication process. The fabricated porous metals show two types of pores in the form of isolated micropores distributed in the wall of the interconnected macropores. This process is initiated by the blending of pure or alloyed titanium powder with an appropriate space holder material, followed by compaction of the blend into a preform (green body). The preform is then sintered at a low temperature (c.a. 200°C) in a vacuum as the initial stage for space holder removal and for creating porosity in the titanium. This stage also leads to initial neck formation. Further sintering at higher temperature (1200-1400°C) develops neck growth leading to densification of the metal matrix structure. Space holder materials in powder form employed to fabricate porous titanium or its alloys involve

carbamide ( $\text{CO}(\text{NH}_2)_2$ ) [54, 349], magnesium, ammonium hydrogen carbonate ( $\text{NH}_4\text{HCO}_3$ ) [45, 335, 350, 351] and polymers such as polypropylene carbonate (PPL) [352, 353].

Bram *et al.* [54] reported that the production of highly porous parts using a suitable space holder material (carbamide) was successfully accomplished with titanium. The space holder was moistened with a suitable solvent by mixing on a rolling bench and the metal powder was then added to the mixture, allowing the powder particles to adhere to the surface of the space holder. The agglomerates were uniaxially pressed at 166 MPa into cylindrical compacts. The space holder material was removed using a thermal treatment below 200°C, followed by sintering of the compacts between 1200° and 1400°C in a vacuum furnace for sintering times ranging between 1 and 2 hours. Porosities of 60-77% with pore sizes in the range 0.1-2.5 mm were achieved. The compressive strength and bending strength values were reported as approximately 10 MPa and 100 MPa for porosities of 77% and 60% respectively. A recent study in which the fabrication of porous titanium using carbamide as a space-holder, with three steps of heat treatment, *i.e.* 200°C for 3 hours, 350°C for 3 hours and 1250°C for 3 hours, was carried out by Niu *et al.* [349], achieving porosities in the range of 55-75%. The compressive strength, *i.e.* plateau stress and the Young's modulus were found to be in the range of 10-35 MPa and 3.0-6.4 GPa, respectively.

Magnesium powder has been used as a space-holder to fabricate porous titanium and titanium alloy (Ti-6Al-4V) structures by Wheeler *et al.* [354]. The magnesium spacer holder was removed by evaporation at 1000°C followed by sintering at 1400°C, which resulted in porosities of 25-82%, strengths from 15-607 MPa and Young's modulus values of 3-9 GPa. One-stage sintering to produce porous titanium foam using magnesium powder with sizes of 425-600 µm as a space holder, was reported by Esen and Bor [46]. This process involved the mixing of the titanium powder, binder and the space holder, mixture compaction at 500 MPa, and heating to 1200°C for 1 hour for debinding, sintering and magnesium evaporation. Yield strength (plateau stress) values and the elastic modulus values of the porous titanium containing porosities in the range 45-70% were found to vary between 15-116 MPa and between 0.42-8.8 GPa, respectively

A porous titanium structure with a porosity of 78% was fabricated by Wen *et al.* [45] using ammonium hydrogen carbonate as the space holder. Decomposition of the space holder was carried out by heat treatment at 200°C, followed by sintering at 1200°C for 2 hours. The porous structure exhibited a compressive strength of 35 MPa and Young's modulus of 5.3 GPa. Further study by the authors [55] produced porous titanium with porosity in the range of 35-80%. The plateau stress and Young's modulus of the porous titanium with a porosity of 80% were found to be approximately 40 MPa and 2.87 GPa respectively. It was also reported by the authors [355] that the porous titanium exhibited a good ability to form a bone-like apatite layer throughout the porous structure after thermochemical pretreatment.

The use of polymer as a space-holder to produce porous titanium has also been studied. Interconnected pores of porous titanium with 10-60% porosity and pore sizes between 50-500  $\mu\text{m}$  was demonstrated by Hong *et al.* [352] who used polypropylene carbonate as space holder. The Young's modulus and the compressive strength were reported in the range of 1.5-8.0 GPa and 80-400 MPa respectively. It can also be found that the cell size and shape can be tailored by the PPC and titanium particle size. The authors also reported a thin apatite formation along the porous titanium surface after alkali treatment and soaking in SBF. Andersen *et al.* [353] developed titanium hollow sphere porosity by coating an expanded polystyrene sphere with titanium powders and a binder suspension in a fluidised bed. The coated spheres were then subjected to a controlled compression process to promote powder coalescence, applied with a suitable forming process, after which the polymer and binder were removed leaving the titanium preforms for subsequent sintering resulting spherical titanium hollows with 4 mm diameter and 0.125 mm wall thickness.

With the intention of obtaining a porous scaffold combined with high porosity and high strength, some porous titanium alloys were developed under this technique [91, 356, 357]. In addition, the bioactivities of the porous titanium alloys were also evaluated. The space holder technique used to produce porous titanium alloys is similar in principle to the previous technique (sintering of powder compacts). Mostly, prealloyed powders prepared by mechanical alloying were used as starting materials. For examples: Wen *et al.* [356] heat treated a mixture of prealloyed TiZr alloy powder and the space holder at 200°C for 5 hours and at 1300°C for 2 hours

resulting in a porous TiZr alloy with a porosity of approximately 70%. The porous TiZr alloy exhibited a compressive plateau stress and Young's modulus value of 78.4 MPa and of 15.3 GPa respectively. A porous Ti-10Nb-10Zr alloy with porosities in the range 42-74% has been successfully prepared by Wang *et al.*[357] using a similar method. The porous TiNbZr presented a higher strength (27-368 MPa) than the unalloyed porous titanium for the same porosity. In addition, cell cultures on the porous alloy showed osteoblast-like cells grew throughout the entire porous structure.

A similar finding on bioactivity and the mechanical properties of fabricated porous TiNbSn has also been reported by Xiong *et al.* [91]. Porous TiNbSn products with four different relative densities, *i.e.* 0.7, 0.6, 0.5 and 0.4 were prepared by adjusting the initial ratio of the space holder to the ball milled TiNbSn powder. Heat treatment at 175°C for 2 hours and sintering at 1200°C for 3 hours was employed for the ball milled TiNbSn alloy powder and the space holder to produce the porous alloy. The compressive plateau stress and Young's modulus of the porous TiNbSn alloy were found to be in the range of 112-420 MPa and 10.8-33.2 GPa respectively. Using alkali heat treatment as a pretreatment, it was observed that a hydroxyapatite layer formed in the porous TiNbSn alloy surface after soaking in a SBF. It indicated that the porous alloy has the potential to be a bioactive material.

Although porous pure titanium and titanium alloys have been developed, the morphology and the porosity level of the resulting porous pure titanium and titanium alloys based on the space holder technique are generally determined by the make up (pore positioning) of the original pores in the powder preform. This technique does not allow the alteration of pore morphology and porosity level after finish sintering at high temperature.

### **2.6.3 Wire space holder**

Elongated pores in titanium are of considerable interest for applications such as filters, heat exchanger and biomedical implants. Using wires incorporated into titanium powder preforms as an initial step before being removed by evaporation or electrochemical dissolution produces macropores with regular shapes and micropores due to partial powder densification. Wheeler *et al.* [354] used magnesium wires

(0.18-0.45 mm in diameter) as spacers, which were removed by evaporation at 1000°C followed by sintering at 1400°C, to produce porous structures from titanium or Ti-6Al-4V powder, achieving 25-82% porosity. However, the use of magnesium wire as a space holder raises concerns due to the unavoidable presence of MgO on its surface leading to mixed magnesium/titanium oxide contamination. Additionally, its low ductility leads to the difficulty of being shaped into sub-millimetre wires, which limits the creation of the meshes. These constraints can be avoided by using steels as a space holder. Elongated pores in pure titanium have been successfully fabricated using this approach, according to Kwok *et al.* [358] and in Ti-6Al-4V according to Jorgensen *et al.* [48]. Titanium or titanium alloy preforms containing steel space holders were sintered to create composites, followed by electrochemical dissolution of the steel under conditions where the titanium was cathodically protected. The interdiffusion layer of Ti-Fe can be inhibited by the *in situ* formation of a Ti-C reaction layer, or can be removed by dissolution resulting in increased porosity. Porous Ti-6Al-4V with 21-41% porosity showed compressive stiffness (5-40 GPa) and strength (176-265 MPa) desirable for biomedical applications.

#### **2.6.4 Gel casting methods**

Another approach to make porous complex shapes is to use a gel casting technique. In this method, metal powder, dispersant, binder (monomer) and solvent are mixed to obtain a slurry. A catalyst and initiator are added to the mixture with appropriate concentration to allow pouring of slurry into the mold before subsequent formation of the gel due to *in situ* polymerisation of the binder. The gel holds the metal particles. After evaporation of the solvent, the gel retains the desired shape of the particles. Subsequent gel removal and sintering of the particles result in the desired porous structure. This method has been previously used in ceramics, but is rare in metals.

Investigations to fabricate porous titanium using this method has been carried out; Li *et al.* [359] used gel casting consisting of acrylamide as a monomer, methylenebisacrylamide as a cross linker, tetramethylethylenediamine as a catalyst and ammonium persulphate as an initiator. The titanium slurry made from the mixing

of the gel former and titanium powder was deaerated under vacuum and then the initiator and the catalyst were added, followed by casting into a non-porous mould at 60°C for 2 hours. Finally, the gel casting porous titanium was sintered at a range of 900-1200°C for 1-2 hours in a vacuum furnace. Using this process porosity ranges from 40.5 to 53.8% were obtained. The 46.5% porosity level porous titanium product showed values of elastic modulus of 8.5 GPa and compressive strength of 158.6 MPa, which match those of bone. A different gel casting system used to fabricate porous titanium consisting of TiH<sub>2</sub> particles suspended in a triblock copolymer gel with an addition of space-holder particles (PMMA or PP) in the gel was developed by Erk *et al* [360]. Organic pyrolysis to remove the gel, followed by sintering at 1000°C, resulted in titanium with controllable porosities ranging from 4 to 44% with relatively low contamination. The compression test specimens with a height to weight ratio of 2 (typical dimensions: 2.5 x 2.5 x 5 mm) were subsequently cut using electrical discharge machining and tested at a strain rate of 10<sup>-3</sup>s<sup>-1</sup>. The compressive stress-strain curves are typical of metallic foam, displaying good yield strength (171 MPa) and low stiffness (24 GPa). This study also presented stiffness values determined by ultrasonic testing, showing higher and more reliable elastic modulus values compared to those derived from compression testing. Local microplasticity at very low strain levels in compression testing can result in near linear stress-strain slopes that are much lower than the true Young's modulus [361, 362].

Again using this technique the morphology and the porosity level of the resulting porous titanium are generally controlled by the make up (pore positioning) of the original pores in the powder preform. Additional polymeric space holder may result in contamination on the porous metal. This technique does not allow for the alteration of pore morphology and porosity level after finish sintering at high temperature.

### **2.6.5 Fugitive scaffold methods**

An approach to fabricate porous titanium that is related to section 2.6.2 is to use a fugitive space holder technique. This technique uses a polymer as a scaffold. The scaffold is then coated by a mixture of titanium powder and binder. After the binder

and scaffold are thermally removed, sintering of the powder results in a reticulated open-cell foam with hollow titanium strut. Li *et al.* [359] developed a reticulated porous titanium alloy using this technique. Titanium alloy slurry consisting of Ti-6Al-4V powder, H<sub>2</sub>O and ammonia solution were coated repeatedly into polyurethane foam until all the struts of the polyurethane were coated by the slurry. After drying, the samples were first heated to burn out the polymer and the binder. The samples were then sintered at 1250°C for 2 hours in vacuum furnace. The reticulated porous Ti-6Al-4V alloys with high porosities (over 80%), pore ranges of 400-1300 µm and compressive strengths of 7-13 MPa have been successfully developed. The rheological properties of the titanium alloy slurry is found to play a critical role in the impregnation process which is influenced by the particle size and shape of the raw powder solid/liquid ratio, pH, the type and content of the binder, sedimentation behaviour of the slurry and the amount of the air bubbles in the mixture. A rapid drying process was also found to be an important factor for maintaining a positive replica shape. A later study revealed that the density and the compressive strength (up to 35.5 MPa) can be increased by repeating the process, *i.e.* the previously sintered foam is subjected to a second thin powder slurry coating and a second sintering process [363].

### **2.6.6 Freeze casting method**

This method has been used to produce porous ceramics. A ceramic slurry, usually using water as the liquid carrier, is frozen. Solidification of the slurry allows dendritic growth of the ice (freezing liquid carrier), leaving interconnected pores after sublimation of the ice water under vacuum (freeze drying). Chino and Dunand [364] in 2008 introduced this method to produce porous titanium. A titanium slurry consisting of < 45 µm particle size titanium powder and deionised-deaerated water was directionally solidified, resulting in a powder preform comprising elongated aligned dendrites of pure ice separated by interdendritic regions with high powder content. After removal of ice dendrites by freeze drying, the powder was sintered, thus resulting in porous titanium with 57-67% aligned pores. Oxygen contamination due to the use of water as the liquid carrier raises a concern. Consequently the resulting porous titanium exhibited high compressive stress (40-60 MPa for 60%),

but showed indication of embrittlement. In order to reduce the contamination, Yook *et al.* [365] used camphene as an alternative liquid carrier. In addition titanium hydride powder was chosen as the source of titanium metal through hydride decomposition. The TiH<sub>2</sub>/camphene slurries were frozen followed by freeze drying and sintering, this resulting in porous titanium with porosity and compressive strengths ranging from 49 to 63% and 81 to 253 MPa respectively.

### **2.6.7 Pressurised pore expansion with argon or hydrogen gas method**

The fabrication procedure involves pressurised gas infusion, densification using hot isostatic pressing (HIP-ing) and pore expansion at elevated temperature; hereafter this technique being named as isothermal foaming. Foaming processes based on a creep and pressurised pore expansion result in porous titanium exhibiting pore morphology independent of that of the original powder preform. The porosity level can be obtained by controlling the foaming parameters, such as argon pressure, foaming time or foaming temperature. To enhance the porosity (up to 50% [366]) and to accelerate the foaming rate, superplasticity in the titanium matrix is induced by thermal cycling. However, according to a model developed by Elzey and Wadley [367], achievable porosities in solid state foaming under isothermal foaming are found to be limited to less than 50%, whereas an upper limit of 65% can be achieved under superplastic conditions, but still much less than that of metals in liquid state foaming. This limitation is due to a decrease in pore pressure as the driving force through a rise in pore volume, and also loss of gas accompanying pore coalescence or escaping as the porosity emerges at the specimen surface. Prealloyed powder Ti-6Al-4V [50, 57, 59, 368], commercially pure titanium [366, 369] and prealloyed NiTi [50] powders have been used to create fully porous titanium materials.

This pore expansion technique was first introduced by Kearns *et al.* [57] for Ti-6Al-4V foam using prealloyed titanium alloy powder as starting material. The prealloyed powder was placed in a stainless steel can which was evacuated and backfilled with argon gas. The powder was then densified by HIP-ing at 950°C under external pressure of 100 MPa. Under HIP-ing conditions, the gas volume is dramatically

decreased and forced into small isolated developed pores. A densified titanium alloy matrix is formed with micron-sized and low volume fraction porosity, typically 1%. The titanium alloy billet with small isolated high pressure argon pores was then exposed to high temperature in a range of 930°C to 1240°C at low pressure to allow the growth of pores (foaming process). The pores expand during the exposure by creep deformation. Porous titanium with porosity levels of around 30% has been obtained with a foaming temperature of 1240°C with 0.1 atmosphere argon backfilled pressure after approximately 12 hours. The pore growth rate was found to decrease with time. They also reported a porosity level approximately 40% by combination of high temperature and relatively high argon backfill pressure. Similar results were reported by Ashworth *et al.* [59] who also developed a porous titanium alloy by this technique using Ti-6Al-4V prealloyed powder as a starting material. Additionally the tensile strength of the porous titanium alloy with a porosity level of approximately 40% was measured as high as 300 MPa.

Investigations of this process for commercially pure titanium were carried out by Dunand and co-workers [49, 366, 370, 371] and a faster foaming rate due to the use of either a lower creep strength material or a higher argon backfill pressure in foaming at lower temperature was demonstrated. Furthermore, the exposure of the HIP-ed billets of commercial purity titanium at 960°C with an argon backfill pressure of 3.3 atmospheres achieved a porosity of 22% for times around 30 minutes of foaming, whereas a porosity of 27% was obtained after 24 hours of the foaming process [366]. The Young's modulus and yield strength of the porous titanium with 22% porosity were found to be 60 GPa and 200 MPa respectively. They also reported the use of transformation superplasticity to achieve similar total porosity to that shown by Kearns *et al.* [57], but for a much shorter time period of 5 hours, and at a lower temperature (thermal cycling in 830 and 980°C) [370, 371]. Superplasticity in the titanium matrix effectively decreases its strength leading to less resistance to gas expansion and also retards pore wall fracture due to higher ductility. The effects of different powder sizes on foaming kinetics and microstructure were also investigated [49], whereby the differently classified powder in the range 30 µm to 400 µm resulted in HIP-ed titanium billets with different initial porosity ranging from 0.06% up to 2.7%. In relation to the foaming process of the billets, it was revealed that foaming rate in the early stages of creep and superplastic foaming

increased with increasing initial porosity. However at a later stage, the high initial porosity billet exhibited earlier foaming termination, since pores more rapidly emerged at the surface, allowing the escape of argon gas. The billet with initial porosity of 0.4% resulted in a high final porosity (47%) and a low Young's modulus (23 GPa). The research group also developed aligned, elongated pores by either applying a directional load during the foaming of titanium powder based foam [366] or replacing the titanium powder employed in this method with titanium wires [372].

Martin and Lederich [373] modified the original Kearns process to fabricate an *in situ* sandwich structure and named this method as the low density core (LDC) process. Blended elemental Ti-6Al-4V powder consisting of particles of commercially pure titanium and master alloy powder 60Al-40V were placed in Ti-6Al-4V rectangular canisters which were connected in line with a vacuum pump for evacuation and argon gas backfilling. The assembly was then HIP-ed and foamed with the canister still attached, thus the canister becoming the face sheet of sandwich structure. A porosity level of 25% in the foamed core was reported. The expansion kinetics and the elastic properties of the rolled Ti-6Al-4V LDC precursor *in situ* were measured during foaming process by Queheillat *et al* [374, 375]. The Ti-6Al-4V canister was filled with Ti-6Al-4V prealloyed powder obtained by the plasma rotating electrode process (PREP), backfilled with argon gas at a pressure of 3 atmospheres sealed and followed by HIP-ing at 1040°C for 6 hours. The HIP-ed canister was then heated at 900°C with several hot working treatments applied. The samples were annealed at 800-1150°C with total heating and soaking times of 10 hours in each cycle. The measurements were carried out by using a combination of eddy current and laser ultrasonic sensor testing. The eddy current data showed that the expansion reached the maximum expansion rate at around 685°C and stabilised to approximately 27% after annealing for 4 hours at 920°C. The Young's modulus was measured at 42 GPa at this porosity. The elastic moduli were shown to decrease with increasing volume fraction of porosity and temperature.

Pressurised gas infusion can also be carried out by using hydrogen produced by *in situ* hydride decomposition. Ricceri and Matteazzi [369] blended a mixture of titanium powder and TiH<sub>2</sub> powders. These blends were then densified using HIP-ing resulting in incomplete decomposition of TiH<sub>2</sub> due to high pressure. Afterwards the

billets were reheated in the HIP chamber to foaming temperature (950-1150°C) under isostatic pressure. Decomposition of  $TiH_2$  developed when the pressure was released, therefore developing expanding gas bubbles to induce creep deformation in the porous billet, leading to increased porosity, in the range of 17-24% after one hour.

This gas pressurised pore expansion technique has also been employed to produce porous NiTi, where Oppenheimer [376] was able to achieve approximately 17% porosity after 16 hours. A mixture of prealloyed equiatomic NiTi powder with pure nickel was used as a starting material to obtain a composition of Ni-49 at% Ti, which is known to exhibit superplastic properties at room temperature. Foaming parameters of argon gas pressure of 2 atmospheres and foaming temperature at 1050°C were applied. A new technique to obtain a higher backfill pressure by soaking the canister into liquid nitrogen during the backfilling process has also been noted. Lagoudas and Vandygrief [377] reported that porous NiTi with 50 % porosity has been achieved by a similar process, although their process may not be directly comparable, since the canister was not sealed during the HIPing allowing entrapment of the high pressure argon gas (200 MPa) in the mixture of nickel and titanium powder. This relied on the infusion of argon gas from the HIP-ing process to act as a pore expansion medium. The high temperature was maintained, while the pressure was released, thus leading to structure expansion.

## **2.7 Synopsis of other methods**

Besides those techniques mentioned earlier, there are several other methods which have been reported as viable for the fabrication porous metal for use in biomedical applications, though not directly related to the current work herein. For example; combustion synthesis (CS) also named as self propagating high temperature synthesis (SHS) [378, 379], metal deposition by using chemical vapour deposition (CVD) [380] and rapid prototyping [120, 381]. Rapid prototyping technology is a recent manufacturing process in terms of three dimensional printing (3DP). It has been used to create porous implants with controlled size, shape and distribution of the porosity which cannot be fabricated using techniques that are previously described. The basic five-step processes are as follow: (1) create a computer aided design (CAD) model of the design, (2) convert the CAD model to a

stereolithographic (STL) format, (3) slice the STL file into thin cross-sectional layers, (4) construct the model one layer to another, and (5) clean and finish the model. For metal parts, large production or simple objects, conventional manufacturing techniques are usually more economical, though this should change in the near future.

## 2.8 Mechanical behaviour of porous structures

The review of literature on mechanical behaviour of porous structures has directed the author specifically to micromechanical models established in several bodies of work. Furthermore, the primary focus of the mechanical behaviour of porous structures within the present work has been on elastic modulus and compressive stress-strain response, in light of the need to eventually simulate these specific properties of human bone into the material under investigation herein.

Compressive stress-strain curves for elastic-plastic foam (metal foam) reveal three regimes: linear elasticity at low stresses, followed by a plateau stage, and then a subsequent densification in which the stress increases dramatically. This typical behaviour is shown in Figure 2.12.

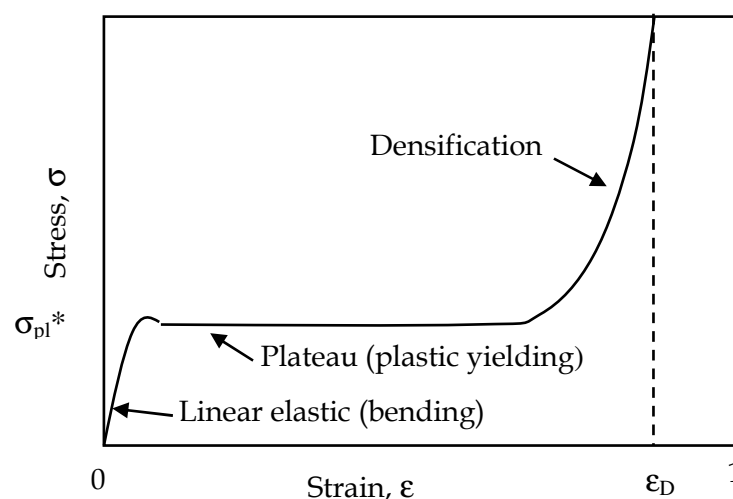


**Figure 2.12 :** Schematic compressive stress-strain diagram for foams illustrating the three regimes of linear elasticity, plateau and densification.

The deformation mechanism of the open-cell foam is dictated by cell edge bending. For closed-cell type foam, the deformation is controlled by cell edge bending and cell face stretching as proposed in the Ashby and Gibson models [362]. This regime is illustrated by the initial slope of the stress strain curve which represents Young's modulus. The plateau regime shows a collapse of the wall of the cell by the formation of a plastic hinge in the foam which subsequently yields. Following this, the opposing cell walls contact one another and further the resulting stress compresses the solid itself, leading to an increase of the stress in the final region. Increasing porosity of the foam decreases the Young's modulus, lowers the plateau stress and reduces the strain level for the onset of densification.

The elastic modulus and yield strength of metallic foams can be predicted using these models, which are simplified and have assumed that the cell structure consists of a periodically arranged beam cell for an open-cell as shown in Figure 2.13(a) or a periodically arranged cell with membrane cell face for closed-cell, as shown in Figure 2.13.

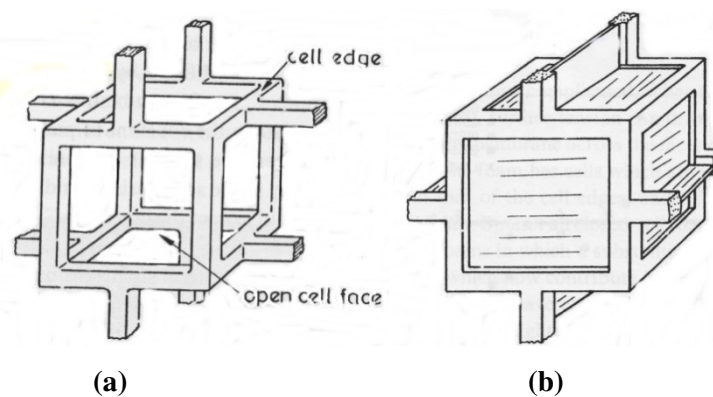


**Figure 2.13 :** A cubic model for (a) open-cell, (b) closed-cell [362] (p.185 and p.194)

The relationship between elastic modulus ( $E$ ) and relative density for open-cell foam was first proposed by Ashby and Gibson [362] (pp.175-234) as shown in Equation 2.1, and subsequently as modified by Wanner [382] (Equation 2.2) where the scaling exponent (2) is allowed to change ( $n$ ) as follows:

$$\frac{E^*}{E_s} = C_1 \left( \frac{\rho^*}{\rho_s} \right)^2 \quad \text{Equation 2.1}$$

$$\frac{E^*}{E_s} = C_1 \left( \frac{\rho^*}{\rho_s} \right)^n \quad \text{Equation 2.2}$$

The relationship between yield, plateau stress, shear and relative density become as follows [383] (p.45) :

$$\frac{\sigma_{pl}^*}{\sigma_{ys}} = C_3 \left( \frac{\rho^*}{\rho_s} \right)^m \quad \text{Equation 2.3}$$

$$\frac{G^*}{G_s} = C_2 \left( \frac{\rho^*}{\rho_s} \right)^n \quad \text{Equation 2.4}$$

where :

$C_1$  is a constant of proportionality and has a value between 0.1 and 4 in which 1 indicates a rigid polymer, elastomer,

$C_2$  is a constant of proportionality and has a value  $\sim 3/8$

$C_3$  is a constant of proportionality and has value typically near 0.3 for metals and polymers, but which can range from 0.1-1.0 [362]

Subscript “s” indicates the properties related to the fully dense materials

Superscript “\*” indicates the properties related to the porous materials

$n$  is scaling exponent and has a value between 1.8 and 2.2 with a commonly acceptable value of 2 [383] (p.45),

$m$  is scaling exponent and has a value between 1.5 and 2.0 with common values of 1.5 for solid materials and foamed materials respectively.

By using the appropriate scaling exponent  $n$ , in Equation 2.2, this model is in good agreement with a model developed by Zhao *et al.* [384] for an isolated, spherical inclusion within an elastic matrix, as shown in Figure 2.14.

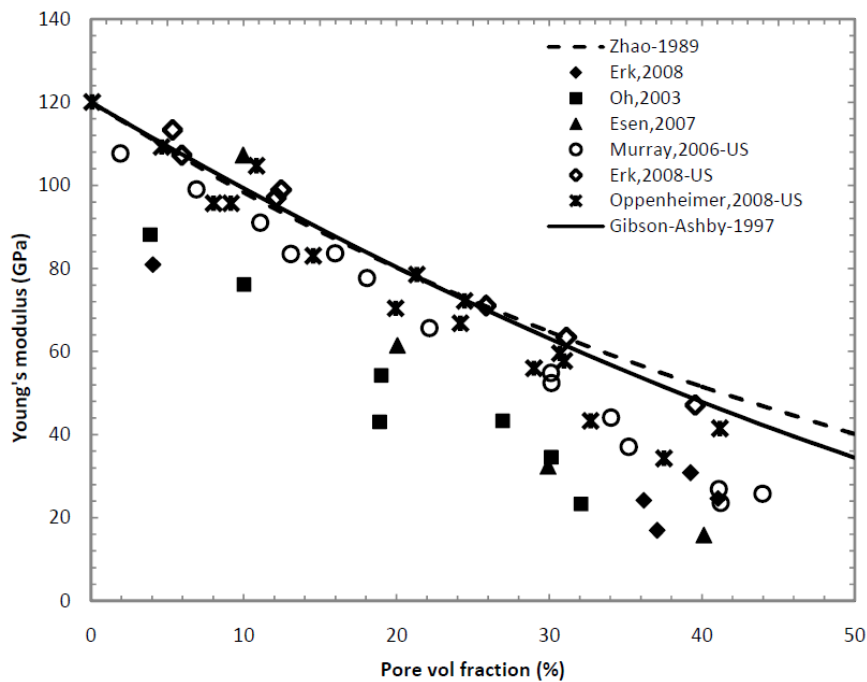


**Figure 2.14 :** Young's modulus values of porous metals fabricated by various techniques vary inversely with pore volume fraction. The filled symbols represent the elastic modulus determined by compression testing, the open symbols denote the moduli determined from ultrasonic testing (US) while the lines show the model developed by Ashby-Gibson or Zhao *et al.* (redrawn from [360] and [50])

All of the investigations exhibit a similar tendency in that an increasing pore volume fraction is accompanied by a decreasing elastic modulus. On the other hand, a negligible effect of pore size on the elastic portion of stress-strain diagram has been reported by Tuncer and Arslan [385]. They also reported that the strain rate did not significantly influence the elastic modulus, yet a slight increase in compressive strength was observed when the strain rate was increased at certain values was observed.

## 2.9 Summary

There has been enormous progress in the development of biomedical materials over time. A large number of biodegradable polymers, bioactive ceramics, highly biocompatible and corrosion resistant metals, and composite materials have been developed to be used in medical devices and prostheses. Although ceramics and

polymers have advantages due their bioactivity and biodegradability, they also exhibit susceptibility to high brittleness and high modulus for ceramics, and low mechanical strength for polymers. Compared to these materials metallic biomaterials can possess a more favourable range of properties in some biomaterial applications. In this regard, metallic biomaterials are widely used as structural materials in areas with high applied load such as, hip and knee prostheses, plates, screws and dental implants. The main requirements which must be fulfilled by metallic biomaterials are biocompatibility, biomechanical compatibility (compressive strength, and appropriate Young's modulus), osseointegration, viable processing including manufacturability, sterilisability, and of course availability. Among the metallic biomaterials such as stainless steel and cobalt based alloys, the use of titanium and its alloys has been growing due to their enhanced corrosion resistance, superior biocompatibility, reduced elastic modulus and high strength to weight ratio.

Based on their microstructures, titanium alloys may be classified into  $\alpha$ , near  $\alpha$ ,  $\alpha + \beta$ , metastable  $\beta$  (hereafter referred to as  $\beta$  alloy) and stable  $\beta$  alloys. Regarding this, alloying elements for titanium fall into three groups, *i.e.*  $\alpha$  stabiliser,  $\beta$  stabiliser and neutral. The most common titanium alloys,  $\alpha$  and  $\alpha + \beta$ ,  $\beta$  titanium alloys (Ti grades 1-4 and Ti-6Al-4V) are still extensively used for biomedical applications. However, in addition to the toxic effect on the human body of aluminium and vanadium in Ti-6Al-4V alloy, they have also been found to exhibit much higher Young's modulus values compared to that of bone. This mismatch can lead to bone resorption due to the stress shielding effect. In this context, metastable  $\beta$  titanium alloys containing  $\beta$  stabiliser elements such as niobium, tantalum, zirconium, molybdenum, tin have been developed due to a good biocompatibility behaviour, an excellent corrosion resistance and a lower elastic modulus. The latter two elements have been found to exhibit lower biocompatibility in comparison to the others. The addition of higher  $\beta$  stabiliser elements allows a number of metastable phases ( $\alpha'$ ,  $\alpha''$ ,  $\omega$  and  $\beta$ ) to occur during transformation from the elevated  $\beta$  phase. The  $\omega$  phase is known to possess the highest elastic modulus among  $\alpha'$ ,  $\alpha''$ ,  $\alpha$  and  $\omega$  phases, whereas the  $\beta$  phase exhibits the lowest elastic modulus. In the 1990's two metastable  $\beta$  titanium alloys were developed namely; Ti-35Nb-7Zr-5Ta (developed in US) and Ti-29-13Ta-4.6Zr (developed in Japan); exhibiting favourable properties

for use as implant materials. Significantly, Ti-35Nb-7Zr-5Ta possesses the lowest Young's modulus of 55 GPa, whereas Ti-29-13Ta-4.6Zr shows an elastic modulus of 67 GPa with a good response to heat treatment. The strength of the  $\beta$  titanium alloy, generally can be increased by aging at low temperature, where the martensitic phase precipitates within the  $\beta$  phase. More recently,  $\beta$  titanium alloy, Ti-24Nb-4Zr-7.9Sn has so far been developed with a minimum Young's modulus of 33-42 GPa.

The introduction of porosity into these alloys may reduce the elastic modulus to match that of bone. In addition to this, the porous structure may have the potential to promote osteoblastic cell attachment leading to an increase of osseointegration. A solid state foaming process based on a powder metallurgy technique is preferable rather than liquid foaming to produce porous titanium alloys due to the high melting point of and the high chemical reactivity of titanium. The range of diversity of methods of producing porous titanium alloys have been discussed in this section, such as the sintering of powder compacts technique, space holder techniques, gel casting techniques, fugitive scaffold technique, freeze casting technique and pressurised pore expansion technique in which CP titanium powder and/or the prealloyed powders being majority utilised as the starting powders. However, in addition to the biocompatibility issue and higher than preferred stiffness level for the porous structure of the commonly used titanium alloys containing alloying elements such as aluminium and vanadium, the use of prealloyed powder adds to the cost and the complexity of the manufacturing route. In this regard, the use of the elemental powders of the biocompatible elements as starting materials would overcome those issues.

The current work has been directed at investigating a production technique for  $\beta$  titanium alloys using a solid state procedure; mixing, alloying and foaming process using elemental powders of biocompatible elements, *i.e.* titanium, niobium, tantalum and zirconium. Subsequent to the foamed alloy development, materials characterisation and testing have been carried out.

# Chapter 3

## Experimental Procedure

### 3.1 Introduction

This chapter describes the experimental strategy of the research. The experimental procedure related to the objectives is outlined in Figure 3.1 and described in the following sections. These procedures were concerned with the fabrication of the porous titanium alloy (Ti-Nb-Ta-Zr) from elemental starting powders using solid state foaming, *i.e.* pressurised gas bubble entrapment. In this procedure microstructure and mechanical properties can be controlled by varying the parameters such as backfill pressure, foaming temperature or foaming time. There were three essential constituents of the experimental procedure: alloy fabrication, alloy characterisation and alloy assessment.

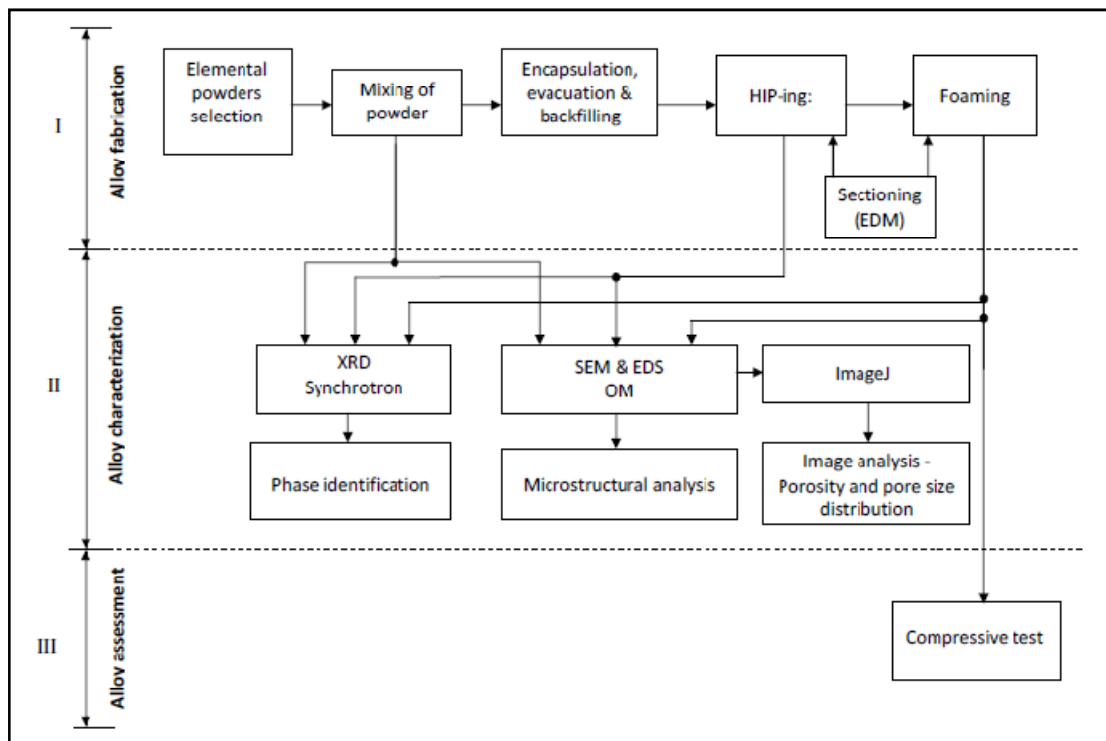
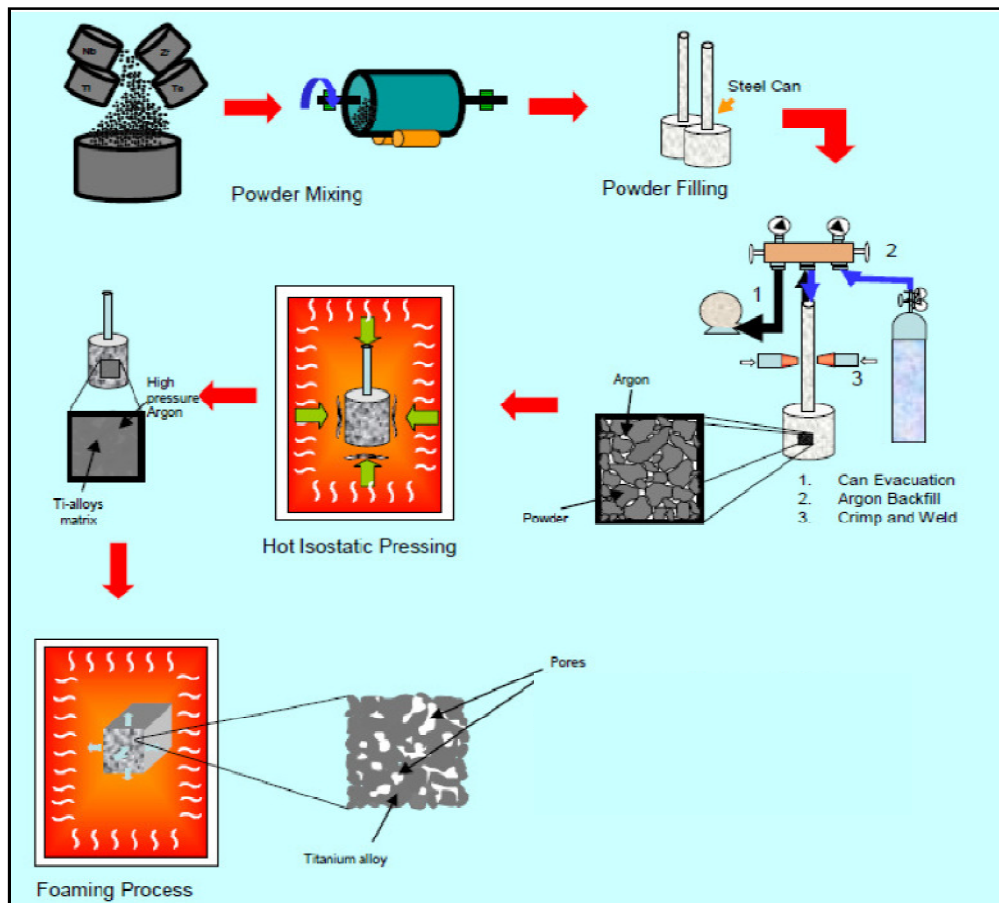


Figure 3.1 : Outline of the experimental work

### 3.2 Alloy fabrication

A critical goal of the fabrication strategy was to develop the porous Ti-Nb-Ta-Zr alloy based on a pressurised gas induced pore expansion technique using elemental powders as starting materials. The various stages carried out to produce the materials are detailed in these following sections. Briefly, the fabrication procedure involved: powder mixing, pressurised argon gas infusion, densification using hot isostatic press (HIP) and pore expansion at elevated temperature. Figure 3.2 shows schematically the steps of the powder metallurgical process employed to fabricate the porous titanium alloy.



**Figure 3.2 :** Schematic diagram of solid state processing to fabricate porous titanium foam based on the expansion of pressurised gas bubbles

### 3.2.1 Powder mixing

A mixed elemental powder metallurgy technique was applied to fabricate the titanium alloy. The starting materials, *i.e.*, titanium, niobium, tantalum and zirconium (supplied by CERAC Inc., Milwaukee U.S.A.) were received in airtight bottles and packaged with argon gas as depicted by Figure 3.3. Pre-weighed cups were prepared to weigh each elemental powders. For each batch of experimental alloy produced, the elemental powders were placed on the cup and were then weighed out in proportion to the composition as shown by Table 3.1 using a digital balance, (series Precisa 8000 C-6000 D from Precisa Gravimetrics AG Switzerland), with an accuracy of 2 decimal points. Following this, the elemental powders were then placed into a cylindrical glass container which was then sealed. The diameter is approximately 14 cm and 20 cm in length. There are 3 lifters inside in order to obtain more homogenous powder mixture. The glass container was then put on a roller mixer for blending. This mixer was set to a speed of 87 RPM for 30 minutes, being interrupted every 10 minutes to change the position of the container.

**Table 3.1** : Powder composition used for the alloy

	Nb	Ta	Zr	Ti
<b>% mass</b>	29.04	13.02	4.51	Bal
<b>Purity</b>	99.8	99.9	99.7	99.5



**Figure 3.3 :** The elemental powder packaging supplied by CERAC

### **3.2.2 Pressurised argon gas infusion**

After blending, the powders were placed into grade 316 stainless steel canisters. The canisters were approximately 31.75 mm outer diameter, 1.6 mm wall thickness and 30mm in length. A diagram of the canister can be seen in Figure 3.4 :. Each end of the canister was sealed with a cap machined from 316 stainless steel. Whilst the lower and the top cap were completely welded to make an airtight seal, the deaeration tube was welded onto a hole drilled in the top cap, in order to allow oxygen and argon gas out and into the canister during the evacuation and backfilling processes. After the canister was machined and the bottom cap was welded, the canister was then washed using soapy water, followed by an ultrasonic cleanse with ethanol as a fluid media, to remove machining oil and other dirt, then dried in a furnace overnight at 105°C.

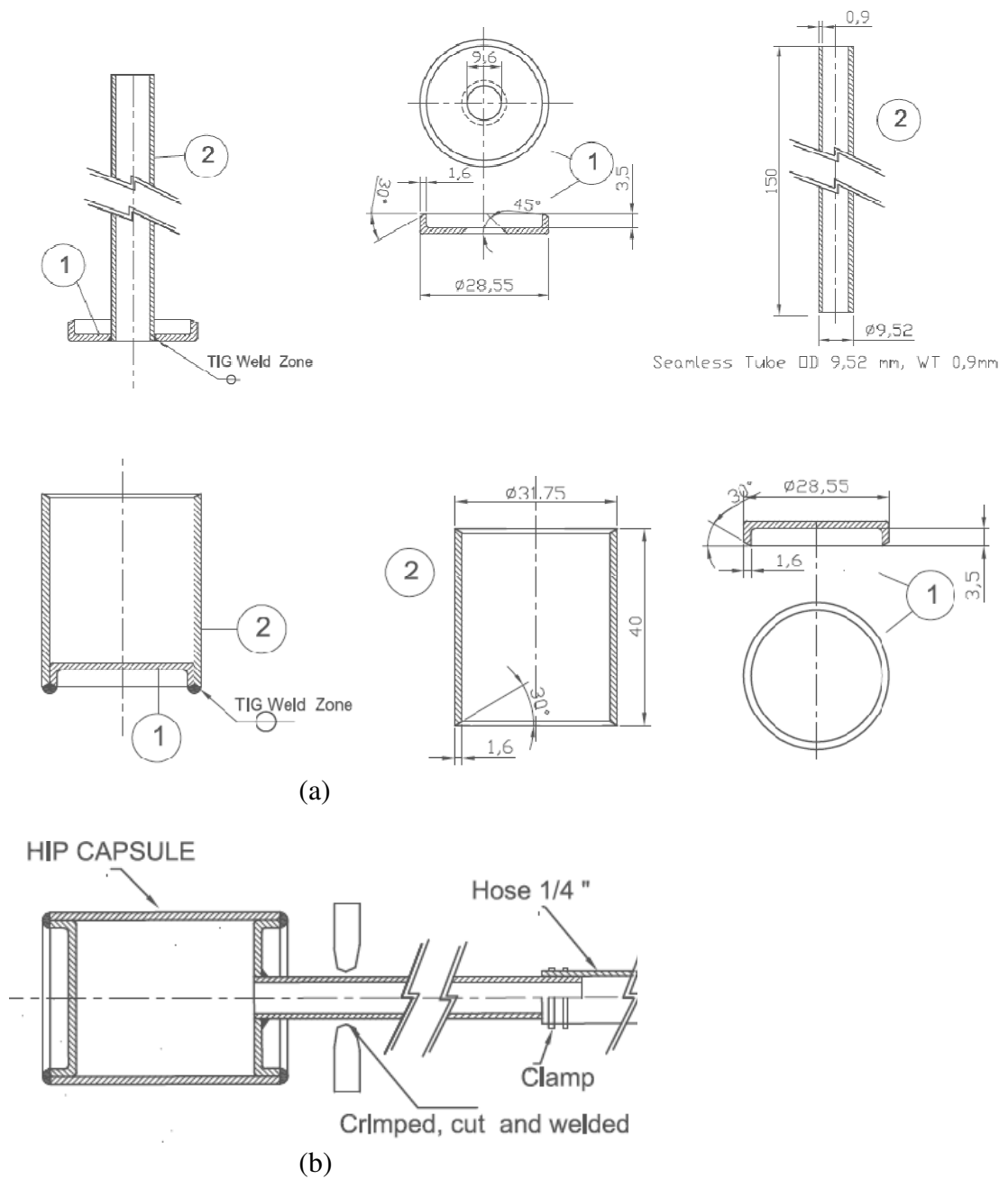


**Figure 3.4 :** HIP canister design (a) Shop drawing of HIP canister and (b) assembled canister showing weld locations.

Afterwards, the blended powder was placed almost completely full into the canister. In order to pack the powders more tightly than through pouring, the canister was constantly tapped during filling. The top cap was then completely welded on the canister. The can was subsequently evacuated equivalent to  $10^{-5}$  Torr, using a

mechanical vacuum pump type Duoseal<sup>®</sup> Vacuum Pump 1400 series (from Welch). A MicroPirani Transducer series 925C, sitting on a three way manifold gauge set through a VCR connector (manufactured by Swagelok), was applied for the vacuum measurement. This transducer was connected to a PDR900-1 digital display series Controller (supplied by MKS HPS) to display the measurement. An ultra high purity Argon gas with a purity of 99.999%, supplied from BOC (British Oxygen Company) Australia, was backfilled into the canister at specific pressures, *i.e.* 0.34, 0.48, 0.68, and 0.86 MPa. The evacuating and backfilling processes were controlled using the manifold and a regulator gauge set up on top of the argon cylinder tank. The canisters were then sealed by crimping and spot welding on the backfilling pipe following by cutting and TIG welding. The canisters were then ready for the HIP-ing procedure.

### **3.2.3 The HIP-ing process**

HIP-ing involves the simultaneous applications of both high pressure gas (usually inert gas) and an elevated temperature in a specially constructed vessel. In most HIP-ing systems, argon gas is used and is required in high purity due to the material being directly exposed to the processing gas. Argon gas is chosen as a pressurising medium due to its inertness and insolubility in any materials. Under high temperature and high pressure this simultaneous application accelerates the process of densification, along with internal pore or defect collapse, resulting in a high densification of powders with better mechanical properties [386] (p.1). Typical HIP-ing of titanium is conducted at a temperature of 920°C and at a pressure of 100 MPa [386] (p.6). The sequence of the HIP-ing process requires approximately 7–12 hours for each total cycle time, and involves evacuation, pressurisation, depressurisation and charge handling. The HIP-ing cycle is detailed as follows : (1) preparation, (2) loading, (3) purging, where the pressure vessel is evacuated and purged with pressurised gas, (4) equalisation, high purity Argon is injected to the vessel until the pressure between the vessel and the storage system is equal, (5) compression, the compressor pumps the gas to the vessel until the prescribed pressure is attained, (6) heating, normally 2-4 hours are required to achieve the HIP-ing temperature, at which the sample is held

at for between 1-4 hours, (7) cooling, the cooling rate (2-10°C/minute) depends on the cooling system chosen and (8) charge removal [386] (pp.67-68).

In this study, the HIP-ing procedure was applied to an encapsulated powder (canned powder) in order to entrap the pressurised argon gas within titanium alloy matrix in addition to facilitate solid state alloying process. Various HIP-ing temperatures for the argon entrapment in titanium or its alloys have been reported such as at 890°C for 2 hours HIP-ing to a pure titanium powder [371, 387], at 950-1000°C for 4 hours for a Ti-6Al-4V prealloyed powder [50, 57, 388], and at 1066°C for 4 hours for a mixed NiTi prealloyed and elemental Ni powder [50].

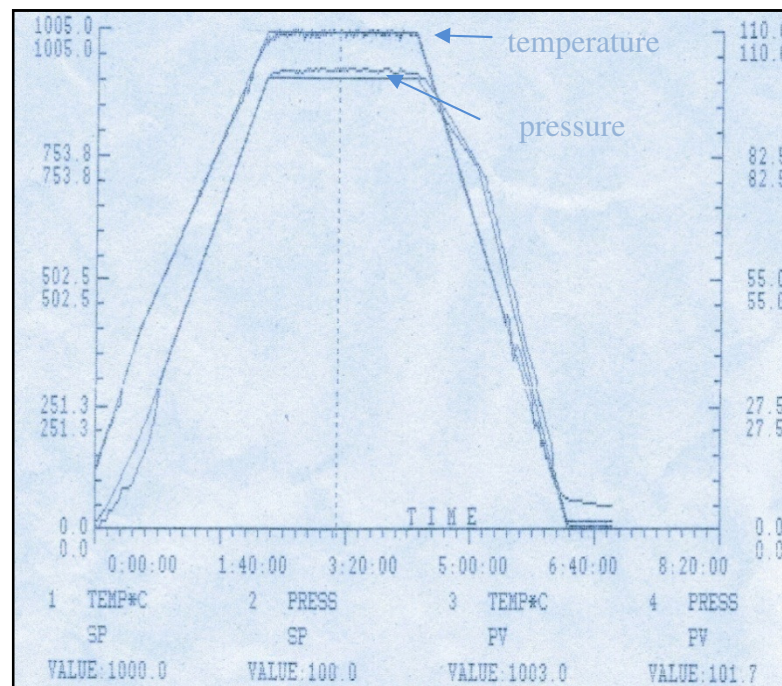


**Figure 3.5** : Diagram of typical trial run HIP-ing cycle, with smooth line and jagged line showing cycle set up and actual cycle data respectively

The HIP-ing procedures were carried out at the Australian Nuclear Science and Technology Organisation (ANSTO), Sydney, New South Wales. The canisters were loaded into alumina box crucibles in which 8 canisters sat in each box. These were then placed into the HIP chamber consisting of a molybdenum furnace, sitting on alumina spools. The trial HIP-ing procedure was run at a temperature of 1000°C for 2

hours with a pressure of 100MPa. The typical HIP-ing cycle diagram is shown by Figure 3.5, showing temperature and pressure achieved.

In order to obtain a titanium alloy billet with a greater degree of alloying, *i.e.* more dissolved elemental particles and a greater proportion of  $\beta$  phase, the HIP-ing parameters were varied. The HIP-ing procedure was undertaken under the conditions as described by Table 3.2.

**Table 3.2 : HIP-ing settings**

<b>Sequence</b>	<b>Setting value</b>	<b>Unit</b>
Ramp up - heating rate	8-10	°C / minute
HIP-ing temperature	1100	°C
HIP-ing pressure	100	MPa
Holding time	4	hour
Cool-ramp –cooling rate	unassisted (6-10)	°C/minute [386](p.68))

Once the HIP was cooled completely from its run, the furnace was opened and the HIP-ed canisters were removed. Due to the high temperatures, long process time and high pressure, the HIP-ed canisters were often found to be slightly flattened in addition to the occurrence of some diffusion between the titanium alloy and the stainless steel canister. These conditions resulted in difficulty in removing the HIP-ed titanium alloy from its canister. Therefore, following the HIP-ing procedure, the HIP-ed canisters were cut directly using a Wire cut Electrical Discharge Machine (WEDM) in order to obtain specimens for further processing (see Section 3.2.4)

### **3.2.4 Sectioning samples**

Due to their unique physical and chemical properties, titanium and its alloys are classified as difficult to machine materials by conventional machining techniques [389]. Some considerations have to be recognised during the machining of titanium. Its lower thermal conductivity inhibits quick heat dissipation caused by machining, this leading to rapid cutting tool wear, whilst its lower hardness and its higher reactivity lead to a tendency for the galling of titanium with the cutting tools [390]

(p.245). In addition, both its strength being maintained at elevated temperatures and its low elastic modulus impairs its machinability [391]. Therefore, nontraditional machining processes are recommended for these materials.

The Wire cut Electrical Discharge Machine (WEDM) is based on material removal by using a series of repeating electrical discharges between an electrode and the workpiece submerged in a dielectric fluid such as hydrocarbon oils or distilled water [392]. It provides the ability to cut materials regardless of the mechanical properties, and minimises material waste, thus, titanium can be machined effectively by this technique [393]. A water-based dielectric was found to result in a better surface finish and was more environmentally safe compared to a hydrocarbon oil dielectric fluid, which would also decompose and release harmful vapours (CO and CH<sub>4</sub>) [394]. Finally, due to the lack of direct contact between the workpiece and the cutting tool (wire electrode), adverse effects such as chatter, mechanical stress and vibration were eliminated [395].

In this study, the cutting process for the HIP-ed canisters and foamed titanium alloy specimens was carried out on specific electrical discharge machining equipment: A FANUC ROBOCUT  $\alpha$ -OiD with a FANUC series 310/s-WA controller (manufactured by FANUC Japan), as shown in Figure 3.6, was used according to the settings as described by Table 3.3

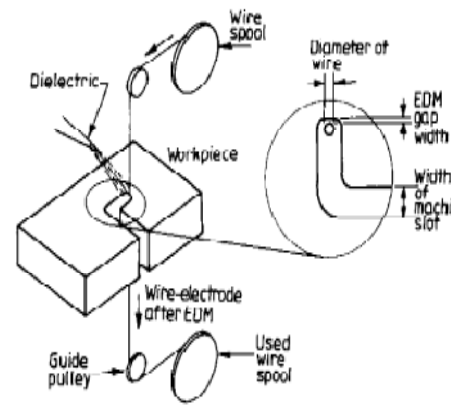


**Figure 3.6 :** A WEDM, a FANUC ROBOCUT  $\alpha$ -0iD machine used in this work (left), basic feature of WEDM process (right) [389]

**Table 3.3 :** The WEDM setting conditions for cutting the titanium alloy specimens:

<b>Input setting</b>	<b>Setting value</b>	<b>unit</b>
Wire diameter	0.25	mm
Wire speed	3	m/minute
Cutting speed	7.63	mm/minute
Machining voltage	69	volt
Ignition pulse current	1.5	ampere
Pulse duration	6	ms
Time between two pulses	26.3	ms
Wire tension	1300	gram
Wire electrode	brass	
Dielectric fluid	Distilled water	

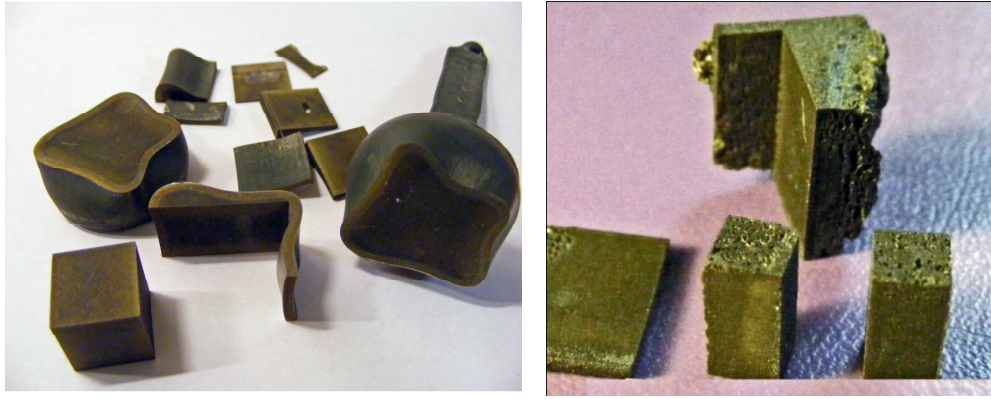


**Figure 3.7 :** Typical WMED-ed specimens of a (a) HIP-ed canister and (b) foamed specimen

After the foaming process, each foamed specimen was cut by a WEDM for a microstructural and phase identification analysis, and compression testing. To produce specimens for microstructural analysis, the HIP-ed canisters were sliced into cubic specimens of approximate dimensions  $10 \times 10 \times 10 \text{ mm}^3$ , depending on the extent of their flattened condition after HIP-ing. For phase identification specimens (Figure 3.7(a)) a flat plate with a thickness of 2 mm was produced, whilst for the compression test specimens, a dimension of  $4 \times 4 \times 8 \text{ mm}^3$  (Figure 3.7(b)) was produced.

### **3.2.5 Pressurised pore expansion – the foaming process**

Prior to this pore expansion process, the WEDM-damaged layers of the cubic specimens (of approximate dimension  $10 \times 10 \times 10 \text{ mm}^3$ ) were removed by light grinding and polishing by means of 600 grit silicon carbide paper, and followed by ultrasonic cleaning in acetone. The cubic HIP-ed billets were then subjected to a pressurised pore expansion process by exposing them to high temperatures in a vacuum furnace. During this time the pressurised pores were expected to expand due to creep of the surrounding metal (foaming process). Previous researchers had reported isothermal foaming processes carried out in vacuum furnaces at temperature ranges of  $900\text{-}980^\circ\text{C}$  for a pure titanium [371, 387] and of  $1000\text{-}1240^\circ\text{C}$  for  $\alpha+\beta$  titanium alloys [50, 57, 388]. They also found that pore sizes grew rapidly during the initial 10 hours of foaming [50, 57] with no further growth being noted after approximately 3 days of foaming [396]. The cubic specimen was seated on an

alumina tray and was then rapidly heated to 1150°C in a graphite element vacuum furnace ( $10^{-2}$  Pa) and held for 10 hours, followed by unassisted cooling, this process being carried out at the Applied Physic Department Laboratory, Curtin University. Due to massive failure of the vacuum furnace after conducting one cycle of the foaming process, the further foaming processes were carried out in a vacuum furnace at the ANSTO facilities, Sydney.

Prior to loading into the graphite element vacuum furnace, the cubic specimens were placed on a graphite tray. The following step sequences were scheduled (considering the vacuum profiles) to carry out the foaming process as shown in Table 3.4.

**Table 3.4 :** The schedule of the foaming process in the vacuum furnace

<b>Step</b>	<b>Schedule</b>
1	Start - ramp 5°/min to 150°C - hold for 5 hours (After specimen loading, the vacuum furnace was evacuated to $10^{-4}$ Torr and flushed once by argon gas followed by evacuating to the required pressure)
2	Soak - ramp 20°/min to 300°C - hold for 1hour
3	Ramp 1 - ramp 10°/min to 1000°C - no hold
4	Ramp 2 - ramp 5°/min to the foaming temperatures (1100°C, 1225°C or 1350°C) hold for 10 hours
5	Cooling - ramp 5°/min to 20°C - end sequence

This sequence shows that each foaming cycle required approximately 24 hours for completion. The specimen tray was unloaded once the vacuum furnace was completely cooled. The specimens tended to stick to the tray; however a gentle tap was found to easily release them.

### **3.3 Characterisation**

A number of different analysis techniques have been used to characterise the nature of the alloys and foams produced with the aforementioned fabrication technique. These are outlined in Figure 3.1 and described in detail in the following sections.

### 3.3.1 X-ray diffraction (XRD) analysis

The diffraction analyses were applied to determine the phases of the titanium alloys developed by the fabrication process. The XRD analyses were initially carried out using a Siemens D-500 X-ray machine, available in the Applied Physics Department at Curtin University of Technology. Plate specimens of titanium alloy with dimensions of 9 mm x 9 mm and a thickness of 1-2 mm were placed in an aluminium holder with a diameter of 23 mm using mild adhesive. In order to identify phase constituents and the phase development during fabrication, elemental starting powders, mixed powder, the HIP-ed specimens and the foamed specimens at the various temperatures were examined. Specimen rotation was applied to reduce the preferred orientation effect. The details of instrument setting for data collection are as follows:

Instrument	Siemens D-500
Radiation	Cu-anode tube, type FF Cu4KE 60 kV 1,5 kW Operated at 40 kV and 30 mA Effective focal spot size 0.004 x 8 mm <sup>2</sup> Unfiltered, Wave length: CuK $\alpha$ = 1.5406 Å
Optics	Bragg-Brentano, measuring circle diameter = 401 mm Incident beam divergence = 0.3°, receiving slit = 0.15° Scatter slit divergence = 1°, soller slit divergence = 1°
Specimen	Holder – circular format, diameter = 23 mm Holder was rotated for all measurements
Detection	Graphite diffracted beam monochromator set for CuK $\alpha$ NAI scintillator with pulse height analysis
Acquisition	: Angular range in 2 $\theta$ = 30 – 90° Step size = 0.04° Counting time = 1 s/step

Recently, the Siemens D-500 was replaced by a new XRD instrument, a Bruker D8 Advance. Using this machine, a specimen with a thickness up to 5 mm can be placed onto the plastic sample holder by mild adhesive (Figure 3.8).



**Figure 3.8 :** The specimen positioned on the sample holder for XRD examination.

The instrument setting for data collection by the Bruker D8 Advance is described below:

Generator /Tube	operated at Voltage = 40 kV and Current = 40 mA
Goniometer radii	Primary radius = 250 mm Secondary radius = 250 mm
LynxEye detector	Primary soller slit = 2.5° Secondary soller Slit = 2.5° Fixed antiscatter slit of 8 mm Ni filter is fitted (0.5 mm)
The divergence slit	0.3°
Specimen	Holder – circular format, diameter = 23 mm Holder was rotated for all measurements with rotation speed = 30 rpm
Acquisition	Angular range in $2\theta = 30 - 90^\circ$ Step size = 0.03891° Time/step = 1s

The collected spectrum data (in RAW format) was analysed using Jade software and/or DIFFRACT plus EVA Software from Bruker AXS to determine the phase constituents developed within the samples.

### 3.3.2 Synchrotron radiation diffraction (SRD) analysis

High resolution X-ray diffraction (HR-XRD) obtainable by a synchrotron radiation source (SRS) has recently been demonstrated as a very useful method for detailed investigation of phase development and structure of materials. The main advantages are the inherent high brightness and tunable monochromatic beam, which allow the development of a high resolution analysis [397]. In this study, elemental powders, mixed powder and flat plates of approximate thickness 2 mm for each specimen (HIP-ed and foamed specimens) were investigated using synchrotron radiation diffraction (SRD) on the Powder Diffraction beamline at the Australian Synchrotron facility in Melbourne, Australia. Prior to analysis, each sample was placed onto an aluminium specimen holder (able to accommodate a sample thickness up to 2.34 mm and a diameter of ~27 mm) that was rotated during the experiment. The synchrotron beam had been passed through a bent Si crystal monochromator with a beam energy of 15 keV (equivalent to a wavelength of 0.08263 nm). The beam width and height were 2.0 mm and 0.2 mm, respectively, whilst the beam angle incident to the specimen was kept constant at 5 degrees. Since the powder diffraction beam line is equipped with a microstrip system for time resolved experiments (MYTHEN), a detector system consisting of 16 detector modules, there is a gap between each module covering approximately  $4.8^\circ 2\theta$  as shown by Figure 3.9. To overcome the gap between modules the diffraction pattern is collected as two or more histograms. The collection of the second histogram is carried out after shifting the detector an arbitrary angle  $x$ , such that  $0.2^\circ < x < 4.8^\circ$ . The histogram pairs were then joined using software that was available at the beamline or MyHIST software which was developed by the Centre for Materials Research Group (CMR) at Curtin University.

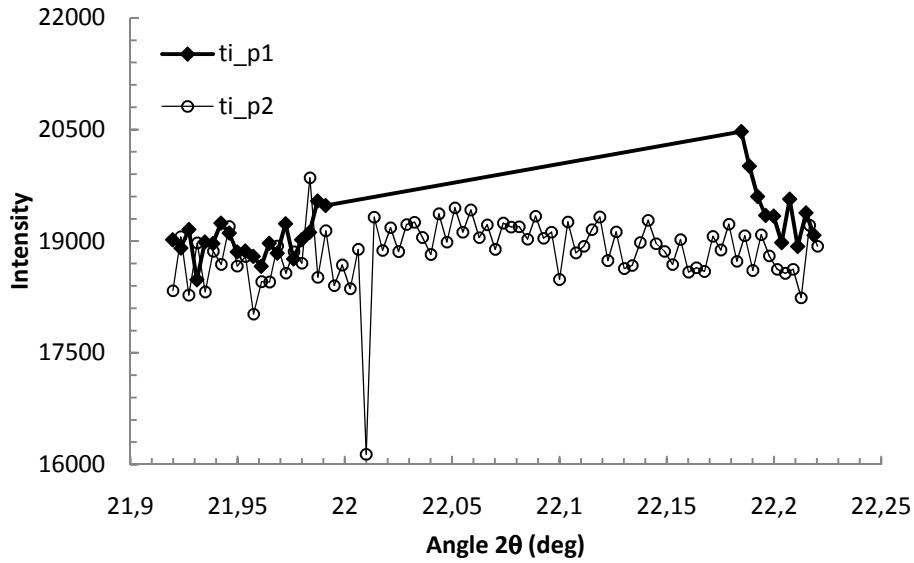


**Figure 3.9 :** Powder diffraction data (pure titanium) of a small region  $2\theta$  showing the gap in the first histogram (ti\_p1)

In order to allow an easier comparison with standard X-ray diffraction (XRD) data, the SRD results for each specimen were converted into angular data equivalent to the wavelength of Cu  $K\alpha$  (0.15418 nm) by using Bragg's law as follows :

$$2d \cdot \sin \theta = \lambda \quad \text{Equation 3-1}$$

$$\theta_{\lambda_{CuK\alpha}} = \arcsin \left( \frac{\lambda}{2 \cdot d} \right) \quad \text{Equation 3-2}$$

Where  $d$  is the interplanar spacing (nm),  $\lambda$  is the synchrotron wavelength (0.08263 nm) and  $\theta$  is the diffraction angle.

### 3.3.3 Microstructural examination and EDS analysis

Prior to microstructural examination, the surface WEDM-ed damaged layer of the specimens was removed by grinding with SiC paper grid 600. The specimens were then mounted with epoxy resin for polishing. A clear epoxy resin and an epoxy hardener, FR-251 (supplied by Fibreglass & Resin Sales Pty Ltd), were used for this purpose. One part hardener was mixed to two part resin by weight. The specimen was placed into a sizing container and which was then filled with the resin. Complete curing of the resin allowing a better polish and a cleaner view under the

metallographic microscope was achieved by leaving the sample to set overnight. Following this, the mounted sample was removed from the container and was then sequentially polished with silicon carbide paper of grid size 400, 600, 800, 1000 and 1200. These processes were carried out on a Minitch 263 polishing machine (manufactured by PRESI, France), at a rotation speed of 100 rpm for 180 seconds in each step. Further polishing was carried out by using cloth and diamond suspensions down to 3 $\mu$ m, and finally a water suspension of 1 $\mu$ m grain size alpha alumina polishing powder (produced by Leco Corp, St Joseph, Michigan, USA) [398]. Afterwards, the specimens were washed in acetone using an ultrasonic cleaner for 10 minutes and then thermally dried. The specimens were then ready for metallographic observation by using optical and/or electron microscopy. For pore size distribution analysis, the HIP-ed and the foamed specimens were examined using an optical microscope (OM) type Eclipse ME 600 (from Nikon, Japan). The images were captured by digital camera, type Spot Insight Colour, model 3.2.0 (from Diagnostic Instrument Inc USA), which was attached to the optical microscope. For microstructural analysis, those specimens were then etched using modified Kroll's solution (2.5% HF, 5 % HNO<sub>3</sub> and 92.5 % H<sub>2</sub>O). The specimens were immersed into the solution for approximately 10 seconds, flushed with water and then dried in a fume cupboard. The samples were stacked with a carbon conductive double-sided tape and were loaded into the electron microscope specimen chamber. The scanning electron microscope (SEM) imaging was undertaken on a Philips XL 30 and Zeiss Evo 40XVP with a voltage of 15-20 kV and working distance 8-11 mm. The electron microscopes were equipped with two detectors, a secondary electron detector (SE-SEM) for obtaining surface topography of the specimens, and a backscattered electron detector (BE-SEM) for analyzing the elemental composition of the specimens.

In order to enable fast identification of the elemental composition of the specimens, an Oxford Instrument energy dispersive X-ray detector (EDS) with INCA peak matching software installed was used. Quantitative analyses of elemental constitution within selected samples were also carried out. Prior to doing this analysis, samples had to be prepared and polished to a smooth and flat condition. The system was calibrated (optimised) using a standard copper sample. Specific sample standards related to the specimens, in this case the titanium standard sample, were also used as

a comparison. Spectra were collected under the same settings of kV, working distance, magnification, spot size, beam current, scanning speed and live time. The setting conditions used during the collection of spectral data is described in Table 3.5.

**Table 3.5 :** Operating conditions for quantitative analysis using EDS on a Zeiss Evo 40XVP SEM

<b>Input setting</b>	<b>Setting value</b>	<b>unit</b>
Accelerating voltage	20	kV
Working distance	8.5	mm
Magnification	1720x and 68795x	
Spot size	400	
Scanning speed	5	
Live time	100	second
Beam current	120	pA

### **3.3.4 Porosity and pore size distribution determination**

Digital image analysis was used to determine porosity and pore size distributions [399] [46]. For this purpose twenty images for each specimen were analysed using open source software, ImageJ version 1.43u (National Institute of Health USA). Prior to image analysis, image micrograph calibration was required. Figure 3.10 is an optical micrograph of the calibration bar at 10x optical magnification. This figure shows that a length of 1368 pixels was equivalent to 1000  $\mu\text{m}$ . Hence, the scaling factor can be obtained of the micrographs captured under 10x optical magnification by the following equation

$$F_{s,10xm} = 1,368 \text{ pixel} / \mu\text{m}$$

Equation 3-3

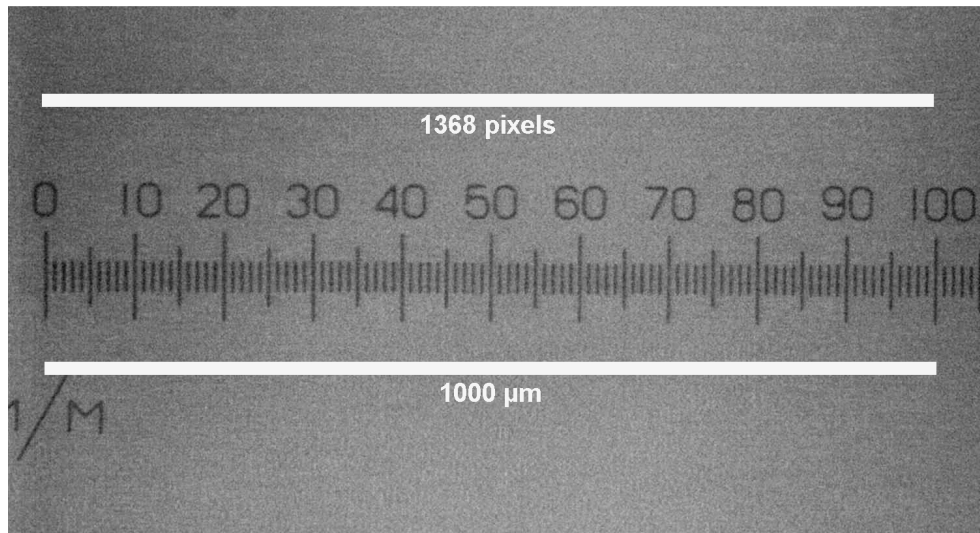


**Figure 3.10 :** Photo micrograph of the calibration bar captured under 10x optical magnification

A series of images illustrating this method is shown in Figure 3.11. In this technique, each colour micrograph of a polished unetched flat surface specimen was captured by an optical microscope. The micrographs were then transferred into an 8-bit grayscale image format (Figure 3.11(a)). Afterwards, the threshold of the images was set to a certain level that produced a two colour image – a binary black and white image, with one colour indicating pores and the other colour indicating the titanium alloy matrix (Figure 3.11(b)). Next, the binary images were subjected to running particle analysis which produced the pore fraction of the image and a list of every pore area. (Figure 3.11(c)) As mentioned earlier, the images were calibrated into the  $\mu\text{m}$  unit, with the area in square  $\mu\text{m}$  and the total area fraction thus calculated. In accordance with research carried out by Oppenheimer [50], the list of pore was then binned into 15 bins with each of the  $i$  bins being calculated by the equation  $D_{\text{max}} \times 10^{-0.1(i-1)}$  where  $D_{\text{max}}$  is the largest pore size measured. The list was then transferred to an EXCEL spread sheet for further processing such as calculation of pore diameter and subsequent binning. Next the binned list was presented in a step plot of percentage distribution using SIGMA plot.

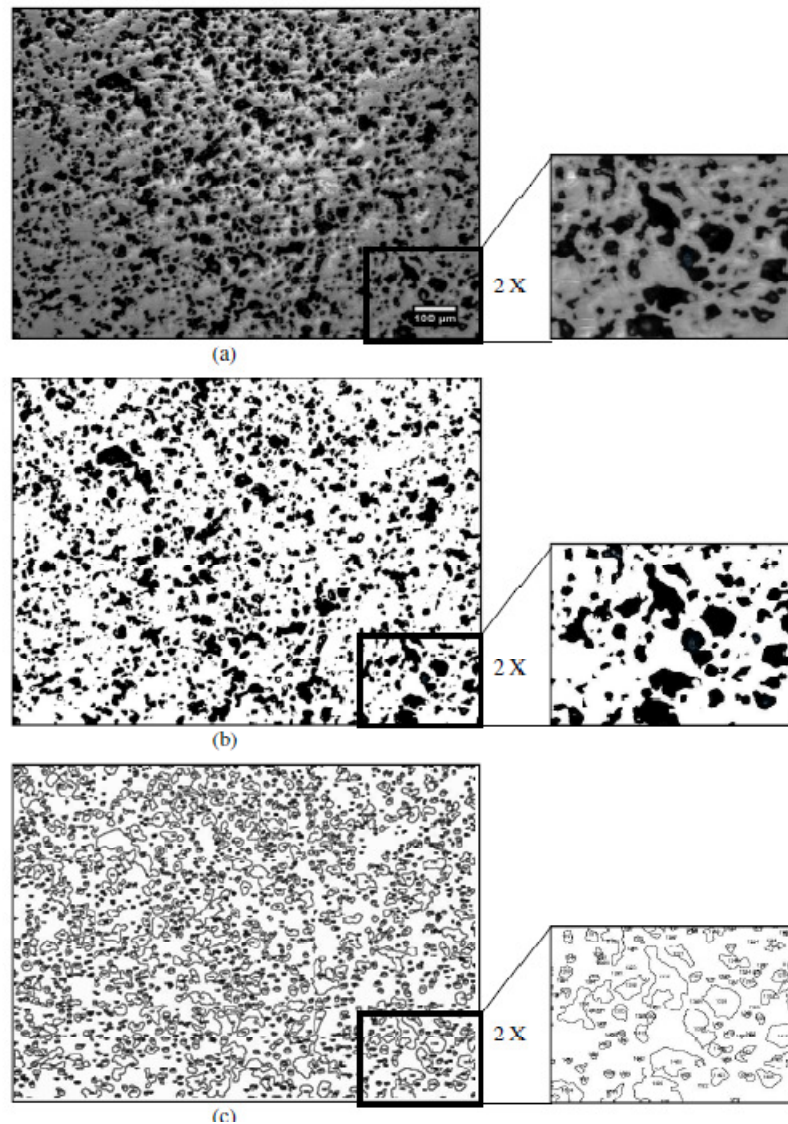


**Figure 3.11 :** Series of steps of digital image analysis using the ImageJ software (same magnification for (a), (b) and (c))

### 3.4 Electrochemical corrosion assesment

Specimens for electrochemical studies were sectioned from cubic foamed specimens using WEDM. The areas to be exposed for electrochemical studies were approximately 10mm x 10 mm square. After soldering a wire to the back of the specimen, each specimen was cold mounted. The surfaces exposed to the electrolyte were prepared by sequential grinding with silicon carbide paper up to 1200 finishing, followed by mechanical polishing with diamond paste. The specimens were then washed in distilled water followed by ultrasonic cleaning in acetone. The

electrochemical studies were conducted using a Gamry G750 potentiostat in Research Centre for Metallurgy Indonesian Institute of Science (LIPI), Jakarta, Indonesia. The electrolyte used for simulating human body fluid conditions was Hank's solution, prepared using laboratory grade chemicals and double distilled water. The pH of the solution was precisely maintained at 7.0. Freshly prepared solution was used for each experiment. The composition of the Hank's solution used was (in gm/l) 8 NaCl, 0.4 KCl, 0.14 CaCl<sub>2</sub>, 0.06 MgSO<sub>4</sub>.7H<sub>2</sub>O, 0.06 NaH<sub>2</sub>PO<sub>4</sub>.2H<sub>2</sub>O, 0.35 NaHCO<sub>3</sub>, 1.00 Glucose, 0.60 KH<sub>2</sub>PO<sub>4</sub> and 0.10 MgCl<sub>2</sub>.6H<sub>2</sub>O. Electrochemical polarisation studies were conducted in a round bottom polarisation cell. The potential of the working electrode was measured against a saturated calomel electrode (SCE). The luggin capillary was placed close to the working electrode. All the potentials mentioned in this thesis are with reference to SCE. A constant electrolyte temperature of 37±1°C was maintained. All the potentiodynamic polarisation studies were conducted after stabilisation of the free corrosion potential. The scan rate used was 1 mV/s in the range from -1,2 to + 2 V. The corrosion potential ( $E_{\text{corr}}$ ) and corrosion current density ( $i_{\text{corr}}$ ) were determined using the Tafel Extrapolation Method. All the tests were duplicated to ensure reproducibility of the electrochemical curves. In the experiment, the evolution of the open circuit potential; i.e. corrosion potential, as a function of immersion time was measured for one hour.

### **3.5 Mechanical properties assessment**

#### **3.5.1 Hardness testing**

The indentation hardness was measured using Buehler Micromet 0055 microhardness tester with Vickers diamond pyramid indenter. The hardness specimens were obtained from the three groups of foaming temperature specimens having been cut off using WEDM with the dimensions of approximately 10mm x 10mm x 2 mm. The surface specimens were prepared by sequential grinding with silicon carbide paper up to grit of 1200, followed by mechanical polishing with diamond paste. The Vickers hardness was measured at the surface of the specimen with a load of 100 gf and a holding time of 20 s. An average of 15 readings was taken from each specimen.

### 3.5.2 Compressive testing

The compressive test specimens were prepared using WEDM with a height-to-width ratio of 2 (typical dimension  $4 \times 4 \times 8 \text{ mm}^3$ ), this being similar to the previous investigation carried out by Erk *et al.* [360]. Both ends of the specimens were lightly polished and cleaned with acetone to remove all traces of grease or oil. Prior to the compressive test, calibration of the clip gauges used for the specimen strain measurement was carried out. The microstrain linear displacement of the clip gauge recorded by the P3 strain recorder was calibrated with a Mitutoyo external micrometer with ratchet stop (0.001 mm) [from Mitutoyo Japan] (Figure 3.12(a)) and plotted (Figure 3.12(b)). All points presented in the curve are average values of measurements, this curve showing correlation between both the linear displacements with the following equations:

$$L_{CG1} = -L_{P3-1}/747,3 + 15.240 \quad \text{Equation 3-4}$$

$$L_{CG2} = -L_{P3-2}/781,9 + 14,805 \quad \text{Equation 3-5}$$

Where  $L_{CG1}$  and  $L_{CG2}$  are the linear displacements of calibrated clip gauge 1 and 2, and  $L_{P3-1}$  and  $L_{P3-2}$  are linear displacements measured by the P3 strain recorder on channel 1 and 2.

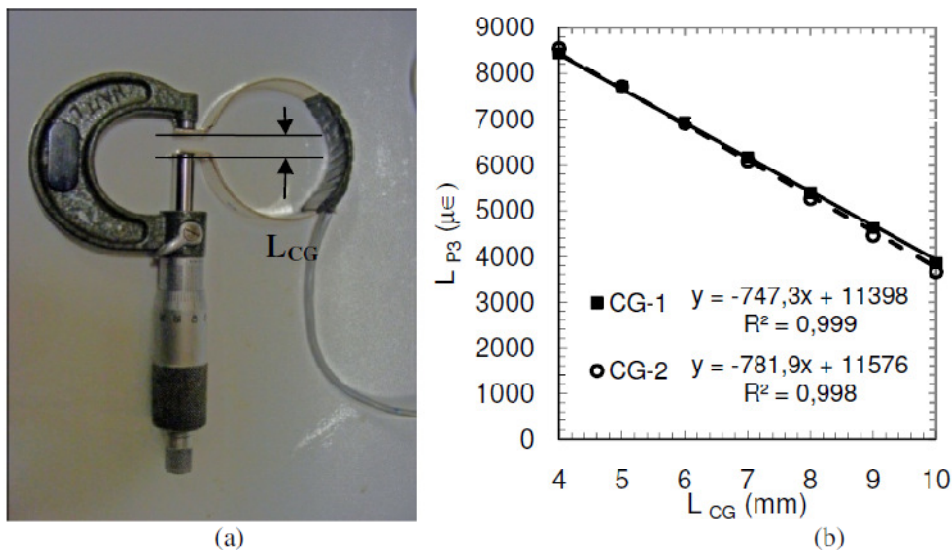


**Figure 3.12** : Clip gauge calibration, (a) Linear displacement of the clip gauge was measured by a Mitutoyo external micrometer, (b) Calibration curves.

Compressive tests were carried out using a standard mechanical testing equipment, an Instron® 5500R, at a strain rate of  $10^{-3} \text{ s}^{-1}$  [360]. The specimen strain was measured using the two clip gauges attached to the tungsten carbide platen surfaces in contact with the specimen (Figure 3.13). This strain was recorded using a 4-channel-strain indicator and recorder, the P3 Strain Indicator and Recorder, (manufactured by Vishay Micro Measurement, Inc., Raleigh, North Carolina, USA). The Young's modulus of the porous titanium alloys was calculated from the initial linear elastic region of the compressive stress-strain curves after the results were analysed using an Excel spreadsheet.

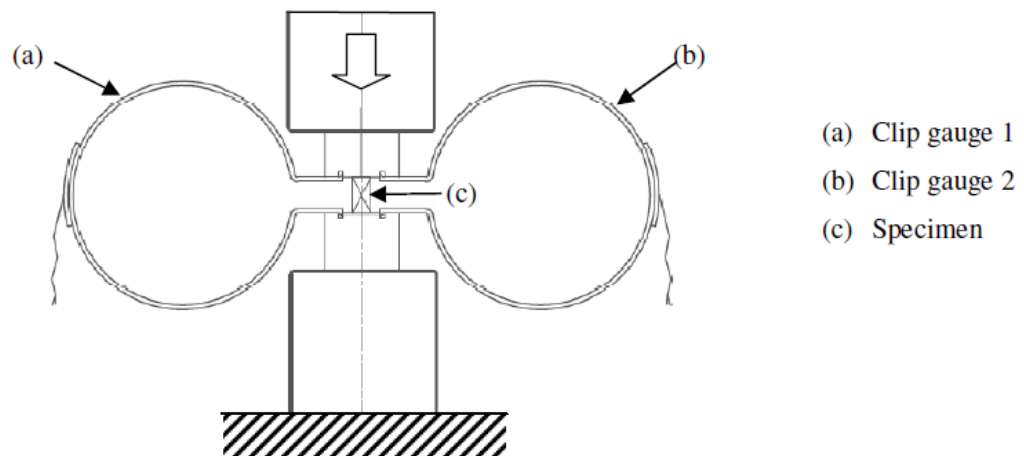


**Figure 3.13 :** Schematic diagram of compressive test set up

Every single data point of the tested specimens obtained from an average value of the two clip gauge measurements is presented in this work. After being tested up to failure, the failure region of the selected specimens was prepared for fracture examination.

# Chapter 4

## Results and Discussion

### 4.1 Introduction

Ti-Nb-Ta-Zr alloy systems have been intensively developed for biomedical applications because of their excellent properties, including biocompatibility, corrosion resistance and low elastic modulus. In order to improve the osseointegration and compatibility in stiffness to bone, the development of porous titanium alloys has been investigated. Recently, it has been demonstrated that it is possible to develop the porous alloys by a pressurised bubble entrapment technique using elemental powders as starting materials. In this chapter, results on synthesis, phase composition and development, and mechanical properties of a porous titanium alloy are described. The characteristics and the properties of the porous alloys have been studied using room temperature x-ray diffraction, synchrotron radiation diffraction, scanning electron microscopy, optical microscopy, image analysis and compressive tests.

### 4.2 Raw material evaluation

The elemental powders, *i.e.* pure titanium, niobium, tantalum and zirconium powder (supplied by CERAC, Inc., Millwaukee, USA) were used as starting/raw materials (see section 3.2.1). The chemical composition of the titanium alloy is shown in Table 3.1. Particle size and purity of the angularly shaped elemental powders used in this study were less than 44  $\mu\text{m}$  (-325 mesh) and over 99.5%, respectively. The morphologies of the elemental powders before the blending procedure are depicted in Figure 4.1, with the corresponding energy spectra from EDS measurement shown in Figure 4.2.

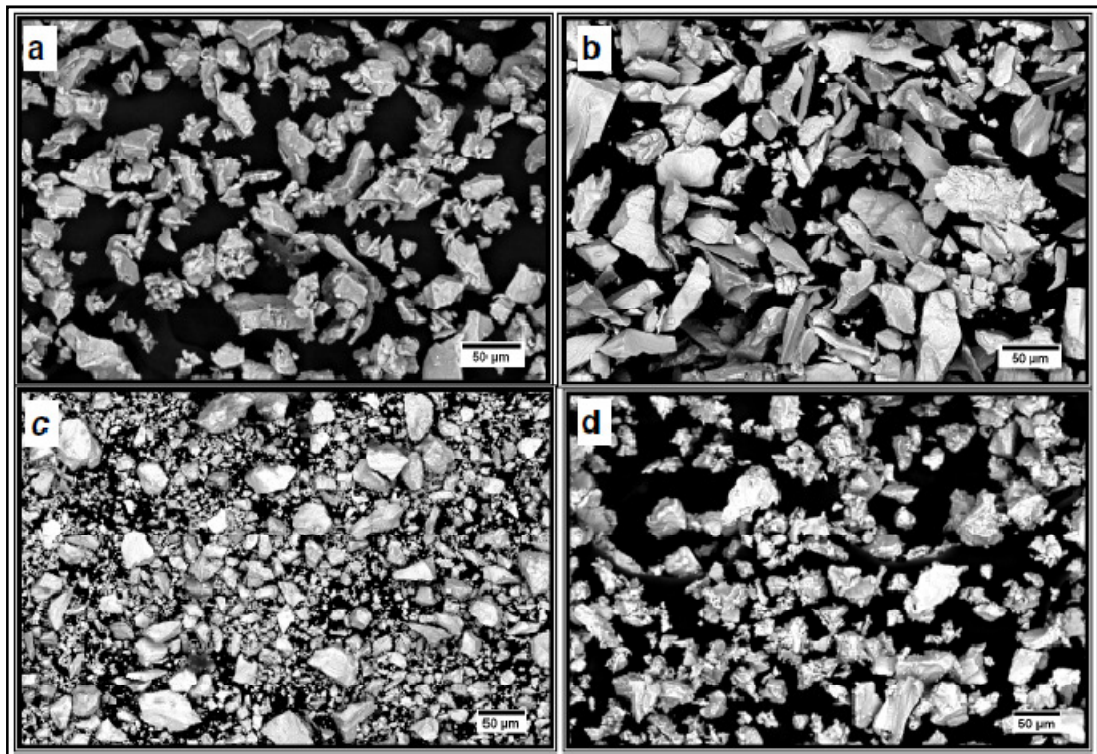


**Figure 4.1** : Backscattered electron image of powder morphologies used for the alloy (a) titanium, (b) niobium, (c) tantalum, (d) zirconium.

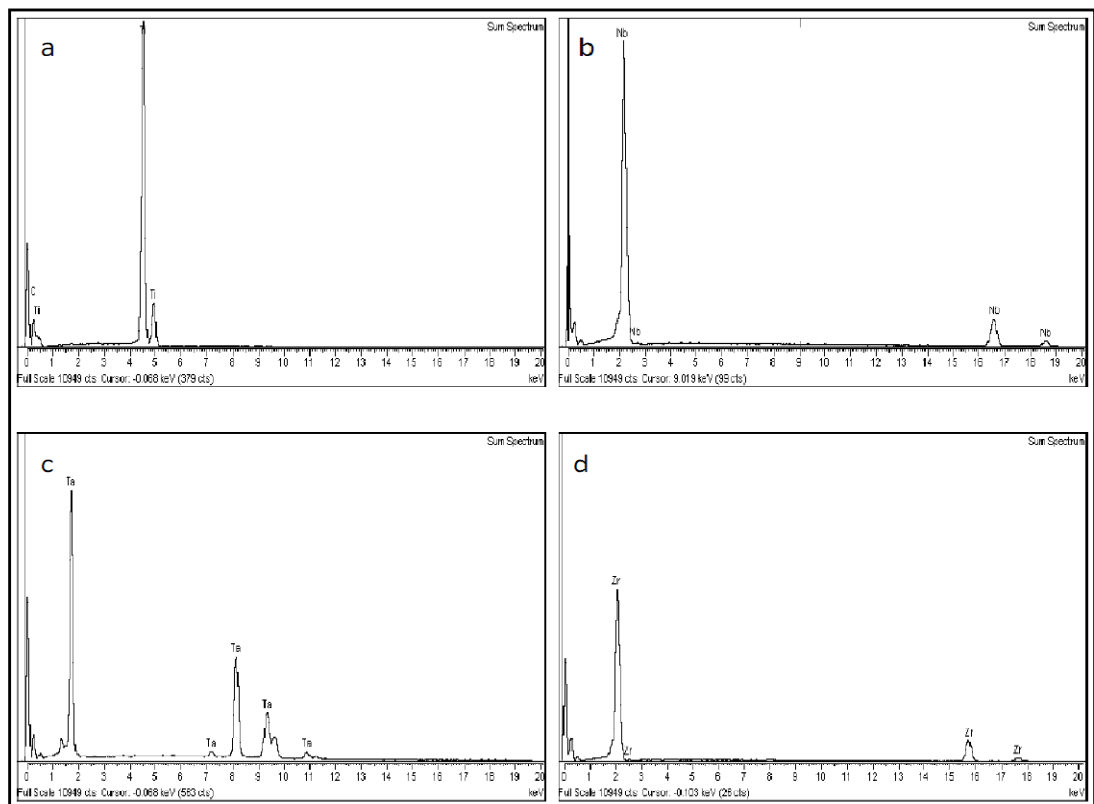


**Figure 4.2** : EDS spectra of elemental powders (a) titanium, (b) niobium, (c) tantalum, (d) zirconium.

The elemental powders were mixed in a roller mixer with the morphology of the mixed powders being presented in Figure 4.3. The tantalum particles appeared brightest due to their high atomic number, followed by niobium, zirconium and titanium (Figure 4.3(a)). As expected, the corresponding EDS spectra for the blended powder indicated that only peaks related to the individual elemental powders were detected (Figure 4.3(b)). Peaks related to other elements, which might indicate the existence of hydrides, oxides or intermetallics, were not detected.

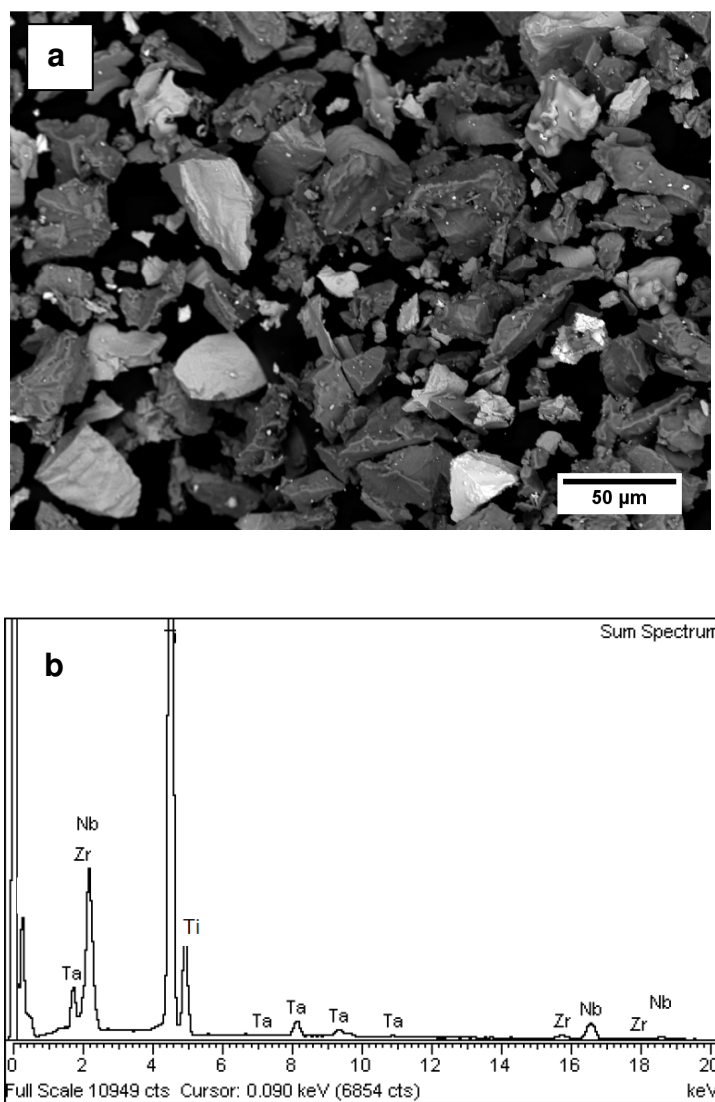


**Figure 4.3** : Backscattered scanning electron micrograph of the mixed powder (a) and corresponding energy spectra from EDS measurement (b).

Laboratory x-ray diffraction (XRD) and synchrotron radiation diffraction (SRD) were used to examine the crystallographic form of the elemental powders and to detect the possible presence of other phases after the blending procedure (Figure 4.4). The x-ray diffraction patterns of the as-mixed powders are shown in Figure 4.4(a), indicating the presence of peaks related to individual elements; the structure of both hexagonal close packed (hcp), *i.e.*  $\alpha$ -titanium,  $\alpha$  zirconium and isomorphous body centered cubic (bcc) structure, *i.e.*, niobium and tantalum. Any additional phases formed after the blending procedure were not detected. This result was confirmed by the SRD pattern which depicts peaks related to individual elements being more pronounced. (Figure 4.4(b)).

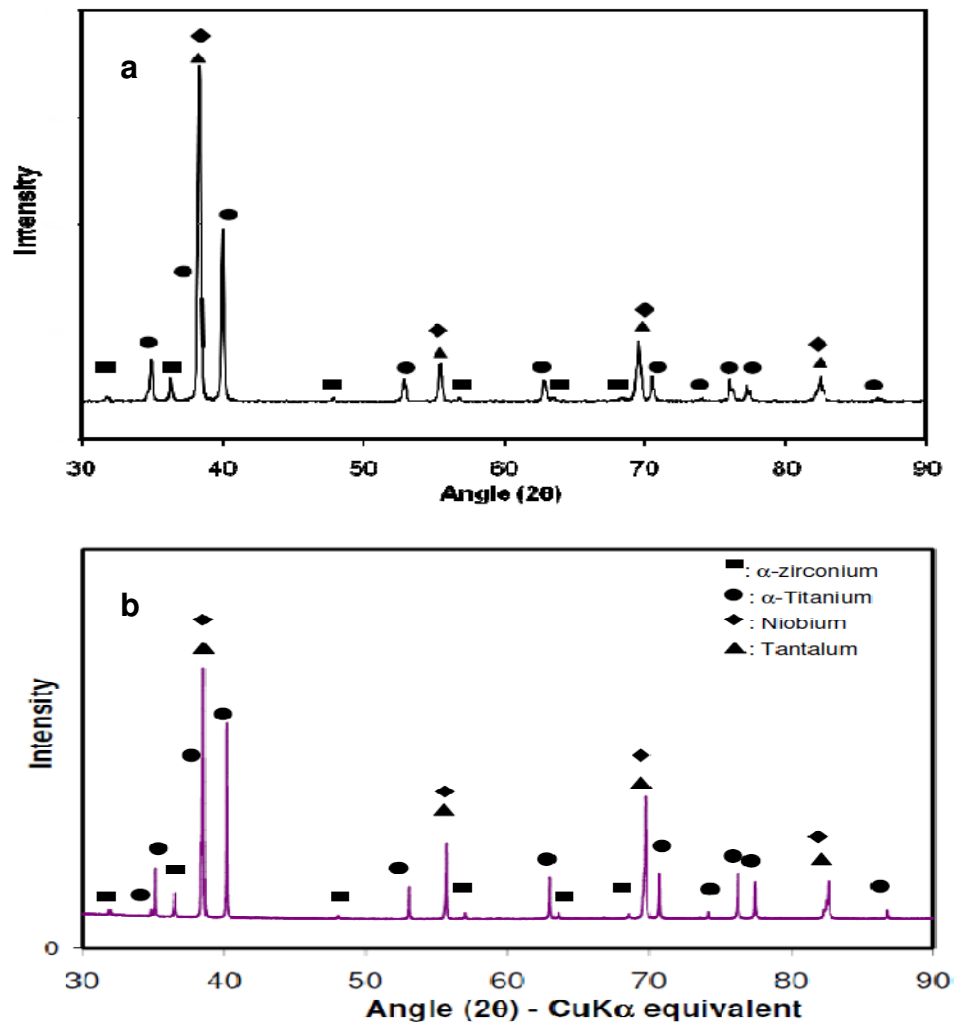


**Figure 4.4 :** Diffraction patterns of samples of the mixed powder obtained from (a) x-ray diffractometer, (b) synchrotron radiation source.

### 4.3 As HIP-ed characterisation

Following powder mixing of approximately 50 g of the alloy, the mixed powder was placed into a stainless steel can. Each can was subsequently evacuated to approximately  $10^{-2}$  Pa and then backfilled with argon and sealed. Various argon pressures, *i.e.* 0.34, 0.48, 0.68 and 0.86 MPa were applied to the cans. The pressurised cans were then densified using HIP-ing at 1000°C for 2 hours or 1100°C for 4 hours under 100 MPa of argon and then furnace cooled. As HIP-ed titanium alloy compacts were characterised by determining the phases formed following the HIP-ing procedure, the initial pore volume fraction and initial pore size.

#### 4.3.1 Microstructure and phase evaluation

As described in section 3.3 the HIP-ed billets were cut into cubic specimens using WEDM, this resulting in surface damage layers being formed on the specimens. Prior to characterising the HIP-ed specimens, examination of the layer was carried out using SEM and EDS. The surface texture of a damaged surface layer is depicted in Figure 4.5.

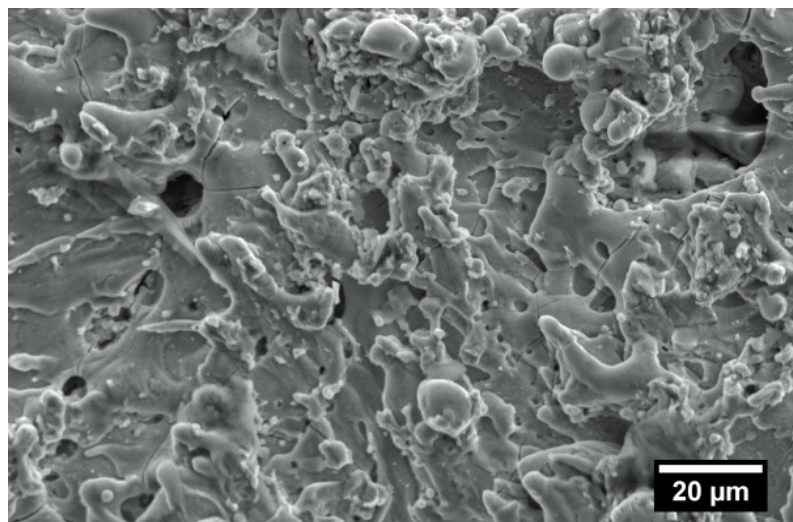


**Figure 4.5 :** Secondary image SEM micrograph of a typical wire electrical discharge machined workpiece surface texture.

This surface consisted of globules of debris, discharge craters and microcracks. The microcracks may be caused by a high cooling rate in a distilled water dielectric fluid during cutting [400]. Drops of recast material, which had been heated to the melting point and then resolidified back on the surface, were observed. Following the SEM examinations, the specimens were analysed with an energy dispersive spectrometer (EDS). This apparatus determines the constituent elements in a specimen's surface. Figure 4.6 shows the EDS output of a typical WEDM-ed surface.

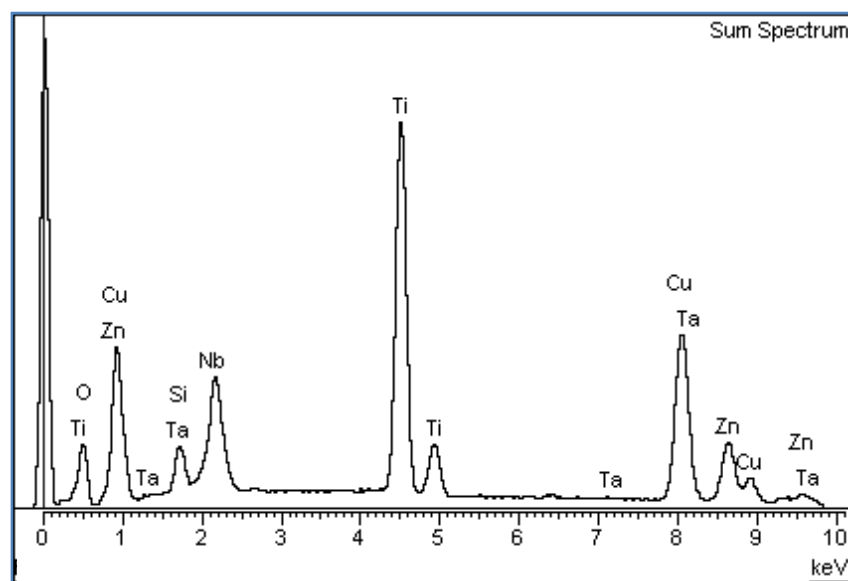


**Figure 4.6 :** Energy Dispersive Spectrometry analysis of the WEDM-ed surface

Large percentages of titanium and the alloying elements niobium and tantalum were expected for the specimen. Surprisingly, noticeable amounts of copper and zinc were detected. These elements are not normally found in this material. The wire used in the WEDM process is a hard brass wire which consists of zinc and copper. It is suggested that some amount of the wire material was deposited on the specimen's surface during the cutting process as reported by previous research [400].

After surface damage removal by grinding and polishing, the phase alteration of the HIP-ed and densified mixed powders was examined by XRD, with typical XRD

patterns being shown in Figure 4.7. Following HIP-ing at 1000°C the XRD pattern was found to contain peaks related to  $\alpha$  and  $\beta$  titanium, niobium and tantalum.

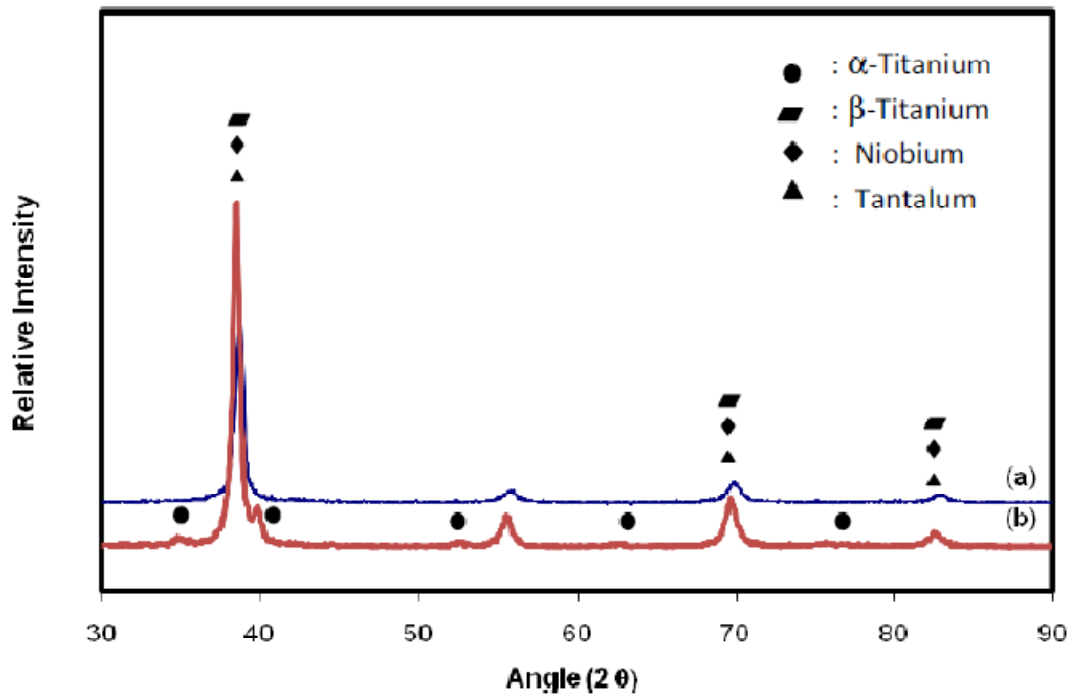


**Figure 4.7 :** X-ray diffraction plots of the densified Ti-Nb-Ta-Zr powder (a) by hot isostatic pressing in argon (1100°C/4hrs/100 MPa), (b) by hot isostatic pressing in argon (1000°C/2 hrs/100 MPa).

As the HIP-ing temperature increased to 1100°C, peaks attributed to  $\alpha$  titanium were suppressed and unobservable, whereas peaks corresponding to isomorphous bcc structures, *i.e.*  $\beta$  titanium, niobium and tantalum were clearly detected. Interestingly, following both the HIP-ing procedures, peaks related to elemental or intermetallic zirconium were not detected within the samples. Although this phenomenon has also been noted in previous studies [240, 301], further examination was carried out using synchrotron radiation diffraction to detect the existence of other phases that may have formed after the HIP-ing procedure. The synchrotron radiation diffraction patterns are shown in Figure 4.8. This figure shows that the two sets of examination using XRD and SRD results are in good agreement, with the peaks related to the each phase in the SRD patterns being depicted more intensely than in the XRD patterns.

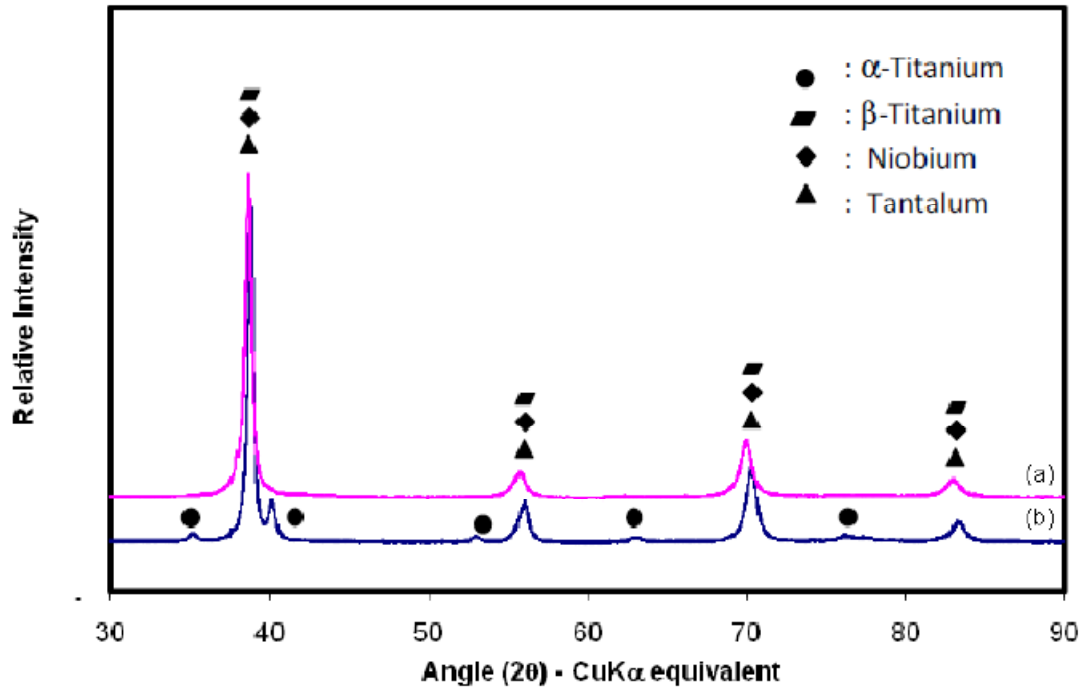


**Figure 4.8 :** Synchrotron radiation diffraction plots of the densified Ti-Nb-Ta-Zr powder (a) by hot isostatic pressing in argon (1100°C/4hrs/100 MPa), (b) by hot isostatic pressing in argon (1000°C/2 hrs/100 MPa).

The resultant patterns indicated that following the HIP-ing, the dissolution of tantalum, niobium and alpha titanium, together with niobium as a beta nucleating agent, was still incomplete. In addition,  $\alpha$  titanium particles had been transformed to  $\beta$  titanium, which was attributed to the HIP-ing temperature of 1100°C and is higher than the  $\beta$  transition temperature (883°C for pure titanium). Furthermore, it is suggested that whilst the presence of isostatic stress during the HIP-ing procedure had enhanced partial conversion of  $\alpha$  phase to  $\beta$  phase within the alloy, it may also have induced retention of the  $\beta$  titanium phase during furnace cooling to room temperature. As a comparison, Taddei *et al* in 2004 [301] reported that a conventional sintering of  $\beta$  alloy powders at 1100°C followed by furnace cooling resulted in peaks related to the  $\alpha$  titanium phase being observed, with the transformation of  $\alpha$  to  $\beta$  titanium phase being completed beyond 1500°C. It was thus concluded that the HIP-ing procedure was considered to have noticeably improved  $\beta$  phase development.

The development of microstructures following HIP-ing in argon at 1000°C/2 hrs/100 MPa, are shown in Figure 4.9, illustrating the grain structure and degree of reaction for the Ti-Nb-Ta-Zr specimens. A typical microstructure of the specimen HIP-ed at 1000°C was found to contain angular titanium particles (dark), niobium (grey) and tantalum (bright), these being similar to the initial particle morphology. The particle boundaries were still observable. The formation of a Widmanstatten structure was also detected.

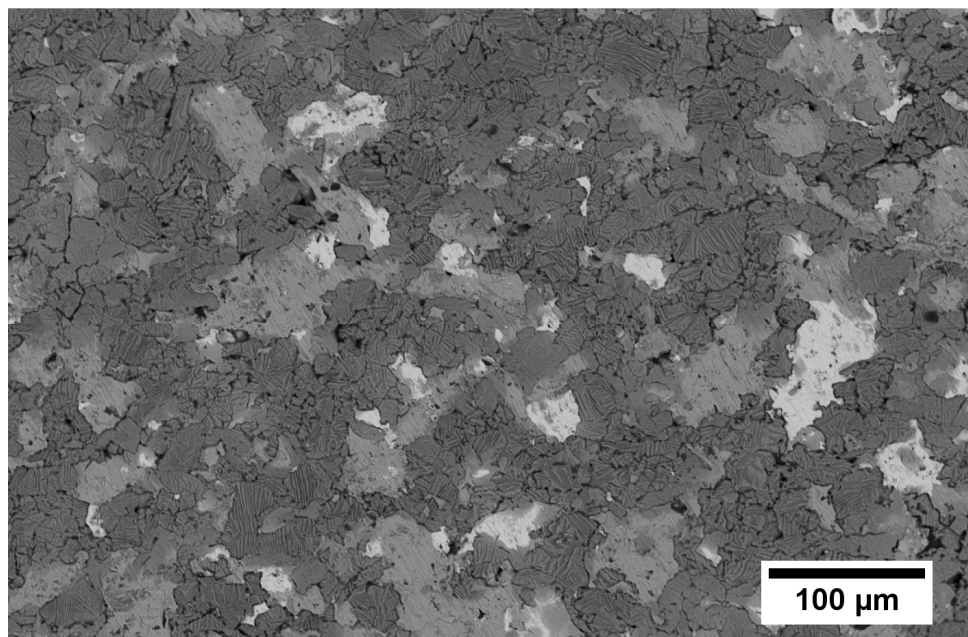


**Figure 4.9** : Backscattered scanning electron micrographs of etched titanium alloy specimens following HIP-ing in argon : (a) 1000°C/2 hrs/100 MPa

In contrast to this, examination of the microstructure of specimens HIP-ed at 1100°C revealed the appearance of titanium particles (dark), niobium (grey) and tantalum (bright). In addition, the particle boundaries had become diffuse, due to the dissolution of niobium and partial dissolution of tantalum particles, indicating that for this HIP-ing condition, homogenisation of the alloy was still incomplete, as shown by Figure 4.10. The Widmanstatten structure became more clearly observable. The structure was formed mainly from the niobium particles, which acts as a  $\beta$  phase nucleating agent

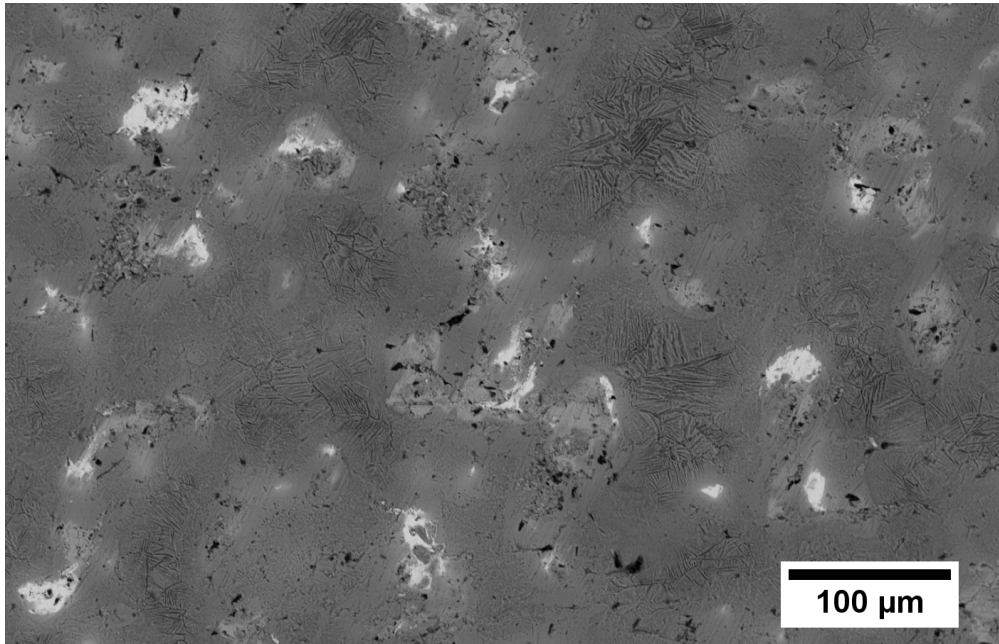


**Figure 4.10 :** Backscattered scanning electron micrographs of etched titanium alloy specimens following HIP-ing in argon 1100°C/4 hrs/100 MPa).

### **4.3.2 Initial porosity and pore size distribution**

The specimens HIP-ed at both conditions (1000°C and 1100°C) were found to contain pores (black spots) that were associated with incomplete dissolution of the elemental powders, with the pore sizes being similar to that of the original inter-powder spacing [401]. Hereafter the porosity resulting from the HIP-ing procedure is named as initial porosity. Average initial porosities of the specimens obtained from the image analysis estimation are presented in Figure 4.11.

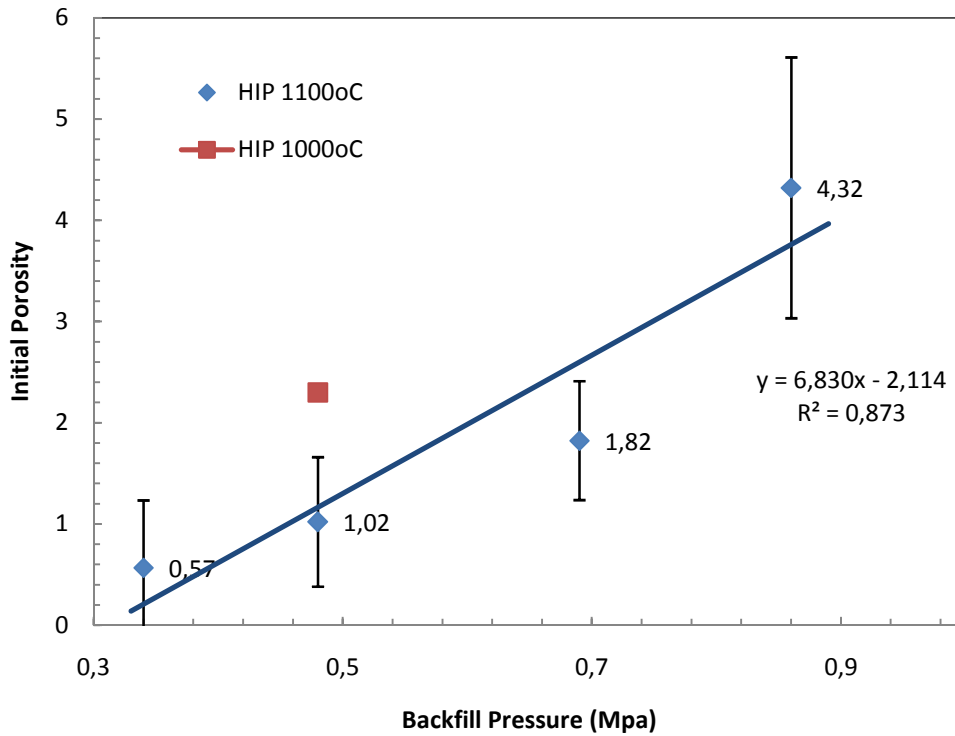


**Figure 4.11** : Initial porosity from HIP-ing procedures with various argon backfill pressures.

In general, as expected, the initial porosity increases as the argon backfill increases. However, according to ideal gas law, the number of gas atoms is linearly proportional with the pressure of the gas. In this case, the backfilled pressure represents the number of atoms which further determine the amount of porosity. Figure 4.11 shows that following the HIP-ing procedures, the majority of initial porosity was estimated to be less than 3%, with the exception of the highest argon backfill pressure that produced an average porosity of 4.32% (obtained from 4 specimens with standard deviation of  $\pm 1.28\%$ ). The initial porosity of the specimens HIP-ed at 1000°C was found to be higher than those processed at 1100°C due to their higher degree of incomplete dissolution of the elemental particles. Following HIP-ing at 1100°C, a 1.4 fold increase in argon backfill pressure from 0.34 MPa to 0.48 MPa resulted in an approximately 1.8 fold increase in initial porosity. A further increase of the argon backfill pressure, *i.e.* 2 and 2.5 fold (0.69 and 0.86 MPa respectively) resulted in an increase of the initial porosity of 3.2 and 7.6 fold respectively. The tendency of an increase in initial porosity due to an increase of argon backfill has also been reported by previous researchers [50, 396]. Davis [396],

who used spherical pure titanium powder with a powder size of 30  $\mu\text{m}$ , found that an increase of argon backfill pressure from 0.33 to 0.71 MPa (a 2.2 fold increase) resulted in an approximate 1.7 fold increase in initial porosity (1.3% to 2.1% initial porosity). In addition, HIP-ing procedures at 1000°C/2 hrs/100 MPa for various powder sizes (30, 75, 165 and 400  $\mu\text{m}$ ) under an argon backfill pressure of 0.33 MPa resulted in a broad range of initial porosities (1.3, 0.14, 0.06 and 1.5% respectively).

Pore geometry was assumed spherical considering that the applied pressure was isostatic; hence pores underwent the same magnitude of pressure from different directions and the highest entrapped gas generating pores would likely be present in the middle, leading to formation of spherical pores. Figure 4.12 shows pore section in 'spherical' form.

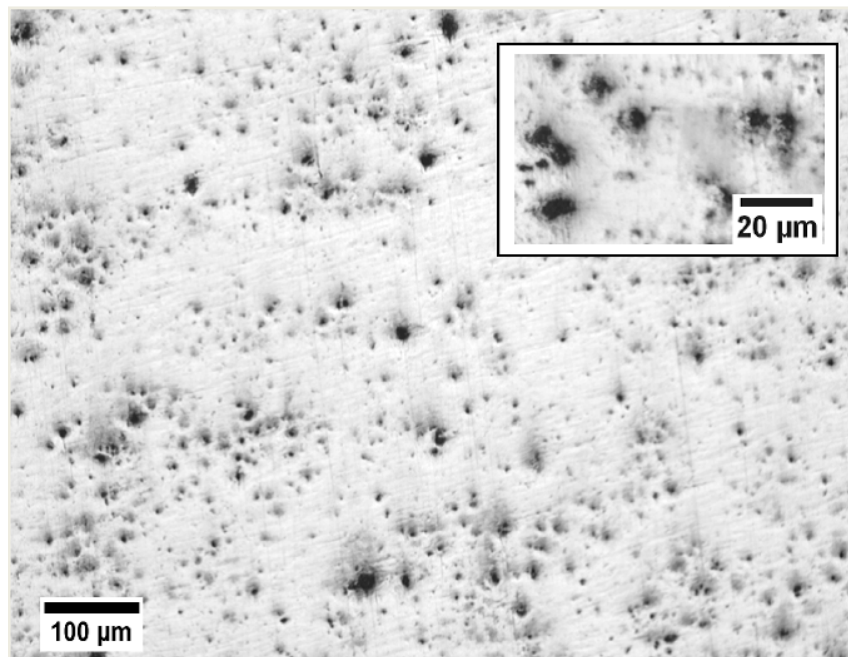


**Figure 4.12 :** Optical microscope image showing pore section in 'spherical' form

The pore size distribution, assuming spherical pores, of HIP-ed specimens at various argon backfill pressures, was determined using digital image analysis [46, 50] as described in detail in section 3.3.4 and plotted in Figure 4.13.

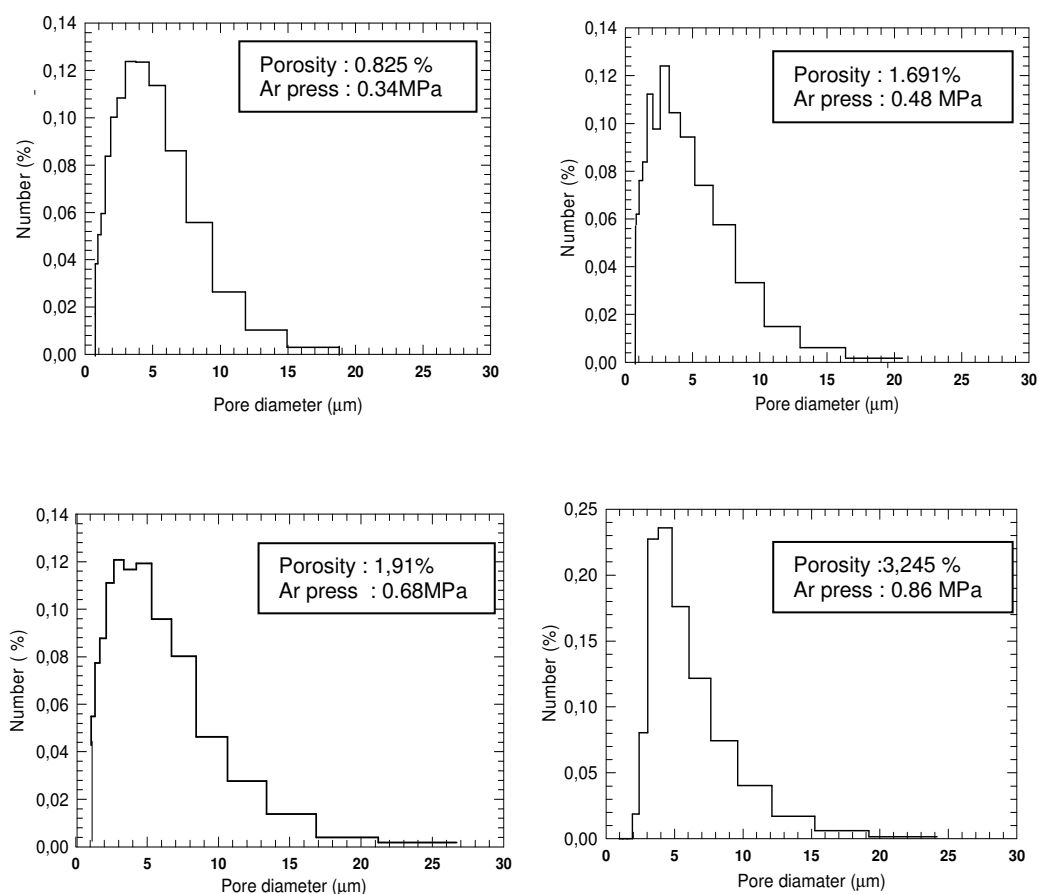


**Figure 4.13 :** Pore size distribution for each of the four argon backfill pressure groups.

One specimen of each group considered representative was plotted and compared to the other groups. The figures show a similarity in the pore size distribution among them. In general, the increase of argon backfill pressure (0.34, 0.48, 0.68 and 0.86 MPa) resulted in a slight increase in the pore diameter range (typically 0.8-18.8, 0.8-20.6, 1.1-26.6 and 0.9-24.2  $\mu\text{m}$  respectively). However, in most cases, the figures reveal that pore diameters were predominantly found in the range of 4.5-6  $\mu\text{m}$ . An increasing pore size diameter, with diameter size larger than 6  $\mu\text{m}$ , was found to be decreased in number. Similar results for average pore size diameters have been noted by the previous study [396], which showed pore size diameters of  $6\pm 3$  and  $7\pm 3$   $\mu\text{m}$  with an initial porosity of 1.3 and 2.1% respectively.

## 4.4 As foamed characterisation

Following the HIP-ing procedure the specimens were loaded into a vacuum furnace to undergo the foaming processes at these specific temperatures; 1100°C, 1225°C and 1350°C. The temperatures, which are above those previously reported  $\beta$  transus temperatures, were chosen in accordance with the properties of  $\beta$  phase titanium alloys that possess lower creep resistance than that of  $\alpha$  phase [238](p.37). In addition, the foaming procedure at those temperatures is expected to allow more alloying. The median temperature, 1225°C, allows an evaluation on how the properties have evolved. This section describes the phases and microstructures formed, and the resultant pore volume fractions after foaming

### 4.4.1 Microstructure and phase identification

#### 4.4.1.1 Microstructure and phase identification of specimens foamed at 1100°C

The typical XRD patterns of the specimens foamed at 1100°C with different argon backfill pressure and foaming times are shown in Figure 4.14. Compared to the as HIP-ed result, these patterns were found to be comparable (*c.f.* Figure 4.7). The XRD pattern of the foamed specimen for 10 hours under argon backfill pressure of 0.34 MPa showed the presence of  $\alpha$  and  $\beta$  phases.

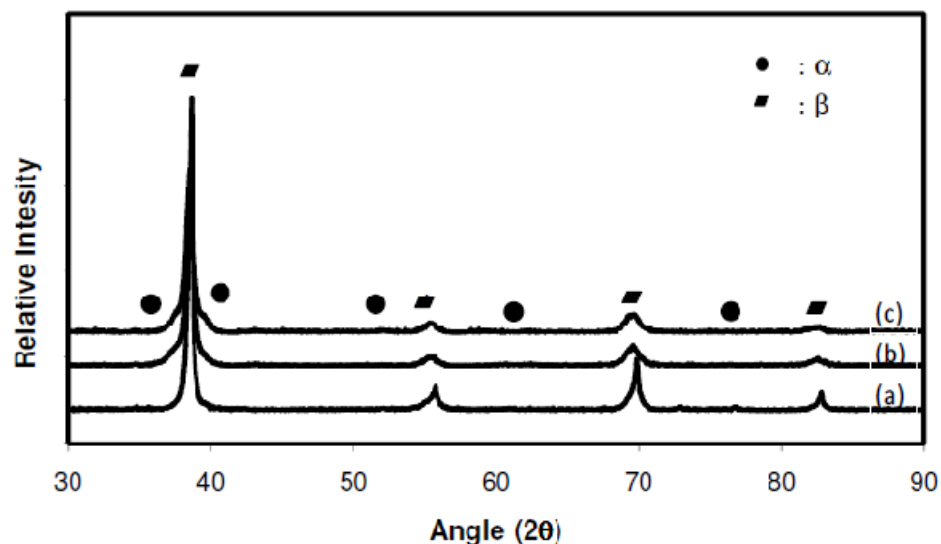


**Figure 4.14:** X-ray diffraction patterns of the foamed titanium alloy at 1100°C with an argon backfill pressure of (a) 0.34 MPa, (b) 0.86 MPa, both foamed for 10 hrs, and (c) 0.68 MPa foamed for 2 x 10 hrs.

Peaks related to  $\beta$  phase were clearly detected, with only minor peaks being noted in relation to the  $\alpha$  titanium phase. Elemental composition, in this case a highly stabilised  $\beta$  alloy, affects the phase transformation during heating and cooling. A higher content of niobium is found to reduce the martensite formation temperature, even possibly down to room temperature, therefore the martensitic  $\alpha$  structure formation may be suppressed [219]. Furthermore, the addition of zirconium in a quaternary alloy may reduce the critical cooling rate, thus allowing  $\beta$  phase to be retained during furnace cooling from 1100°C to room temperature [219], with only small portions of  $\beta$  phase being transformed to  $\alpha$  phase. This explanation is consistent with the current observation that the peaks related to the  $\alpha$  phase are severely suppressed (Figure 4.14(a)). Similar XRD patterns were also observed for the foamed specimen with the highest argon backfill pressure, *i.e.* 0.86 MPa (Figure 4.14(b)). A foaming procedure lasting 2 x 10 hours was carried out for some of the foamed specimens. The typical XRD pattern of refoamed specimens was similar to those of the foamed specimen (Figure 4.14(b)). This figure suggests that at a given foaming temperature, the amount of argon gas (backfill pressure) and the refoaming procedure does not noticeably affect phase transformation during the foaming process.

An example of the microstructure of the foamed specimen at 1100°C for 10 hours is shown in Figure 4.15.

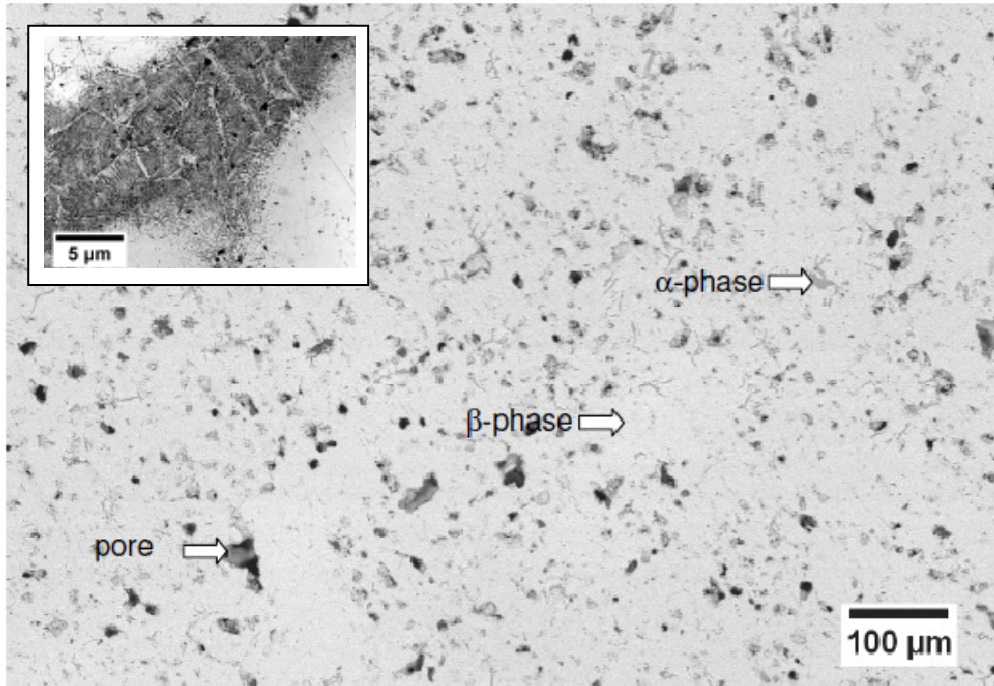


**Figure 4.15:** Back scattered electron image of a titanium alloy specimen foamed at 1100°C for 10 hours showing a black spot representing a pore, a smaller dark area which represents  $\alpha$  phase, and light grey area corresponding to  $\beta$  phase. Insert, backscattered electron image of an etched specimen presenting a dark area with Widmanstatten structure.

The image in Figure 4.15 reveals the dissolution of elemental powders. The niobium and tantalum particles have diffused and become indistinguishable (compared to the HIP-ed specimen figures). This result suggests that foaming at 1100°C for 10 hours may encourage additional alloying, even while the pressurised pores are causing the metal matrix to expand due to creep. In the micrograph the presence of three distinct regions can be seen, a black spot representing a pore, a smaller dark area which represents  $\alpha$  phase, and the light grey area corresponding to  $\beta$  phase, with the regions being dominated by the light grey area ( $\beta$  phase). The darker area surrounded by the light grey area may become an initiation point of two-phase islands resembling the Widmanstatten structure. Thus the micrograph is consistent with the XRD pattern, showing that foaming at 1100°C for 10 hours resulted in a high dissolution of  $\beta$  stabilising elements (niobium, tantalum) with  $\beta$  phase being predominantly produced.

The typical microstructure of foamed specimen for 2 x 10 hours is shown in Figure 4.16. The micrograph depicts a similar microstructure to the foamed specimens for 10 hours, with more pores and the smaller dark areas ( $\alpha$  phase) being more obvious.

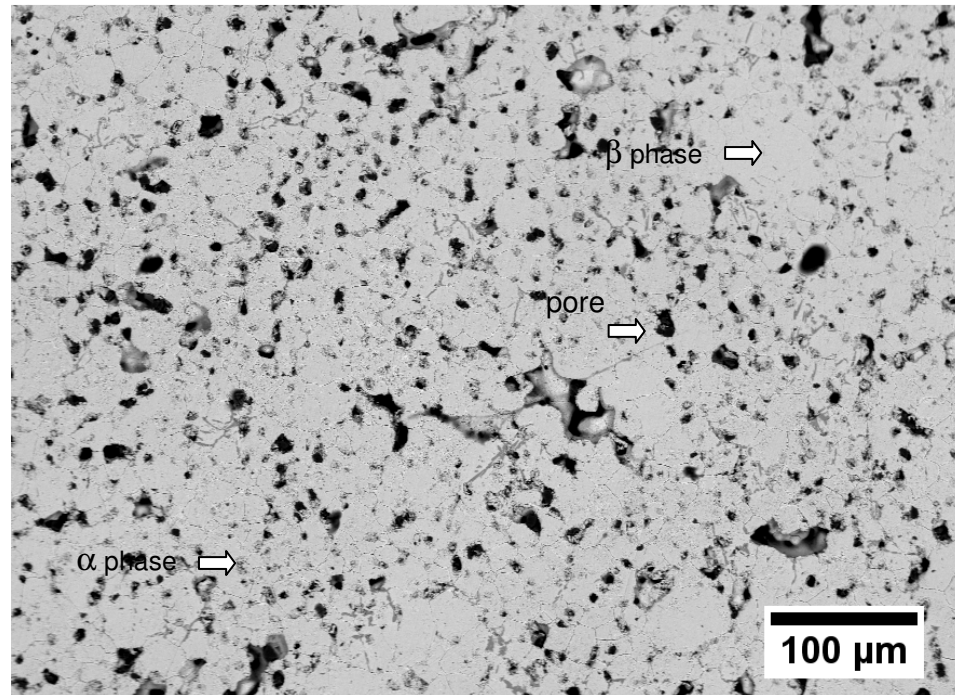


**Figure 4.16:** Backscattered electron image of titanium alloy specimen foamed at 1100°C/0.68MPa/ 2 x 10 hours.

From quantitative analysis of the dark area and the light grey area using EDS (Figure 4.17), it was found that  $\beta$  phase (grey area) consisted of a higher composition of  $\beta$  stabilising elements, *i.e.* niobium and tantalum (Figure 4.17(b)) when compared to the  $\alpha$  phase (dark area) as shown in Figure 4.17(a). Chemical inhomogeneity, as shown by grey and darker areas detected by BSE SEM and EDS, has also been reported in previous research [250].

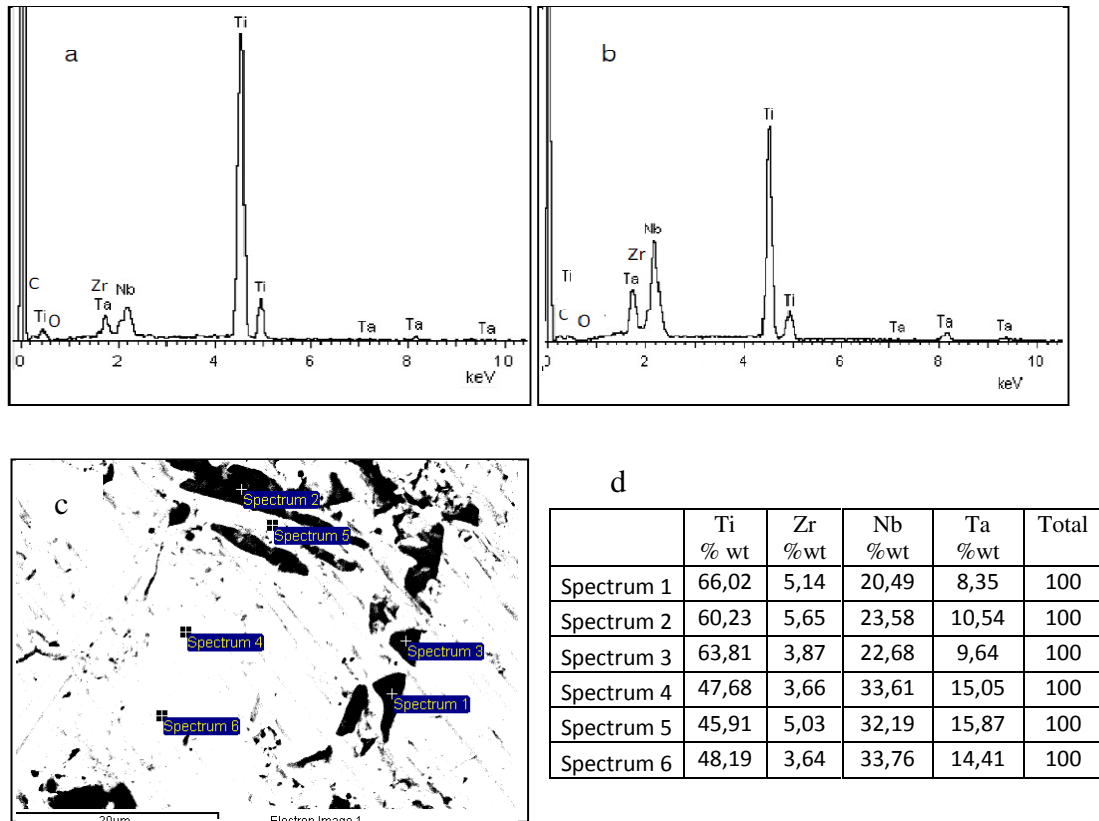


**Figure 4.17:** Composition analysis of titanium alloy specimens foamed at 1100°C for 10 hours using EDS. (a) spectra of small dark area, (b) spectra of light grey area, (c) low resolution backscattered image where data were taken, and (d) chemical composition of the alloy at different points shown in (c).

#### 4.4.1.2 Microstructure and phase identification of specimens foamed at 1150°C

Foaming specimens at 1150°C for 10 hours resulted in significantly different XRD patterns as shown in Figure 4.18.

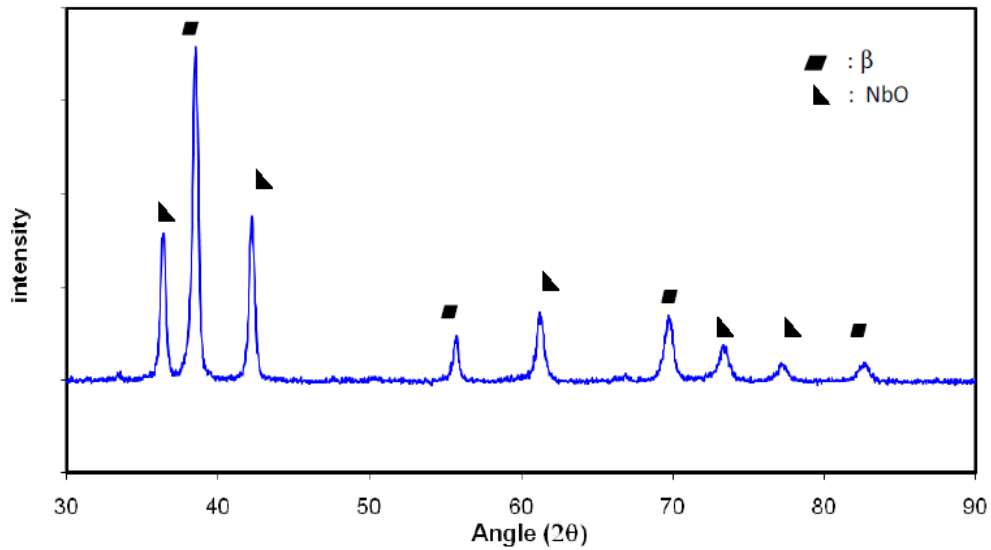


**Figure 4.18** : X-ray diffraction patterns of a foamed specimen at 1150°C with argon backfill pressure of 0.48 MPa.

The figure indicates the peaks related to the presence of two phases within the specimen, *i.e.* the  $\beta$  titanium and NbO phases. It is noted that the presence of NbO phase in the specimen foamed at 1150°C was attributed to reduced vacuum conditions due to leakage of the vacuum furnace during a portion of the treatment [401].

Interestingly, a backscattered scanning electron micrograph presented in Figure 4.19 of the specimen foamed at 1150°C shows the microstructure being reasonably uniform across the specimen. Also noted in this micrograph was the presence of some bright areas representing regions rich in tantalum particles indicating the incomplete dissolution of the tantalum particles.

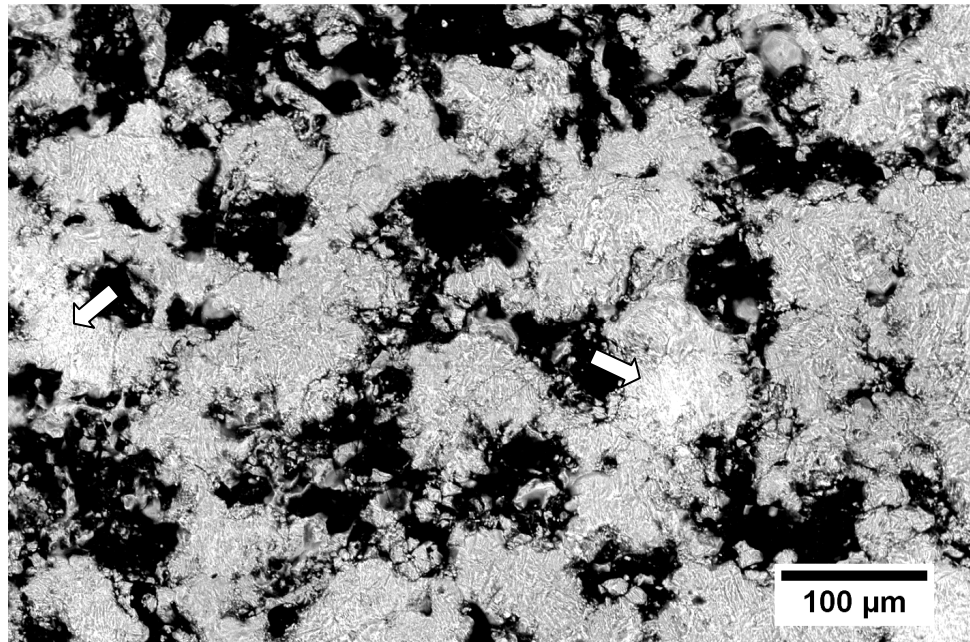


**Figure 4.19 :** Backscattered scanning electron micrograph of the titanium alloy specimen foamed in vacuum furnace at 1150°C, showing incomplete dissolution of tantalum particles (arrow; brighter areas)

#### **4.4.1.3 Microstructure and phase identification of specimens foamed at 1225°C**

When the foaming temperature was increased to 1225°C with a holding time of 10 hours, the XRD patterns of the foamed specimens showed peaks corresponding to the presence of  $\beta$  phase and  $\alpha$  phase as shown in Figure 4.20. Patterns similar to the XRD spectra of the specimens with different argon backfill pressures (Figure 4.20 a and b) were found. The effect of the “refoaming” process (2 x 10 hours at the temperatures) was also found to be insignificant with regard to the spectra. It is interesting that whilst  $\alpha$  phase peaks were found to become more pronounced compared to those of the specimens foamed at 1100°C, the  $\beta$  phase peaks were still clearly detected.

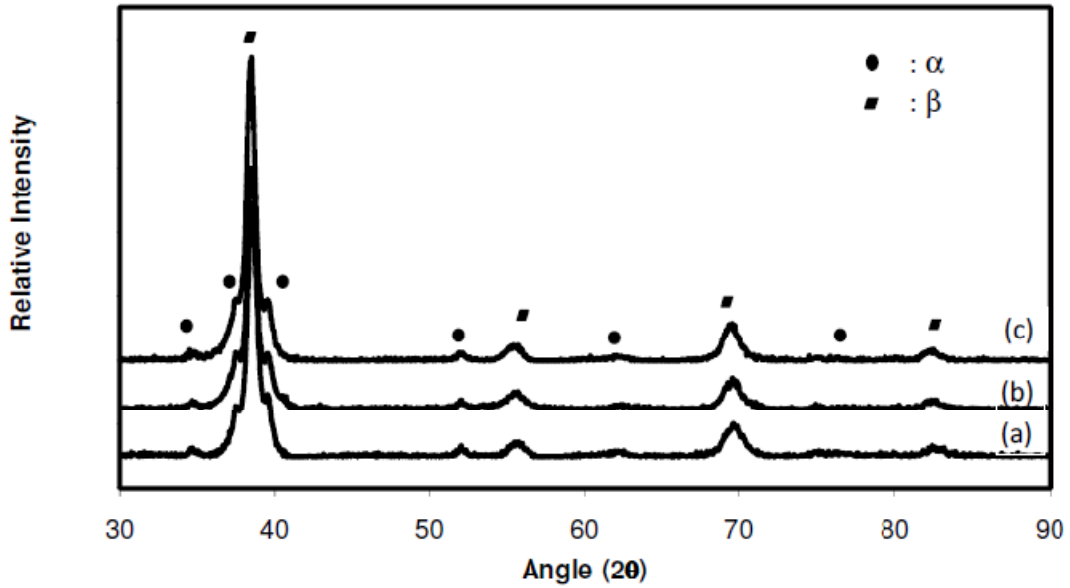


**Figure 4.20:** X-ray diffraction patterns of the foamed Ti-Nb-Ta-Zr powder at 1225°C with argon backfill pressure of (a) 0.34 MPa, (b) 0.86 MPa (both held for 10 hrs), (c) 0.68 MPa foamed for 2 x 10 hrs.

The higher foaming temperature, which was much higher than the  $\beta$  transus temperature, allowed more grain growth and more alloying. However, a longer time to reach room temperature would be required during furnace cooling, thus allowing greater intrusion into  $\beta+\alpha$  field. In accordance with the continuous cooling transformation (CCT) diagram proposed by Tang *et al.* [219], a higher volume fraction of  $\beta$  phase may transform to  $\alpha$  phase. Since  $\beta$  phase may also transform to  $\omega$  phase during slow cooling [219], a very small portion of the remaining  $\beta$  phase may transform to  $\omega$  phase. From XRD analysis of the foamed specimens, the presence of  $\omega$  phase could not be detected, although this may simply be due to the  $\omega$  phase being present below the detection limit of the XRD analysis [231, 402].

The backscattered electron micrographs of the samples foamed at higher temperature revealed the development of  $\alpha$  phase as shown in Figure 4.21.

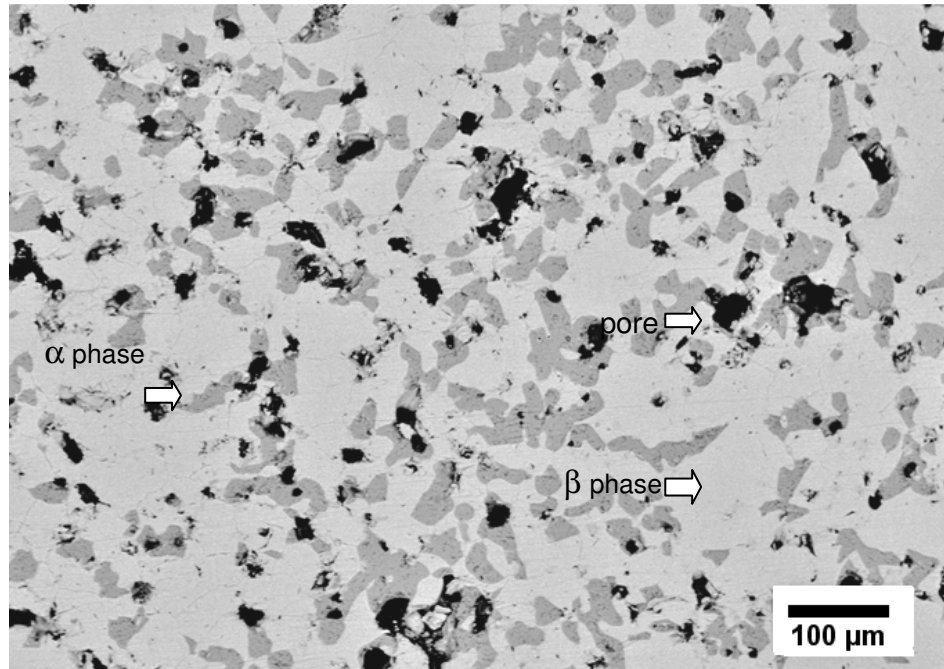


**Figure 4.21:** Backscattered electron image of titanium alloy specimen foamed at 1225°C for 10 hours.

Dark areas representing  $\alpha$  phase and black spot areas illustrating pores were found to be distributed across the specimen. When foamed at 1225°C, the proportion of  $\alpha$  phase increased compared to that of the specimens foamed at 1100°C. These areas appeared as  $\alpha$  islands surrounded by  $\beta$  phase (light grey areas). Thus the microstructural analysis is in good agreement with XRD analysis.

From EDS analysis, the peak height ratio of the dark and the light areas seems to change with increased foaming temperature as shown in Figure 4.22. Whilst the dark area expanded, the proportion of titanium content in the grey area decreased (Figure 4.22(b)). It is suggested that furnace cooling to room temperature from a higher foaming temperature may cause the transformation of a portion of the  $\beta$  phase in the grey area to  $\alpha$  phase (dark area). Thus, the EDS analysis supported the XRD analysis.

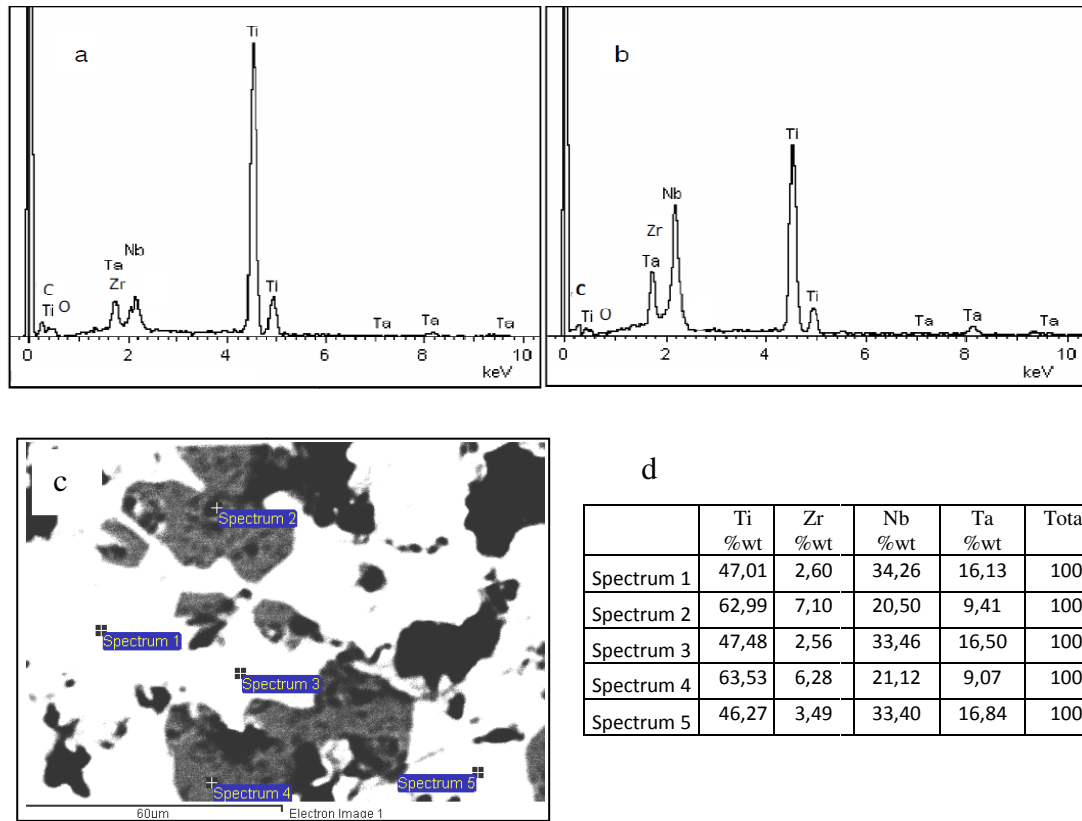


**Figure 4.22:** Composition analysis of titanium alloy specimens foamed at 1225°C for 10 hours using EDS, (a) spectra of small dark area, (b) spectra of light grey area, (c) low resolution backscattered image from where data were taken, and (d) chemical composition of the alloy at different points shown in (c).

#### 4.4.1.4 Microstructure and phase identification of specimens foamed at 1350°C

The development of the  $\alpha$  phase continued with an increase in the foaming temperature to 1350°C. The XRD pattern of the specimens foamed at 1350°C is depicted in Figure 4.23. The two phases, *i.e.*  $\alpha$  and  $\beta$  phase were clearly detected, with the XRD pattern of the specimen foamed at 1350°C/0.34 MPa/10 hours (Figure 4.23a) being noticeably unchanged by either an increase in argon backfill pressure (Figure 4.23b) or by foaming for 2 x 10 hours (Figure 4.23c).

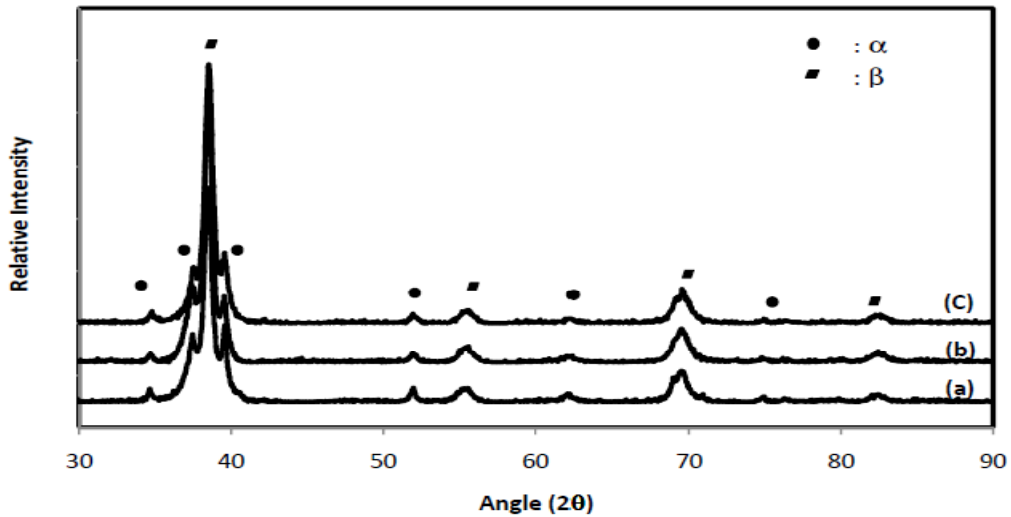


**Figure 4.23:** X-ray diffraction patterns of the foamed titanium alloy powder at 1350°C with argon backfill pressure of (a) 0.34 MPa, (b) 0.86 MPa (foamed for 10 hrs), (c) 0.48 MPa (foamed for 2 x 10 hrs).

Compared to the specimens foamed at lower temperatures (1100°C and 1225°C), the relative intensities of the peaks corresponding to the  $\alpha$  phase are the highest, indicating that the volume fraction of  $\alpha$  phase increased with an increase in foaming temperature. As mentioned earlier in Section 4.4.1.3, at the higher foaming temperature of 1350°C, a greater intrusion into the  $\alpha+\beta$  phase field may occur during furnace cooling to room temperature and a higher volume fraction of  $\beta$  phase may transform to  $\alpha$  phase. In addition to the presence of  $\beta$  phase, the presence of peaks corresponding to  $\alpha$  phase due to transformation from  $\beta$  phase during slow cooling was also reported by previous research [306]. These previous researchers did apply solution treatment to a Ti-20Nb-10-Ta-5Zr alloy into the  $\beta$  field, followed by furnace cooling. Conversely, Taddei *et al.*[301] found that an increase of sintering temperature for a Ti-35Nb-7Zr-5Ta alloy followed by furnace cooling decreased the peak height of the  $\alpha$ -phase. The peaks disappeared and the  $\alpha$  phase was completely transformed to  $\beta$  phase at a sintering temperature above 1500°C (followed by furnace cooling). Higher niobium content (35 wt%) in the titanium alloy was suggested to encourage the transformation.

As mentioned earlier that further development of  $\alpha$  phase (dark area) is indicated by the increase of that dark area, and the portion of titanium content in the grey area

decreased as indicated by the lowering peak height of the titanium shown in Figure 4.24(b).

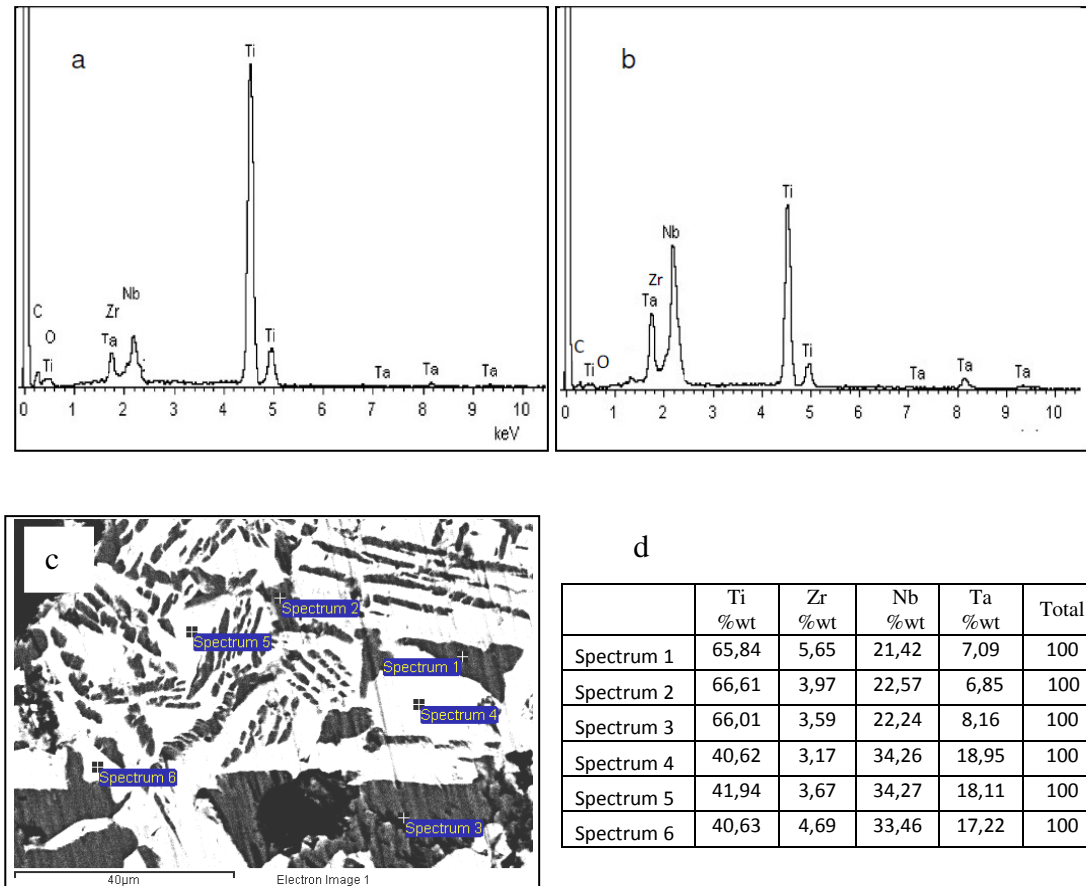


**Figure 4.24:** Composition analysis of titanium alloy specimens foamed at 1350°C for 10 hours using EDS. (a) spectra of small dark area, (b) spectra of light grey area, (c) low resolution backscattered image from where data were taken, and (d) chemical composition of the alloy at different points shown in (c).

In the current research, the development of the  $\alpha$  phase (dark area) continued within the specimen foamed at 1350°C, as shown in Figure 4.25. Whilst the foaming temperature of 1225°C resulted in  $\alpha$  phase being revealed only as islands surrounded by  $\beta$  phase, this figure illustrates that the  $\alpha$  phase continued to grow by forming  $\alpha$  platelets within the  $\beta$  phase matrix, along with further pore expansion. These platelets were found to be dispersed across the specimen. This result shows a good agreement with the XRD pattern.

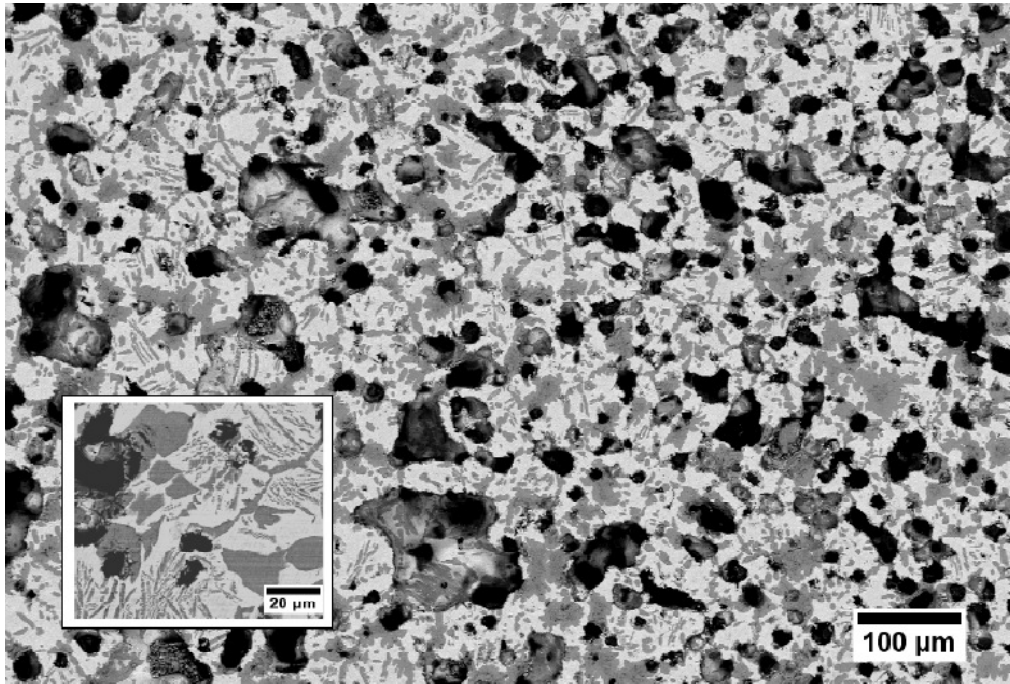


**Figure 4.25** : Backscattered electron image of the titanium alloy specimen foamed at 1350°C for 10 hours.

#### **4.4.2 Porosity, pore morphology and pore distribution**

Porosity and pore morphology, including pore size and shape, has an important role in affecting the mechanical properties and possible technological applications of porous materials. This section describes the porosity level, pore morphology and pore distribution of the fabricated porous titanium alloy.

Prior to the evaluation, as-foamed specimens and a polished HIP-ed specimen were visually compared as shown in Figure 4.26. Figure 4.26(a) shows a foamed specimen which was EDM cut and lightly polished on the top, depicting two distinct regions, *i.e.* a larger pore size area – close to the specimen surface (pores are black spots indicated by the white arrow) and a smaller pore size area – the deeper area which is found to be relatively uniform in pore size. In addition, “metal bubbling” (black arrow) was found on the surfaces of some specimens foamed at higher temperatures.

Accordingly, the evaluations (porosity, pore size and mechanical properties) were confined to the area with smaller pores – the deeper area.

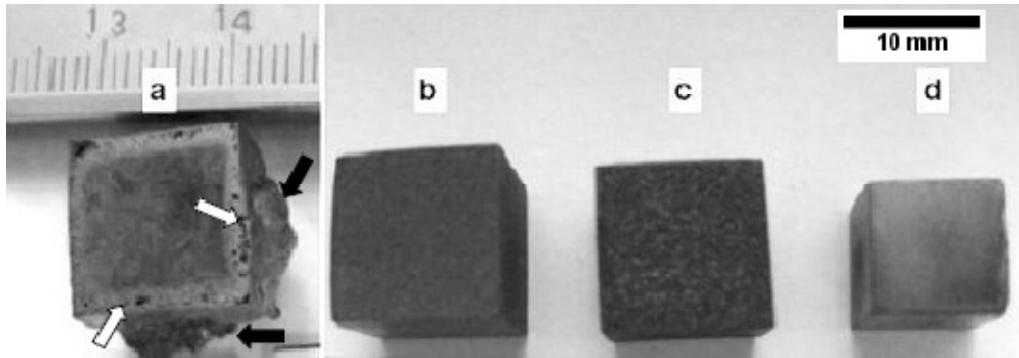


**Figure 4.26 :** Image of titanium alloy specimen isothermally foamed at 1350°C (a) and (b), 1225°C (c) and the polished HIP-ed billet (d).

As-foamed specimens were often found as depicted in Figure 4.26 (b) and (c), showing the pores expanded relatively uniformly, with the extent of pore expansion depending on their foaming conditions. The dimensional changes of the specimens following the foaming procedure were clearly observed. The middle of the foamed specimens appeared to be slightly thicker than on the edge. From the figures it could be expected that the porosity of a foamed specimen at 1350°C was higher than that of a specimen foamed at 1225°C.

After cutting, surface damage layer removal and polishing, the foamed specimens were examined for pore size and pore morphology. The areas examined in this section refer to areas close to the specimen centre unless specifically stated otherwise. The porosity levels (pore volume fractions) reached for the titanium alloys foamed at 1100°C, 1225°C and 1350°C with four set argon backfill pressures applied were found to be in the range of 3.5-17.87%, 6.49-37.1% and 10.9-40.21% respectively. The detailed porosity levels are presented Table 4.1 and Figure 4.27.

**Table 4.1 :** Pore volume fraction of the specimens foamed at various foaming temperatures and backfill pressures for 10 hours and for 2 x 10 hours

No	Foaming Temp. (°C)	Pore volume fraction (%) at Argon Backfill Pressure						
		Foaming for 1 x 10 hours				Foaming for 2 x 10 hours		
		0.34 (MPa)	0.48 (MPa)	0.67 (MPa)	0.86 (MPa)	0.34 (MPa)	0.48 (MPa)	0.67 (MPa)
1	1100	3.4	6.9	10.2	11.3	8.1	7.3	17.9
2				10.7			1.5	
3							16.0	
4	1225	6.5	15.9	21.9	29.8	9.0	17.4	21.6
5		12.9	19.9	22.9	37.1	14.7	20.8	
6				27.0				
7	1350	10.9	20.5	23.4	29.1	22.9	33.0	40.2
8		14.8	21.1	27.8	30.2		33.2	
9		15.3	21.7	28.2	31.5			
10		19.8	27.8		32.1			
11		25.2			35.3			
12		25.9			35.6			
13					36.8			
14				38.5				

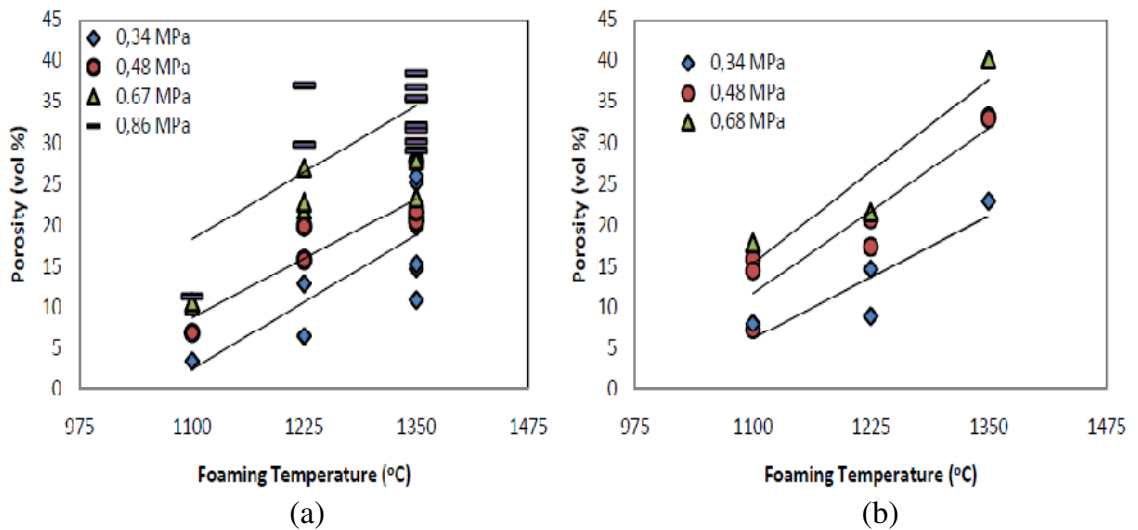


**Figure 4.27 :** Porosity levels achieved for the porous titanium alloys; (a) foamed for 10 hours, and (b) foamed for 2 x 10 hours.

It is noted that porosity levels of the specimens foamed at 1350°C at the same argon backfill pressure were found to be the highest, followed by 1225°C and 1100°C, whilst the porosity level of the specimens foamed at 1100°C with argon backfill pressure of 0.34 MPa were found to be the lowest. The porosity levels of the alloys

increased with an increase of argon backfill pressure to 0.48, 0.68 and 0.86 MPa. In addition, an increase of the porosity level was also found for the majority of specimens isothermally foamed for a longer time period (2 x10 hours). Thus, in general, the porosity level of the foamed titanium alloys is clearly affected by the foaming temperature, the argon backfill pressure and the foaming holding time as expected.

A typical microstructure illustrating pore morphology of a specimen isothermally foamed at 1100°C for 10 hours is shown in Figure 4.28.

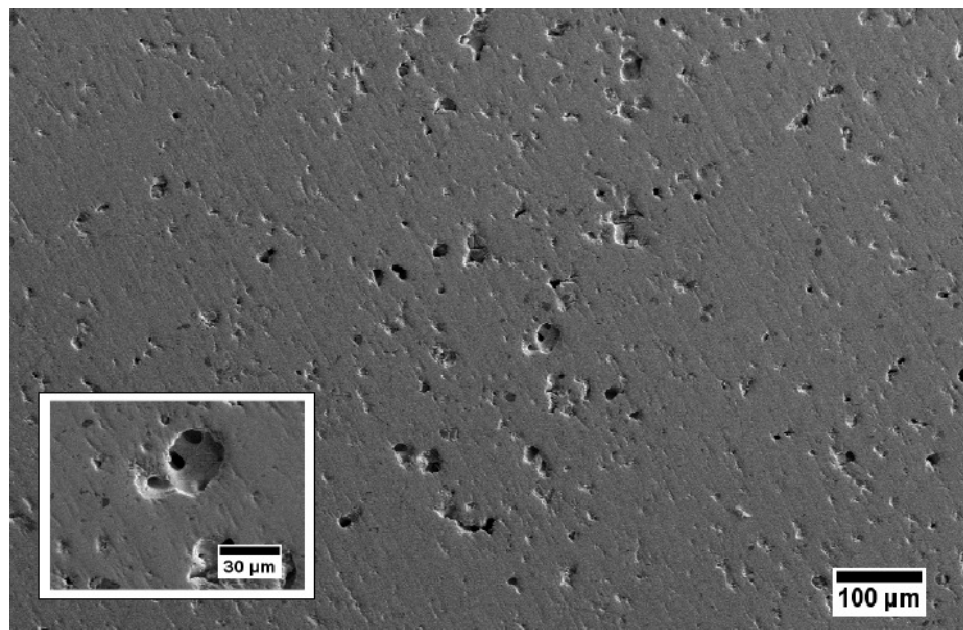


**Figure 4.28** : Secondary electron micrograph showing pore morphology of a specimen foamed at 1100°C/0.68 MPa/10 hours (Porosity of 10.2%).

The micrograph shows that the foaming process resulted in a titanium alloy with a low porosity (10.2%). At low porosity, the pore distribution in the specimen was varied, with the pores being very discrete and with very limited pore coalescence. Pore shape was mainly equiaxed, and presumably spherical in shape in 3 dimensions (see the inset). In addition, pore shapes similar to the expanded interpowder-spacings (angular) were also observed. A maximum porosity level of 11.3% was obtained under an argon backfill pressure of 0.86 MPa. The porosity level is quite similar to a previous study on porous Ti-Ni alloy which reported a porosity level of

approximately 12% [50]. In that study, the porous Ti-Ni alloy was fabricated using a mix of a prealloyed Ti-Ni master powder and an elemental nickel powder isothermally foamed at 1200°C for 10 hours.

Pore expansion due to creep of the metal matrix is more obvious in the typical pore morphology of the specimens foamed at 1225°C, as shown in Figure 4.29. The figure shows a typical specimen with porosity of 21.6% and a small number of pores exceeding 44  $\mu\text{m}$  (powder size <44  $\mu\text{m}$ ). The pore morphology remained discrete with a more frequent coalescence of pores being visible (see the inset) compared to the specimen foamed at 1100°C. The increase in pore interconnectivity also becomes evident.

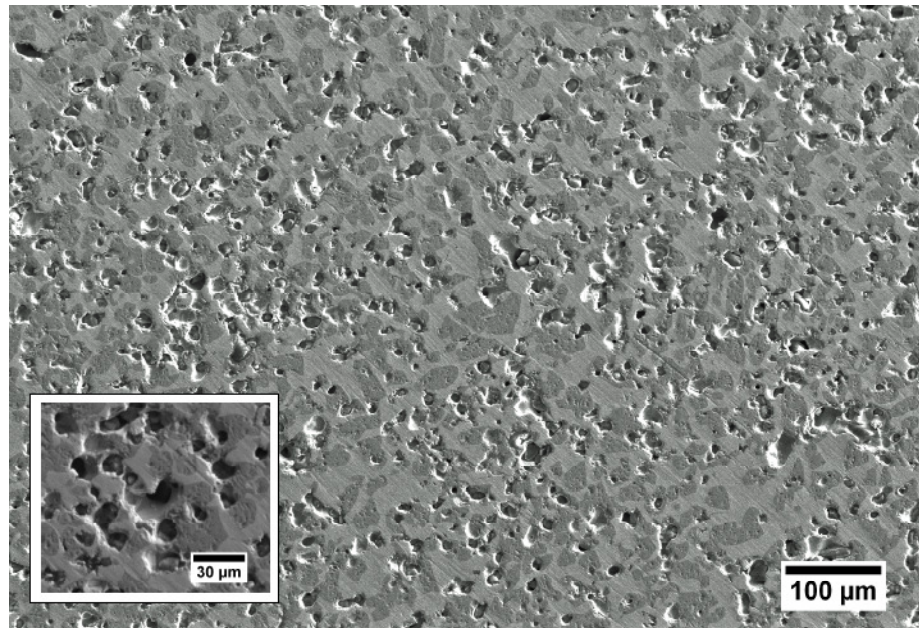


**Figure 4.29** : Secondary electron micrograph showing pore morphology of a specimen foamed at 1225°C/0.68 MPa/10 hours with porosity level of 21.6%

A maximum porosity level of 37.1% was achieved under foaming conditions of 1225°C/0.86 MPa/10 hours. It was noted that the surfaces of the specimen were found to have bubbled, with the presence of two distinct regions clearly identifiable.

For specimens isothermally foamed at 1350°C, pore sizes and porosity levels were found to increase as shown in Figure 4.30. This figure shows the typical

microstructure of a specimen foamed at 1350°C/0.86 MPa/10 hours, achieving a porosity level of 38.7%. In comparison to the porosity level achieved at lower foaming temperatures (1100°C and 1225°C), porosities obtained at a foaming temperature of 1350°C indicated that the increase of the porosity level was attributed to creep deformation of the metal and was found to increase with higher foaming temperatures. Equiaxed pore morphologies and elongated pores due to pore interconnection were observed. The pathway from one pore to the next had grown to a larger size. The pore walls generally remained thick, with the connectivity often being observable. Faceted pores reported to be observed in Ti-6Al-4V alloy [57] or foamed CP Ti [371] were not found in this study. An absence of the faceted pores has also been reported by previous research [50].

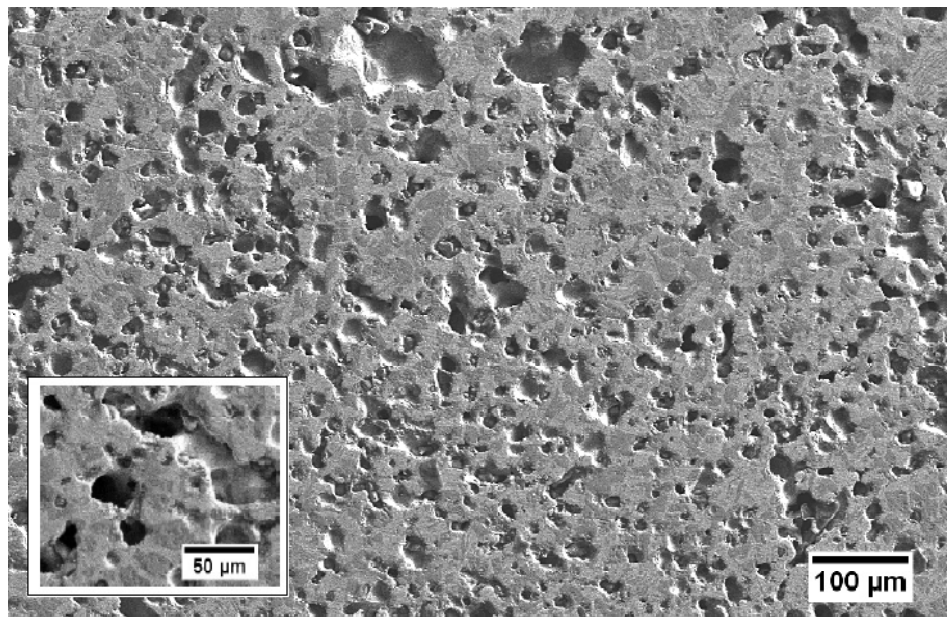


**Figure 4.30** : Secondary electron micrograph showing pore morphology of a specimen foamed at 1350°C/0.86 MPa/10 hours (38.7%).

An early stage of pore coalescence during isothermal foaming at 1350°C, leaving round protrusions of less than 44 μm in diameter, is illustrated in Figure 4.31 (arrows highlight protrusion). Rupturing of some pore walls due to pore expansion (foaming) was also observed, indicating that many pores had coalesced with multiple pores sometimes having become interconnected. The foaming rate is known to decrease

and further expansion reduces when pore volume is increased [371]. A rise in pore volume decreases pore pressure, which is known to be the driving force for pore expansion.

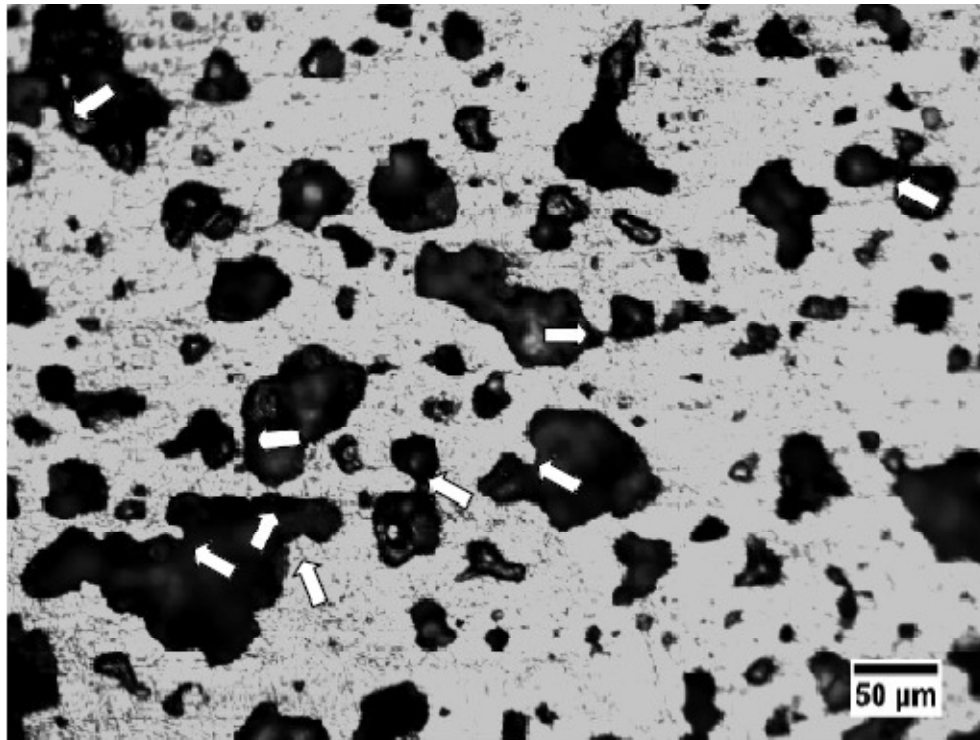


**Figure 4.31** : Optical micrograph of a specimen close to the centre, showing the early stage of pore coalescence during isothermal foaming at 1350°C/0.86MPa/10 hours. Arrows indicate protrusion.

Interestingly, as mentioned earlier (see also Figure 4.26(a)), most specimens isothermally foamed, particularly at 1225°C or 1350°C, showed a region near the surface having a larger pore size due to noticeable pore expansion. Thicknesses of the region were measured in the range of 1-2 mm as shown in Figure 4.32. The figures illustrate morphology of the larger pore in the region.

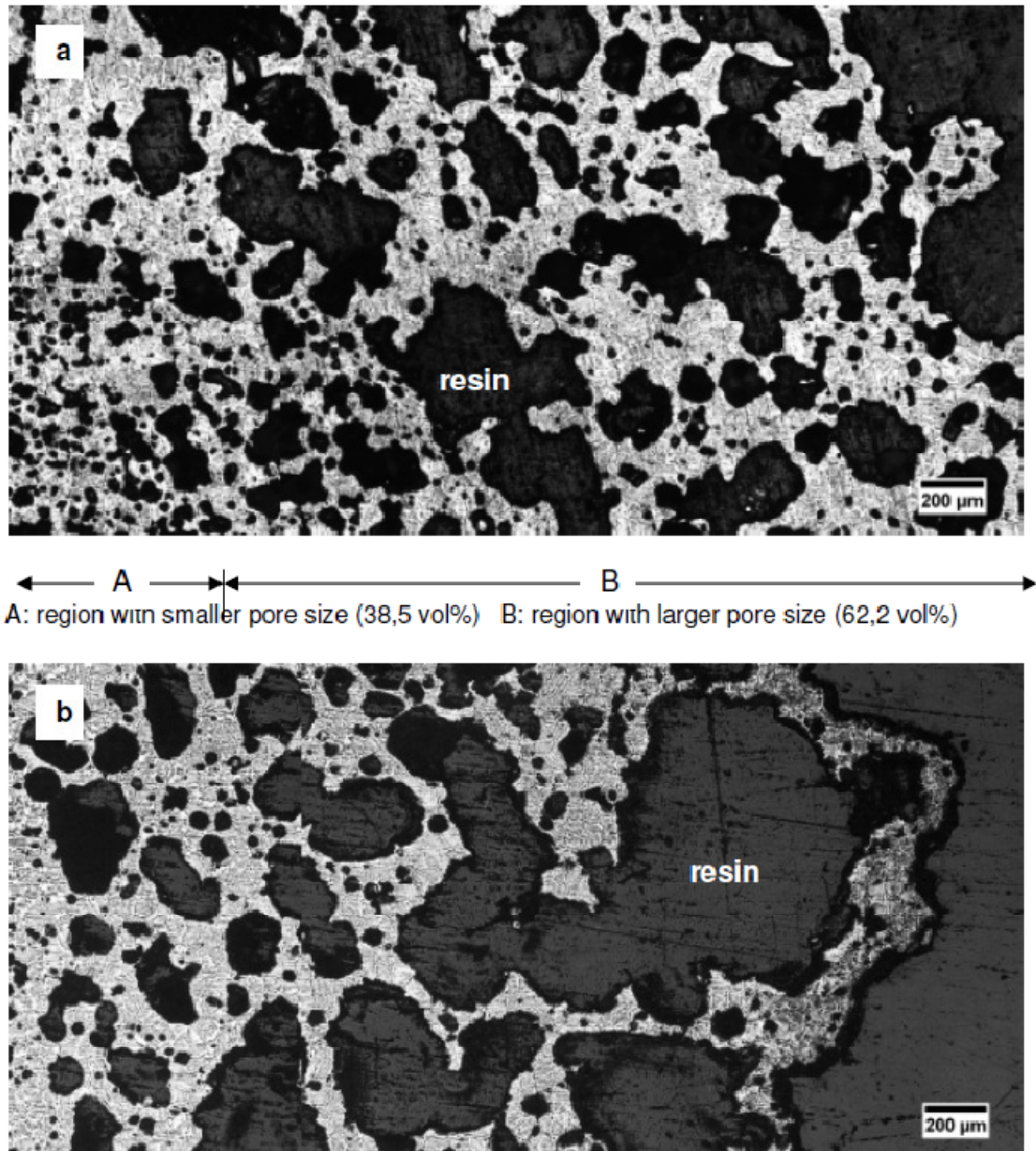


**Figure 4.32** : Optical micrograph of the region close to the surface with larger pore size under foaming conditions of 1350°C/0.86MPa/10 hours.

- (a) a cross section of the larger pore region
- (b) a cross section of the metal bubble in the larger pore size region (Porosity level of 67%)

The porosity level of the surface region was typically found to be 45-67 vol%, and the pore size diameter typically 20-500 μm. The pore walls were found to be thinner compared to the pore size. An expansion of pores, a collapse of the interpore walls and a coalescence of pores had taken place to a much greater extent than that of the interior. Interconnected pores were frequently found, suggesting that the pores may

be classified as open pores (Figure 4.32(a)). This phenomenon was attributed to fewer constraints against expansion being present close to the surface of the specimen [401]. Figure 4.32(b) shows the cross section of the specimen and illustrates pore coalescence prior to opening at the specimen surface. These large pores appeared as bubbles on the specimen surface, with typical pore sizes of 1388  $\mu\text{m}$  being present. However, the expansion would presumably be inhibited as the pore volume increased and/or the pressurised argon escaped into the atmosphere.

In contrast, specimens with relatively uniform pore expansion were produced, as shown in Figure 4.33. The pores in the region close to the specimen surface had only moderately expanded with the increase in porosity level.

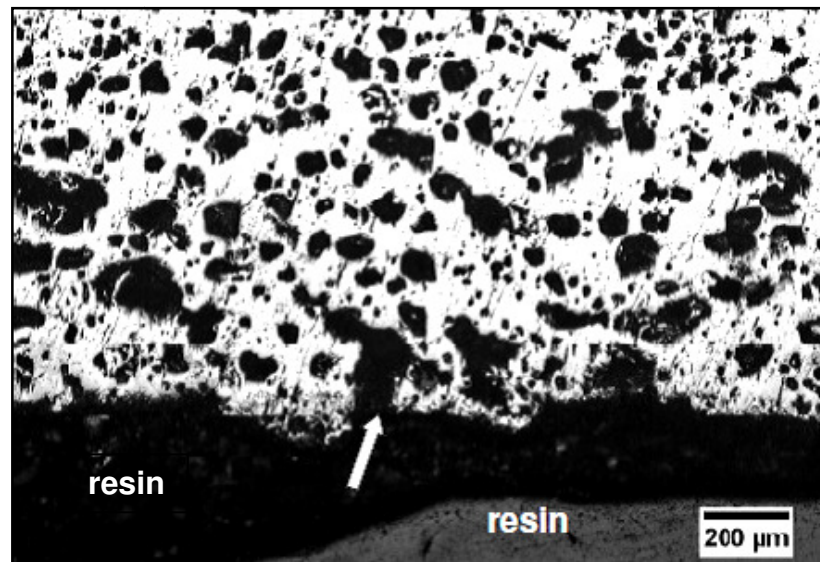


**Figure 4.33** : Optical micrograph of the region close to the surface of a typical specimen foamed at 1225°C/0.68 MPa/10 hours showing a relatively uniform pore expansion (porosity level of 26.7%).

The pores were still found to be discrete and the pore walls remained thick with no distinct increase in the amount of pore coalescence, the pores still being classified as closed pores. However, some pore coalescence followed by the emergence of the pores to the specimen surface was also observed on the edge, as indicated by the arrow in Figure 4.33.

The pore morphology of specimens foamed at the given temperatures and argon pressures but with foaming time of 2 x 10 hours was found to be more interconnected than that of the single 10 hours foaming period. For comparison, Figure 4.34 shows the typical pore morphology of a specimen foamed at 1350°C/0.68 MPa/2 x 10 hours with a porosity level of approximately 40.2%.

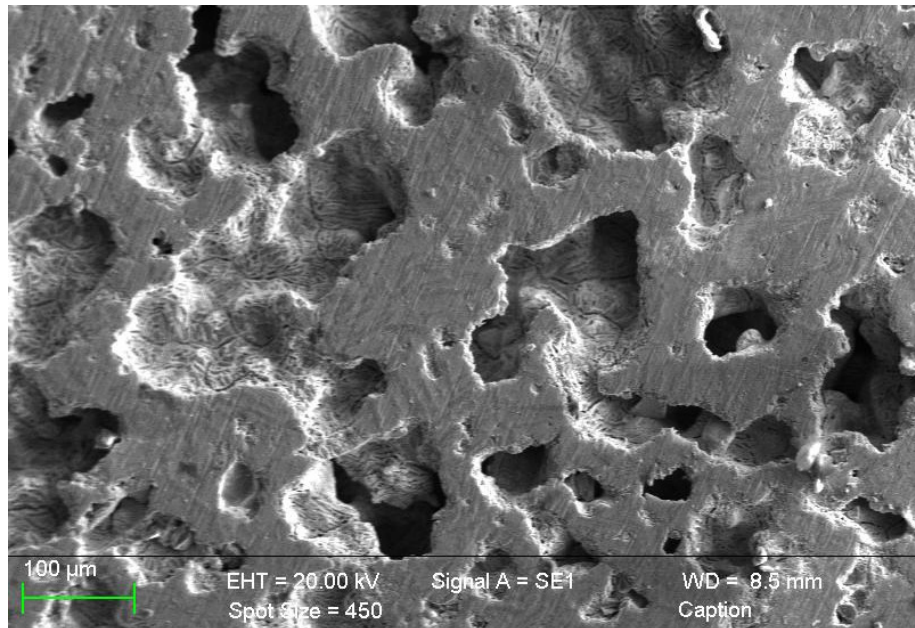


**Figure 4.34 :** Secondary electron micrograph showing pore morphology of a specimen foamed at 1350°C/0.68 MPa/2 x10 hours (porosity level of 40.2%).

Based upon the image analysis subjected to foamed sample micrographs using ImageJ software, both the number of pores and the area of pores fitting in each interval (bin) were counted and step plots of percentage distribution were plotted, as depicted in Figure 4.35.

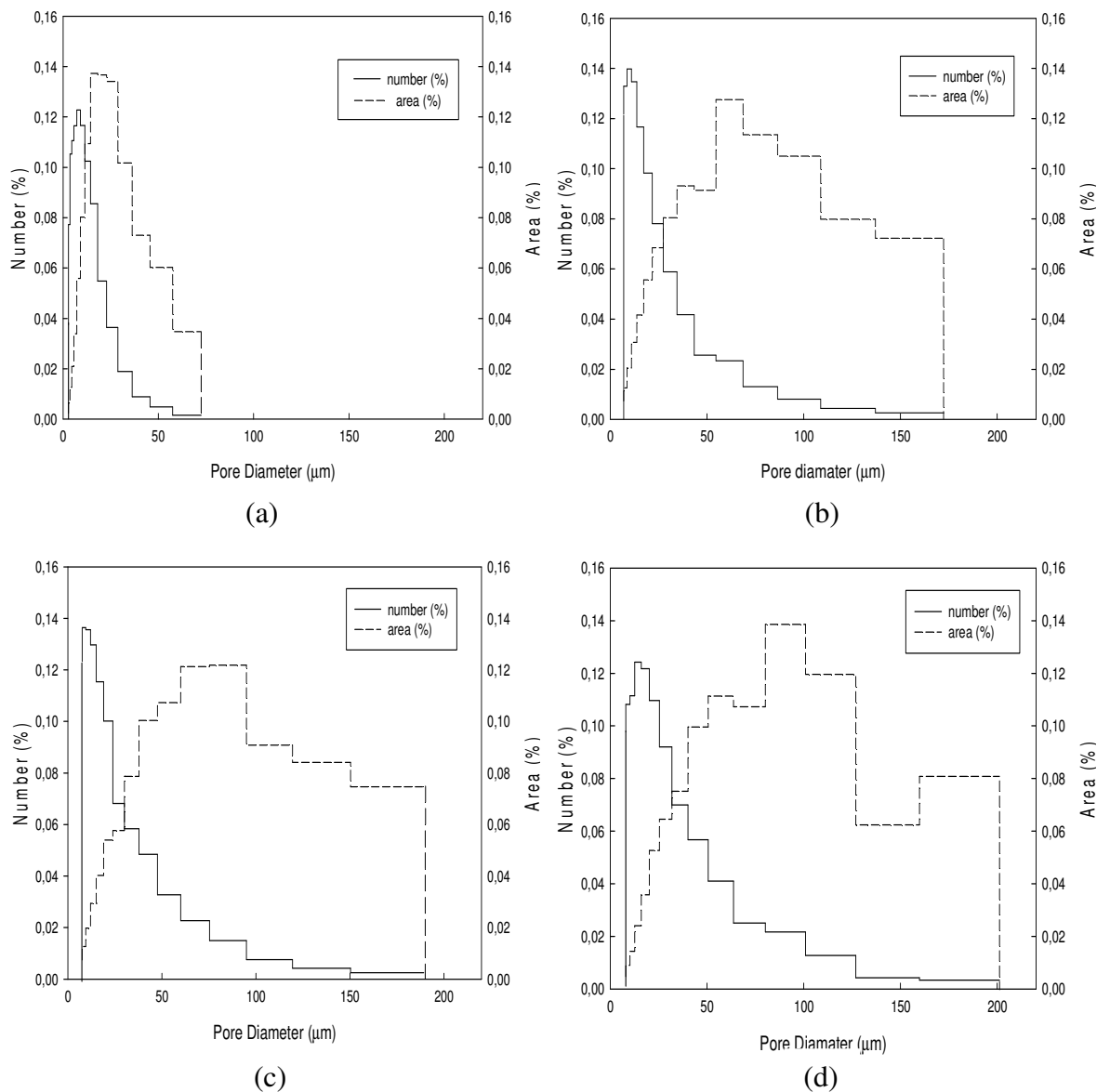


**Figure 4.35 :** A typical pore size distribution of samples foamed at (a) 1100°C/0.86 MPa/10 hours with a porosity level of 11.3%, (b) at 1225°C/0.86 MPa/10 hours with a porosity level of 37.1%.(c) at 1350°C/0.86 MPa/10 hours with a porosity level of 38.7% (d) 1350°C/0.68 MPa/ 2 x 10 hours with a porosity level of 40.2%.

The graphs were created from data obtained from the analysed sample images that represent the largest porosity in each foaming temperature group. Firstly, Figure 4.35(a) illustrates a typical pore size distribution of the porous titanium foamed at 1100°C with a porosity level of 11.3%, and a typical pore size diameter in the range of 3-75μm. The highest pore area fraction was found in pores with diameter sizes in the range of 18.2-22.9 μm. Secondly, from image analysis of the micrograph of the

sample foamed at 1225°C/0.86 MPa/10 hours, the porous titanium alloy with a maximum porosity level achieved of 37.1%, the pore size distribution is shown in Figure 4.35(b). The pore size was estimated to be in the range of 6.9-172.6  $\mu\text{m}$ , with pore sizes 54.5-68.6  $\mu\text{m}$  being the highest pore area fraction. Thirdly, the pore size distribution of the sample foamed at 1350°C/0.86 MPa/10 hours with porosity level 38.7% revealed that the pore size range and the size diameter of the dominant pore area fraction were found with typical pore sizes of 7.5-189  $\mu\text{m}$  and of 59.6-94.5  $\mu\text{m}$  respectively as shown in Figure 4.35(c). Lastly, a typical sample foamed at 1350°C/0.68 MPa/2 x10 hours with porosity level of 40.2%, the pore size distribution of the specimen shows the resultant pore size to be in the range of 8-200 $\mu\text{m}$  (Figure 4.35(d)). Pore sizes of 16-20  $\mu\text{m}$  were found to be dominant in terms of frequency, whilst the highest pore area fraction was attained by pore sizes of 80.1-110.8  $\mu\text{m}$ . This can be seen as confirmation that the dominant pore sizes range, either in terms of frequency or pore area fraction, increased with an increase of foaming temperature and foaming holding time due to the pore growth.

As mentioned earlier, isothermal foaming shows a specific character in that very rapid foaming rates at the early stage of foaming are developed followed by a steady decrease in the foaming rate until the terminal porosity is reached. The initial foaming rate is attributed to the initial porosity (as HIP-ed porosity) which is affected by the HIP-ing pressure and temperature, the gas pressure in the canister and the packing density of the powder before densification [49]. In the present study, these latter two parameters were suggested to result in a large range of the initial porosities in which the initial porosity increased with the increase of gas pressure. A relative broad powder size (< 44 $\mu\text{m}$ ) was used which may pack less effective than monosized powder [403]. The fine powder size may result in less packing density due to the occurrence of agglomeration and flocculation. Additionally, the powder shape also affects packing density, due to the higher probability of pore formation between particles of irregular shape [47]. The experimental results show that within the foaming period, the foamed sample porosities exhibited similar tendency in that samples with the higher initial porosity achieved higher pore fraction as shown in Figure 4.36. In the other words, samples with higher initial porosity resulted in a

higher foaming rate. Similar findings have previously also been noted by other researchers [49, 50].

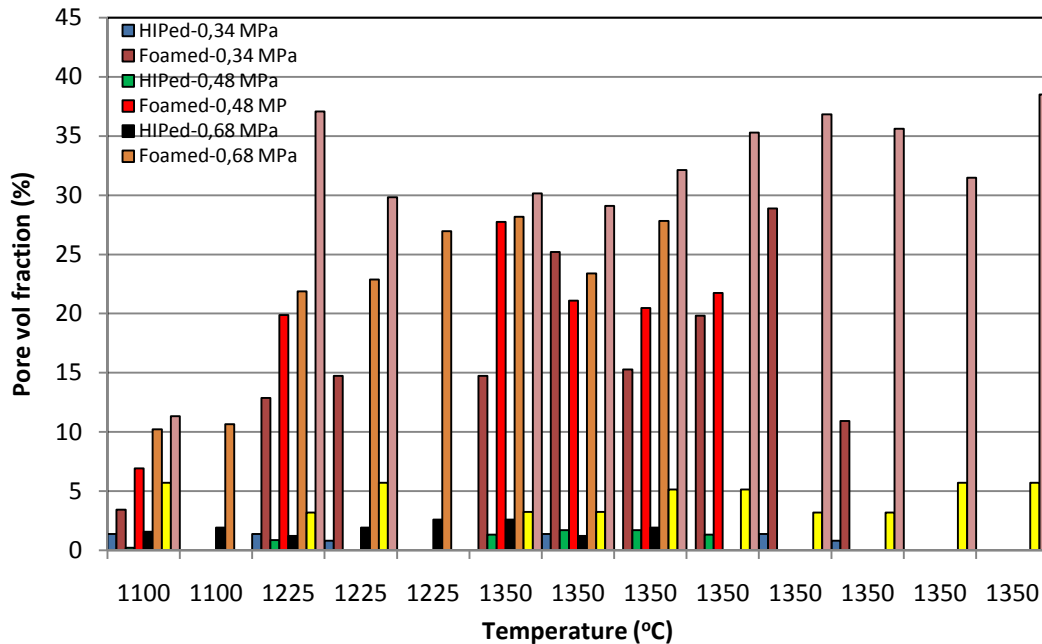


**Figure 4.36 :** Plot of as HIP-ed porosity corresponding to as-foamed porosity at 10 hours foaming holding time for various argon backfill pressures and foaming temperatures.

From the microstructural examination and mechanical evaluation; described in Section 4.4.4; in terms of the number of pores, the majority of pores of the foamed samples might be classified as closed pore, but interconnected pores can be observed to have dominated the outer surface of the micrograph samples (Figure 4.31). In this case, the decrease in foaming rate was due possibly to the reduction in pore pressure along with a rise in the pore volume during pore growth where occasionally multiple pores were coalesced due to the rupturing of interpore walls. The decrease in foaming rate was not considered to be due to gas escaping through to the samples surfaces due to the robust pore morphology in the surface region. A similar finding has previously been noted in other research [371]. On the other hand, in the specimens with the two distinct regions where larger pores existed, the decrease in foaming rate was mainly caused by a combination of the reduction in pore pressure due to pore growth and loss of the driving force due to pore opening at the surface (gas escaping).

Whilst isothermal foaming studies by Kearns *et al.*[57] and Davis *et al.*[366] resulted in porosity levels of 32% and 27%, both being lower than the present study (40.2%), there are four differences between those studies and the current study that potentially explain the variations namely; alloy composition, backfill pressure, foaming temperature and foaming time. In terms of alloy composition, those studies used CP Ti and Ti-6Al-V which are known to be  $\alpha$  and  $\alpha + \beta$  type titanium alloys. Such alloys show high creep resistance and are thus suitable for high temperature service, whereas  $\beta$  titanium alloys show low creep resistance and are not meant to be applied at high temperatures [268]. In isothermal foaming, the pore expansion is affected by creep of the matrix, thus foaming materials with a lower creep resistance, in this study  $\beta$  titanium alloys, allow a higher degree of pore expansion than that of the highly creep resistant materials ( $\alpha$  titanium or  $\alpha + \beta$  titanium alloys). Another consideration is argon backfill pressure; in the present study, higher argon backfill pressures were used (0.68 MPa versus 0.11 and 0.33 MPa). The samples in the current study were foamed at a higher temperature (1350°C versus 1240°C and 960°C) allowing a greater extent of creep and a higher driving force. Although in the other studies the samples were foamed at a longer holding times (24 and 46 hours versus 20 hours), these foaming holding times may not give any noticeable effect in terms of the difference of porosity growth, since in these experiments [50, 57, 366], it was found that pore size grew rapidly during the initial 10 hours of foaming and subsequently increased very slightly. Comparatively, the first three parameters favour higher porosities in this study and the last one in the other studies, it is thus suggested that the higher porosities of the specimens in this study were due to the three aforementioned parameters.

Although titanium is known to be biocompatible, titanium still initiates a foreign body reaction, *i.e.* an encapsulation process, with the thickness of the capsule (layer of collagen) for titanium being around 100-200 Å whereas other metals sit in a capsule greater than that (*e.g.* 50 µm) [18]. Porosity may be critical to biocompatibility and avoiding the foreign body reaction. Pore morphology such as size and interconnectivity are known to be important factors to initiate bone ingrowth into a porous implant. Previous researchers have noted that optimal porosity and

pore size for bone ingrowth into porous coating occurs in the range of 20-60% [404] and pore size down to 50  $\mu\text{m}$  [30, 31], while the porosity interconnection should be larger than 100 $\mu\text{m}$  for generation of mineralized bone [25]. This fabricated porous titanium alloy achieved porosity levels greater than 20% and together with the pore sizes mentioned earlier, suggests potential for biomedical applications.

#### 4.4.3 Electrochemical corrosion assesment

In this work, corrosion assesment was performed by open circuit potential (OCP) measurement which monitors film formation and passivation of the alloy in a solution, and by potentiodynamic polarisation measurement to identify electrochemical behaviour of material when exposed to a particular environment. The result of OCP measurement is shown in Figure 4.37.

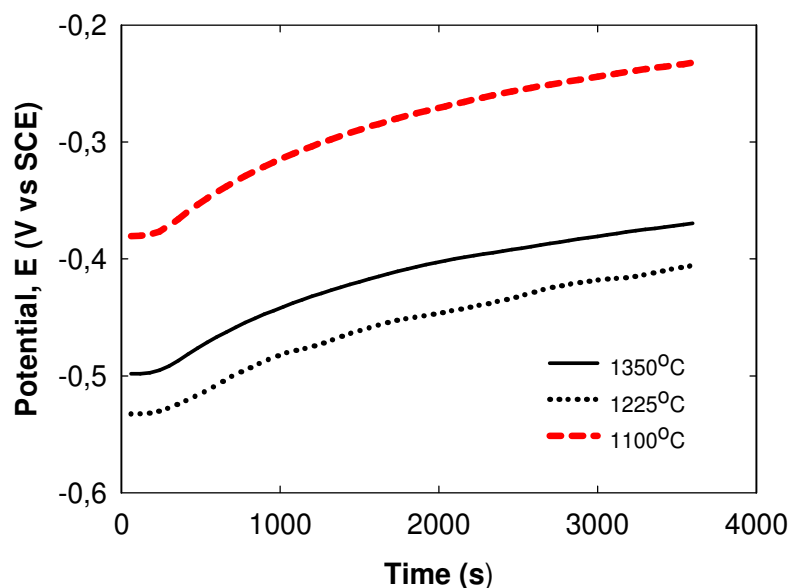


**Figure 4.37:** The open circuit electrode potential (OCP) as a function of time of the specimens foamed at 1100°C, 1225°C and 1350°C in Hank's solution at 37°C

Figure 4.37 shows the measurement of the open circuit electrode potential (OCP) as a function of time for titanium alloy specimens foamed at 1100°C, 1225°C and 1350°C. The results were fairly reproducible, and it can be clearly seen that all the curves are comparable and run essentially parallel to each other. It is observed that there is an initial shift of potential and a very slight increase within the initial few minutes followed by a continuous rise in potential towards the noble direction to

attain finally the steady state potentials. The initial  $E_{\text{corr}}$  for the specimen foamed at 1225°C was approximately -533 mV. It moderately increased in a decreasing rate of increment, reaching -406 mV after one hour. Similarly, the initial  $E_{\text{corr}}$  of the specimen foamed at 1350°C and 1100°C were approximately -498 mV and -380 mV, reaching -370 mV and -232 mV after one hour respectively. The specimen foamed at 1100°C exhibited a more noble potential compared to the two forementioned specimens. A more noble potential was also observed on the specimen foamed at 1350°C compared to that at 1225°C, which may due to lower porosity. Increasing the potential in the positive direction indicates the formation of a passive film and a steady state potential indicates that the film remains intact and protective. These results revealed a presence of competition between film dissolution and film formation, which ends by a potential indicating thickness and self healing of surface film. The potential variation rate, which reflects oxide formation rate, was high after few minutes of immersion, and decreased with time to reach a steady state.

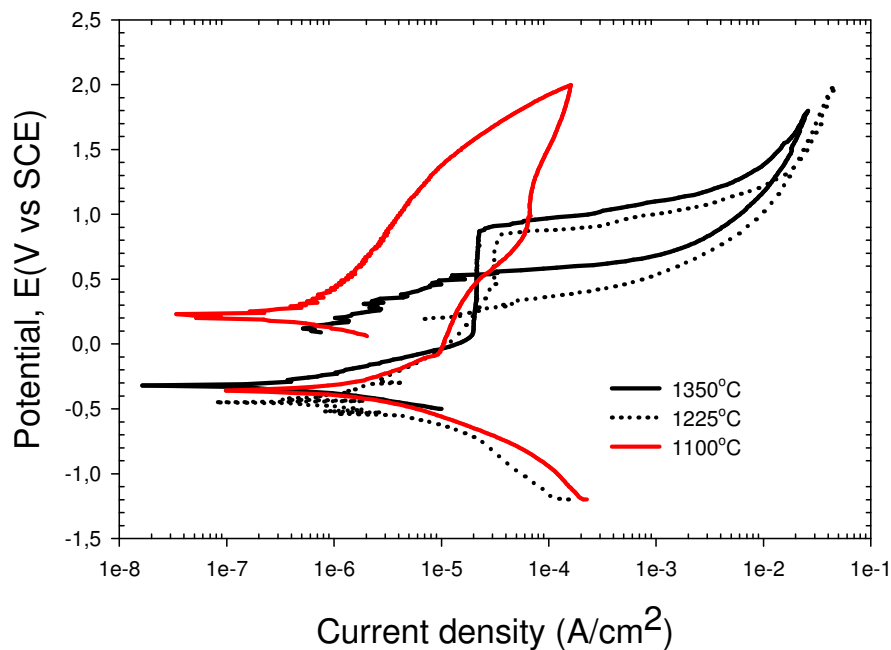


**Figure 4.38:** Potentiodynamic polarisation curves for specimens foamed at 1100°C, 1225°C and 1350°C in Hank's solution at 37°C.

Figure 4.38 shows the potentiodynamic polarisation curves for the specimen foamed at three different temperatures, in Hank's solution at 37°C. The corrosion potentials ( $E_{\text{corr}}$ ) ranged from 320 to 445 mV. The discrepancy in corrosion potentials among

the specimens may be caused by a tiny difference in the surface condition [405], despite the fact that the specimens were prepared using the same procedure. The corrosion potentials, corrosion current densities ( $i_{\text{corr}}$ ) and passivation current densities ( $i_{\text{pass}}$ ) for the specimen obtained from their polarisation curves are summarised in Table 4.2. The corrosion current densities were obtained from the polarisation curves using the Tafel extrapolation method.

Corrosion potentials from the polarisation curves are lower compared to those obtained from open circuit potential. This may suggest, as the polarisation tests were started at a cathodic potential relative to the corrosion potential, that the passive film at the surface was at least partially removed due to the highly reducing initial potentials [130].

**Table 4.2 :** Main electrochemical parameters in Hank's solution at 37°C for 10 hours and for 2 x 10 hours

Foaming Temperature (Pore volume fraction)	Breakdown Potential, $E_b$ (mV)	Passivation Current Density, $i_{\text{pass}}$ ( $\mu\text{A}/\text{cm}^2$ )	Corrosion Current Density, $I_{\text{corr}}$ ( $\mu\text{A}$ )	Corrosion Potential, $E_{\text{corr}}$ (mV)	Beta A (V/decade)	Beta C (V/decade)
1350°C (10.9%)	899	34.9	0.322	-321	0.191	-0.117
1225°C (12.9%)	829.3	43.8	1.230	-445	0.444	-0,194
1100°C (6.9%)	N/A	N/A	1.510	-362	0.378	-0.221

Concerning the corrosion densities, the corrosion resistance of specimen foamed at 1100°C and 1225°C were comparable while specimen foamed at 1350°C exhibited lower corrosion rate ( $i_{\text{corr}}$ ) compared to the two other specimens (Table 4.2). The specimen foamed at 1225°C and 1350°C were characterised by a partial stabilisation of their current densities of 27 and 40  $\mu\text{A}/\text{cm}^2$ , respectively. This suggests that a protective passive film is formed within these current densities. The breakdown potentials of specimens foamed at 1350°C and 1225°C were in the range of 829-899

mV. The higher porosity of specimen foamed at 1225°C may be responsible for lower breakdown potential [131]. In contrast, the specimen foamed at 1100°C demonstrated no breakdown potential and no hysteresis loop. This indicates that the specimen foamed at 1100°C has higher pitting and crevice corrosion resistance [406] due to its constitution, which comprised  $\beta$  phase predominantly [112]. The values of corrosion current density and corrosion potential of the specimens foamed at the three different temperatures in Hank's solution at 37°C are comparable to those of CP Ti, Ti-6Al-4V [406, 407].

#### 4.4.4 Mechanical properties assessment

##### 4.4.4.1 Hardness testing

The indentation hardness was measured using a Buehler Micromet 0055 microhardness tester with a Vickers diamond pyramid indenter. An average of 15 readings was taken from each specimen. The results are shown in Figure 4.39.

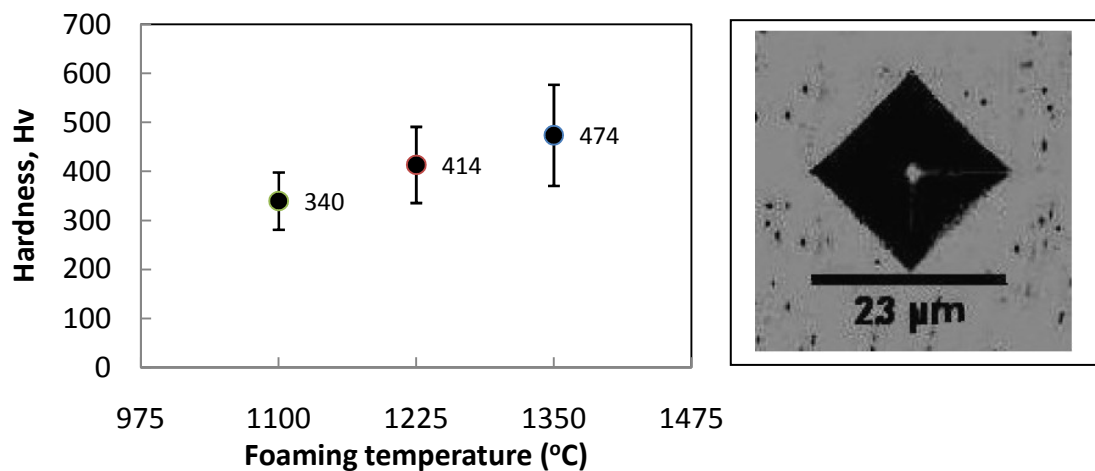


**Figure 4.39:** (a) Hardness values of specimens foamed at 1100°C, 1225°C and 1350°C, (b) optical image micrograph of the Vickers indentation on the specimen foamed at 1100°C.

The Vickers hardness tests were performed randomly on the surface of polished specimens, using a load of 100g. Figure 4.39 shows the variation of hardness versus foaming temperature. The plot illustrates the hardness markedly increased with increasing foaming temperature. This increase in hardness is as expected because the proportion of  $\alpha$  phase, which is known to possess a higher elastic modulus than that

of  $\beta$  phase, is also higher with the increase of foaming temperature. The largest scatter in hardness values was shown by the specimens foamed at 1350°C, followed by specimens foamed at 1225°C and at 1100°C. The high discrepancy of the hardness values for higher foaming temperatures may be caused by the fact that the higher the foaming temperature the closer were the proportions for  $\alpha$  phase and  $\beta$  phase, resulting in higher possibility of obtaining respective hardness values of those phases. The lower foaming temperatures, producing higher proportions of  $\beta$  phase, resulted in lower values and narrower scatter in hardness values. The result also indicates that the specimens foamed at 1100°C are more homogenous in  $\alpha$  phase compared to the two a forementioned.

The hardness values of the specimen foamed at 1100°C, containing high portion of  $\beta$  phase are comparable to the those commonly reported for hot wrought alloys (about 350 HV) [27], Ti-6Al-7Nb (200-400 HV),  $\beta$  titanium alloy Ti-35Nb-7Zr-5Ta(326-356 HV) [408], Ti-13Zr-13Nb (250-350 HV) [409] and various biomedical titanium alloys developed by Niinomi et al.(300-400 HV) [251]. However, these values are slightly higher than those of titanium alloys fabricated by the conventional P/M method; sintered at 1600°C (300 HV) [24]. Hardness values of the specimens foamed at 1350°C are comparable to those of specific cast titanium alloys (500 HV) [28].

#### **4.4.4.2 Compressive testing**

In this work, mechanical properties of the porous titanium alloy were evaluated by using compression tests resulting in stress-strain curves by which the elastic moduli and strengths of the alloys were determined. Typical stress-strain curves for the specimens foamed at 1100°C, 1225 °C and 1350°C have been presented in Figure 4.40 with a remarkable difference in stress-strain behaviour being noted.

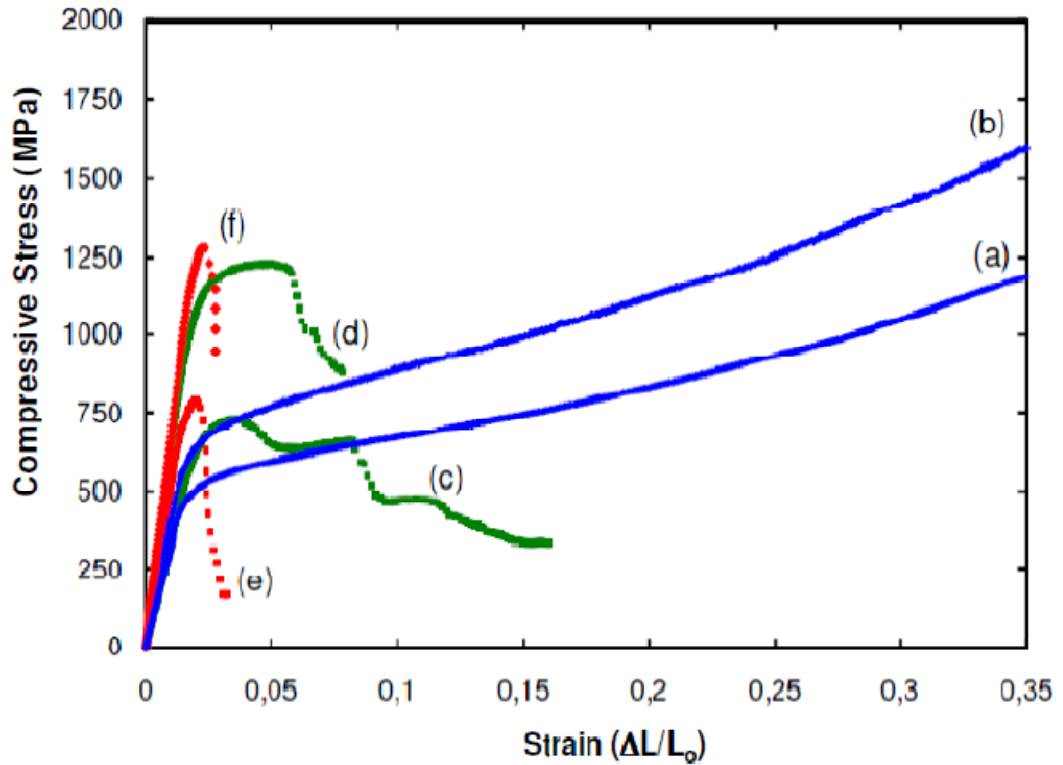


**Figure 4.40:** Typical compression stress-strain curves for the specimens foamed at different temperatures: (a & b) 1100°C, (c & d) 1225°C, and (e & f) 1350°C.

The typical curves for the samples foamed at 1100°C as shown in Figure 4.40 (a and b) indicated a large amount of ductility in compression with three stages of deformation being apparent; an elastic deformation stage, second elastic (with larger strain) deformation stage and densification stage. The samples were able to sustain compression strains of more than 35% without collapse. The deformation ability of the foamed specimen is illustrated by the 2 photographs in Figure 4.41(a) (up to 60% strain). The ductility was found to be improved due to the stabilisation of  $\beta$  phase, which is more ductile than the other phases [410]. Figure 4.40(c and d) depicts a typical stress-strain response for the samples foamed at 1225°C with this curve being typical for ductile porous materials.

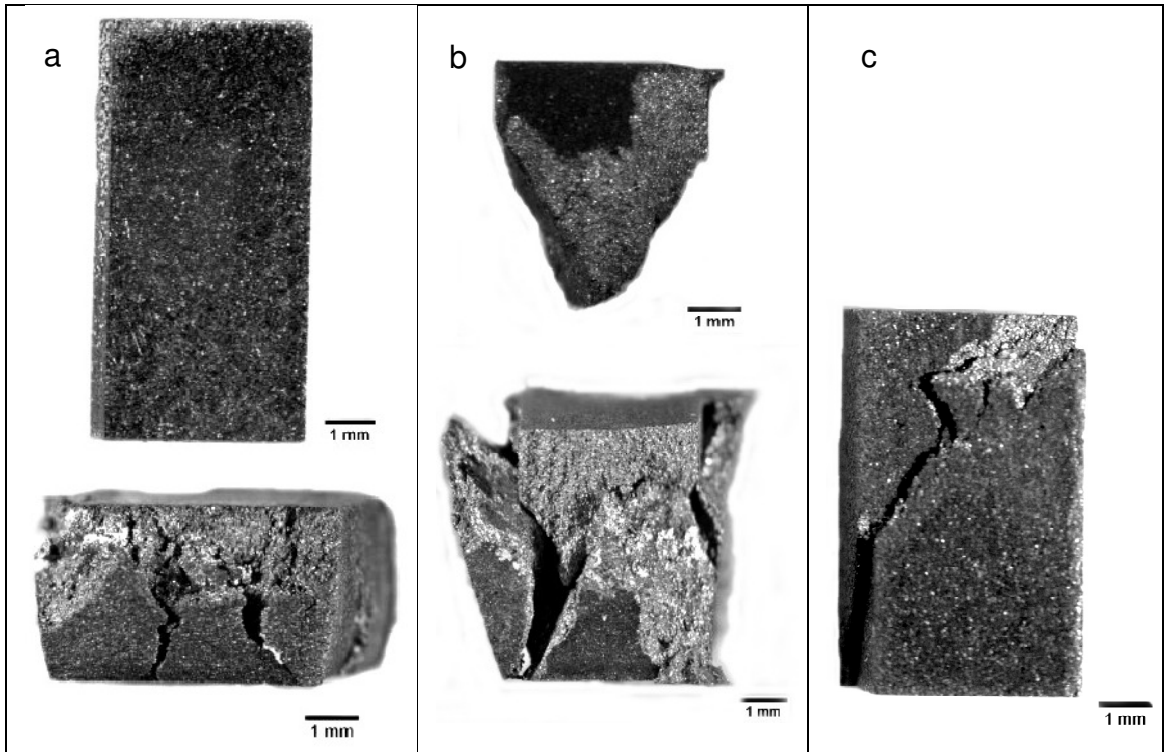


**Figure 4.41:** Pictures showing typical deformation of the foamed samples, (a) undeformed (upper image) and deformed (lower image) sample foamed at 1100°C, (b) deformed sample foamed at 1225°C; bottom and V shape of the compressed sample (upper image), (c) deformed sample foamed at 1350°C.

According to Guden *et al.* [411] the curve can also be considered in three distinct deformation stages. In the first stage, the specimen is elastically compressed up to the proportional limit. In the second stage, inelastic deformation takes place under normal and shear forces, this region being observed between the proportion limit to maximum stress. In the last stage, at the maximum stress (compressive strength), deformation presumably begins to become non-uniform and localised to the shear band resulting in a reduction in the load carrying capacity of the deforming specimen. Occasionally, complete failure was observed at relatively large strains of the local deformation, illustrated by Figure 4.40(a & b) and Figure 4.41(a) - lower image.

Interestingly, the failure of the sample foamed at 1225°C occurred by separation of the sample, with a typical rupture section taking the appearance of a V shape or

conical shape (Figure 4.41(b) - upper image). Similar findings have also been reported by previous researchers [47, 349]. In contrast, the curves shown in Figure 4.40(e & f) for typical specimens foamed at 1350°C were characteristic of brittle failure. The occurrence of an increase in brittleness for titanium alloys has previously been linked to the existence of oxygen in the porous metal [23]. The failures were found to be due to the separation of the sample (cleavage) starting from the corner as shown in Figure 4.41(c). This failure may be due to shear stresses on the shear band occurring around 45° to the loading direction [411]. Whilst the strengths of the specimens were higher than that of the less porous specimens foamed at 1100°C and 1225°C, the strain at maximum stress was significantly lower at generally less than 3%. Of interest, the plateau regions commonly found in porous materials was not observed in the present study. A lower porosity [46] and/or a higher brittleness [23] of the samples were attributed to the disappearance of the plateau region. The presence of closed pore morphology may be linked to the increase in stress after yielding with the increase in strain in place of the plateau region (Figure 4.40(a & b)) [46].

The fracture surfaces of foamed specimens were examined further by SEM and are shown in Figure 4.42. The samples foamed at 1100°C show a failure mode whereby the interpore walls experienced a high degree of deformation and some crack formation due to the application of compressive stress (Figure 4.42(a)). Small parts of the pore walls were pulled off by the crack after being severely deformed. Typical surface fractures of the samples foamed at 1225°C show shear and/ or normal stresses resulted in the coalescence of microvoids along the fracture path, dimples, and complete separation of the interpore walls. The presence of dimpled rupture on the fracture surface indicated the occurrence of ductile failure on the specimen (Figure 4.42(b)). A brittle failure on the specimen foamed at 1350°C was expected, and was confirmed since the surface fracture displayed interpore wall fracture resembling a more faceted mode of failure (Figure 4.42(c)). The fracture path was seen to propagate between pores which were in line with the shear band crossing the phases (Figure 4.42(d)).

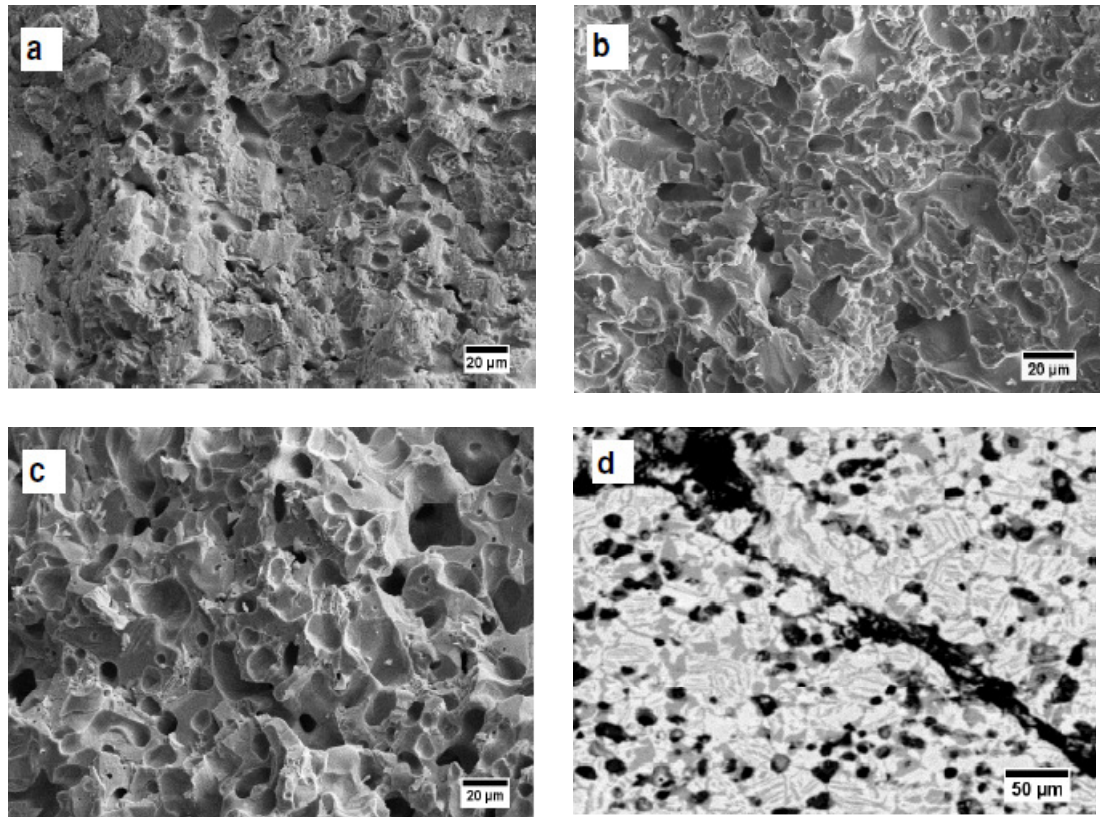


**Figure 4.42:** Secondary electron micrographs showing a typical surface fracture of specimen foamed at (a) 1100°C (b) 1225°C (c) 1350°C. A backscattered electron micrograph (d) of a cross section of fractured specimen foamed 1350°C shows the fracture path propagating between pores crossing the phases.

The Young's moduli of the porous titanium alloys were determined in the initial linear elastic region of the compressive stress-strain curves with the results from several specimens foamed at 1100 °C, 1225 °C and 1350°C being presented in Figure 4.43 as a function of pore volume fraction (f).

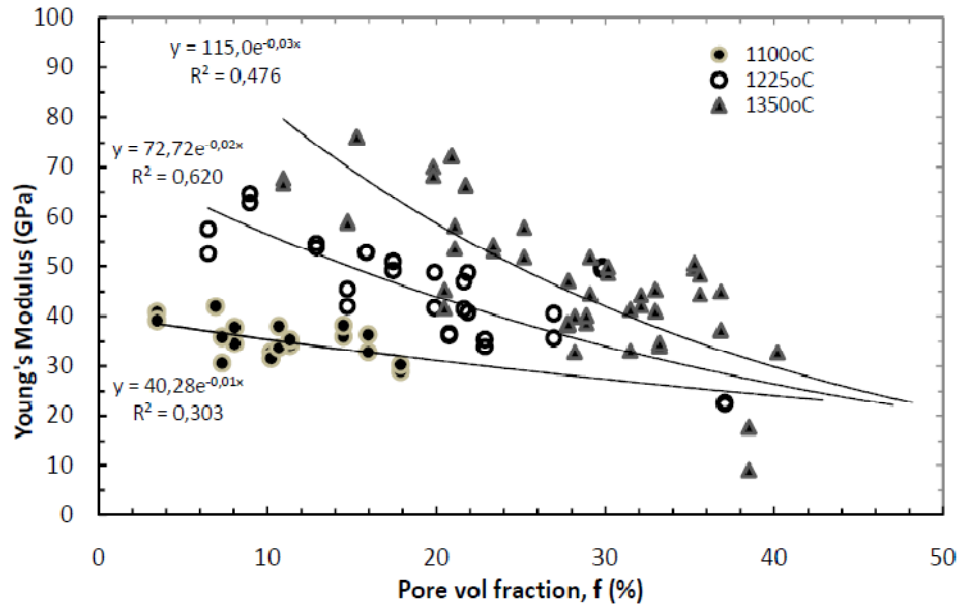


**Figure 4.43 :** Influence of pore volume fraction on the elastic modulus of foamed samples at 1350°C, 1225°C and 1100°C.

Figure 4.43 shows Young's moduli and pore volume fraction of the porous titanium alloys foamed at 1100°C, 1225 °C and 1350°C. These are summarised in Table 4.3.

**Table 4.3 :** The elastic modulus of the fabricated porous titanium alloys foamed at 1100°C, 1225 °C and 1350°C

Foaming Temperature (°C)	Pore volume fraction (%)	Elastic modulus (GPa)
1100	3.5-17.9	29.0-41.9
1225	6.5-37.1	22.4-64.7
1350	10.9-40.2	9.1-72.3

In general, the elastic moduli of the porous alloys decreased with increasing pore volume fraction, whereas the degree of the elastic modulus reduction varied due to specific alloy phase development at the higher temperature. *i.e.*  $\alpha$  phase formation at 1225°C and 1350°C tended to induce high elastic modulus values. When the presence of porosity results in density loss, relative density,  $\rho^*/\rho_s$ , then equates to  $1-f$ . The

relationship between the elastic modulus and the pore volume fraction can be expressed by Equation 4.1 [382] which is derived from Equation 2.2, as written below:

$$\frac{E^*}{E_s} = (1 - f)^n \quad \text{Equation 4.1}$$

Where: f is pore volume fraction

By using Equation 4.3, Figure 4.43 can be redrawn to express either the relationship between Young's Modulus and relative density (as shown in Figure 4.44) or the relative Young's modulus as a function of relative density, as in Figure 4.45.

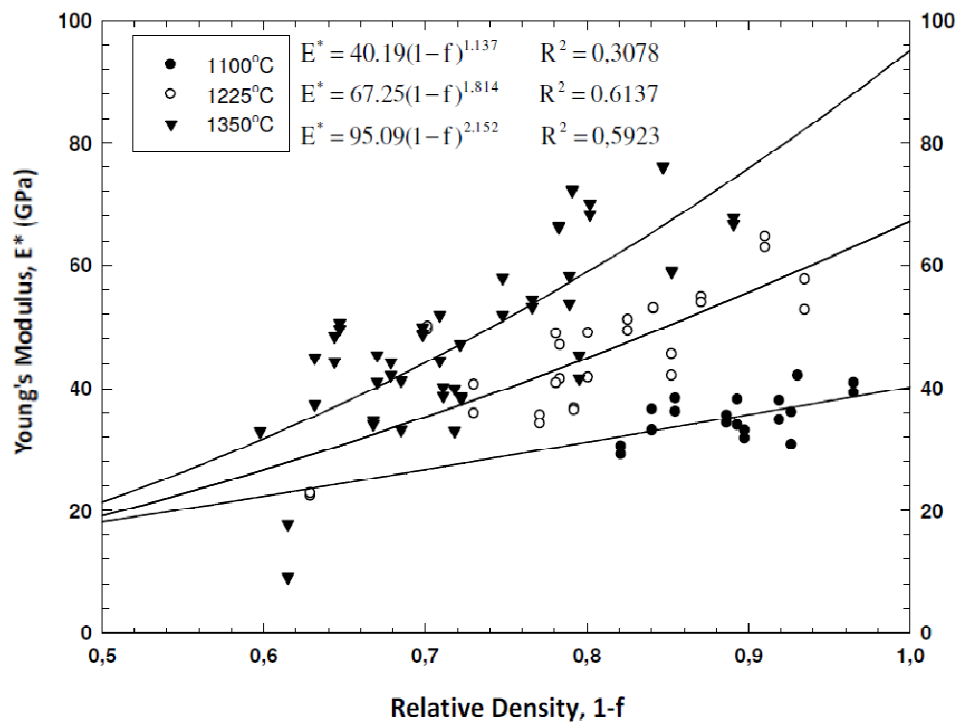


**Figure 4.44** : Influence of relative density on Young's modulus of foamed samples at 1350°C, 1225°C and 1100°C. R<sup>2</sup> is coefficient of determination.

Figure 4.44 shows the generation of theoretical curves of the porous alloys foamed at 1100 °C, 1225 °C and 1350°C. Commonly, the value of the proportionality constant

( $C_1$ ) in Equation 2.2 for a rigid polymer, metal or glass is 1. Thus the models can be written as follows:

$$E^* = 40.19 (1-f)^{1.137} \quad \text{Equation 4.2}$$

$$E^* = 67.25 (1-f)^{1.814} \quad \text{Equation 4.3}$$

$$E^* = 95.09 (1-f)^{2.152} \quad \text{Equation 4.4}$$

From the generated models, the elastic moduli of the fully dense alloys foamed at the specified temperatures can be estimated, giving values of 40.19, 67.25 and 95.09 GPa, respectively. As expected, due to microstructural variations, the estimated Young's moduli of fully dense titanium alloys were found to be in the range of 33–117 GPa (based on the elastic modulus of  $\beta$  alloy, 33 GPa [228] and  $\alpha$  alloy, 117 GPa [412]).

The relationship between the relative Young's modulus and the relative density of the porous titanium alloys is presented on a log-log axis in Figure 4.45.

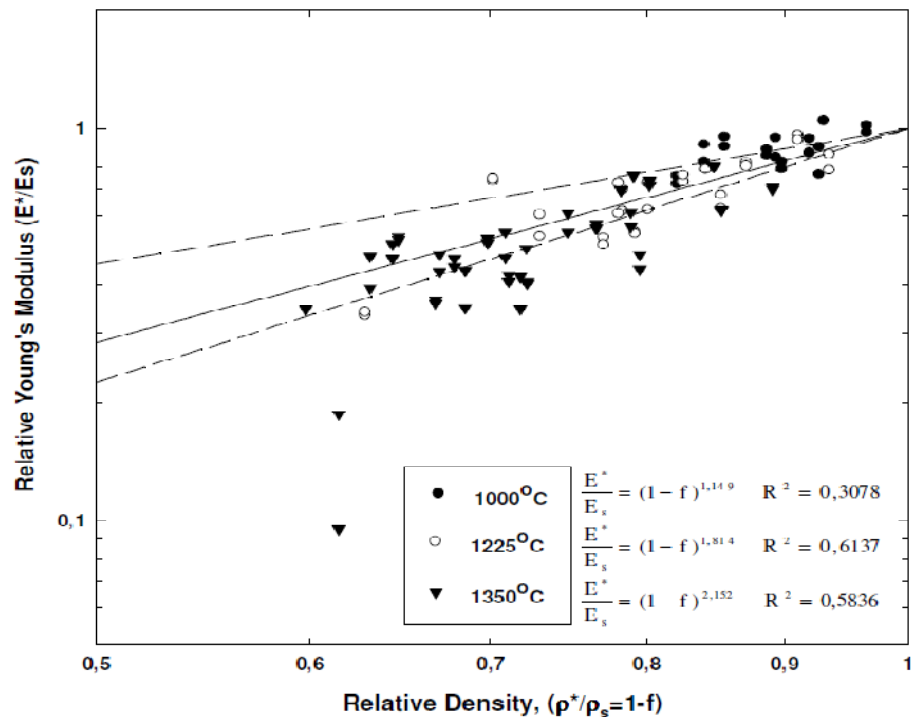


**Figure 4.45** : Plot of relative Young's modulus versus relative density of foamed samples at 1350°C, 1225°C and 1100°C

This figure shows the slopes of the straight lines connecting the data points of the porous materials with the corresponding fully dense materials, corresponding to the scaling exponent  $n$  and being regarded as a measure of the reduction of the elastic modulus [382]. This exponent reflects the foam parameters such as pore morphology and shape and arrangement of the pore walls [46]. Whilst the scaling exponents  $n$  of the specimens foamed at 1225°C and 1350°C were found to be 1.814 and 2.192 respectively, they were still in the range of 1.8-2.2 as indicated in the literature [319] with values of coefficient of determination (0.6137 and 0.5836). An  $n$  value of 1.149 was found for samples foamed at 1100°C, indicating that an alteration in the relative density of the samples foamed at 1100°C resulted in only a slight change in the relative elastic modulus compared to that of the samples foamed at 1225 °C and 1350°C. Besides the sensitivity of the elastic modulus to the microstructural parameters in which the samples contained predominantly  $\beta$  phase, the lower pore fraction and the fewer data available compared to those of samples foamed at 1225°C and 1350°C was attributed to the low  $n$  value attained. In this regards a further study for samples foamed at 1100°C is required.

All of the foamed samples exhibited a similar tendency in that the elastic modulus increased with increasing relative density; the porous alloys foamed at 1100°C showed the lowest values of elastic modulus, with a general increase in modulus as the foaming temperature increased. The generally low values of stiffness in the samples foamed at 1100°C was attributed to the increased presence of  $\beta$  phase, which is known to possess the lowest elastic modulus of the three phases, *i.e.*,  $\beta$ ,  $\alpha$  and  $\omega$  [25]. As mentioned earlier, an increase in the foaming temperature increased the proportion of  $\alpha$  phase, thus leading to an increase in the elastic modulus. Thus the mechanical property evaluation was confirmed by the XRD and the microstructural analysis.

The elastic moduli of the three sets of porous alloys, containing pore volume fractions in the range 3.5-40.2 vol%, were observed to vary between 9.1-76.2 GPa, thereby illustrating that a wide range of porosities and stiffnesses in  $\beta$  stabilised titanium can be achieved from elemental starting powders. The typical range of elastic modulus for natural bone was noted to vary between 10-40 GPa [2] and

therefore, the elastic modulus of the porous titanium alloys developed in the present investigation (9-76.2 GPa) is comparable with the reported elastic modulus for natural bone.

Whilst the data points followed the general trends in the theory predicted from Equation 4.1, a significant amount of scatter was present within each foaming condition. This scatter was attributed to the presence of imperfections in the porous alloys such as irregular pore shapes, non uniform pore sizes, and random pore size and shape distributions [46], whereas the theory applicable to Equation 4.1 is based on an idealised microstructure, *e.g.* uniform cellular or pore shapes arranged in a cubic array.

The yield strengths of the porous alloys determined by a strain offset of 0.002 of the curves as a function of relative density are presented in Figure 4.46. The figure shows similar trend to that of the elastic modulus, *i.e.* the yield strength increased with an increase in relative density whereas an increase in foaming temperature resulted in an increase in the yield strengths.

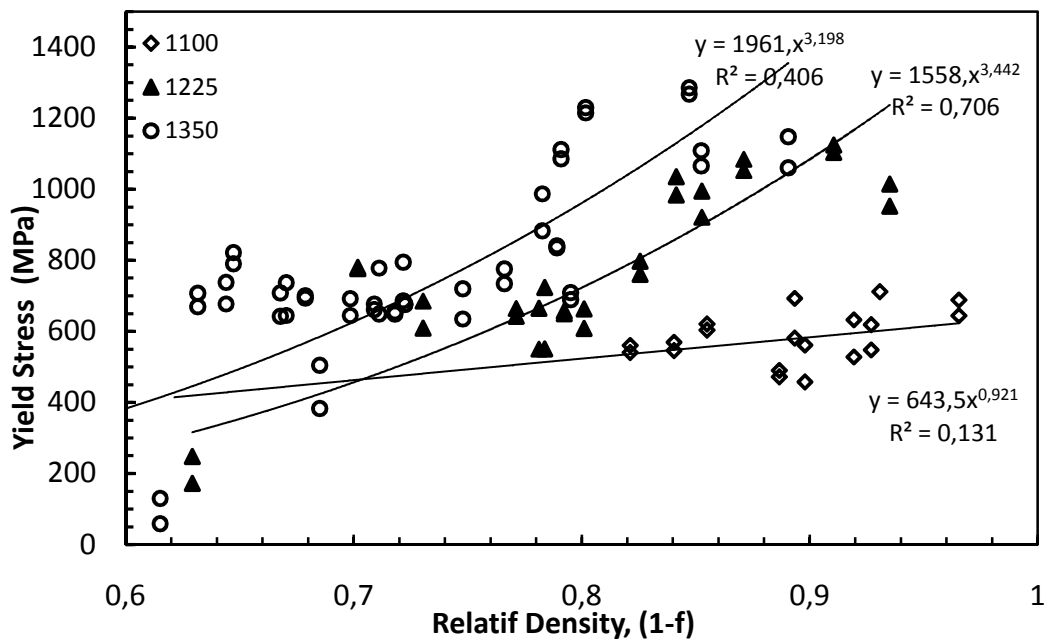


**Figure 4.46 :** Plot of yield strength versus relative density of samples foamed at 1350°C, 1225°C and 1100°C.

The yield strength of the porous titanium alloy foamed at 1100°C, 1225°C and 1350°C was found to vary from 477 to 713 MPa, from 172 to 1124 MPa, and from 58.67 to 1290 MPa, respectively, depending upon the degrees porosity. The increase in yield stress may be attributed to the amount of  $\alpha$  phase present which was, during furnace cooling to room temperature, observed to increase with the increase in foaming temperature. The maximum value of the yield strength of the porous titanium alloy (porosity level of 15.3%; the sample foamed at 1350°C) was comparable to that of  $\beta$  Ti-Mo alloys developed by Delvat *et al.* [410]. The Ti-Mo alloys were fabricated using sintering of elemental powders at 1350°C for 2 hours with their compressive elastic limit observed at approximately 1100-1300 MPa, at porosity level of 5-10%. However, the deformation model was found to be different. Whilst the  $\beta$  Ti-Mo alloy showed high ductility deformation due to the presence of  $\beta$  phase, in the present study, failures were observed to occur by shear in planes diagonal to the loading axis which may be caused by the presence of brittleness and  $\alpha$  phase within the porous Ti-Nb-Ta-Zr alloy. Within the same range of porosity level, whilst the failure strains of the porous titanium alloy were found to be considerably lower in comparison with those of other methods such as the powder compact technique [35, 47], and the space holder techniques [54, 349], the yield strengths were found to be relatively higher. In addition, the majority of the porous titanium alloys with porosity levels higher than 20% showed a higher yield strength in comparison with that of cortical bone (104-121 MPa [413]); therefore, possibly able to satisfy the strength requirement for the cortical bone replacement. Since the titanium alloy containing such composition is known to be heat treatable to obtain different microstructures [304], the lower failure strain could be further optimised by controlling the microstructure development through heat treatment.

## 4.5 Summary

Porous titanium alloys containing  $\beta$  stabilising elements, *i.e.* niobium, tantalum and zirconium have been fabricated by employing a powder metallurgy process based on an argon gas pressurised pore expansion method using elemental powders as starting materials, and subsequently tested and analysed. This fabrication procedure involved;

powder mixing, pressurised gas infusions, densification using HIP-ing and pore expansion at elevated temperatures. A nominal composition of the  $\beta$  titanium alloy, *i.e.* Ti-29Nb-13Ta-4.6Zr was used in this study. Following fabrication, the specimens were subjected to phase identification and microstructural and pore size examination as well as compressive testing for mechanical properties evaluation.

The HIP-ing procedure was carried out at 1100°C for 4 hours in order to promote increased alloying due to the high melting temperature of the  $\beta$  stabilising elements. After the HIP-ing, the grain boundaries of the particles have been shown to be diffused but the dissolution of the particles was still incomplete, especially in the case of tantalum. Whilst the stabilisation of homogenous  $\beta$  areas was observed in the area with a large amount of dissolved niobium, a two-phase structure ( $\alpha+\beta$ ) was also observed. Phase identification revealed the presence of predominantly  $\beta$  phase which indicating a portion of the titanium alloy to have allotropically transformed from  $\alpha$  phase to  $\beta$  phase. The presence of the applied stress during the HIP-ing and a higher content of niobium which acts as  $\beta$  phase nucleating agent may stabilise  $\beta$  phase during furnace cooling. The initial porosities in the HIP-ed alloys were estimated to be <5%. The initial porosity which was attributed to incomplete dissolution between the elemental powders showed the tendency to increase with the increase of argon backfill pressure. In most cases, the pore size diameters were predominantly found in the range of 4.5-6  $\mu\text{m}$ .

The microstructure of the specimens foamed at 1100°C showed evidence of alloying through particle dissolution. The tantalum and niobium particles became diffused and indistinguishable. Microstructural and a chemical inhomogeneities were apparent as a prominent light area representing  $\beta$  phase, with higher composition of  $\beta$  stabilising elements (*i.e.* niobium, tantalum, zirconium), and a smaller dark area representing  $\alpha$  phase with higher composition of titanium were also observed. The porosity level of the specimens foamed at 1100°C/0.86 MPa was approximately 17.3%. The pore morphology of the samples was found to be very discrete with typical pore sizes in the range of 3-75  $\mu\text{m}$ . The development of  $\alpha$  phase could be observed at the higher foaming temperature (1225°C) indicated by the dark area which became larger. The pore morphology still remained discrete with slight coalescence of pores being

observed and pore size of typically 7.5-189 $\mu\text{m}$  on the specimen with the maximum porosity level (37.1 vol %). The  $\alpha$  phase was found to increase by forming  $\alpha$  platelets within  $\beta$  phase matrix when the foaming temperature was increased to 1350 $^{\circ}\text{C}$ . At this temperature, creep deformation of the material increased allowing the pores to grow considerably larger with the porosity level reaching 40.2% and pores sizes of typically 8–200  $\mu\text{m}$ . Many pores that had coalesced sometimes became interconnected due to rupturing pore walls. It was also found that the majority of porous titanium alloy samples with a higher initial porosity exhibited a higher foaming rate.

The OCP measurements indicated that specimens foamed at 1100 $^{\circ}\text{C}$  were more noble compared to specimens foamed at the other two temperatures, and the passive film formation was continuing during one hour measurement. Steady state potentials were not reached but the corrosion potentials steadily increased in a diminishing trend. Potentiodynamic polarisation measurements showed similar tendency in that the specimen foamed at 1100 $^{\circ}\text{C}$  possessed a higher pitting and crevice corrosion resistance. Those values are comparable to those of Ti-6Al-4V or CP Ti.

Hardness values of the specimens increased with increasing of foaming temperature of 1100 $^{\circ}\text{C}$ , 1225 $^{\circ}\text{C}$  and 1350 $^{\circ}\text{C}$  with the values of 340 HV, 414HV and 470 HV respectively, due to the development of  $\alpha$  phase at the higher foaming temperatures. A restricted development of  $\alpha$  phase at lower foaming temperatures narrowed the scatter of the hardness values. The compressive stress-strain curves of the samples foamed at 1100 $^{\circ}$ , 1225 $^{\circ}$  and 1350 $^{\circ}\text{C}$  showed clear differences in stress-strain behaviour. The typical stress-strain curves for specimens foamed at 1100 $^{\circ}\text{C}$  demonstrated a high ductility in compression indicated by their ability to be deformed (up to 50%) without collapse. The ductility may be due to the presence of the prominent  $\beta$  phase. Whilst the stress-strain curves of the specimens foamed at 1225 $^{\circ}\text{C}$  showed a typical pattern for ductile porous materials, specimens foamed at 1350 $^{\circ}\text{C}$  showed behaviour typical of brittle failure which may due to the increase of  $\alpha$  phase and the brittleness which is linked to the existence of oxygen in the porous metal. All the foamed specimens demonstrated a similar trend in which Young's modulus decreased with the increase of porosity. The elastic moduli of the porous

titanium alloys foamed at 1100°C were found to be the lowest values with a general increase in modulus when the foaming temperature increased to 1225°C and further to 1350°C. Whilst the Young's modulus of the three sets of fabricated porous alloys containing pore volume fractions in the range of 3.5-40.2 vol% were found to vary between 9.1-76.2 GPa, the yield strengths varied between 477-713 MPa and 172-1124 MPa and 58.67–1290 MPa, respectively, with respect to the pore volume fractions. Considering the results, a wide range of porosities, stiffnesses and strengths in  $\beta$  stabilised titanium can thus be achieved from elemental starting powder. The magnitude of the measured elastic modulus can be estimated by the model developed by Wanner derived from the Gibson-Ashby model in which the relationship between relative Young's modulus and relative density is determined by the scaling exponent,  $n$ . This parameter,  $n$ , was found to increase with the increase of foaming temperature ( $n$ : 1.137, 1.814 and 2.152 respectively).

In addition, electron microscopy confirmed that the three sets of porous alloy specimens exhibited remarkable differences in failure mode. A high degree deformation of the metal matrix was observed on specimens foamed at 1100°C indicating the existence of a very ductile failure mode. Specimens foamed at 1225°C showed a ductile fracture mode composed of dimples on the separated inter-pore walls, whereas the fracture surface of specimens foamed at 1350°C resembled a more faceted mode of failure. Overall, it is clear that pore volume fraction and microstructures may play a dominant role in determining the mechanical properties of the porous titanium alloys. It should be noted that the range of elastic moduli, pore size and pore volume fraction exhibited in this study for the fabrication of porous titanium alloys included the typical range of values noted for materials for use in biomedical applications. Therefore, this porous titanium alloy is expected to be a promising candidate for low stiffness biocompatible implant materials.

# Chapter 5

## Conclusions and Recommendations

### 5.1 Conclusions

Porous titanium alloy samples containing  $\beta$  stabilising elements with low toxicity, *i.e.* niobium, tantalum and zirconium developed using a powder metallurgy technique incorporating elemental powders as starting materials, and based on the pressurised pore expansion argon gas technique have been fabricated and subsequently examined for phase composition, microstructure and mechanical properties. The following points summarise and conclude this study.

The HIP-ing of blended elemental powders carried out at 1100°C/100MPa/4 hours resulted in titanium alloy billets possessing the following characteristics:

- $\beta$  phase was predominantly identified.
- Three distinct areas were observed, *i.e.*; incomplete dissolution areas mainly relating to tantalum particles; the two-phase structure areas - those containing titanium and niobium; and homogenous  $\beta$  areas with a large amount of dissolved niobium being detected
- The mean values of initial porosity were at less than 5%. The initial porosity showed a tendency to increase with the increase of argon backfill pressure.

The fabricated porous titanium alloy foamed at 1100°, 1225° and 1350°C with various argon backfill pressures (0.34, 0.49, 0.68 and 0.86 MPa) achieved porosity levels in the range of 3.5–17.9 %, 6.5-37.1 %, and 14.8-40.2 %, respectively. Pore size distribution analysis of the three sets of foamed alloys showed that the highest pore area fraction was attained by pore sizes in the range of 18.2-110.8  $\mu\text{m}$ , while pore sizes of up to approximately 200  $\mu\text{m}$  were achieved. Each group of the fabricated porous titanium alloys exhibited a similar trend where the porosity level increased with increased argon backfill pressure.

Microstructures of the porous titanium alloys foamed at 1100°C exhibited the presence of a prominent  $\beta$  phase with a small amount of  $\alpha$  phase. The development of  $\alpha$  phase could be observed when the foaming temperature was increased to 1225°C and further to 1350°C indicated by the appearances of larger darker areas (representing  $\alpha$  phase) and a platelets within the  $\beta$  phase matrix (represented by grey areas), respectively.

Electrochemical corrosion measurements showed that specimens foamed at 1100°C were more noble compared to specimens foamed at the other two temperatures. To reiterate, in the OCP testing, steady state potentials were not reached but the corrosion potentials steadily increased in a diminishing trend. Potentiodynamic polarisation measurements showed similar tendency in that the specimen foamed at 1100°C possessed a higher pitting and crevice corrosion resistance.

Hardness values of the specimens were shown to increase with increasing foaming temperature of 1100°C, 1225°C and 1350°C with the values of 340 HV, 414HV and 470 HV respectively, due to the development of  $\alpha$  phase at the higher foaming temperatures. A restricted development of  $\alpha$  phase at lower foaming temperature narrowed the scatter of hardness values.

A general trend being noted is that all of the porous titanium alloys demonstrated a decrease in both the elastic modulus and yield strength with increase of pore volume fraction. The porous titanium alloys foamed at 1100°C exhibited the lowest values of elastic modulus and yield strength (29-41.9 GPa and 477-713 MPa, respectively) with a general increase in modulus as the foaming temperature increased to 1225°C (22.3-65,7 GPa and 172-1124 MPa, respectively) and 1350°C (9.1-76.2 GPa and 58.7–1290 MPa, respectively). The magnitude of the measured elastic modulus can be estimated by Wanner's model derived from the Gibson-Ashby model in which the scaling exponent,  $n$ , was found to increase with the increase in foaming temperature ( $n$ : 1.137, 1.814 and 2.152 respectively). The failure modes of the three sets of porous alloys were found to be clearly different. Porous titanium alloys foamed at 1100°C indicated a very ductile failure mode. Whilst a ductile fracture mode, demonstrated by the presence of dimples on the separated interpore surfaces, was

found in the porous titanium foamed at 1225°C, the fracture surface of the porous alloys foamed at 1350°C resembled a more faceted mode of failure indicating a brittle failure mode.

Considering that the current results, in terms of the microstructure, porosity levels and pore size, and the mechanical properties of the porous titanium alloy containing low toxicity elements, has included the typical range of values noticed for materials used in biomedical applications, this porous titanium alloy thus is expected to be a promising candidate for low stiffness biocompatible implant materials.

## **5.2 Recommendations for future work**

Based on the outcomes of this study, future work is necessary. The obvious focus should be on the improvement of the mechanical properties performance, but investigations into other performance and fabrication aspects should be carried out as well.

### **1. Fabrication process variations**

The ability in varying the argon backfill pressure and foaming temperature during the foaming procedure combined with variations in either powder size or powder shape to affect porosity and other characteristics should be studied. Care should be taken during the argon backfilling and sealing process, as this stage is a critical process since the pressurised pore gas expansion is a key aspect and a driving force for the foaming process. Through a study of this type, a superior combination may be revealed which results in higher porosity or better mechanical performance or both. For example, an optimum combination of powder size and argon backfill pressure for foaming at a certain temperature may increase the porosity and the strength of the porous titanium alloys incorporating an optimisation of the elastic modulus. The study of near, but varied, compositions of the  $\beta$  titanium alloys, should be considered in order to further optimise the achievable elastic modulus values in relation to natural bone.

2. Mechanical properties evaluation

Further mechanical property tests can be undertaken, *e.g.* incorporating parameter variations, such as strain rate and/or specimen size. The interest in strain rate dependent properties of the porous titanium alloys for biomedical applications purposes simply arises from the fact that the mechanical properties of bone are known to be strain rate sensitive [414].

3. Biocompatible performance

*In vitro* assessment, for instance by soaking the porous alloy into simulated body fluid, would help to ascertain the effect of porosity on the bioactivity of the porous titanium alloys, since titanium and its alloys are bioinert materials which commonly exhibit low bioactivity.

## References

- 1 **Lidgren, L.** The Bone and Joint Decade 2000 -2010. *Bulletin of the World Health Organization*, 2003, **81**, 629-629.
- 2 **Conaghan, P.G. and Brooks, P.** How to manage musculoskeletal conditions. *Best Practice & Research Clinical Rheumatology*, 2008, **22**(3), 387-394.
- 3 **Australian Bureau of Statistics**, Musculoskeletal Conditions in Australia: A Snapshot, 2004-05, Catalog no. 4823.0.55.001, Canberra, <http://www.abs.gov.au/ausstats/abs@.nsf/mf/4823.0.55.001>, Access date: 15-01-2011. 2006.
- 4 **AIHW.** (Australian Institute of Health and Welfare), Australia's Health 2008: The eleventh biennial health report of the Australian Institute of Health and Welfare, Canberra 2008, Cat. no. AUS 99.
- 5 **Niinomi, M.** Metallic biomaterials. *Journal of Artificial Organs*, 2008, **11**(3), 105-110.
- 6 **Bai, Z. and Gilbert, e.L.** Corrosion performance of stainless steels, cobalt, and titanium alloys in biomedical applications. In Cramer, S.D. and B.S. Covino, J., eds. *ASM Handbook, Corrosion: Environments and Industries*, pp. 837-853 (ASM International, 2006).
- 7 **Gotoh, E. and Okazaki, Y.** Corrosion resistance, mechanical properties, fatigue properties, and tissue response of Ti-15Zr-4Nb-4Ta alloy. *Journal of ASTM International*, 2006, **2**(9), 15.
- 8 **Long, M. and Rack, H.J.** Titanium alloys in total joint replacement-a materials science perspective. *Biomaterials*, 1998, **19**, 1621-1639.
- 9 **Wang, K.** The use of titanium for medical applications in the USA. *Materials Science and Engineering A*, 1996, **213**(1-2), 134-137.
- 10 **Hildebrand, H.F., Veron, C. and Martin, P.** Nickel, chromium, cobalt dental alloys and allergic reactions: an overview. *Biomaterials*, 1989, **10**(8), 545-548.
- 11 **Hallab, N.J., Anderson, S., Caicedo, M., Brasher, A., Mikecz, K. and Jacobs, J.J.** Effects of soluble metals on human peri-implant cells. *Journal of Biomedical Materials Research Part A*, 2005, **74**(1), 124-140.
- 12 **Gummow, B.** Vanadium: Environmental Pollution and Health Effects. In Editor-in-Chief: Jerome, O.N., ed. *Encyclopaedia of Environmental Health*, pp. 628-636 (Elsevier, Burlington, 2011).

- 13 **Silva, H.M., Schneider, S.G. and Neto, C.M.** Study non toxic aluminium and vanadium-free titanium alloys for biomedical applications. *Materials science and Engineering C*, 2004, **24**(5), 679-682.
- 14 **Matsuno, H., Yokoyama, A., Watari, F., Uo, M. and Kawasaki, T.** Biocompatibility and osteogenesis of refractory metal implants, titanium, hafnium, niobium, tantalum and rhenium. *Biomaterials*, 2001, **22**(11), 1253-1262.
- 15 **Eisenbarth, E., Velten, D., Muller, M., Thull, R. and Breme, J.** Biocompatible of  $\beta$ -stabilising elements of titanium alloys. *Biomaterials*, 2004, **25**, 5705-5713.
- 16 **Song, Y., Xu, D., Yang, R., Li, D., Wu, W.T. and Guo, Z.X.** Theoretical study of the effects of alloying elements on the strength and modulus of  $\beta$ -type bio-titanium alloys. *Materials Science and Engineering A*, 1999, **260**, 269-274.
- 17 **Olszta, M.J., Cheng, X., Jee, S.S., Kumar, R., Kim, Y.-Y., Kaufman, M.J., Douglas, E.P. and Gower, L.B.** Bone structure and formation: A new perspective. *Materials Science and Engineering: R: Reports*, 2007, **58**(3), 77-116.
- 18 **Ratner, B.** Presentation highlights: Tissue engineering. *Journal of Rehabilitation Research and Development*, 2002, **39**(3), 2.
- 19 **Stojanovic, D., Jokic, B., Veljovic, D., Petrovic, R., Uskokovic, P.S. and Janackovic, D.** Bioactive glass-apatite composite coating for titanium implant synthesized by electrophoretic deposition. *Journal of the European Ceramic Society*, 2007, **27**(2-3), 1595-1599.
- 20 **Lincks, J., Boyan, B.D., Blanchard, C.R., Lohmann, C.H., Liu, Y., Cochran, D.L., Dean, D.D. and Schwartz, Z.** Response of MG63 osteoblast-like cells to titanium and titanium alloy is dependent on surface roughness and composition. *Biomaterials*, 1998, **19**(23), 2219-2232.
- 21 **Yang, S., Leong, K.F., Du, Z. and Chua, C.K.** The design of scaffolds for use in tissue engineering. Part I. Traditional factors. *Tissue Engineering*, 2001, **7**(6), 679-689.
- 22 **Thieme, M., Wieters, K., Bergner, F., Scharnweber, D., Worch, H., Ndop, J., Kim, T. and Grill, W.** Titanium powder sintering for preparation of a porous functionally graded material destined for orthopaedic implants. *Journal of Materials Science: Materials in Medicine*, 2001, **12**(3), 225-231.
- 23 **Rouwkema, J., Rivron, N.C. and van Blitterswijk, C.A.** Vascularisation in tissue engineering. *Trends in Biotechnology*, 2008, **26**(8), 434-441.
- 24 **Murphy, C.M., Haugh, M.G. and O'Brien, F.J.** The effect of mean pore size on cell attachment, proliferation and migration in collagen-glycosaminoglycan scaffolds for bone tissue engineering. *Biomaterials*, 2010, **31**(3), 461-466.

- 25 **Hulbert, S., Young, F., Mathews, R., Klawiter, J., Takbert, C. and Stelling, F.** Potential of ceramic materials as permanently implantable skeletal prostheses. *Journal of Biomedical Materials Research*, 1970, **4**, 433-456.
- 26 **Spector, M., Flemming, W.R., Kreutner, A. and Sauer, B.W.** Bone growth into porous high-density polyethylene. *Journal of Biomedical Materials Research*, 1976, **10**(4), 595-603.
- 27 **Nilles, J.L., M., C.J. and Wilson, C.** Biomechanical evaluation of bone-porous material interfaces. *Journal of Biomedical Materials Research*, 1973, **7**, 231.
- 28 **Welsh, R.P., Pilliar, R.M. and Macnab, I.** Surgical implants-the role of surface porosity in fixation to bone and acrylic. *Journal of bone & Joint surgery*, 1971, **53A**.
- 29 **Cameron, H.U., Pilliar, R.M. and Macnab, I.** The rate of bone ingrowth into porous metal. *Journal of Biomedical Materials Research*, 1976, **10**.
- 30 **Itala, A.I., Ylanen, H.O., Ekholm, C., Karlsson, K.H. and Aro, H.T.** Pore diameter of more than 100 micrometer is not requisite for bone ingrowth in rabbits. *Journal of Biomedical Materials Research*, 2001, **58**, 679-683.
- 31 **Bobyn, J.D., Cameron, H. and Weatherly, G.** The optimum pore size for the fixation of porous surfaced metal implant by ingrowth of bone. *Clin Orthop*, 1980, **150**, 263-270.
- 32 **Ayers, R.A., Simske, S.J., Bateman, T.A., Petkus, A., Sachdeva, R.L.C. and Gyunter, V.E.** Effect of nitinol implant porosity on cranial bone ingrowth and apposition after 6 weeks. *Journal of Biomedical Materials Research*, 1999, **45**(1), 42-47.
- 33 **Bobyn, J.D. and Miller, J.E.** Features of biologically fixed devices. In Simon, S., ed. *Orthopaedic Basic Science*. Chicago: American Academy of Orthopaedic Surgeons (1994).
- 34 **Frosch, K.H., Barvencik, F., Dresing, K., Lohmann, C.H., Viereck, V., Siggelkow, H., Breme, J. and Stuermer, K.M.** Migration, matrix production & lamellar bone formation of human osteoblast-like cell in porous Ti implants. *Cells Tissues Organs*, 2002, **170**, 214-227.
- 35 **Oh, I.H., Nomura, N., Masahashi, N. and Hanada, S.** Mechanical properties of porous titanium compacts prepared by powder sintering. *Scripta Materialia*, 2003, **49**, 1197-1202.
- 36 **Banerjee, R., Nag, S., Stechschulte, J. and Fraser, H.L.** Strengthening mechanism in Ti-Nb-Zr-Ta and Ti-Mo-Zr-Fe orthopaedic alloys. *Biomaterials*, 2004, **25**, 3413-3419.

- 37 **Li, S.J., Yang, R., Li, S., Hao, Y.L., Cui, Y.Y., Niinomi, M. and Guo, Z.X.** Wear characteristics of Ti-Nb-Ta-Zr and Ti-6Al-4V alloys for biomedical application. *Wear*, 2004, **257**, 869-876.
- 38 **Li, S.J., Yang, R., Niinomi, M., Hao, Y.L. and Cui, Y.Y.** Formation and growth of calcium phosphate on the surface of oxidised Ti-29Nb-13Ta-4.6Zr alloy. *Biomaterials*, 2004, **25**(13), 2525-2532.
- 39 **Niinomi, M.** Fatigue performance and cyto-toxicity of low titanium alloys, Ti-29Nb-13Ta-4.6Zr. *Biomaterials*, 2003, **24**, 2673-2683.
- 40 **Niinomi, M., Kuroda, D., Fukunaga, K., Morinaga, M., Kato, Y., Yashiro, T. and Suzuki, A.** Corrosion wear fracture of new  $\beta$  type biomedical titanium alloys. *Materials Science and Engineering A*, 1999, **263**(2), 193-199.
- 41 **Okazaki, Y., Nishimura, E., Nakada, H. and Kobayashi, K.** Surface analysis of Ti-15Zr-4Nb-4Ta alloy after implantation in rabbit tibia. *Biomaterials*, 2001, **22**, 599-607.
- 42 **Okazaki, Y. and Ito, Y.** New Ti-alloy without Al and V for medical implants. *Advanced Engineering Materials*, 2000, **2**(5), 278-281.
- 43 **Okazaki, Y. and Gotoh, E.** Comparison of metal release from various metallic biomaterials in vitro. *Biomaterials*, 2005, **26**(1), 11-21.
- 44 **Qazi, J.I. and Rack, H.J.** Metastable beta titanium alloys for orthopaedic applications. *Advanced Engineering Materials*, 2005, **7**(11), 993-998.
- 45 **Wen, C.E., Yamada, Y., Shimojima, K., Chino, Y., Asahina, T. and Mabuchi, M.** Processing of biocompatible porous Ti and Mg. *Scripta Materialia*, 2001, **45**, 1147-1153.
- 46 **Esen, Z. and Bor, S.** Processing of titanium foams using magnesium spacer particles. *Scripta Materialia*, 2007, **56**(5), 341-344.
- 47 **Güden, M., Çelik, E. and Inöç, A.** Effects of compaction pressure and particle shape on the porosity and compression mechanical properties of sintered Ti6Al4V powder compacts for hard tissue implantation. *Journal of Biomedical Materials Research Part B: Applied Biomaterials*, 2007, **85**(2), 547-555.
- 48 **Jorgensen, D.J. and Dunand, D.C.** Ti-6Al-4V with micro- and macropores produced by powder sintering and electrochemical dissolution of steel wires. *Materials Science and Engineering: A*, 2010, **527**(3), 849-853.
- 49 **Murray, N. and Dunand, D.** Effect of initial preform porosity on solid-state foaming of titanium. *Journal of Materials Research*, 2006, **21**(5), 1175-1188.
- 50 **Oppenheimer, S.** Processing and characterisation of porous Ti-6Al-4V and NiTi *Materials Science and Engineering*, p. 170 (Northwestern University, Illinois, 2007).

- 51 **Queheillalt, D.T., Sypeck, D.J. and Wadley, H.N.G.** Ultrasonic characterisation of cellular metal structures. *Materials Science and Engineering A*, 2002, **323**(1-2), 138-147.
- 52 **Jee, C.S.Y., Ozguven, N., Guo, Z.X. and Evans, J.R.G.** Preparation of high porosity metal foam. *Metallurgical Materials Transactions*, 2000, **31B**, 1345-1352.
- 53 **Guo, Z.X., Jee, C.S.Y., Ozguven, N. and Evans, J.R.G.** Novel polymer-metal based method for open cell metal foam production. *Material Science and Technology*, 2000, **16**, 776-780.
- 54 **Bram, M., Stiller, C., Buchkremer, H.P., Stover, D. and Baur, H.** High-porosity titanium, stainless steel, and superalloy parts. *Advanced Engineering Materials*, 2000, **2**(4), 196-199.
- 55 **Wen, C.E., Yamada, Y., Shimojima, K., Chino, Y., Asahina, T. and Mabuchi, M.** Processing and mechanical properties of autogenous titanium implant materials. *Journal of Material Science: Materials in Medicine*, 2002, **13**, 397-401.
- 56 **Li, J.P., Li, S.H., De Groot, K. and Layrolle, P.** Preparation and characterisation of porous titanium. *Key Engineering Materials*, 2001, **218-220**, 51-54.
- 57 **Kearns, M.W., Blenkinsop, P.A., Barber, A.C. and Farthing, T.W.** Manufacture of a novel porous materials. *Metals and Materials (Institute of Metals)*, 1987, **3**(2), 85-88.
- 58 **Davies, N.G., Teisen, J., Schuh, C. and Dunand, D.C.** Solid state foaming of Ti by superplastic expansion of argon-filled pores. *J. Mater. Res*, 2001, **16**(5), 1508-1519.
- 59 **Ashworth, M.A., Jacobs, M.H., Unwin, P. and Blunn, G.** The development and characterisation of porous Ti-6Al-4V manufactured by hot isostatic pressing for orthopaedic applications. *Proceedings of 7th World Biomaterials Congress-2004*, pp. 1394, May, 17-24 2004, Sydney, Australia, 2004).
- 60 **William, D.F.** Concensus and definition in biomaterials. In de Putter, C., de Lang, K., de Groot, K. and Lee, A.J.C., eds. *Advances in Biomaterials*, pp. 11-16 (Elsevier Science, Amsterdam, 1988).
- 61 **Black, J.** *Biological performance of materials: Fundamentals of biocompatibility*. (Marcel Dekker, New York, 2006).
- 62 **Hin, T.S.** Introduction to biomaterials engineering and processing -an overview. In Teoh, S.H., ed. *Engineering Materials for Biomedical Applications*, pp. 1-16 (World Scientific Publishing Co. Pte.Ltd, Toh Tuck Link, Singapore, 2004).

- 63 **Meyers, M.A., Chen, P.-Y., Lin, A.Y.-M. and Seki, Y.** Biological materials: structure and mechanical properties. *Progress in Materials Science*, 2008, **53**(1), 1-206.
- 64 **Ramakrishna, S., Mayer, J., Wintermantel, E. and Leong, K.W.** Biomedical applications of polymer-composite materials: A review. *Composites Science and Technology*, 2001, **61**(9), 1189-1224.
- 65 **Williams, D.F.** *Definitions in biomaterials*. (Elsevier Amsterdam, 1987).
- 66 **Peters, K., Unger, R.E. and Kirkpatrick, C.J.** Biocompatibility testing. In Narayan, R., ed. *Biomedical materials*, pp. 261-290 (Springer Science+Business Media New York, 2009).
- 67 **Binyamin, G., Shafi, B.M. and Mery, C.M.** Biomaterials: A primer for surgeons. *Seminars in Paediatric Surgery*, 2006, **15**(4), 276-283.
- 68 **Katti, K.S.** Biomaterials in total joint replacement. *Colloids and Surfaces B: Biointerfaces*, 2004, **39**(3), 133-142.
- 69 **Geetha, M., Singh, A.K., Asokamani, R. and Gogia, A.K.** Ti based biomaterials, the ultimate choice for orthopaedic implants - A review. *Progress in Materials Science*, 2009, **54**(3), 397-425.
- 70 **Ratner, B.D.** Biomaterials Science : An Interdisciplinary Endeavor. In Ratner, B.D., Hoffman, A.S., Schoen, F.J. and Lemons, J.E., eds. *Biomaterials Science: An Introduction to Materials in Medicine* (Academic Press, San Diego, USA, 1997).
- 71 **Kusy., R.P.** Orthodontic biomaterials: from the past to the present. *Angle Orthodontist*, 2002, **72**(6), 501.
- 72 **Alan, J.T.** Pare and prosthetics : The early history of artificial limbs. *ANZ Journal of Surgery*, 2007, **77**(12), 1114-1119.
- 73 **Sumita, M. and Teoh, S.H.** Durability of Metallic Implant Materials. In Teoh, S.H., ed. *Engineering Materials for Biomedical Applications* (World Scientific Publishing Co, Pte. Ltd, Toh Tuck Link, Singapura, 2004).
- 74 **Niinomi, M.** Recent research and development in titanium alloys for biomedical applications and healthcare goods. *Science and Technology of Advanced Materials*, 2003, **4**, 445–454.
- 75 **Navarro, M., Michiardi, A., Castano, O. and Planell, J.A.** Biomaterials in orthopaedics. *Journal of the Royal Society Interface*, 2008, **5**(27), 1137-1158.
- 76 **Hulbert, S.F., Hench, L.L., Forbers, D. and Bowman, L.S.** History of bioceramics. *Ceramics International*, 1982, **8**(4), 131-140.
- 77 **Hench, L.L. and Paschall, H.A.** Direct chemical bond of bioactive glass-ceramic materials to bone and muscle. *Journal of Biomedical Materials Research*, 1973, **7**(3), 25-42.

- 78 **Rickert, D.** Polymeric implant materials for the reconstruction of tracheal and pharyngeal mucosal defects in head and neck surgery. *GMS Current Topics in Otorhinolaryngology - Head and Neck Surgery*, 2009, **8**(6), 22.
- 79 **Rajpurkar, A., Shah, R., Starkman, J. and Dhabuwala, C.B.** Tissue ingrowth in penile implants and its effect on repeat penile surgery. *International Journal of Impotence Reseach*, **16**(2), 203-206.
- 80 **Peppas, N.A. and Langer, R.** New challenges in biomaterials. *Science*, 1994, **263**, 1715-1720.
- 81 **Burke, J.F., Didisheim, P., Goupil, D., Heller, J., Kane, J.B., Katz, J.L., Kim, S.W., Lemons, J.E., Refojo, M.F., Robblee, L.S., Smith, D.C., Sweeney, J.S., Tompkins, R.G., Watson, J.T., Yager, P. and Yarmush, M.L.** Application of Materials in Medicine and Dentistry. In Ratner, B.D., Hoffman, A.S., Schoen, F.J. and Lemons, J.E., eds. *Biomaterials Science : An Introduction to Materials in Medicine* pp. 283-388 (Academic Press, london, UK, 1996).
- 82 Global biomaterials market (2009-2014). 2009, <http://www.reportlinker.com/p0148007/Global-Biomaterial-Market-2009-2014-.html?v=2>, Accessed date : 16 June 2010.
- 83 **Marketandmarkets.com.** Global biomaterial market. (Marketandmarkets.com, September 2009).
- 84 The Bone & Joint Decade 2000-2010 : Annual Report 2009. <http://www.bjdonline.org/HTML/musconline/images/BJD%20Annual%20Report%202009.pdf>(Accessed date : 30 June 2010).
- 85 **Browne, M. and Gregson, P.J.** Effect of mechanical surface pretreatment on metal ion release. *Biomaterials*, 2000, **21**(4), 385-392.
- 86 **Clemow, J.T., Weinstein, A.M., Klawitter, J.J., Koeneman, J. and Anderson, J.** Interface mechanics of porous titanium implants. *Journal of Biomedical Materials Research*, 1981, **15**, 73-82.
- 87 **Elias, C.N., Oshida, Y., Lima, J.H.C. and Muller, C.A.** Relationship between surface properties (roughness, wettability and morphology) of titanium and dental implant removal torque. *Journal of the Mechanical Behaviour of Biomedical Materials*, 2008, **1**(3), 234-242.
- 88 **Eriksson, C., Lausmaa, J. and Nygren, H.** Interactions between human whole blood and modified TiO<sub>2</sub>-surfaces: Influence of surface topography and oxide thickness on leukocyte adhesion and activation. *Biomaterials*, 2001, **22**(14), 1987-1996.
- 89 **Huanlong, L.** Effects of pore morphology and bone ingrowth on mechanical properties of microporous titanium as an orthopaedic implant material. *Materials Transactions*, 2004, **45**(4), 1124-1131.

- 90 **Okazaki, Y., Rao, S., Tateishi, T. and Ito, Y.** Cytocompatibility of various metal and development of new titanium alloys for medical implants. *Materials Science and Engineering A*, 1998, **243**(1-2), 250-256.
- 91 **Xiong, J., Li, Y., Wang, X., Hodgson, P. and Wen, C.** Mechanical properties and bioactive surface modification via alkali-heat treatment of a porous Ti-18Nb-4Sn alloy for biomedical applications. *Acta Biomaterialia*, 2008, **4**(6), 1963-1968.
- 92 **William, D.F.** On the mechanism of biocompatibility. *Biomaterials*, 2008, **29**, 2941-2953.
- 93 **Singh, R. and Dahotre, N.B.** Corrosion degradation and prevention by surface modification of biometallic materials. *Journal of Materials Science: Materials in Medicine*, 2007, **18**(5), 725-751.
- 94 **Savich, V.** Criteria for selecting powder composite materials for orthopaedic implants. *Powder Metallurgy and Metal Ceramics*, 2009, **48**(3), 216-224.
- 95 **Kamitakahara, M., Ohtsuki, C. and Miyazaki, T.** Review paper: Behaviour of ceramic biomaterials derived from tricalcium phosphate in physiological condition. *Journal of Biomaterials Applications*, 2008, **23**(3), 197-212.
- 96 **Barradas, A., Yuan, H., Blitterswijk, C.A. and Habibovic, P.** Osteoinductive biomaterials: current knowledge of properties, experimental models and biological mechanisms. *European Cells & Materials*, 2011, **21**, 407-429.
- 97 **Hench, L.L.** Bioceramics: From concept to clinic. *Journal of the American Ceramic Society*, 1991, **74**(7), 1487-1510.
- 98 **Burke, D.W., Bragdon, C.R., O'Connor, D.O., Jasty, M., Haire, T. and Harris, W.H.** Dynamic measurement of interface mechanics *in vivo* and the effect of micromotion on bone ingrowth into a porous surface device under controlled loads *in vivo*. *Transactions of Orthopaedic Research Society*, 1991, **16**, 103-104.
- 99 **Kasuga, T.** Bioactive calcium pyrophosphate glasses and glass-ceramics. *Acta Biomaterialia*, 2005, **1**(1), 55-64.
- 100 **Kim, H.M., Fujibayashi, S., Nishiguchi, S. and Nakamura, T.** Bioactive macroporous titanium surface layer on titanium substrate. *Journal of Biomedical Materials Research*, 2000, **52**, 553-557.
- 101 **Kokubo, T.** Bioactive glass ceramics : Properties and applications. *Biomaterials*, 1991, **12**(2), 155-163.
- 102 **Yamasaki, H. and Sakai, H.** Osteogenic Response to Porous Hydroxyapatite Ceramics under the Skin of Dogs. *Biomaterials*, 1992, **13**, 308-312.

- 103 Klein, C., de Groot, K., Chen, W., Li, Y. and Zhang, X.** Osseous substance formation induced in porous calcium phosphate ceramics in soft tissues. *Biomaterials*, 1994, **15**(1), 31-34.
- 104 Muschler, G.F., Nakamoto, C. and Griffith, L.G.** Engineering Principles of Clinical Cell-Based Tissue Engineering. *Journal of Bone Joint Surgery, American Volume*, 2004, **86-A**, 1541-1558.
- 105 Kulkarni, R.K., Moore, E.G., Hegyeli, A.F. and Leonard, F.** Biodegradable poly(lactic acid) polymers. *Journal of Biomedical Materials Research*, 1971, **5**(3), 169-181.
- 106 Kulkarni, R., Pani, K., Neuman, C. and Leonard, F.** Polylactic acid for surgical implants. *Archives of Surgery*, 1966, **93**(5), 839.
- 107 Rae, T.** The toxicity of metals used in orthopaedic prostheses. An experimental study using cultured human synovial fibroblasts. *Journal of Bone & Joint Surgery, British Volume*, 1981, **63**(3), 435.
- 108 Maurer, A.M., Merritt, K. and Brown, S.A.** Cellular uptake of titanium and vanadium from addition of salts or fretting corrosion in vitro. *Journal of Biomedical Materials Research*, 1994, **28**(2), 241-246.
- 109 Yamamoto, A., Honma, R., Sumita, M. and Hanawa, T.** Cytotoxicity evaluation of ceramic particles of different sizes and shapes. *Journal of Biomedical Materials Research - Part A*, 2004, **68**(2), 244-256.
- 110 Kuroda, D., Niinomi, M., Morinaga, M., Kato, Y. and Yashiro, T.** Design and mechanical properties of new  $\beta$  type titanium alloys for implant materials. *Materials Science and Engineering*, 1998, **A243**, 244-249.
- 111 Plecko, M., Sievert, C., Andermatt, D., Frigg, R., Kronen, P., Klein, K., Stübinger, S., Nuss, K., Bürki, A. and Ferguson, S.** Osseointegration and biocompatibility of different metal implants-a comparative experimental investigation in sheep. *BMC Musculoskeletal Disorders*, 2012, **13**(1), 32.
- 112 Niinomi, M.** Recent metallic materials for biomedical applications. *Metallurgical and Materials Transactions*, 2002, **33 A**(3), 477-486.
- 113 Piattelli, A., Piattelli, M., Scarano, A. and Montesani, L.** Light and scanning electron microscopic report of four fractured implants. *The International Journal of Oral & Maxillofacial implants*, **13**(4), 561.
- 114 Chao, J. and López, V.** Failure analysis of a Ti6Al4V cementless HIP prosthesis. *Engineering Failure Analysis*, 2007, **14**(5), 822-830.
- 115 Culleton, T.P., Prendergast, P.J. and Taylor, D.** Fatigue failure in the cement mantle of an artificial hip joint. *Clinical Materials*, 1993, **12**(2), 95-102.

- 116 **Paliwal, M., Gordon Allan, D. and Filip, P.** Failure analysis of three uncemented titanium-alloy modular total hip stems. *Engineering Failure Analysis*, 17(5), 1230-1238.
- 117 **Karageorgiou, V. and Kaplan, D.** Porosity of 3D biomaterial scaffolds and osteogenesis. *Biomaterials*, 2005, 26(27), 5474-5491.
- 118 **Ryan, G., Pandit, A. and Apatsidis, D.P.** Fabrication methods of porous metals for use in orthopaedic applications. *Biomaterials*, 2006, 27(13), 2651-2670.
- 119 **Liu, X., Chu, P.K. and Ding, C.** Surface modification of titanium, titanium alloys, and related materials for biomedical applications. *Materials Science and Engineering: R: Reports*, 2004, 47(3-4), 49-121.
- 120 **Krishna, B.V., Bose, S. and Bandyopadhyay, A.** Low stiffness porous Ti structures for load-bearing implants. *Acta Biomaterialia*, 2007, 3(6), 997-1006.
- 121 **Ben-Nissan, B. and Pezzoti, G.** Bioceramic : an introduction. In Teoh, S.H., ed. *Engineering Materials for Biomedical Applications*, pp. 6-1 - 6-28 (World Scientific Publishing Co, Pte. Ltd, Toh Tuck Link, Singapura, 2004).
- 122 **Kurtz, S.M. and Devine, J.N.** PEEK biomaterials in trauma, orthopaedic, and spinal implants. *Biomaterials*, 2007, 28(32), 4845-4869.
- 123 **Cheal, E., Spector, M. and Hayes, W.** Role of loads and prosthesis material properties on the mechanics of the proximal femur after total hip arthroplasty. *Journal of Orthopaedic Research*, 1992, 10(3), 405-422.
- 124 **Prendergast, P. and Taylor, D.** Stress analysis of the proximo-medial femur after total hip replacement. *Journal of Biomedical Engineering*, 1990, 12(5), 379-382.
- 125 Structure of bone. 2010,  
<http://www.doitpoms.ac.uk/tlplib/bones/structure.php>, Accessed date: 28 August 2010.
- 126 **Sumner, D.R., Turner, T.M., Igloria, R., Urban, R.M. and Galante, J.O.** Functional adaptation and ingrowth of bone vary as a function of hip implant stiffness. *Journal of Biomechanics*, 1998, 31(10), 909-917.
- 127 **Jacobs, J.J., Gilbert, J.L. and Urban, R.M.** Current concepts review- Corrosion of metal orthopaedic implants. *The Journal of Bone and Joint Surgery*, 1998, 80(2), 268.
- 128 **Vasilescu, E., Drob, P., Vasilescu, C., Drob, S.I., Bertrand, E., Gordin, D.M. and Gloriant, T.** Corrosion resistance of the new Ti-25Ta-25Nb alloy in severe functional conditions. *Materials and Corrosion*, 2010, n/a-n/a.

- 129 Choubey, A., Basu, B. and Balasubramaniam, R.** Electrochemical behaviour of Ti-based alloys in simulated human body fluid environment. *Trends in Biomaterials & Artificial Organs*, 2005, **18**(2), 64-72.
- 130 Assis, S.L.d., Wolyne, S. and Costa, I.** Corrosion characterisation of titanium alloys by electrochemical techniques. *Electrochimica Acta*, 2006, **51**(8), 1815-1819.
- 131 Seah, K.H.W., Thampuran, R. and Teoh, S.H.** The influence of pore morphology on corrosion. *Corrosion Science*, 1998, **40**(4-5), 547-556.
- 132 Franzén, H. and Mjöberg, B.** Wear and loosening of the hip prosthesis: a roentgen stereophotogrammetric 3-year study of 14 cases. *Acta Orthopaedica*, 1990, **61**(6), 499-501.
- 133 Engh, G.A., Dwyer, K.A. and Hanes, C.K.** Polyethylene wear of metal-backed tibial components in total and unicompartmental knee prostheses. *Journal of Bone & Joint Surgery, British Volume*, 1992, **74**(1), 9.
- 134 Braceras, I., Alava, J.I., Onate, J.I., Brizuela, M., Garcia-Luis, A., Garagorri, N., Viviente, J.L. and de Maeztu, M.A.** Improved osseointegration in ion implantation-treated dental implants. *Surface and Coatings Technology*, 2002, **158-159**, 28-32.
- 135 Kienapfel, H., Sprey, C., Wilke, A. and Griss, P.** Implant fixation by bone ingrowth. *The Journal of Arthroplasty*, 1999, **14**(3), 355-364.
- 136 Shackelford, J.F.** *Introduction to Materials Science for Engineers*. (Pearson Prentice Hall, New Jersey 2009).
- 137 Park, J.B. and Bronzino, J.D.** Chapter 1. Metallic Biomaterials. In Park, J.B. and Bronzino, J.D., eds. *Biomaterials: Principles and Applications*, pp. 1-20 (crc press Boca Raton, FL, 2003).
- 138 Hallab, N.J., Anderson, S., Caicedo, M., Brasher, A., Mikecz, K. and Jacobs, J.J.** Effects of soluble metals on human peri-implant cells. *Journal of Biomedical Materials Research Part A*, 2005, **74A**(1), 124-140.
- 139 Niinomi, M.** Mechanical properties of biomedical titanium alloys. *Materials Science and Engineering*, 1998, **A243**, 231-236.
- 140 Hao, Y.L., Li, S.J., Sun, S.Y., Zheng, C.Y. and Yang, R.** Elastic deformation behaviour of Ti-24Nb-4Zr-7.9Sn for biomedical applications. *Acta Biomaterialia*, 2007, **3**(2), 277-286.
- 141 Niinomi, M.** Fatigue characteristics of metallic biomaterials. *International Journal of Fatigue*, 2007, **29**(6), 992-1000.
- 142 Atanda, P., Fatudimu, A. and Oluwole, O.** Sensitisation Study of Normalized 316L Stainless Steel. *Journal of Minerals & Materials Characterisation & Engineering*, 2010, **9**(1), 13-23.

- 143 Pilliar, R.M.** Metallic Biomaterials. In Nayaran, R., ed. *Biomedical Materials*, pp. 41-82 (Springer Science Business Media, New York, 2009).
- 144 Lo, K.H., Shek, C.H. and Lai, J.K.L.** Recent developments in stainless steels. *Materials Science and Engineering: R: Reports*, 2009, **65**(4–6), 39-104.
- 145 Singh, V. and Singhal, L.** *In vitro* corrosion fatigue behaviour of low nickel high nitrogen austenitic stainless steel. *Materials Science and Engineering: A*, 2012.
- 146 Yang, K. and Ren, Y.** Nickel-free austenitic stainless steels for medical applications. *Science and Technology of Advanced Materials*, 2010, **11**(1), 014105.
- 147 Sumita, M., Hanawa, T. and Teoh, S.** Development of nitrogen-containing nickel-free austenitic stainless steels for metallic biomaterials—review. *Materials Science and Engineering: C*, 2004, **24**(6), 753-760.
- 148 Reclaru, L., Ziegenhagen, R., Eschler, P.Y., Blatter, A. and Lemaître, J.** Comparative corrosion study of “Ni-free” austenitic stainless steels in view of medical applications. *Acta Biomaterialia*, 2006, **2**(4), 433-444.
- 149 Gavriljuk, V.G., Tyshchenko, A.I., Razumov, O.N., Petrov, Y.N., Shanina, B.D. and Berns, H.** Corrosion-resistant analogue of Hadfield steel. *Materials Science and Engineering: A*, 2006, **420**(1–2), 47-54.
- 150 Devasenapathi, A. and Asawa, M.** Effect of high Mn on SCC behaviour of an austenitic stainless steel in 42% boiling MgCl<sub>2</sub> solution. *Journal of Materials Science letters*, 1997, **16**(16), 1363-1365.
- 151 Niinomi, M., Hanawa, T. and Narushima, T.** Japanese research and development on metallic biomedical, dental, and healthcare materials. *JOM*, 2005, **57**(4), 18-24.
- 152 Kuroda, D., Hanawa, T., Hibar, T., Kobayashi, M., Kuroda, S. and Kobayashi, T.** New manufacturing process of nickel-free stainless steel through nitrogen absorption treatment. *Journal of the Japan Institute of Metals*, 2006, **70**(4), 287-294.
- 153 Marti, A.** Cobalt-base alloys used in bone surgery. *Injury*, 2000, **31**, Supplement 4(0), D18-D21.
- 154 McKee, G. and Watson-Farrar, J.** Replacement of arthritic hips by the McKee-Farrar prosthesis. *Journal of Bone & Joint Surgery, British Volume*, 1966, **48**(2), 245.
- 155 Walker, P. and Gold, B.** The tribology (friction, lubrication and wear) of all-metal artificial hip joints. *Wear*, 1971, **17**(4), 285-299.

- 156 **Alvarado, J., Maldonado, R., Marxuach, J. and Otero, R.** Biomechanics of HIP and knee prostheses, *Application of Engineering Mechanics in Medicine*, University of Puerto Rico Mayaguez, 2003, pp 6-22
- 157 **Ramsden, J., Allen, D., Stephenson, D., Alcock, J., Peggs, G., Fuller, G. and Goch, G.** The design and manufacture of biomedical surfaces. *CIRP Annals-Manufacturing Technology*, 2007, **56**(2), 687-711.
- 158 **Navarro, M., Michiardi, A., Castano, O. and Planell, J.** Biomaterials in orthopaedics. *Journal of the Royal Society Interface*, 2008, **5**(27), 1137-1158.
- 159 **Vidal, C.V. and Muñoz, A.I.** Effect of thermal treatment and applied potential on the electrochemical behaviour of CoCrMo biomedical alloy. *Electrochimica Acta*, 2009, **54**(6), 1798-1809.
- 160 **Öztürk, O., Türkan, U.u. and Eroğlu, A.E.** Metal ion release from nitrogen ion implanted CoCrMo orthopaedic implant material. *Surface and Coatings Technology*, 2006, **200**(20–21), 5687-5697.
- 161 **Okazaki, Y. and Gotoh, E.** Metal release from stainless steel, Co-Cr-Mo-Ni-Fe and Ni-Ti alloys in vascular implants. *Corrosion Science*, 2008, **50**(12), 3429-3438.
- 162 **Haasters, J., Salis-Solio, G.V. and Bensmann, G.** The Use of Ni-Ti as an Implant Material in Orthopaedics. *Butterworth-Heinemann, Engineering Aspects of Shape Memory Alloys(UK)*, 1990, 1990, 426-444.
- 163 **Wever, D.J., Veldhuizen, A.G., Sanders, M.M., Schakenraad, J.M. and Van Horn, J.R.** Cytotoxic, allergic and genotoxic activity of a nickel-titanium alloy. *Biomaterials*, 1997, **18**(16), 1115-1120.
- 164 **Kapanen, A., Ryhänen, J., Danilov, A. and Tuukkanen, J.** Effect of nickel-titanium shape memory metal alloy on bone formation. *Biomaterials*, 2001, **22**(18), 2475-2480.
- 165 **Oliveira, N.T.C., Biaggio, S.R., Rocha-Filho, R.C. and Bocchi, N.** Studies on the stability of anodic oxides on zirconium biocompatible alloys. *Journal of the Brazilian Chemical Society*, 2002, **13**(4), 463-468.
- 166 **Ehrman, J.D., Bender, E.T., Stojilovic, N., Sullivan, T., Ramsier, R.D., Buczynski, B.W., Kory, M.M. and Steiner, R.P.** Microbial adhesion to zirconium alloys. *Colloids and Surfaces B: Biointerfaces*, 2006, **50**(2), 152-159.
- 167 **Zardiackas, L.D., Parsell, D.E., Dillon, L.D., Mitchell, D.W., Nunnery, L.A. and Poggie, R.** Structure, metallurgy, and mechanical properties of a porous tantalum foam. *Journal of Biomedical Materials Research Part B: Applied Biomaterials*, 2001, **58**(2), 180-187.
- 168 **Cardonne, S.M., Kumar, P., Michaluk, C.A. and Schwartz, H.D.** Tantalum and its alloys. *International Journal of Refractory Metals and Hard Materials*, 1995, **13**(4), 187-191, 193-194.

- 169 Staiger, M.P., Pietak, A.M., Huadmai, J. and Dias, G.** Magnesium and its alloys as orthopaedic biomaterials: A review. *Biomaterials*, 2006, **27**(9), 1728-1734.
- 170 Davis, J.R., ed.** *Metallic Materials Chapter 3 in Handbook of Materials for Medical Devices*. (ASM International Materials Park, Ohio, USA, 2003).
- 171 Callister, W.D.** *Materials Science and Engineering: an introduction*. (John Wiley & Son Inc, New York, 2007).
- 172 Teoh, S.H., Tang, Z.G. and Hastings, G.W.** Thermoplastic polymers in biomedical applications : Structures, properties and processing In Black, J. and Hastings, G., eds. *Handbook of Biomaterials Properties*, pp. 270-300 (Chapman & Hall, London, 1998).
- 173 Wang, M.** Developing bioactive composite materials for tissue replacement. *Biomaterials*, 2003, **24**, 2133-2151.
- 174 Desai, S. and Shankar, M.R.** Chapter 2 Polymer, composite and nano biomaterials : current and future development. In Bartolo, P. and Bidanda, B., eds. *Bio-materials and prototyping application in medicine*, pp. pp. 16-16 (Springer US, 2008).
- 175 Srichana, T. and Domb, A.J.** Polymeric Biomaterials. In Narayan, R., ed. *Biomedical Materials*, pp. 83-119 (Springer Science -Busines Media, New York, 2009).
- 176 Lee, H.B., Khang, G. and Lee., J.H.** Chapter 3 Polymeric Biomaterials. In Park, J.B. and Bronzino, J.D., eds. *Biomaterials: Principles and Applications*, pp. 55-77 (CRC press Boca Raton., Florida, 2003).
- 177 Boretos, J.W. and Boretos, S.J.** Chapter 4 Biomedical Elastomer. In Black, J. and Hastings, G., eds. *Handbook of Biomaterials Properties*, pp. 302-340 (Chapman & Hall, London, 1998).
- 178 Brannon-Peppas, L. and Peppas, N.A.** Equilibrium swelling behaviour of pH-sensitive hydrogels. *Chemical Engineering Science*, 1991, **46**(3), 715-722.
- 179 Woo, R.K., Jenkins, D.D. and Greco, R.S.** Biomaterials: historical overview and current directions. In Greco, R.S., Prinz, F.B. and Smith, F.L., eds. *Nanoscale Technology in Biological Systems*, pp. 1-24 (CRS Press, Boca Raton, FL 2005).
- 180 Billote., W.G.** Chapter 2 Ceramic Biomaterials. In Park, J.B. and Bronzino, J.D., eds. *Biomaterials: principles and applications*, pp. 21-54 (CRC Press Boca Raton, Florida, 2003).
- 181 Marti, A.** Inert bioceramics ( $\text{Al}_2\text{O}_3$ ,  $\text{ZrO}_2$ ) for medical application. *Injury*, 2000, **31**(Supplement 4), 33-36.

- 182 Catledge, S.A., Fries, M.D., Vohra, Y.K., Lacefield, W.R., Lemons, J.E., Woodard, S. and Venugopalan, R.** Nanostructured ceramics for biomedical implants. *Journal of Nanoscience and Nanotechnology*, 2002, **2**(3-4), 293-312.
- 183 Hench, L.L.** Ceramic, Glasses and Glass Ceramics. In Ratner, B.D., Hoffman, A.S., Schoen, F.J. and Lemons, J.E., eds. *Biomaterials Science: an Introduction to Materials in Medicine*, pp. 73-84 (Academic Press, San Diego, USA, 1997).
- 184 Frakes, J.T., Brown, S.D. and Kenner, G.H.** Delayed failure and aging of porous alumina in water and physiological media. *Am. Ceram. Soc. Bull.*, 1974, **53**, 183-187.
- 185 Kenner, G.H., Pasco, W.D., Frakes, J.T. and Brown, S.D.** Mechanical properties of calcia stabilised zirconia following in vivo and in vitro aging. *Journal of Biomedical Materials Research*, 1975, **9**(4), 63-66.
- 186 Schnittgrund, G.D., Kenner, G.H. and Brown, S.D.** In vivo and in vitro changes in strength of orthopaedic calcium aluminates. *Journal of Biomedical Materials Research*, 1973, **7**(3), 435-452.
- 187 Krainess, F.E. and Knapp, W.J.** Strength of a dense alumina ceramic after aging in vitro. *Journal of Biomedical Materials Research*, 1978, **12**(2), 241-246.
- 188 Cales, B., Stefani, Y. and Lilley, E.** Long-term in vivo and in vitro aging of a zirconia ceramic used in orthopaedy. *Journal of Biomedical Materials Research*, 1994, **28**(5), 619-624.
- 189 Binzer, T.J. and Bajpai, P.K.** The Use of Zinc-Calcium-Phosphorous Oxide (ZCAP) Ceramics in Reconstructive Bone Surgery. pp. 182–185 (1987).
- 190 Scheidler, P.A. and Bajpai, P.K.** Zinc sulphate calcium phosphate (ZSCAP) composite for repairing traumatized bone. *Biomedical Sciences Instrumentation*, 1992, **28**, 183.
- 191 Larrabee, R.A., Fuski, M.P. and Bajpai, P.K.** A ferric calcium phosphorous oxide (FECAP) ceramic for rebuilding bone. *Biomedical Sciences Instrumentation*, 1993, **29**, 59.
- 192 Ashby, M.F. and Jones, D.R.H.** *Engineering materials 2: an Introduction to Microstructures, Processing and Design*. (Butterworth-Heinemann, 1998).
- 193 Agarwal, B.D. and Broutman, L.J.** *Analysis and performance of fiber composites*. (2nd ed. John Wiley & Son, Inc., New York, 1990).
- 194 Ambrosio, L., Carotenuto, G. and Nicolais, L.** Chapter 2 Composite Materials. In Black, J. and Hastings, G., eds. *Handbook of Biomaterials Properties*, pp. 214-241 (Chapman & Hall, London, 1998).

- 195 Huang, Z.M. and Ramakrishna, S.** Chapter 9 : Composites in biomedical applications. In Teoh, S.H., ed. *Engineering Materials for Biomedical Applications*, pp. 9.1-9.50 (World Scientific Publishing Co, Pte. Ltd, Toh Tuck Link, Singapura, 2004).
- 196 Agarwal, B.D., Broutman, L.J. and Chandrashekhara, K.** *Analysis and performance of fiber composites*. (John Wiley & Son, Inc, New York, 1980).
- 197 Park, H.C., Liu, Y.K. and Lakes, R.S.** The material properties of bone-particle impregnated PMMA. *Journal of Biomechanical Engineering*, 1986, **108**, 141.
- 198 Lake, R.S.** Chapter 3 : Composites biomaterials. In Park, J.B. and Bronzino, J.D., eds. *Biomaterials: Principles and Applications*, pp. 79-94 (CRC press Boca Raton,, Florida, 2003).
- 199 Alexander, H.** Composites. In Ratner, B.D., Hoffman, A.S., Schoen, F.J. and Lemons, J.E., eds. *Biomaterials Science: an Introduction to Materials in Medicine*, pp. 94-105 (Academic Press, San Diego, USA, 1997).
- 200 Bradley, J.S., Hastings, G.W. and Johnson-Nurse, C.** Carbon fibre reinforced epoxy as a high strength, low modulus material for internal fixation plates. *Biomaterials*, 1980, **1**(1), 38-40.
- 201 McKenna, G.B., Bradley, G.W., Dunn, H.K. and Statton, W.O.** Mechanical properties of some fibre reinforced polymer composites after implantation as fracture fixation plates. *Biomaterials*, 1980, **1**(4), 189-192.
- 202 Fujihara, K., Huang, Z.M., Ramakrishna, S., Satkunanantham, K. and Hamada, H.** Development of braided carbon/PEEK composite bone plates. *Advanced Composites Letters(UK)*, 2001, **10**(1), 13-20.
- 203 Morrison, C., Macnair, R., MacDonald, C., Wykman, A., Goldie, I. and Grant, M.H.** In vitro biocompatibility testing of polymers for orthopaedic implants using cultured fibroblasts and osteoblasts. *Biomaterials*, 1995, **16**(13), 987-992.
- 204 Peluso, G., Ambrosio, L., Cinquegrani, M., Nicolais, L., Saiello, S. and Tajana, G.** Rat peritoneal immune response to carbon fibre reinforced epoxy composite implants. *Biomaterials*, 1991, **12**(2), 231-235.
- 205 Zimmerman, M., Parsons, J.R. and Alexander, H.** The design and analysis of a laminated partially degradable composite bone plate for fracture fixation. *J. Biomed. Mater. Res.*, 1987, **21**, 345-361.
- 206 Christel, P., Meunier, A., Leclercq, S., Bouquet, P. and Buttazzoni, B.** Development of a carbon-carbon hip prosthesis. *Journal of Biomedical Materials Research*, 1987, **21**(A2), 191-218.
- 207 Chang, F.K., Perez, J.L. and Davidson, J.A.** Stiffness and strength tailoring of a hip prosthesis made of advanced composite materials. *Journal of Biomedical Materials Research*, 1990, **24**(7), 873-899.

- 208 **Allcock, S. and Ali, M.A.** Early failure of a carbon-fiber composite femoral component. *The Journal of Arthroplasty*, 1997, **12**(3), 356-358.
- 209 **Adam, F., Hammer, D.S., Pfautsch, S. and Westermann, K.** Early failure of a press-fit carbon fiber hip prosthesis with a smooth surface. *The Journal of Arthroplasty*, 2002, **17**(2), 217-223.
- 210 **Minovic, A., Milosev, I., Pisot, V., Cör, A. and Antolic, V.** Isolation of polyacetal wear particles from periprosthetic tissue of isoelastic femoral stems. *Journal of Bone & Joint Surgery, British Volume*, 2001, **83**(8), 1182-1190.
- 211 **Fujihara, K., Teo, K., Gopal, R., Loh, P.L., Ganesh, V.K., Ramakrishna, S., Foong, K.W.C. and Chew, C.L.** Fibrous composite materials in dentistry and orthopaedics: review and applications. *Composites Science and Technology*, 2004, **64**(6), 775-788.
- 212 **Donachie, M.J., Jr.** *Titanium : A technical guide.* (ASM International, Ohio, 1989).
- 213 **AIMR2009.** *Mineral Sands: Australia's Identified Mineral Resources 2009* (Australian Government, Geoscience Australia, 2009).
- 214 **Peters, M., Hemtenmacher, J., Kumpfert, J. and Leyens, C.** Structure and properties of titanium and titanium alloys. In Peters, M. and Leyens, C., eds. *Titanium and Titanium Alloys*, pp. 1-36 (Willey-VCH, 2003).
- 215 **Collings, E.W.** *The Physical Metallurgy of Titanium Alloys.* (American Society for Metals, Metals Park, Ohio, 1984).
- 216 **Lütjering, G. and Williams, J.** *Titanium.* (Springer Verlag Berlin Heiderberg, Germany, 2003).
- 217 **Lutjering, G. and Williams, J.C.** *Titanium.* Berlin Heidelberg Germany, 2003).
- 218 **Geetha, M., Singh, A.K., Muraleedharan, K., Gogia, A.K. and Asokamani, R.** Effect of thermomechanical processing on microstructure of a Ti-13Nb-13Zr alloy. *Journal of Alloys and Compounds*, 2001, **329**(1-2), 264-271.
- 219 **Tang, X., Ahmed, T. and Rack, H.J.** Phase Transformation in Ti-Nb-Ta and Ti-Nb-Ta-Zr Alloys. *Journal of Materials and Science*, 2000, **35**, 1805-1811.
- 220 **Greenwood, N.N. and Earnshaw, A.** *Chemistry of the Elements.* (Reed Educational and Profesional Publishing Ltd, Oxford, 1998).
- 221 **ASM.** *ASM Handbook: Volume 3: Alloy Phase Diagrams* (Materials Park, OH: ASM International Metal Park. Ohio, U.S.A, 1993).
- 222 **Leyens, C. and Peters, M.** *Titanium and titanium alloys : Fundamentals and applications.* (Willey-VCH, Cologne, Germany, 2008).

- 223 "Product Information : REMBAR Niobium Technical Info " *Dobbs Ferry, NY, U.S.A., The REMBAR Company, Inc, <http://www.rembar.com/niobium.htm> , Accessed date : February 10th, 2010.*
- 224 "Product Information : Tantalum Properties"  
West Park Court Talbott, TN, U.S.A.: EAGLE ALLOY CORPORATION;  
*<http://www.eaglealloys.com/t-TantalumProperties.aspx> Accessed date: February 2nd , 2010.*
- 225 **Kenneth L Barbalace (J.K. Barbalace, i.** Periodic Table of Elements: Element Zirconium - Zr.
- 226 "Product Information: Zirconium alloy data sheet grade 702C and 705C "  
*Flowsolve Corporation, Dayton, Ohio, USA, Bulletin A/12c, 1998.*
- 227 **Zhou, Y.L. and Niinomi, M.** Microstructures and mechanical properties of Ti-50 mass% Ta alloy for biomedical applications. *Journal of Alloys and Compounds*, 2008, **466**(1-2), 535-542.
- 228 **Zhou, Y.L. and Niinomi, M.** Ti-25Ta alloy with the best mechanical compatibility in Ti-Ta alloys for biomedical applications. *Materials Science and Engineering: C*, 2009, **29**(3), 1061-1065.
- 229 **Boyer, R.R.** An overview on the use of titanium in the aerospace industry. *Materials Science and Engineering: A*, 1996, **213**(1-2), 103-114.
- 230 **Moffat, D.L. and Larbalestier, D.C.** The competition between martensite and omega in quenched Ti-Nb alloys. *Metallurgical and Materials Transactions A*, 1988, **19**(7), 1677-1686.
- 231 **Ikeda, M., Komatsu, S.Y., Sowa, I. and Niinomi, M.** Aging behaviour of the Ti-29Nb-13Ta-4.6 Zr new beta alloy for medical implants. *Metallurgical and Materials Transactions A*, 2002, **33**(3), 487-493.
- 232 **Vohra, Y., Sikka, S. and Chidambaram, R.** Electronic structure of omega phase of titanium and zirconium. *Journal of Physics F: Metal Physics*, 1979, **9**, 1771.
- 233 **Ahmed, T. and Rack, H.J.** Phase transformations during cooling in [alpha]+[beta] titanium alloys. *Materials science and Engineering A*, 1998, **243**(1-2), 206-211.
- 234 **Dobromyslov, A.V. and Elkin, V.A.** The orthorhombic  $\alpha'$ -phase in binary titanium-base alloys with d-metals of V-VIII groups. *Materials Science and Engineering: A*, 2006, **438-440**, 324-326.
- 235 **Grosdidier, T. and Philippe, M.J.** Deformation induced martensite and superelasticity in a [beta]-metastable titanium alloy. *Materials Science and Engineering A*, 2000, **291**(1-2), 218-223.

- 236 **Yang, Y., Li, G.P., Cheng, G.M., Wang, H., Zhang, M., Xu, F. and Yang, K.** Stress-introduced  $\alpha''$  martensite and twinning in a multifunctional titanium alloy. *Scripta Materialia*, 2008, **58**(1), 9-12.
- 237 **Qazi, J.I., Marquardt, B. and Rack, H.J.** High-strength metastable beta-titanium alloys for biomedical applications. *JOM*, 2004, **56**(11), 79-51(73).
- 238 **Terlinde, G. and Fischer, G.** Chapter 2 : Beta titanium alloys. In Peters, M. and Leyens, C., eds. *Titanium and Titanium Alloys*, pp. 37-57 (Wiley-VCH, Weinheim, Germany, 2008).
- 239 **Hao, Y.L., Niinomi, M., Kuroda, D., Fukunaga, K., Zhou, L. and Yang, R.** Aging response of the Young's modulus and mechanical properties of Ti-29Nb-13Ta-4.6Zr for biomedical applications. *Metalurgical and Materials Transactions*, 2003, **34A**(4), 1007-10112.
- 240 **Sakaguchi, N., Mitsuo, N., Akahori, T., Saito, T. and Furuta, T.** Effect of alloying elements on elastic modulus of Ti-Nb-Ta-Zr system alloy for biomedical applications. *Material Science Forum*, 2004, **449-452**(II), 1269-1272.
- 241 **Sakaguchi, N., Niinomi, M., Akahori, T., Takeda, J. and Toda, H.** Effect of Ta content on mechanical properties of Ti-30Nb-XTa-5Zr. *Materials Science and Engineering: C*, 2005, **25**(3), 370-376.
- 242 **Fanning, J.C. and Fox, S.P.** Recent developments in metastable  $\beta$  strip alloys. *Journal of Material Engineering and Performance*, 2005, **14**(6), 6.
- 243 **Ferrero, J.G.** Candidate materials for high-strength fastener applications in both the aerospace and automotive industries. *Journal of Materials Engineering and Performance*, 2005, **14**(6), 691-696.
- 244 **Fanning, J.C.** Military application for  $\beta$  titanium alloys. *Journal of Materials Engineering and Performance*, 2005, **14**(6), 5.
- 245 **Rack, H.J. and Qazi, J.I.** Titanium alloys for biomedical applications. *Materials Science and Engineering: C*, 2006, **26**(8), 1269-1277.
- 246 **Thomas, R.** Titanium in the geothermal industry. *Geothermics*, 2003, **32**(4-6), 679-687.
- 247 **Mandl, S., Sader, R., Thorwarth, G., Krause, D., Zeilhofer, H.F., Horch, H.H. and Rauschenbach, B.** Biocompatibility of titanium based implants treated with plasma immersion ion implantation in Nuclear Instruments and Methods in Physics Research Section B: Beam Interactions with Materials and Atoms. *13th International Conference on Ion Beam Modification of Materials*, pp. 517-521(2003).
- 248 **Jablokov, V.R., Naomi, G.D.M., Rack, H.J. and Fresse, H.L.** Influence of oxygen content on the mechanical properties of Titanium-35Niobium-7Zirconium-5Tantalum beta titanium alloy. *Journal of ASTM International, September 2005*, 2005, **2**(8), 40-51.

- 249 **Breme, J. and Biehl, V.** Metallic Biomaterials. In Black, J. and Hastings, G.W., eds. *Handbook of Biomaterial Properties*, pp. 179-180 (Springer Us, 1998).
- 250 **Hao, Y.L., Yang, R., Niinomi, M., Kuroda, D., Zhou, Y.L., Fukunaga, K. and Suzuki, A.** Young's modulus and mechanical properties of Ti-29Nb-13Ta-4.6 Zr in relation to martensite. *Metallurgical and Materials Transactions A*, 2002, **33**(10), 3137-3144.
- 251 **Niinomi, M., Akahori, T., Takeuchi, T., Katsura, S., Fukui, H. and Toda, H.** Mechanical properties and cyto-toxicity of new beta type titanium alloy with low melting points for dental applications. *Materials Science and Engineering: C*, 2005, **25**(3), 417-425.
- 252 **Sutherland, D.S., Forshaw, P.D., Allen, G.C., Brown, I.T. and Williams, K.R.** Surface analysis of titanium implants. *Biomaterials*, 1993, **14**(12), 893-899.
- 253 **Oshida, Y.** *Bioscience and bioengineering of titanium materials*. (Elsevier Science Ltd, 2007).
- 254 **Thomsen, P., Larsson, C., Ericson, L., Sennerby, L., Lausmaa, J. and Kasemo, B.** Structure of the interface between rabbit cortical bone and implants of gold, zirconium and titanium. *Journal of Materials Science: Materials in Medicine*, 1997, **8**(11), 653-665.
- 255 **Ellingsen, J.E.** A study on the mechanism of protein adsorption to TiO<sub>2</sub>. *Biomaterials*, 1991, **12**(6), 593-596.
- 256 **Wapner, K.L.** Implications of metallic corrosion in total knee arthroplasty. *Clinical Orthopaedics and Related Research*, 1991(271), 12-20.
- 257 **Semlitsch, M.F., Weber, H., Streicher, R.M. and Schön, R.** Joint replacement components made of hot-forged and surface-treated Ti-6Al-7Nb alloy. *Biomaterials*, 1992, **13**(11), 781-788.
- 258 **Iijima, D., Yoneyama, T., Doi, H., Hamanaka, H. and Kurosaki, N.** Wear properties of Ti and Ti-6Al-7Nb castings for dental prostheses. *Biomaterials*, 2003, **24**(8), 1519-1524.
- 259 **Zwicker, J., Etzold, U. and Moser, T.** Abrasive properties of oxide layers on TiAl15Fe2. 5 in contact with high density polyethylene. In: *Titanium '84 Science and Technology, vol.2. Munich. Deutsche Gesellschaft Fur Metalkunde EV*, 1985, **2**, 1343—1350.
- 260 **Tzanno-Martins, C., Azevedo, L.S., Orii, N., Futata, E., Jorgetti, V., Marcondes, M. and da Silva Duarte, A.J.** The role of experimental chronic renal failure and aluminium intoxication in cellular immune response. *Nephrology Dialysis Transplantation*, 1996, **11**(3), 474-480.
- 261 **Ward, R.J., McCrohan, C.R. and White, K.N.** Influence of aqueous aluminium on the immune system of the freshwater crayfish *Pacifasticus*

- leniusculus. *Aquatic toxicology (Amsterdam, Netherlands)*, 2006, **77**(2), 222-228.
- 262 Glynn, W., Thuvander, A., Sundström, B., Sparen, A., Danielsson, L.G. and Jorhem, L.** Does aluminium stimulate the immune system in male rats after oral exposure? *Food Additives and Contaminants.*, 1999, **16**, 129-135.
- 263 Jordan, M.B., Mills, D.M., Kappler, J., Marrack, P. and Cambier, J.C.** Promotion of B Cell Immune Responses via an Alum-Induced Myeloid Cell Population. *Science*, 2004, **304**(5678), 1808-1810.
- 264 Miller, P.D. and Holladay, J.W.** Friction and wear properties of titanium. *Wear*, 1958, **2**(2), 133-140.
- 265 Zhou, Y.L., Niinomi, M. and Akahori, T.** Effects of Ta content on Young's modulus and tensile properties of binary Ti-Ta alloys for biomedical applications. *Materials science and Engineering A*, 2004, **371**(1-2), 283-290.
- 266 Dieter, G.E.** Mechanical Metallurgy. 1986. (McGraw-Hill, New York).
- 267 Lee, Y.T. and Welsch, G.** Young's modulus and damping of Ti-6Al-4V alloy as a function of heat treatment and oxygen concentration. *Materials Science and Engineering: A*, 1990, **128**(1), 77-89.
- 268 Balazic, M., Kopac, J., Jackson, M.J. and Ahmed, W.** Review: titanium and titanium alloy applications in medicine. *International Journal of Nano and Biomaterials*, 2007, **1**(1), 3-34.
- 269 Niinomi, M., Hattori, T., Morikawa, K., Kasuga, T., Suzuki, A., Fukui, H. and Niwa, S.** Development of low rigidity  $\beta$ -type titanium alloy for biomedical applications. *Materials Transactions.*, 2002, **43**, (12, ), p 2970-2977.
- 270 Peters, M., Hemtenmacher, J., Kumpfert, J. and Leyens, C.** Structure and Properties of Titanium and Titanium Alloys. In Peters, M. and Leyens, C., eds. *Titanium and Titanium Alloys*, pp. 1-55 (Willey-VCH, 2003).
- 271 Steinemann, S.G.** Metal implants and surface reactions. *Injury*, 1996, **27**(Supplement 3), S-S.
- 272 Wang, K., Gustavson, L. and Dumbleton, J.** The characterisation of Ti-12 Mo-6 Zr-2 Fe: A new biocompatible titanium alloy developed for surgical implants. *Beta Titanium Alloys in the 1990's*, pp. 49-60, Denver, Colorado, USA : 22-24 February 1993 1993).
- 273 Steinemann, S., Mäusli, P., Szmukler-Moncler, S., Semlitsch, M., Pohler, O., Hintermann, H. and Perren, S.** Beta-titanium alloy for surgical implants. In Froes, F.H. and Caplain, I., eds. *Titanium'92, Science and Technology*, pp. 2689-2696 (The Mineral, Metals & Materials Society, Warrendale, PA, 1993).

- 274 Rao, V. and Houska, C.** Kinetics of the Phase Transformation in a Ti-15Mo-5Zr-3Al Alloy as Studied by X-Ray Diffraction. *Metallurgical Transactions A*, 1979, **10**, 355-358.
- 275 Fanning, J.** Properties and processing of a new metastable beta titanium alloy for surgical implant applications: TIMETAL 21 SRx. *Institute of Materials(UK)*, 1996, 1800-1807.
- 276 Zardiackas, L.D., Mitchell, D.W. and Disegi, J.A.** Characterisation of Ti-15Mo Beta Titanium Alloy for Orthopaedic Implant Applications. In Brown, S.A. and Lemons, J.E., eds. *Medical Applications of Titanium and Its Alloys : The Material and Biological Issues*, pp. 60-75 (ASTM West Conshohocken, PA, USA, 2004).
- 277 Laing, P., Ferguson Jr, A. and Hodge, E.** Tissue reaction in rabbit muscle exposed to metallic implants. *Journal of Biomedical Materials Research*, 1967, **1**(1), 135-149.
- 278 Doran, A., Law, F.C., Allen, M.J. and Rushton, N.** Neoplastic transformation of cells by soluble but not particulate forms of metals used in orthopaedic implants. *Biomaterials*, 1998, **19**(7-9), 751-759.
- 279 He, G. and Hagiwara, M.** Ti alloy design strategy for biomedical applications. *Materials Science and Engineering: C*, 2006, **26**(1), 14-19.
- 280 Hao, Y., Li, S., Sun, S., Zheng, C., Hu, Q. and Yang, R.** Super-elastic titanium alloy with unstable plastic deformation. *Applied Physics Letters*, 2005, **87**, 091906.
- 281 Kobayashi, E., Matsumoto, S., Doi, H., Yoneyama, T. and Hamanaka, H.** Mechanical properties of the binary titanium-zirconium alloys and their potential for biomedical materials. *Journal of Biomedical Materials Research*, 1995, **29**(8), 943-950.
- 282 Hon, Y.H., Wang, J.Y. and Pan, Y.N.** Composition/phase structure and properties of titanium-niobium alloys. *Materials Transactions*, 2003, **44**(11), 2384-2390.
- 283 Afonso, C.R.M., Aleixo, G.T., Ramirez, A.J. and Caram, R.** Influence of cooling rate on microstructure of Ti-Nb alloy for orthopaedic implants. *Materials Science and Engineering: C*, 2007, **27**(4), 908-913.
- 284 Santos, D., Henriques, V., Cairo, C. and Pereira, M.** Production of a low young modulus titanium alloy by powder metallurgy. *Materials Research*, 2005, **8**, 439-442.
- 285 Lee, C.M., Ju, C.P. and Lin, J.H.C.** Structure-property relationship of cast Ti-Nb alloys. *Journal of Oral Rehabilitation*, 2002, **29**(4), 314-322.
- 286 Murray, J.L.** Phase diagram of binary titanium alloys. In Murray, J.L., ed, pp. 340-345 (ASM International, Metals Park, OHIO, USA, 1987).

- 287 **Johansson, C.B., Hansson, H.A. and Albrektsson, T.** Qualitative interfacial study between bone and tantalum, niobium or commercially pure titanium. *Biomaterials*, 1990, **11**(4), 277-280.
- 288 **Bermudez, M.D., Carrion, F.J., Martinez-Nicolas, G. and Lopez, R.** Erosion-corrosion of stainless steels, titanium, tantalum and zirconium. *Wear*, 2005, **258**, pp. 693–700
- 289 **Verani, M.S., Guidry, G.W., Mahmarian, J.J., Nishimura, S., Athanasoulis, T., Roberts, R. and J. L. Lacy.** Effects of acute, transient coronary occlusion on global and regional right ventricular function in humans. *Journal of American College of Cardiology*, 1992, **20**, **1**, 490-1497.
- 290 **Jaschke, W., Klose, K.J. and Strecker, E.P.** A new balloon expandable tantalum stent (Strecker-Stent) for the biliary system: Preliminary experience. *Cardiovasc. Intervent. Radiol.*, 1992, **15**, 356-359.
- 291 **Hacking, S.A., Bobyn, J.D., Toh, K.K., Tanzer, M. and Krygier, J.J.** Fibrous tissue ingrowth and attachment to porous tantalum. *Journal of Biomedical Materials Research*, 2000, **52**(4), 631-638.
- 292 **Findlay, D.M., Welldon, K., Atkins, G.J., Howie, D.W., Zannettino, A.C.W. and Bobyn, D.** The proliferation and phenotypic expression of human osteoblasts on tantalum metal. *Biomaterials*, 2004, **25**(12), 2215-2227.
- 293 **Zhou, Y.L., Niinomi, M. and Akahori, T.** Decomposition of martensite  $\alpha''$  during aging treatments and resulting mechanical properties of Ti-Ta alloys. *Materials science and Engineering A*, 2004, **384**(1-2), 92-101.
- 294 **Hao, Y.L., Li, S.J., Sun, S.Y. and Yang, R.** Effect of Zr and Sn on Young's modulus and superelasticity of Ti-Nb-based alloys. *Materials Science and Engineering: A*, 2006, **441**(1-2), 112-118.
- 295 **Davidson, J.A. and P. Kovacs.** New biocompatible, low modulus titanium alloy for medical implants, U.S. Patent No. 5,169,597, December 8, 1992. (1992).
- 296 **Ahmed, T., Long, M., Silvestri, J., Ruiz, C. and Rack, H.J.** A new low modulus, biocompatible titanium alloy. *Titanium'95.*, 1995, **2**, 1760-1767.
- 297 **Ahmed, T. and Rack, H.** Low modulus biocompatible titanium base alloys for medical devices. In Patent, U.S., ed, p. 5 (Osteonic Corp, Allendale, N.J., 1999).
- 298 **Mishra, A.K., Davldson, J.A., Poggie, R.A., Kovacs, P. and Fitzgerald, T.J.** Mechanical and tribological properties and biocompatibility of diffusion hardened Ti-13Nb-13Zr-a new titanium alloy for surgical implants. In Brown, S.A. and Lemons, J.E., eds. *Medical Applications of Titanium and Its Alloys : The Material and Biological Issues, ASTM STP 1272*, pp. 96-116 (American Society for Testing Materials West Conshohocken, PA, USA, 1996).

- 299 Kohn, D.H. and Ducheyne, P.** Materials Science and Technology. In Cahn, R.W., Haasen, P. and Kramer, E.J., eds, pp. 33-109 (VCH, USA, 1992).
- 300 Geetha, M., Singh, A.K., Gogia, A.K. and Asokamani, R.** Effect of thermomechanical processing on evolution of various phases in Ti-Nb-Zr alloys. *Journal of Alloys and Compounds*, 2004, **384**(1-2), 131-144.
- 301 Taddei, E.B., Henriques, V.A.R., Silva, C.R.M. and Cairo, C.A.A.** Production of new titanium alloy for orthopaedic implants. *Materials science and Engineering C*, 2004, **24**(5), 683-687.
- 302 Long, M., Crooks, R. and Rack, H.J.** High-cycle fatigue performance of solution-treated metastable-[beta] titanium alloys. *Acta Materialia*, 1999, **47**(2), 661-669.
- 303 Qazi, J.I., Marquardt, B., Allard, L.F. and Rack, H.J.** Phase transformations in Ti-35Nb-7Zr-5Ta-(0.06-0.68)O alloys. *Materials Science and Engineering: C*, 2005, **25**(3), 389-397.
- 304 Li, S., Hao, Y., Yang, R., Cui, Y. and Niinomi, M.** Effect of Nb on microstructural characteristics of Ti-Nb-Ta-Zr alloy for biomedical applications. *Materials Transactions*, 2002, **43**(12), 2964-2969.
- 305 Li, S.J., Yang, R., Niinomi, M., Hao, Y.L., Cui, Y.Y. and Guo, Z.X.** Phase transformation during aging and resulting mechanical properties of two Ti-Nb-Ta-Zr alloys. *Materials Science and Technology*, 2005, **21**(6), 678-686(679).
- 306 Sakaguchi, N., Niinomi, M., Akahori, T., Takeda, J. and Toda, H.** Relationships between tensile deformation behaviour and microstructure in Ti-Nb-Ta-Zr system alloys. *Materials Science and Engineering: C*, 2005, **25**(3), 363-369.
- 307 Hanawa, T.** *In vivo* metallic biomaterials and surface modification. *Materials Science and Engineering A*, 1999, **267**(2), 260-266.
- 308 Tateishi, T., Ito, Y. and Okazaki, Y.** Corrosion resistance of implant alloys in pseudo physiological solution and role of alloying elements in passive film. *Materials Transactions. JIM*, 1997, **38**(1), 78-84.
- 309 Kobayashi, E., Wang, T.J., Doi, H., Yoneyama, T. and Hamanaka, H.** Mechanical properties and corrosion resistance of Ti-6Al-7Nb alloy dental castings. *Journal of Materials Science: Materials in Medicine*, 1998, **9**(10), 567-574.
- 310 Khan, M.A., Williams, R.L. and Williams, D.F.** The corrosion behaviour of Ti-6Al-4V, Ti-6Al-7Nb and Ti-13Nb-13Zr in protein solutions. *Biomaterials*, 1999, **20**(7), 631-637.
- 311 Khan, M.A., Williams, R.L. and Williams, D.F.** Conjoint corrosion and wear in titanium alloys. *Biomaterials*, 1999, **20**(8), 765-772.

- 312 Zhou, Y.L., Niinomi, M., Akahori, T., Fukui, H. and Toda, H.** Corrosion resistance and biocompatibility of Ti-Ta alloys for biomedical applications. *Materials science and Engineering A*, 2005, **398**(1-2), 28-36.
- 313 Okazaki, Y., Ito, Y., Kyo, K. and Tateishi, T.** Corrosion resistance and corrosion fatigue strength of new titanium alloys for medical implants without V and Al. *Materials Science and Engineering A*, 1996, **213**(1-2), 138-147.
- 314 Thair, L., Kamachi Mudali, U., Asokamani, R. and Raj, B.** Influence of microstructural changes on corrosion behaviour of thermally aged Ti-6Al-7Nb alloy. *Materials and Corrosion*, 2004, **55**(5), 358-366.
- 315 Rosa, S., Barbosa, P., Button, S. and Bertazzoli, R.** In-vitro corrosion resistance study of hot worked Ti-6Al-7Nb alloy in a isotonic medium. *Brazilian Journal of Chemical Engineering*, 2001, **18**, 47-59.
- 316 Ishizaki, K., Komarneni, S. and Nanko, M.** *Porous Materials: Process Technology and Applications* (Kluwer Academic Publisher, Dordrecht, The Netherlands, 1998).
- 317 Gibson, L.J.** Modelling the mechanical behaviour of cellular materials. *Materials Science and Engineering: A*, 1989, **110**, 1-36.
- 318 Liu, P.S. and Liang, K.M.** Review functional materials of porous metals made by P/M, electroplating and some other techniques. *Journal of Materials Science*, 2001, **36**(21), 5059-5072.
- 319 Ashby, M.F., Evans, A., Fleck, N.A., Gibson, L.J., Hutchinson, J.W. and Wadley, H.N.G.** *Metal foams : A design guide*. (Butterworth-Heinemann: Burlington, 2000).
- 320 Bobyn, J., Glassman, A., Goto, H., Krygier, J., Miller, J. and Brooks, C.** The effect of stem stiffness on femoral bone resorption after canine porous-coated total hip arthroplasty. *Clinical Orthopaedics and Related Research*, 1990, **261**, 196.
- 321 Yan, W., Berthe, J. and Wen, C.** Numerical investigation of the effect of porous titanium femoral prosthesis on bone remodeling. *Materials & Design*, 2011, **32**(4), 1776-1782.
- 322 Hulbert, S.F., Klawitter, J.J. and Bowman, L.S.** History of ceramic orthopaedic implants. *Materials Research Bulletin*, 1972, **7**(11), 1239-1246.
- 323 Chiroff, R., White, E., Weber, J. and Roy, D.** Tissue ingrowth of replamineform implants. *Journal of Biomedical Materials Research*, 1975, **9**(4), 29-45.
- 324 White, E., Weber, J., Roy, D., Owen, E., Chiroff, R. and White, R.** Replamineform porous biomaterials for hard tissue implant applications. *Journal of Biomedical Materials Research*, 1975, **9**(4), 23-27.

- 325** White, R., Weber, J. and White, E. Replamineform: a new process for preparing porous ceramic, metal, and polymer prosthetic materials. *Science*, 1972, **176**(4037), 922.
- 326** Klawitter, J.J., Bagwell, J.G., Weinstein, A.M., Sauer, B.W. and Pruitt, J.R. An evaluation of bone growth into porous high density polyethylene. *Journal of Biomedical Materials Research*, 1976, **10**(2), 311-323.
- 327** Spector, M., Michno, M., Smarook, W. and Kwiatkowski, G. A high-modulus polymer for porous orthopaedic implants: biomechanical compatibility of porous implants. *Journal of Biomedical Materials Research*, 1978, **12**(5), 665-677.
- 328** Karagianes, M. Porous metals as a hard tissue substitute. *Artificial Cells, Blood Substitutes, and Biotechnology*, 1973, **1**(1), 171-181.
- 329** Hirschhorn, J., McBeath, A. and Dustoor, M. Porous titanium surgical implant materials. *Journal of Biomedical Materials Research*, 1971, **5**(6), 49-67.
- 330** Hahn, H. and Palich, W. Preliminary evaluation of porous metal surfaced titanium for orthopaedic implants. *Journal of Biomedical Materials Research*, 1970, **4**(4), 571-577.
- 331** Kuboki, Y., Takita, H., Kobayashi, D., Tsuruga, E., Inoue, M., Murata, M., Nagai, N., Dohi, Y. and Ohgushi, H. BMP-Induced osteogenesis on the surface of hydroxyapatite with geometrically feasible and nonfeasible structures: Topology of osteogenesis. *Journal of Biomedical Materials Research*, 1998, **39**(2), 190-199.
- 332** Klenke, F.M., Liu, Y., Yuan, H., Hunziker, E.B., Siebenrock, K.A. and Hofstetter, W. Impact of pore size on the vascularisation and osseointegration of ceramic bone substitutes in vivo. *Journal of Biomedical Materials Research Part A*, 2007, **85**(3), 777-786.
- 333** Nishiguchi, S., Kato, H., Neo, M., Oka, M., Kim, H.M., Kokubo, T. and Nakamura, T. Alkali- and heta treated porous titanium for orthopaedic implant. *Journal of Biomedical Materials Research*, 2001, **54**, 198-208.
- 334** Jones, A.C., Arns, C.H., Sheppard, A.P., Hutmacher, D.W., Milthorpe, B.K. and Knackstedt, M.A. Assessment of bone ingrowth into porous biomaterials using MICRO-CT. *Biomaterials*, 2007, **28**(15), 2491-2504.
- 335** Otsuki, B., Takemoto, M., Fujibayashi, S., Neo, M., Kokubo, T. and Nakamura, T. Pore throat size and connectivity determine bone and tissue ingrowth into porous implants: Three-dimensional micro-CT based structural analyses of porous bioactive titanium implants. *Biomaterials*, 2006, **27**(35), 5892-5900.
- 336** Simancik, F. Introduction : The strange world of cellular metals. In Degisher, H.P. and Kriszt, B., eds. *Handbook of Cellular Metals : Production*,

*Processing and Applications*, pp. 1-4 (Willey-VCH GmbH & Co. KGaA, 2002).

- 337 Hutmacher, D.W.** Scaffolds in tissue engineering bone and cartilage. *Biomaterials*, 2000, **21**(24), 2529-2543.
- 338 Jacobs, J., Goodman, S., Sumner, D. and Hallab, N.** Biologic response to orthopaedic implants  
In Buckwalter JA, Einhorn TA and Simon SR, eds. *Orthopaedic Basic Science.*, pp. 401-426 (American Academy of Orthopaedic Surgeons, Rosemont, IL, 2000).
- 339 Anderson, J.** The future of biomedical materials. *Journal of Materials Science: Materials in Medicine*, 2006, **17**(11), 1025-1028.
- 340 Wilson, C.J., Clegg, R.E., Leavesley, D.I. and Percy, M.J.** Mediation of biomaterial-cell interactions by adsorbed proteins: a review. *Tissue Engineering*, 2005, **11**(1-2), 1-18.
- 341 Engh, C., Bobyn, J. and Glassman, A.** Porous-coated hip replacement. The factors governing bone ingrowth, stress shielding, and clinical results. *Journal of Bone and Joint Surgery-British Volume*, 1987, **69**(1), 45.
- 342 Dewidar, M., Yoon, H. and Lim, J.** Mechanical properties of metals for biomedical applications using powder metallurgy process: A review. *Metals and Materials International*, 2006, **12**(3), 193-206.
- 343 Asaoka, K., Kuwayama, N., Okuno, O. and Miura, I.** Mechanical properties and biomechanical compatibility of porous titanium for dental implants. *Journal of Biomedical Materials Research*, 1985, **19**(6), 699-713.
- 344 Nomura, N., Kohama, T., Oh, I.H., Hanada, S., Chiba, A., Kanehira, M. and Sasaki, K.** Mechanical properties of porous Ti-15Mo-5Zr-3Al compacts prepared by powder sintering. *Materials Science and Engineering: C*, 2005, **25**(3), 330-335.
- 345 Li, B., Rong, L. and Li, Y.** Porous NiTi alloy prepared from elemental powder sintering. *J. Mater. Res*, 1998, **13**(10), 2847-2851.
- 346 Rausch, G. and Banhart, J.** Making cellular metal from metals other than aluminium. In Degistcher, H.P. and Kriszt, B., eds. *Handbook of cellular metals*, pp. 21-28 (Willey-VCH Verlag, Weinheim, 2002).
- 347 Yamada, H.** *Strength of Biological Materials*. (The William & Wilkins Company, Baltimore Press, Maryland, 1970).
- 348 Cirincione, R., Anderson, R., Zhou, J., Mumm, D. and Soboyejo, W.O.** An investigation of the effects of sintering duration and powder sizes on the porosity and compression strength of porous Ti-6Al-4V. *Processing and properties of lightweight cellular metals and structures*, 2002, 189.

- 349 Niu, W., Bai, C., Qiu, G.B. and Wang, Q.** Processing and properties of porous titanium using space holder technique. *Materials Science and Engineering: A*, 2009, **506**(1-2), 148-151.
- 350 Wang, X., Li, Y., Xiong, J., Hodgson, P.D. and Wen, C.** Porous TiNbZr alloy scaffolds for biomedical applications. *Acta Biomaterialia*, 2009.
- 351 Imwinkelried, T.** Mechanical properties of open-pore titanium foam. *Journal of Biomedical Materials Research Part A*, 2007, **81**(4), 964-970.
- 352 Hong, T.F., Guo, Z.X. and Yang, R.** Fabrication of porous titanium scaffold materials by a fugitive filler method. *Journal of Materials Science. Materials in Medicine*, 2008, **19**(12), 3489-3495.
- 353 Andersen, O., Waag, U., Schneider, L., Stephani, G. and Kieback, B.** Novel metallic hollow sphere structures. *Advanced Engineering Materials*, 2000, **2**(4), 192-195.
- 354 Wheeler, K.R., Karagianes, T. and Sump, K.R.** Porous titanium alloy for prosthesis attachment. In Luckey, H.A. and Fred Kubli, J., eds. *Titanium Alloys in Surgical Implants-ASTM STP 796*, pp. 241-254 (ASTM Phoenix, Arizona, 11-12 May 1981, 1983).
- 355 Wen, C.E., Yamada, Y., Shimojima, K., Chino, Y., Hosokawa, H. and Mabuchi, M.** Novel titanium foam for bone tissue engineering. *Journal of Materials Research*, 2002, **17**(10), 2633-2639.
- 356 Wen, C.E., Yamada, Y. and Hodgson, P.D.** Fabrication of novel TiZr alloy foams for biomedical applications. *Materials Science and Engineering: C*, 2006, **26**(8), 1439-1444.
- 357 Wang, X., Li, Y., Xiong, J., Hodgson, P.D. and Wen, C.e.** Porous TiNbZr alloy scaffolds for biomedical applications. *Acta Biomaterialia*, 2009, **5**(9), 3616-3624.
- 358 Kwok, P.J., Oppenheimer, S.M. and Dunand, D.C.** Porous Titanium by electro-chemical Dissolution of Steel Space-holders. *Advanced Engineering Materials*, 2008, **10**(9), 820-825.
- 359 Li, Y., Guo, Z., Hao, J. and Ren, S.** Porosity and mechanical properties of porous titanium fabricated by gelcasting. *Rare Metals*, 2008, **27**(3), 282-286.
- 360 Erk, K.A., Dunand, D.C. and Shull, K.R.** Titanium with controllable pore fractions by thermoreversible gelcasting of TiH<sub>2</sub>. *Acta Materialia*, 2008, **56**(18), 5147-5157.
- 361 Thelen, S., Barthelat, F. and Brinson, C.L.** Mechanics considerations for microporous Ti as an orthopaedic implant material,. *Journal Biomed Mater Res*, 2004, **69A**, 601-610.
- 362 Gibson, L.J. and Ashby, M.F.** *Cellular Solids : Structure and Properties*. (Cambridge University Press, Cambridge, 1997).

- 363** Li, J., Li, S., De Groot, K. and Layrolle, P. Improvement of porous titanium with thicker struts. *Key Engineering Materials*, 2003, **240**, 547-550.
- 364** Chino, Y. and Dunand, D.C. Directionally freeze-cast titanium foam with aligned, elongated pores. *Acta Materialia*, 2008, **56**(1), 105-113.
- 365** Yook, S., Kim, H. and Koh, Y. Fabrication of porous titanium scaffolds with high compressive strength using camphene-based freeze casting. *Materials Letters*, 2009, **63**(17), 1502-1504.
- 366** Davis, N.G., Teisen, J., Schuh, C. and Dunand, D.C. Solid state foaming of titanium by superplastic expansion of argon-filled pores. *Journal of Materials Research*, 2001, **16**(5), 1508-1519.
- 367** Elzey, D.M. and Wadley, H.N.G. The limits of solid state foaming. *Acta Materialia*, 2001, **49**, 849-859.
- 368** Dunand, D. and Teisen, J. Superplastic foaming of titanium and Ti-6Al-4V. In Schwartz, D.S., Shih, D.S., Wadley, H.N.G. and Evan, A.G., eds. *Proceedings Porous and Cellular Materials for Structural Applications*, pp. 231-236 (Materials Research Society, April 13-15, 1998, San Francisco California, USA, 1998).
- 369** Ricceri, R. and Matteazzi, P. P/M processing of cellular titanium. *International journal of powder metallurgy*, 2003, **39**(3), 53-61.
- 370** Murray, N.G.D. and Dunand, D.C. Microstructure evolution during solid state foaming of titanium. *Composites Science and Technology*, 2003, **63**, 2311-2316.
- 371** Murray, N.G.D. and Dunand, D.C. Effect of thermal history on the superplastic expansion of argon-filled pores in titanium: Part I kinetics and microstructure. *Acta Materialia*, 2004, **52**(8), 2269-2278.
- 372** Spoerke, E.D., Murray, N.G.D., Li, H., Brinson, L.C., Dunand, D.C. and Stupp, S.I. Titanium with aligned, elongated pores for orthopaedic tissue engineering applications. *Journal of Biomedical Materials Research Part A*, 2008, **84A**(2), 402-412.
- 373** Martin, J.Y. and Lederich. Porous core PM structures for airframes. *Metal Powder Report*, 1992, **47**(10), 30-35.
- 374** Queheillalt, D.T., Choi, B.W., Schwartz, D.S. and Wadley, H.N.G. Creep expansion of porous Ti-6Al-4V sandwich structures. *Metallurgical and Materials Transactions A : Physical Metallurgy and Materials Science.*, 2000, **31A**(1), 261-273.
- 375** Queheillalt, D.T., Gable, K.A. and Wadley, H.N.G. Temperature dependent creep expansion of Ti-6Al-4V low density core sandwich structures. *Scripta Materialia*, 2001, **44**(3), 409-414.

- 376 Oppenheimer, S.M., O'Dwyer, J.G. and Dunand, D.C.** Porous, superelastic NiTi produced by powder-metallurgy. *TMS Letters*, 2003, **1**(5) Processing, Microstructure and Properties of Powder-Based Materials, 93-94.
- 377 Lagoudas, D. and Vandygriff, E.** Processing and characterisation of NiTi porous SMA by elevated pressure sintering. *Journal of Intelligent Material Systems and Structures*, 2002, **13**(12), 837.
- 378 Li, B., Rong, L., Li, Y. and Gjunter, V.** Synthesis of porous Ni-Ti shape-memory alloys by self-propagating high-temperature synthesis: reaction mechanism and anisotropy in pore structure. *Acta Materialia*, 2000, **48**(15), 3895-3904.
- 379 Chu, C., Chung, C., Lin, P. and Wang, S.** Fabrication of porous NiTi shape memory alloy for hard tissue implants by combustion synthesis. *Materials Science and Engineering A*, 2004, **366**(1), 114-119.
- 380 Bobyn, J., Stackpool, G., Hacking, S., Tanzer, M. and Krygier, J.** Characteristics of bone ingrowth and interface mechanics of a new porous tantalum biomaterial. *Journal of Bone & Joint Surgery, British Volume*, 1999, **81**(5), 907.
- 381 Curodeau, A., Sachs, E. and Caldarise, S.** Design and fabrication of cast orthopaedic implants with freeform surface textures from 3-D printed ceramic shell. *Journal of Biomedical Materials Research Part B: Applied Biomaterials*, 2000, **53**(5), 525-535.
- 382 Wanner, A.** Elastic modulus measurements of extremely porous ceramic materials by ultrasonic phase spectroscopy. *Materials Science and Engineering A*, 1998, **248**(1-2), 35-43.
- 383 Ashby, M.F., Fleck, N.A., Hutchinson, J.W. and Wadley, H.N.G.** *Metal foams: a design guide*. (Elsevier, 2000).
- 384 Zhao, Y.H., Tandon, G.P. and Weng, G.J.** Elastic moduli for a class of porous materials. *Acta Mechanica*, 1989, **76**(1), 105-131.
- 385 Tuncer, N. and Arslan, G.** Designing compressive properties of titanium foams. *Journal of Materials Science*, 2009, **44**(6), 1477-1484.
- 386 Atkinson, H.V. and Rickinson, B.A.** *Hot Isostatic Pressing*. (Adam Hilger, Norfolk, 1991).
- 387 Murray, N.G.D., Schuh, C.A. and Dunand, D.C.** Solid-state foaming of titanium by hydrogen-induced internal-stress superplasticity. *Scripta Materialia*, 2003, **49**(9), 879-883.
- 388 Ashworth, M.A., Jacobs, M.H., Unwin, P. and Blunn, G.** Surgical Implant. In OFFICE, E.P., ed, p. 11 (Stanmore Implants Worldwide Ltd, Middlesex HA7 4LP (GB), Great Britain, 2007).

- 389 Kuriakose, S. and Shunmugam, M.S.** Characteristics of wire-electro discharge machined Ti6Al4V surface. *Materials Letters*, 2004, **58**(17-18), 2231-2237.
- 390 Peters, M. and Leyens, C.** Chapter 8. Fabrication of titanium alloys, In Peters, M. and Leyens, C., eds. *Titanium and Titanium Alloys*, pp. 245-261 (Willey-VCH, 2003).
- 391 Hong, H., Riga, A., Gahoon, J. and Scott, C.** Machinability of steels and titanium alloys under lubrication. *Wear*, 1993, **162**, 34-39.
- 392 Bojorquez, B., Marloth, R.T. and Es-Said, O.S.** Formation of a crater in the workpiece on an electrical discharge machine. *Engineering Failure Analysis*, 2002, **9**(1), 93-97.
- 393 Yan, B., Chung Tsai, H. and Yuan Huang, F.** The effect in EDM of a dielectric of a urea solution in water on modifying the surface of titanium. *International Journal of Machine Tools and Manufacture*, 2005, **45**(2), 194-200.
- 394 Mohd Abbas, N., Solomon, D.G. and Fuad Bahari, M.** A review on current research trends in electrical discharge machining (EDM). *International Journal of Machine Tools and Manufacture*, 2007, **47**(7-8), 1214-1228.
- 395 Ho, K. and Newman, S.** State of the art electrical discharge machining (EDM). *International Journal of Machine Tools and Manufacture*, 2003, **43**(13), 1287-1300.
- 396 Davis, N.G.** Enhancement of solid state foaming of titanium by transformation superplasticity. *Materials Science and Engineering*, p. 339 (Northwestern University, Illinois, 2002).
- 397 Novoselova, T., Malinov, S., Sha, W. and Zhecheva, A.** High-temperature synchrotron X-ray diffraction study of phases in a gamma TiAl alloy. *Materials science and Engineering A*, 2004, **371**(1-2), 103-112.
- 398 Hickman, B.S.** The formation of omega phase in titanium and zirconium alloys: A review. *Journal of Materials Science*, 1969, **4**(6), 554-563.
- 399 Shen, H., Oppenheimer, S.M., Dunand, D.C. and Brinson, L.C.** Numerical modeling of pore size and distribution in foamed titanium. *Mechanics of Materials*, 2006, **38**(8-10), 933-944.
- 400 Williams, R.E. and Rajurkar, K.P.** Study of wire electrical discharge machined surface characteristics. *Journal of Materials Processing Technology*, 1991, **28**(1-2), 127-138.
- 401 Nugroho, A.W., Leadbeater, G. and Davies, I.** Processing of a porous titanium alloy from elemental powders using a solid state isothermal foaming technique. *Journal of Materials Science: Materials in Medicine*, 2010, **21**(12), 3103-3107.

- 402 Banumathy, S., Mandal, R.K. and Singh, A.K.** Structure of orthorhombic martensitic phase in binary Ti–Nb alloys. *Journal of Applied Physics*, 2009, **106**, 093518.
- 403 Reed, J.S.** Introduction to principles of ceramic processing. (John Wiley, New York, 1988).
- 404 Thieme, M., Wieters, K.P., Bergner, F., Scharnweber, D., Worch, H., Ndop, J., Kim, T.J. and Grill, W.** Titanium powder sintering for preparation of porous FGM destined as skeletal replacement implant. *Materials Science Forum*, 1999, **308-311**, 374-380.
- 405 Kim, H.-K. and Jang, J.-W.** Electrochemical corrosion behaviour and MG-63 osteoblast-like cell response of surface-treated titanium. *Metals and Materials International*, 2004, **10**(5), 439-446.
- 406 Bidhendi, A.R.H. and Pouranvari, M.** Corrosion study of metallic biomaterials in simulated body fluid. *Metallurgia*, 2011, **17**(1), 13-22.
- 407 Kim, S.E., Son, J.H., Hyun, Y.T., Jeong, H.W., Lee, Y.T., Song, J.S. and Lee, J.H.** Electrochemical corrosion of novel beta titanium alloys. *Metals and Materials International*, 2007, **13**(2), 151-154.
- 408 Taddei, E., Henriques, V., Silva, R. and Cairo, C.** Age-hardening of Ti-35Nb-7Zr-5Ta alloy for orthopaedic implants. *Materials Research*, 2007, **10**, 289-292.
- 409 Majumdar, P., Singh, S.B. and Chakraborty, M.** Wear response of heat-treated Ti-13Zr-13Nb alloy in dry conditions and simulated body fluid. *Wear*, 2008, **264**(11-12), 1015-1025.
- 410 Delvat, E., Gordin, D., Gloriant, T., Duval, J. and Nagel, M.** Microstructure, mechanical properties and cytocompatibility of stable beta Ti-Mo-Ta sintered alloys. *Journal of the Mechanical Behaviour of Biomedical Materials*, 2008, **1**(4), 345-351.
- 411 Guden, M., Celik, E., Akar, E. and Cetiner, S.** Compression testing of a sintered Ti6Al4V powder compact for biomedical applications. *Materials Characterisation*, 2005, **54**(4-5), 399-408.
- 412 Fan, Z.** On the young's moduli of Ti---6Al---4V alloys. *Scripta Metallurgica et Materialia*, 1993, **29**(11), 1427-1432.
- 413 Burstein, A., Reilly, D. and Martens, M.** Aging of bone tissue: mechanical properties. *The Journal of Bone and Joint Surgery*, 1976, **58**(1), 82.
- 414 Yeni, Y.N. and Fyhrie, D.P.** A rate-dependent microcrack-bridging model that can explain the strain rate dependency of cortical bone apparent yield strength. *Journal of Biomechanics*, 2003, **36**(9), 1343-1353.

*Every reasonable effort has been made to acknowledge the owners of copyright material. I would be pleased to hear from any copyright owner who has been omitted or incorrectly acknowledged*

# Appendices

## Appendix A : Series of spreadsheets for pore fraction calculation

Specimen : Foamed at 1350°C/0.86 MPa/10 hrs (F30\_125\_1350)

Optical magnification : 10X

Micrographs : 20 pieces

Linear scale factor : 1.368

Image size 1605 x 1200 px<sup>2</sup> = 1926000 px<sup>2</sup> = 1029163 μm<sup>2</sup>

**A1** : Pore area fraction of specimen foamed at 1350°C/0.86 MPa/10 hrs (F30\_125\_1350)

No	Micrographs	Count	Pore total Area	Pore Area Fraction
1	F30_125_1350-1.tif	479	414072,375	40,2
2	F30_125_1350-2.tif	295	423539,29	41,1
3	F30_125_1350-3.tif	338	429816,042	41,7
4	F30_125_1350-4.tif	267	405628,95	39,4
5	F30_125_1350-5.tif	292	419240,296	40,7
6	F30_125_1350-6.tif	438	415746,891	40,3
7	F30_125_1350-7.tif	330	427467,967	41,5
8	F30_125_1350-8.tif	364	386205,101	37,5
9	F30_125_1350-9.tif	387	375679,801	36,5
10	F30_125_1350-10.tif	556	379805,982	36,9
11	F30_125_1350-11.tif	561	379905,271	36,9
12	F30_125_1350-12.tif	504	388308,444	37,7
13	F30_125_1350-13.tif	567	408021,041	39,6
14	F30_125_1350-14.tif	453	375781,777	36,5
15	F30_125_1350-15.tif	340	432458,238	42
16	F30_125_1350-16.tif	256	441555,368	42,8
17	F30_125_1350-17.tif	398	396436,822	38,5
18	F30_125_1350-18.tif	602	336577,708	32,7
19	F30_125_1350-19.tif	433	383503,874	37,2
20	F30_125_1350-20.tif	586	363015,203	35,2
	<b>Average</b>	<b>422,45</b>	<b>399138,322</b>	<b>38,7</b>

**A2 : Pore size diameter list of F30\_125\_1350-8.tif micrograph**

No	Area (mm)	Diameter (mm)	Groups
1	128,809	12,81	D
2	6775,886	92,88	L
3	379,986	22,00	F
4	75,675	9,82	C
5	2042,695	51,00	J
6	57,427	8,55	B
7	290,357	19,23	F
8	128,809	12,81	D
9	27283,876	186,38	P
10	1871,486	48,81	J
11	289,82	19,21	F
12	332,756	20,58	F
13	3177,823	63,61	K
14	1063,21	36,79	H
15	611,306	27,90	G
16	108,951	11,78	D
17	137,933	13,25	D
18	265,668	18,39	E
19	132,029	12,97	D
20	92,85	10,87	C
21	1439,44	42,81	I
22	1143,716	38,16	I
23	88,019	10,59	C
24	266,205	18,41	E
25	230,783	17,14	E
26	92,85	10,87	C
27	88,556	10,62	C
28	100,364	11,30	C
29	257,618	18,11	E
30	876,437	33,41	H
31	61,721	8,86	B
32	70,845	9,50	C
33	307,531	19,79	F
34	445,464	23,82	G
35	2123,2	51,99	J
36	137,933	13,25	D
37	178,186	15,06	E
38	88,556	10,62	C
39	1788,834	47,72	J
40	1204,9	39,17	I
41	174,965	14,93	E
42	8268,459	102,60	M
43	81,042	10,16	C
44	283,916	19,01	F

No	Area (mm)	Diameter (mm)	Groups
45	69,235	9,39	C
46	296,261	19,42	F
47	62,794	8,94	B
48	112,171	11,95	D
49	515,772	25,63	G
50	137,933	13,25	D
51	68,698	9,35	C
52	60,111	8,75	B
53	72,455	9,60	C
54	370,862	21,73	F
55	46,693	7,71	B
56	2849,361	60,23	K
57	834,574	32,60	H
58	472,836	24,54	G
59	180,869	15,18	E
60	128,272	12,78	D
61	817,4	32,26	H
62	80,506	10,12	C
63	96,607	11,09	C
64	58,501	8,63	B
65	207,704	16,26	E
66	57,964	8,59	B
67	1174,845	38,68	I
68	166,915	14,58	D
69	151,887	13,91	D
70	194,287	15,73	E
71	177,649	15,04	E
72	1134,055	38,00	I
73	305,384	19,72	F
74	48,84	7,89	B
75	9517,369	110,08	M
76	1040,669	36,40	H
77	142,227	13,46	D
78	1232,272	39,61	I
79	212,535	16,45	E
80	826,524	32,44	H
81	97,143	11,12	C
82	50,45	8,01	B
83	52,597	8,18	B
84	137,933	13,25	D
85	157,791	14,17	D
86	49,377	7,93	B
87	44,01	7,49	B
88	53,134	8,23	B

No	Area (mm)	Diameter (mm)	Groups
89	349,931	21,11	F
90	246,347	17,71	E
91	870,534	33,29	H
92	2972,266	61,52	K
93	150,277	13,83	D
94	106,267	11,63	C
95	54,744	8,35	B
96	302,701	19,63	F
97	256,008	18,05	E
98	131,492	12,94	D
99	70,308	9,46	C
100	711,669	30,10	H
101	82,116	10,23	C
102	7025,453	94,58	M
103	345,637	20,98	F
104	160,474	14,29	D
105	59,037	8,67	B
106	4000,054	71,37	K
107	295,724	19,40	F
108	1600,988	45,15	I
109	371,936	21,76	F
110	127,199	12,73	D
111	254,934	18,02	E
112	137,396	13,23	D
113	6603,067	91,69	L
114	59,037	8,67	B
115	96,607	11,09	C
116	15555,824	140,73	N
117	189,993	15,55	E
118	1016,517	35,98	H
119	144,373	13,56	D
120	601,645	27,68	G
121	1066,431	36,85	H
122	107,877	11,72	C
123	199,117	15,92	E
124	317,729	20,11	F
125	50,45	8,01	B
126	247,957	17,77	E
127	685,907	29,55	H
128	112,171	11,95	D
129	46,157	7,67	B
130	57,964	8,59	B
131	528,653	25,94	G
132	474,983	24,59	G
133	47,23	7,75	B
134	48,303	7,84	B

No	Area (mm)	Diameter (mm)	Groups
135	7825,142	99,82	M
136	390,72	22,30	F
137	362,812	21,49	F
138	153,497	13,98	D
139	791,101	31,74	H
140	83,189	10,29	C
141	49,913	7,97	B
142	52,06	8,14	B
143	1027,251	36,17	H
144	240,443	17,50	E
145	65,478	9,13	B
146	573,2	27,02	G
147	5480,283	83,53	L
148	664,976	29,10	G
149	3035,597	62,17	K
150	123,979	12,56	D
151	237,76	17,40	E
152	338,66	20,77	F
153	3992,54	71,30	K
154	260,301	18,21	E
155	1539,267	44,27	I
156	143,837	13,53	D
157	776,074	31,43	H
158	2071,677	51,36	J
159	277,476	18,80	F
160	1591,327	45,01	I
161	75,139	9,78	C
162	103,584	11,48	C
163	132,029	12,97	D
164	1743,751	47,12	J
165	46,157	7,67	B
166	428,29	23,35	F
167	421,849	23,18	F
168	56,354	8,47	B
169	1855,922	48,61	J
170	2037,864	50,94	J
171	45,083	7,58	B
172	47,767	7,80	B
173	203,411	16,09	E
174	883,951	33,55	H
175	53,134	8,23	B
176	2657,757	58,17	J
177	518,993	25,71	G
178	2626,629	57,83	J
179	8666,694	105,05	M
180	146,52	13,66	D

No	Area (mm)	Diameter (mm)	Groups
181	354,225	21,24	F
182	221,122	16,78	E
183	112,171	11,95	D
184	78,359	9,99	C
185	96,607	11,09	C
186	64,404	9,06	B
187	153,497	13,98	D
188	6086,758	88,03	L
189	13178,763	129,54	N
190	219,512	16,72	E
191	407,358	22,77	F
192	179,796	15,13	E
193	101,437	11,36	C
194	65,478	9,13	B
195	88,556	10,62	C
196	1089,509	37,25	I
197	1737,31	47,03	J
198	148,667	13,76	D
199	44,01	7,49	B
200	84,799	10,39	C
201	284,99	19,05	F
202	95,533	11,03	C
203	523,286	25,81	G
204	115,391	12,12	D
205	492,157	25,03	G
206	179,796	15,13	E
207	65,478	9,13	B
208	1666,465	46,06	I
209	570,516	26,95	G
210	454,051	24,04	G
211	1554,831	44,49	I
212	50,45	8,01	B
213	265,132	18,37	E
214	194,287	15,73	E
215	472,299	24,52	G
216	1401,334	42,24	I
217	451,905	23,99	G
218	669,27	29,19	G
219	1016,517	35,98	H
220	1465,201	43,19	I
221	52,597	8,18	B
222	90,703	10,75	C
223	133,639	13,04	D
224	6712,555	92,45	L
225	229,709	17,10	E
226	3003,395	61,84	K

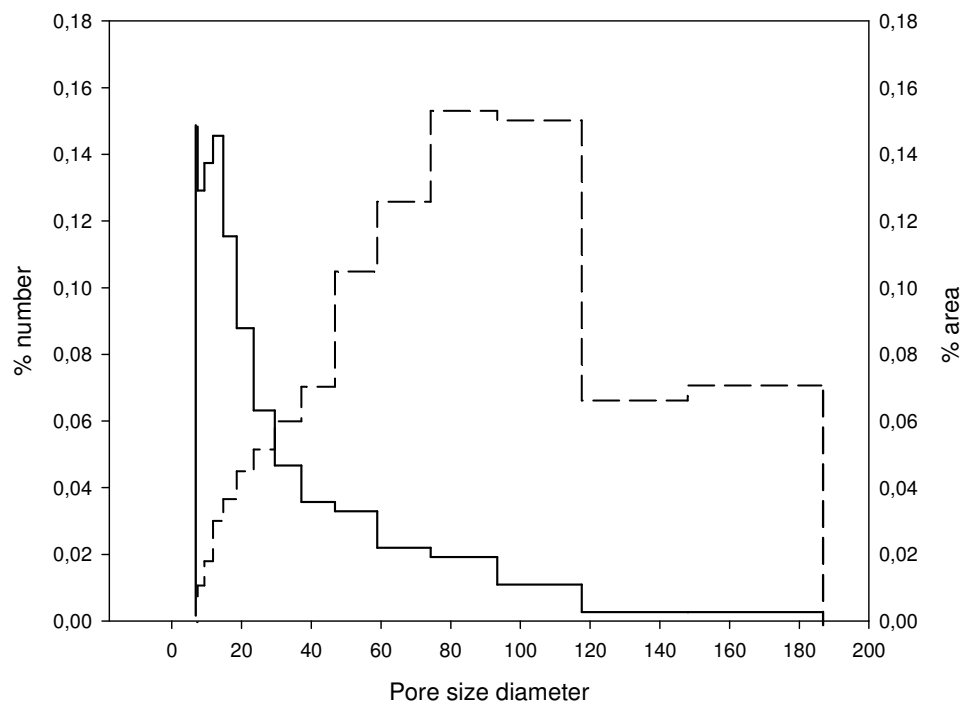
No	Area (mm)	Diameter (mm)	Groups
227	148,667	13,76	D
228	62,258	8,90	B
229	3848,166	70,00	K
230	171,745	14,79	D
231	146,52	13,66	D
232	45,083	7,58	B
233	577,493	27,12	G
234	116,465	12,18	D
235	781,441	31,54	H
236	242,59	17,57	E
237	89,093	10,65	C
238	552,805	26,53	G
239	25568,034	180,43	O
240	48,84	7,89	B
241	378,376	21,95	F
242	13987,039	133,45	N
243	165,841	14,53	D
244	240,443	17,50	E
245	699,862	29,85	H
246	2464,544	56,02	J
247	107,877	11,72	C
248	98,754	11,21	C
249	45,62	7,62	B
250	246,347	17,71	E
251	100,364	11,30	C
252	150,814	13,86	D
253	61,184	8,83	B
254	193,213	15,68	E
255	589,838	27,40	G
256	8081,15	101,44	M
257	55,28	8,39	B
258	234,54	17,28	E
259	60,111	8,75	B
260	98,217	11,18	C
261	44,546	7,53	B
262	3248,668	64,31	K
263	225,416	16,94	E
264	1274,672	40,29	I
265	222,195	16,82	E
266	2935,233	61,13	K
267	194,287	15,73	E
268	328,999	20,47	F
269	219,512	16,72	E
270	207,168	16,24	E
271	4899,033	78,98	L
272	170,672	14,74	D

No	Area (mm)	Diameter (mm)	Groups
273	374,619	21,84	F
274	105,194	11,57	C
275	596,815	27,57	G
276	84,263	10,36	C
277	214,145	16,51	E
278	9717,023	111,23	M
279	307,531	19,79	F
280	718,11	30,24	H
281	334,903	20,65	F
282	1126,005	37,86	I
283	611,842	27,91	G
284	3633,485	68,02	K
285	653,169	28,84	G
286	950,502	34,79	H
287	132,566	12,99	D
288	178,186	15,06	E
289	5291,9	82,08	L
290	329,536	20,48	F
291	70,308	9,46	C
292	232,393	17,20	E
293	165,841	14,53	D
294	374,619	21,84	F
295	15278,348	139,47	N
296	94,46	10,97	C
297	220,585	16,76	E
298	120,758	12,40	D
299	260,301	18,21	E
300	817,4	32,26	H
301	146,52	13,66	D
302	581,787	27,22	G
303	203,411	16,09	E
304	52,597	8,18	B
305	227,562	17,02	E
306	516,309	25,64	G
307	72,992	9,64	C
308	638,141	28,50	G
309	75,139	9,78	C
310	53,134	8,23	B
311	521,139	25,76	G
312	178,722	15,08	E
313	185,7	15,38	E
314	46,157	7,67	B
315	109,488	11,81	D
316	1525,849	44,08	I
317	89,63	10,68	C
318	69,771	9,43	C

No	Area (mm)	Diameter (mm)	Groups
319	49,377	7,93	B
320	187,31	15,44	E
321	2115,15	51,90	J
322	260,838	18,22	E
323	99,827	11,27	C
324	525,97	25,88	G
325	77,822	9,95	C
326	294,65	19,37	F
327	51,524	8,10	B
328	783,051	31,58	H
329	6722,216	92,51	L
330	841,015	32,72	H
331	113,245	12,01	D
332	43,473	7,44	B
333	133,639	13,04	D
334	78,895	10,02	C
335	507,722	25,43	G
336	50,45	8,01	B
337	202,874	16,07	E
338	3789,129	69,46	K
339	327,389	20,42	F
340	520,066	25,73	G
341	67,088	9,24	B
342	280,159	18,89	F
343	211,998	16,43	E
344	288,21	19,16	F
345	191,603	15,62	E
346	319,875	20,18	F
347	125,589	12,65	D
348	431,51	23,44	F
349	283,916	19,01	F
350	311,825	19,93	F
351	452,441	24,00	G
352	459,955	24,20	G
353	150,277	13,83	D
354	243,127	17,59	E
355	57,964	8,59	B
356	50,987	8,06	B
357	349,931	21,11	F
358	377,839	21,93	F
359	153,497	13,98	D
360	338,66	20,77	F
361	151,887	13,91	D
362	117,538	12,23	D
363	74,602	9,75	C
364	44,01	7,49	B

**A3** : A summary of diameter ranges of F30\_125\_1350-8.tif micrograph

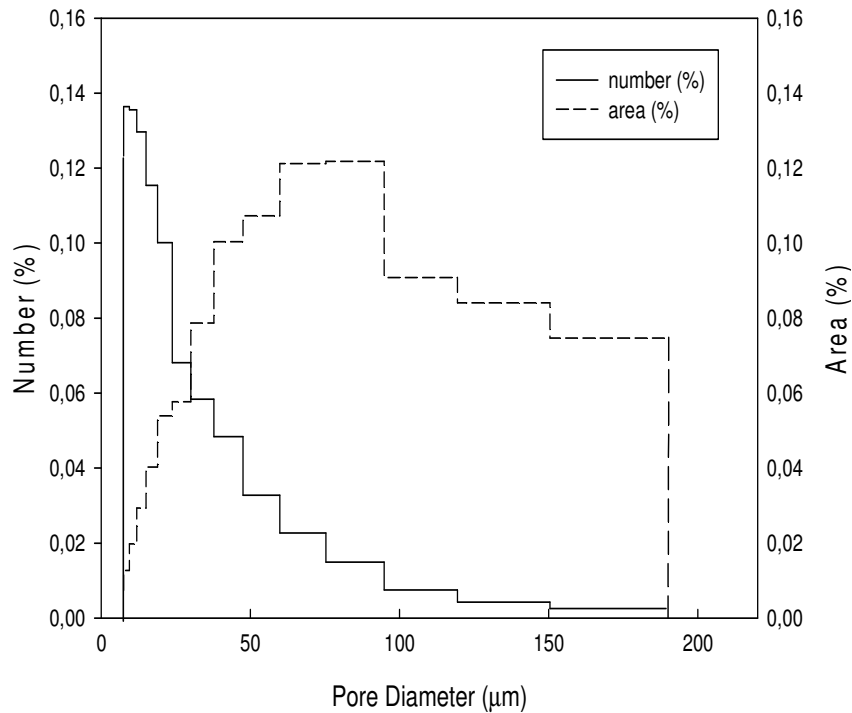
No	D Range(um)	groups	frequency	Area	% area	% frequency
1	7,420072	B	54	2874,59	0,00744	0,14835
2	9,341317	C	47	4111,69	0,01065	0,12912
3	11,76002	D	50	6927,77	0,01794	0,13736
4	14,80499	E	53	11596,6	0,03003	0,1456
5	18,63838	F	42	14139,5	0,03661	0,11539
6	23,46433	G	32	17346,8	0,04492	0,08791
7	29,53984	H	23	19896,2	0,05152	0,06319
8	37,18845	I	17	23164,7	0,05998	0,0467
9	46,81749	J	13	27136,8	0,07027	0,03571
10	58,93972	K	12	40485,7	0,10483	0,03297
11	74,20072	L	8	48571,7	0,12577	0,02198
12	93,41317	M	7	59101,3	0,15303	0,01923
13	117,6002	N	4	58000	0,15018	0,01099
14	148,0499	O	1	25568	0,0662	0,00275
15	186,3838	P	1	27283,9	0,07065	0,00275
			364	386205	1	1



**A3**: A figure of a typical pore size distribution micrograph sample foamed at 1350°C/0.86 MPa/10 hours particularly for F30\_125\_1350-8 micrograph (obtained from A3 data)

**A4** : Average of pore size range of F30\_125\_1350 specimen calculated from 20 micrographs

No	D Range(um)	Stdev	% area	% frequency
1	7,53691	2,22207	0,00768	0,126199
2	9,4884	2,79742	0,01294	0,136846
3	11,9452	3,52174	0,02007	0,135947
4	15,0381	4,43361	0,02942	0,1287
5	18,9319	5,58158	0,04091	0,115643
6	23,8338	7,02679	0,05403	0,099041
7	30,005	8,84621	0,0583	0,067952
8	37,774	11,1367	0,08034	0,058785
9	47,5547	14,0203	0,10008	0,047682
10	59,8678	17,6505	0,11074	0,032961
11	75,3691	22,2207	0,11458	0,021264
12	94,884	27,9742	0,12431	0,015142
13	119,452	35,2174	0,08708	0,00714
14	150,381	44,3361	0,08396	0,004304
15	189,319	55,8158	0,07104	0,002393



**A5** : A figure of a typical pore size distribution micrograph sample foamed at 1350°C/0.86Mpa/10hours (F30\_125\_1350)

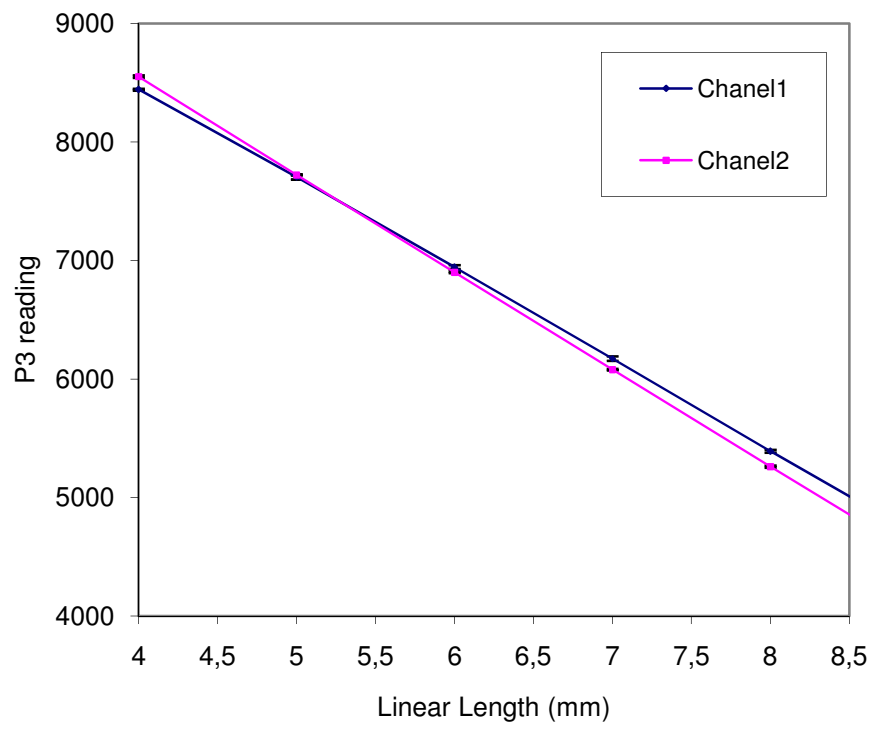
## Appendix B : Calibration data of the Clip Gages

**B1** : Calibration data of the clip gage 1 (Chanel 1)

No	mm	P3-Chanel 1-C4 CLIP GAGE 1							Average	StDev
		1	2	3	4	5	6	7		
1	16	11	10	37	11	7	11	17	14,8571	10,2050
2	15	445	447	429	498	447	427	477	452,8571	25,7839
3	14	1072	1069	1066	1089	1071	1068	1069	1072,0000	7,7460
4	13	1720	1716	1700	1729	1711	1755	1715	1720,8571	17,4301
5	12	2369	2367	2354	2361	2343	2366	2337	2356,7143	12,5527
6	11	3112	3134	3098	3094	3096	3133	3098	3109,2857	17,5377
7	10	3875	3858	3856	3860	3838	3865	3850	3857,4286	11,6025
8	9	4640	4628	4615	4619	4636	4636	4620	4627,7143	9,8778
9	8	5409	5390	5394	5386	5369	5400	5383	5390,1429	12,7988
10	7	6189	6173	6200	6145	6178	6158	6165	6172,5714	18,6267
11	6	6970	6944	6956	6941	6921	6947	6928	6943,8571	16,4462
12	5	7721	7704	7710	7677	7675	7721	7719	7703,8571	20,0369
13	4	8441	8442	8450	8449	8430	8434	8446	8441,7143	7,4992

**B21** : Calibration data of the clip gage 2 (Chanel 2)

No	mm	P3-Chanel 2-C3 CLIP GAGE 2							Average	St Dev
		1	2	3	4	5	6	7		
1	16	2	5	1	5	7	8	4	4,5714	2,5071
2	15	136	138	150	121	139	136	140	137,1429	8,5718
3	14	754	793	795	803	849	769	790	793,2857	29,8480
4	13	1468	1476	1459	1463	1493	1488	1483	1475,7143	12,9321
5	12	2177	2174	2172	2166	2188	2177	2162	2173,7143	8,4205
6	11	2862	2857	2859	2859	2852	2866	2844	2857,0000	7,1647
7	10	3700	3654	3646	3656	3636	3650	3635	3653,8571	21,9274
8	9	4464	4451	4446	4462	4436	4448	4449	4450,8571	9,5991
9	8	5278	5260	5255	5261	5248	5265	5255	5260,2857	9,5169
10	7	6085	6070	6082	6082	6071	6083	6076	6078,4286	6,0788
11	6	6916	6901	6898	6891	6900	6903	6895	6900,5714	7,8921
12	5	7724	7722	7721	7719	7713	7729	7728	7722,2857	5,4685
13	4	8546	8552	8558	8540	8551	8545	8574	8552,2857	11,1761



B3: Linier relationship between clip gage measurement and micrometer

## Appendix C : P3 data acquisitions from the clip gage

Specimen Foamed at 1225°C/0,67 MPa/10 hrs (F31\_100\_1225 \_\_1)

Vishay Model P3 Strain Indicator and Recorder

Serial No : 170055

File Created : 12/03/2009 13:41:33

	Ch 1	Ch 2
	ue	ue
	----	----
13:41:33	-5365	-5145
13:41:34	-5371	-5151
13:41:35	-5378	-5158
13:41:36	-5384	-5165
13:41:37	-5390	-5171
13:41:38	-5397	-5179
13:41:39	-5402	-5184
13:41:40	-5406	-5188
13:41:41	-5412	-5195
13:41:42	-5416	-5199
13:41:43	-5422	-5206
13:41:44	-5426	-5210
13:41:45	-5431	-5214
13:41:46	-5435	-5218
13:41:47	-5440	-5223
13:41:48	-5445	-5229
13:41:49	-5449	-5233
13:41:50	-5455	-5239
13:41:51	-5459	-5244
13:42:06	-5529	-5317
13:42:07	-5535	-5323
13:42:08	-5539	-5327
13:42:09	-5543	-5332



13:46:39	-6896	-6747
13:46:40	-6902	-6753
13:46:41	-6906	-6757
13:46:42	-6912	-6763
13:46:43	-6916	-6767
13:46:44	-6922	-6774
13:46:45	-6927	-6779
13:46:46	-6933	-6785

-----

## **Appendix D : Spreadsheet sample for the compressive property calculation**

NOTES :

A particular cell, C, in the following spreadsheet is identified by its column,  $i$ , and its row,  $j$ . Whilst the capital letter(s) is (are) assigned to identify a column, a number used to identify a row, e.g.  $C_{ij}$  = cell AB210 is a cell located in column AB at row 210. And  $k$  is assigned as column index number.

Cell formulas :

D6 to I6,  $m$  : = SLOPE ( $i_15:i_1213, i_25:i_2213$ ),  $i_1=BG, BH, BI, \dots, BL, i_2 = BA, BB, BC, \dots, BF$

D7 to I7,  $c$  : = INTERCEPT ( $i_15:i_1213, i_25:i_2213$ ),  $i_1=BG, BH, BI, \dots, BL, i_2 = BA, BB, BC, \dots, BF$

D8 to I8,  $r$  : = CORREL ( $i_15:i_1213, i_25:i_2213$ ),  $i_1=BG, BH, BI, \dots, BL, i_2 = BA, BB, BC, \dots, BF$

D9 to I9,  $\Delta D$  : =  $-i_7/i_6, I = D, E, F, \dots, I$

D10 to I10,  $F_{max}$  : = MIN( $i:i$ ),  $I = N, N, N, T, T, T$

D11 to I11,  $D$  : = VLOOKUP ( $i_110, i_2: i_3, k, FALSE$ )\*D14,  $i_1=D, E, F, \dots, I, i_2 = N, N, N, T, T, T, k = 34, 35, 36, 31, 32, 33, i_3=AU, AV, AW, \dots, AZ$

D15 to I15,  $\sigma_{max}$  : = MAX( $i:i$ ),  $I = R, R, R, X, X, X$

D16 to I16,  $E$  : =  $i_6*0.001, i = D, E, F, G, H, I$

D17 to I17,  $\epsilon_{max}$  : = VLOOKUP( $i_115, i_2: i_3, k, FALSE$ ),  $i_1=D, E, F, \dots, I, i_2 = R, R, R, X, X, X, k = 30, 31, 32, 27, 28, 29, i_3=AU, AV, AW, \dots, AZ$

D18 to I18,  $\sigma_{ys}$  : = VLOOKUP(MIN( $i:i$ ),  $i_1\$6:i_2\$320, k, FALSE$ ),  $i_1= O, P, Q, U, V, W, i_2= R, R, R, X, X, X, k = 4, 3, 2, 4, 3, 2$

D19 to I19,  $\epsilon_{ys}$  : = VLOOKUP( $i_115, i_2: i_3, k, FALSE$ ),  $i_1=D, E, F, G, H, I, i_2 = U, U, U, AD, AD, AD, k = 38, 39, 40, 33, 34, 35, i_3=BF, BG, BH, BJ, BK, BL$

$Y4 = 11398/747,35 - (-1*Y5/747,35)$

$Z4 = 11576/781,95 - (-1*Z5/781,95)$

Extension (see the spreadsheet on cells AC3, ..., AH3)

$AC_j = 11398/747,35 - (-1*Y5/747,35) - \$Y\$4, j = 5, 6, 7 \dots$

$AD_j = 11576/781,95 - (-1*Z5/781,95) - \$Z\$4, j = 5, 6, 7 \dots$

$AE_j = AVERAGE(AC_j; AD_j), j = 5, 6, 7 \dots$

All Strain Curve (see the spreadsheet on cells AI3,...,AN3)

$$AI_j = -AC_j / \$D\$14, j = 5,6,7\dots$$

$$AJ_j = -AD_j / \$D\$14, j = 5,6,7\dots$$

$$AK_j = \text{AVERAGE}(AI_j:AJ_j), j = 5,6,7\dots$$

SLOPE FORMULA (see the spreadsheet on cells BA2,...,BL2)

Strain (see the spreadsheet on cells BA3,...,BF3)

$$BA_j = \text{IF}(\text{AND}(AO_j \geq \$D\$4; AO_j \leq \$D\$5); AO_j; ""), j = 5,6,7\dots$$

$$BB_j = \text{IF}(\text{AND}(AP_j \geq \$E\$4; AP_j \leq \$E\$5); AP_j; ""), j = 5,6,7\dots$$

$$BC_j = \text{IF}(\text{AND}(AQ_j \geq \$F\$4; AQ_j \leq \$F\$5); AQ_j; ""), j = 5,6,7\dots$$

Stress (see the spreadsheet on cells BG3,...,BG3)

$$BG_j = \text{IF}(BA_j = ""; "", R_j), j = 5,6,7\dots$$

$$BH_j = \text{IF}(BB_j = ""; "", R_j), j = 5,6,7\dots$$

$$BJ_j = \text{IF}(BC_j = ""; "", R_j), j = 5,6,7\dots$$

Where :

$m$  = the gradient of the linear part of the curve

$c$  = the constant of the equation of initial linear part of the curve

$r$  = the coefficient correlation of the linear part of the curve

$\Delta D$  = the displacement correction (mm)

$F_{max}$  = maximum load (N)

$D$  = true displacement at maximum load (mm)

$\sigma_{max}$  = compressive strength (MPa)

$E$  = Young's modulus (GPa) =  $m$

$\epsilon_{max}$  = the strain to compressive strength

$\sigma_{ys}$  = yield strength (MPa)

$\epsilon_{ys}$  = the strain to yield strength

**D1 : Spreadsheet sample for compressive property calculation**

Name : Aris Widyo Nugroho  
 Operator ID : Dereck Oxley  
 Test Date : 03/12/2009  
 Specimen name : Porous Titanium Alloy  
 Crosshead speed : 0.480 mm/mnt

	A	B	C	D	E	F	G	H	I
1									
2	Sample			F31_100_1225_1			F31_100_1225_2		
3				Ch1-1	Ch2-1	Ave-1	Ch1-2	Ch2-2	Ave-2
4	Linear Cut-Offs (Read From Plot)	Min		0,0343	0,0343	0,0343	0,0242	0,0244	0,0243
5		Max		0,0446	0,0447	0,0446	0,0317	0,0317	0,0317
6	Toe Correction Analysis	m		35654,5828	35545,6714	35607,0021	33792,6030	33829,7740	33827,1843
7		c		-992,6539	-991,3974	-992,2956	-505,8832	-510,7635	-508,7645
8		r		0,9992	0,9985	0,9989	0,9990	0,9983	0,9989
9		toe correction (x-intercept)		0,0278	0,0279	0,0279	0,0150	0,0151	0,0150
10	Maximum Point	Max Load (N)		-12,466	-12,466	-12,466	-11,860	-11,860	-11,860
11		True Displ.at Max Load (mm)		0,318	0,32	0,32	0,2718	0,2726	0,2722
12	Sample Dimensions	width (mm)		4,0183	4,0183	4,0183	4,0167	4,0167	4,0167
13		thicknes (mm)		4,0330	4,0330	4,0330	4,0337	4,0337	4,0337
14		Length (mm)		8,0467	8,0467	8,0467	8,0303	8,0303	8,0303
15	Results	Comp Strength (Mpa)		763,73	763,73	763,73	729,60	729,60	729,60
16		Young's Modulus (GPa)		35,65	35,55	35,61	33,79	33,83	33,83
17		Strain to Max Stress		0,0395	0,0395	0,0395	0,0339	0,0340	0,0339
18		Yield Strength (Mpa)		664,5358	664,5358	664,5358	642,2915	636,1472	636,1472
19		Strain to Yield Strength		0,0205	0,0204	0,0205	0,0212	0,0206	0,0205
20									
21									

Continuous to the column; M (Column J,K,L are blank)





	Y	Z	AA	AB	AC	AD	AE	AF	AG	AH
<b>1</b>	P3									
<b>2</b>	P3-specimen1		P3-specimen2		Extension					
<b>3</b>	8,073	8,224311017	8,060	8,27162862	Ch1-1	Ch2-1	Ave1	Ave2	Ch1-2	Ch2-2
<b>4</b>	-5365	-5145	-5374	-5108	0,000	0,000	0,000	0,000	0,000	0,000
<b>5</b>	-5371	-5151	-5379	-5113	-0,008	-0,008	-0,008	-0,007	-0,007	-0,006
<b>6</b>	-5378	-5158	-5385	-5120	-0,017	-0,017	-0,017	-0,015	-0,015	-0,015
<b>7</b>	-5384	-5165	-5390	-5125	-0,025	-0,026	-0,026	-0,022	-0,021	-0,022
<b>8</b>	-5390	-5171	-5396	-5131	-0,033	-0,033	-0,033	-0,029	-0,029	-0,029
<b>9</b>	-5397	-5179	-5402	-5138	-0,043	-0,043	-0,043	-0,038	-0,037	-0,038
<b>10</b>	-5402	-5184	-5409	-5145	-0,050	-0,050	-0,050	-0,047	-0,047	-0,047
<b>11</b>	-5406	-5188	-5415	-5152	-0,055	-0,055	-0,055	-0,056	-0,055	-0,056
<b>12</b>	-5412	-5195	-5420	-5157	-0,063	-0,064	-0,063	-0,062	-0,062	-0,063
<b>13</b>	-5416	-5199	-5424	-5162	-0,068	-0,069	-0,069	-0,068	-0,067	-0,069
<b>14</b>	-5422	-5206	-5428	-5166	-0,076	-0,078	-0,077	-0,073	-0,072	-0,074
<b>15</b>	-5426	-5210	-5434	-5172	-0,082	-0,083	-0,082	-0,081	-0,080	-0,082
<b>16</b>	-5431	-5214	-5438	-5175	-0,088	-0,088	-0,088	-0,086	-0,086	-0,086
<b>17</b>	-5435	-5218	-5443	-5180	-0,094	-0,093	-0,094	-0,092	-0,092	-0,092
<b>18</b>	-5440	-5223	-5447	-5184	-0,100	-0,100	-0,100	-0,097	-0,098	-0,097
<b>19</b>	-5445	-5229	-5452	-5190	-0,107	-0,107	-0,107	-0,105	-0,104	-0,105
										
<b>314</b>	-6916	-6767	-6946	-6753	-2,075	-2,074	-2,075	-2,104	-2,103	-2,104
<b>315</b>	-6922	-6774	-6951	-6758	-2,083	-2,083	-2,083	-2,110	-2,110	-2,110
<b>316</b>	-6927	-6779	-6957	-6764	-2,090	-2,090	-2,090	-2,118	-2,118	-2,118
<b>317</b>	-6933	-6785	-6962	-6769	-2,098	-2,097	-2,098	-2,125	-2,125	-2,124
<b>318</b>	-6851	-6551			-1,988	-1,798	-1,893			

Continuous to the next column; AI

	AI	AJ	AK	AL	AM	AN	AO	AP	AQ	AR	AS	AT
<b>1</b>	Clip gages' Strain											
<b>2</b>	All Strain Curve						Slope					
<b>3</b>	Ch1-1	Ch2-1	Ave1	Ave2	Ch1-2	Ch2-2	Ch1-1	Ch2-1	Ave1	Av2	Ch1-2	Ch2-2
<b>4</b>	0	0			0	0	0	0	0	0	0	0
<b>5</b>	0,000998	0,00095	0,00098	0,00081	0,0008	0,0008	0,000998	0,000954	0,000976	0,000815	0,000833	0,0008
<b>6</b>	0,002162	0,00207	0,00211	0,00187	0,0018	0,0019	0,002162	0,002066	0,002114	0,001872	0,001833	0,0019
<b>7</b>	0,003159	0,00318	0,00317	0,00269	0,0027	0,0027	0,003159	0,003179	0,003169	0,002687	0,002666	0,0027
<b>8</b>	0,004157	0,00413	0,00414	0,00366	0,0037	0,0037	0,004157	0,004132	0,004145	0,003664	0,003666	0,0037
<b>9</b>	0,005321	0,0054	0,00536	0,00472	0,0047	0,0048	0,005321	0,005404	0,005362	0,004722	0,004666	0,0048
<b>10</b>	0,006153	0,0062	0,00618	0,00586	0,0058	0,0059	0,006153	0,006198	0,006175	0,005862	0,005832	0,0059
<b>11</b>	0,006818	0,00683	0,00683	0,00692	0,0068	0,007	0,006818	0,006834	0,006826	0,006919	0,006832	0,007
<b>12</b>	0,007815	0,00795	0,00788	0,00773	0,0077	0,0078	0,007815	0,007946	0,007881	0,007734	0,007665	0,0078
<b>13</b>	0,008481	0,00858	0,00853	0,00847	0,0083	0,0086	0,008481	0,008582	0,008531	0,008466	0,008331	0,0086
<b>14</b>	0,009478	0,00969	0,00959	0,00912	0,009	0,0092	0,009478	0,009695	0,009587	0,009117	0,008998	0,0092
<b>15</b>	0,010144	0,01033	0,01024	0,01009	0,01	0,0102	0,010144	0,01033	0,010237	0,010095	0,009998	0,0102
<b>16</b>	0,010975	0,01097	0,01097	0,01067	0,0107	0,0107	0,010975	0,010966	0,010971	0,010667	0,010664	0,0107
<b>17</b>	0,01164	0,0116	0,01162	0,01148	0,0115	0,0115	0,01164	0,011602	0,011621	0,011482	0,011497	0,0115
<b>18</b>	0,012472	0,0124	0,01243	0,01213	0,0122	0,0121	0,012472	0,012396	0,012434	0,012134	0,012164	0,0121
<b>19</b>	0,013303	0,01335	0,01333	0,01303	0,013	0,0131	0,013303	0,01335	0,013326	0,013028	0,012997	0,0131
												
<b>313</b>	0,257246	0,25715	0,2572	0,2609	0,2609	0,2609	0,257246	0,257147	0,257197	0,260897	0,260937	0,2609
<b>314</b>	0,257911	0,25778	0,25785	0,26195	0,2619	0,262	0,257911	0,257783	0,257847	0,261955	0,261937	0,262
<b>315</b>	0,258909	0,2589	0,2589	0,26277	0,2628	0,2628	0,258909	0,258895	0,258902	0,262769	0,26277	0,2628
<b>316</b>	0,25974	0,25969	0,25972	0,26375	0,2638	0,2637	0,25974	0,25969	0,259715	0,263747	0,26377	0,2637
<b>317</b>	0,260738	0,26064	0,26069	0,26456	0,2646	0,2645	0,260738	0,260644	0,260691	0,264562	0,264603	0,2645
<b>318</b>	0,247102	0,22345	0,23528				0,247102	0,223454	0,235278			

Continuous to the next column: AU

	<b>AU</b>	<b>AV</b>	<b>AW</b>	<b>AX</b>	<b>AY</b>	<b>AZ</b>
<b>1</b>						
<b>2</b>	<b>Toe Corrected</b>					
<b>3</b>	<b>Ch1</b>	<b>Ch2</b>	<b>Ave1</b>	<b>Ch1-2</b>	<b>Ch2-2</b>	<b>Ave2</b>
<b>4</b>	0	0				
<b>5</b>	-4,1E-06	-4,138E-06	-4,131E-06	-8,13E-06	-8,1E-06	-8,12113E-06
<b>6</b>	1,76E-06	1,761E-06	1,758E-06	-1,37E-06	-1,4E-06	-1,36864E-06
<b>7</b>	2,6E-06	2,613E-06	2,608E-06	3,43E-07	3,43E-07	3,42644E-07
<b>8</b>	2,02E-05	2,024E-05	2,02E-05	3,78E-06	3,77E-06	3,77237E-06
<b>9</b>	3,03E-05	3,043E-05	3,038E-05	9,07E-06	9,06E-06	9,06311E-06
<b>10</b>	4,8E-05	4,813E-05	4,805E-05	1,41E-05	1,41E-05	1,40972E-05
<b>11</b>	7,07E-05	7,094E-05	7,082E-05	1,96E-05	1,95E-05	1,95448E-05
<b>12</b>	8,18E-05	8,202E-05	8,188E-05	4,48E-05	4,48E-05	4,47863E-05
<b>13</b>	0,000106	0,0001059	0,0001058	7,69E-05	7,68E-05	7,68374E-05
<b>14</b>	0,000126	0,0001269	0,0001266	0,000138	0,000138	0,000138301
<b>15</b>	0,000165	0,0001652	0,0001649	0,000179	0,000178	0,000178445
<b>16</b>	0,00021	0,0002106	0,0002103	0,000256	0,000255	0,000255404
<b>17</b>	0,000248	0,0002486	0,0002482	0,000323	0,000323	0,000322529
<b>18</b>	0,000315	0,0003163	0,0003157	0,000424	0,000423	0,000423396
<b>19</b>	0,000364	0,0003649	0,0003643	0,000553	0,000553	0,000552862
						
<b>313</b>	0,229405	0,2292563	0,2293285	0,245967	0,245759	0,245857171
<b>314</b>	0,23007	0,2298921	0,229979	0,246967	0,246874	0,246914438
<b>315</b>	0,231068	0,2310046	0,2310341	0,2478	0,24767	0,247729139
<b>316</b>	0,231899	0,2317992	0,2318471	0,2488	0,248626	0,248706779
<b>317</b>	0,232897	0,2327528	0,2328228	0,249633	0,249422	0,249521479
<b>318</b>	0,219262	0,1955634	0,2074103			

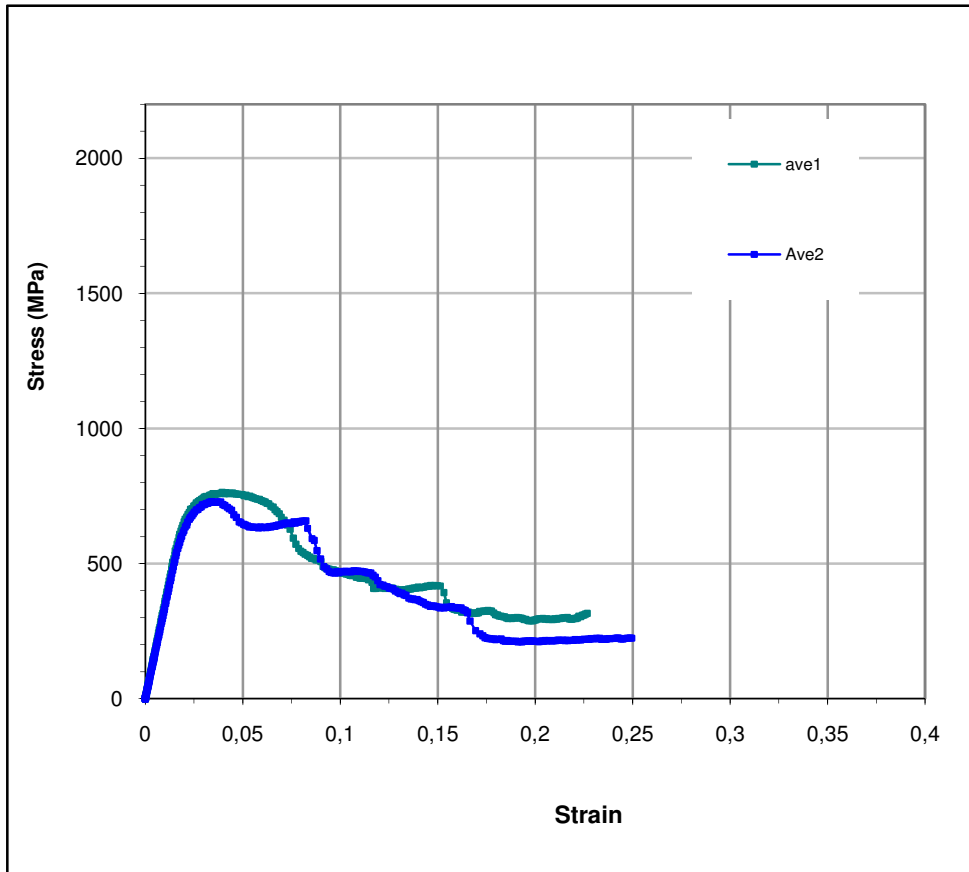
Continuous to the next column; BA

	BA	BB	BC	BD	BE	BF	BG	BH	BI	BJ	BK	BL
1	Slope Formula											
2	Strain						Stress					
3	Ch1-1	Ch2-1	Ave1	Ch1-2	Ch2-2	Ave2	Ch1-1	Ch2-1	Ave1	Ch1-2	Ch2-2	Ave2
4												
5												
6												
7												
8												
9												
10												
11												
12												
												
56												
57												
58												
59												
60	0,034	0,034	0,034	0,024	0,024	0,024	224,3	224,3	224,3	307,4	307,4	307,4
61	0,035	0,035	0,035	0,024	0,025	0,025	234,0	234,0	234,0	319,7	319,7	319,7
62	0,035	0,035	0,035	0,025	0,025	0,025	243,8	243,8	243,8	330,2	330,2	330,2
63	0,035	0,035	0,035	0,025	0,025	0,025	256,0	256,0	256,0	339,9	339,9	339,9
64	0,035	0,035	0,035	0,025	0,025	0,025	264,0	264,0	264,0	352,8	352,8	352,8
65	0,036	0,036	0,036	0,026	0,026	0,026	275,2	275,2	275,2	361,7	361,7	361,7
66	0,036	0,036	0,036	0,026	0,026	0,026	285,2	285,2	285,2	375,9	375,9	375,9
67	0,036	0,036	0,036	0,026	0,026	0,026	296,2	296,2	296,2	383,3	383,3	383,3
68	0,036	0,036	0,036	0,027	0,027	0,027	308,9	308,9	308,9	397,1	397,1	397,1
69	0,037	0,037	0,037	0,027	0,027	0,027	316,8	316,8	316,8	408,9	408,9	408,9
70	0,037	0,037	0,037	0,027	0,027	0,027	330,2	330,2	330,2	421,6	421,6	421,6
71	0,037	0,038	0,037	0,028	0,028	0,028	339,1	339,1	339,1	436,5	436,5	436,5

<b>72</b>	0,038	0,038	0,038	0,028	0,028	0,028	352,2	352,2	352,2	447,4	447,4	447,4
<b>73</b>	0,038	0,038	0,038	0,028	0,029	0,029	361,8	361,8	361,8	462,3	462,3	462,3
<b>74</b>	0,038	0,038	0,038	0,029	0,029	0,029	373,6	373,6	373,6	475,4	475,4	475,4
<b>75</b>	0,039	0,039	0,039	0,029	0,030	0,029	385,8	385,8	385,8	489,1	489,1	489,1
<b>76</b>	0,039	0,039	0,039	0,030	0,030	0,030	396,0	396,0	396,0	504,2	504,2	504,2
<b>77</b>	0,039	0,039	0,039	0,030	0,030	0,030	410,5	410,5	410,5	514,6	514,6	514,6
<b>78</b>	0,040	0,040	0,040	0,031	0,031	0,031	422,4	422,4	422,4	529,6	529,6	529,6
<b>79</b>	0,040	0,040	0,040	0,031	0,031	0,031	436,1	436,1	436,1	541,2	541,2	541,2
<b>80</b>	0,040	0,040	0,040	0,032	0,032	0,032	450,9	450,9	450,9	555,8	555,8	555,8
<b>81</b>	0,041	0,041	0,041				463,3	463,3	463,3			
<b>82</b>	0,041	0,041	0,041				479,6	479,6	479,6			
<b>83</b>	0,042	0,042	0,042				490,3	490,3	490,3			
<b>84</b>	0,042	0,042	0,042				505,4	505,4	505,4			
<b>85</b>	0,042	0,043	0,042				518,4	518,4	518,4			
<b>86</b>	0,043	0,043	0,043				532,5	532,5	532,5			
<b>87</b>	0,043	0,043	0,043				547,6	547,6	547,6			
<b>88</b>	0,044	0,044	0,044				557,3	557,3	557,3			
<b>89</b>	0,044	0,044	0,044				572,4	572,4	572,4			
<b>90</b>	0,045	0,045	0,045				582,6	582,6	582,6			
<b>91</b>												
<b>92</b>												
<b>93</b>												
												
<b>316</b>												
<b>317</b>												
<b>318</b>												

Continuous to the next column, BM





**D2:** A toe corrected stress strain curve of the specimens foamed at 1225°C/0.68 MPa/10 hours obtained from the calculation (see appendix D:1)

## D2 : Samples of specimen dimensions for compression test

Name : Aris W Nugroho  
 Operator ID : Dereck Oxley  
 Test date : 17 & 18 /11/2009  
 Material : Titanium alloy  
 Strain rate : 0,001/s /

No		Width, w(mm)				Length, l(mm)				Area, (mm <sup>2</sup> )	Gauge length (mm)				Cross head speed (mm/m)
		1	2	3	Ave	1	2	3	Ave					Av	
1	F20_100_1225r-1	3,996	4,000	4,001	4,001	3,985	3,985	3,990	3,987	15,951	8,000	8,009	8,014	8,008	0,480
2	F20_100_1225r-2	4,025	4,030	4,031	4,031	3,989	3,995	3,996	3,993	16,097	7,998	8,000	8,025	8,008	0,480
3	F11_100_1350r-1	3,982	3,989	4,002	3,991	4,023	4,001	4,011	4,012	16,011	8,014	8,015	8,015	8,015	0,481
4	F11_100_1350r-2	4,003	4,009	4,012	4,008	3,987	4,014	4,005	4,002	16,040	7,993	8,023	8,025	8,014	0,481
5	F33-125-1350-1	3,998	4,003	4,005	4,005	4,000	4,000	4,004	4,001	16,025	8,005	8,005	8,005	8,005	0,480
6	F33-125-1350-2	3,997	3,995	3,999	3,999	4,005	4,005	4,000	4,003	16,009	8,000	8,000	8,004	8,001	0,480
7	F33_125_1350-3	4,009	4,005	4,010	4,008	4,035	4,040	4,035	4,037	16,179	8,015	8,020	8,020	8,018	0,481
8	F33_125_1350-4	4,000	4,019	4,000	4,006	4,040	4,035	4,040	4,038	16,179	8,017	8,005	8,019	8,014	0,481
9	F25_125_1350-1	3,989	3,987	3,995	3,990	4,050	4,060	4,061	4,057	16,189	8,042	8,041	8,062	8,048	0,483
10	F25_125_1350-2	3,995	3,995	3,999	3,996	4,021	4,014	4,022	4,019	16,061	8,040	8,051	8,054	8,048	0,483
11	F25_125_1225-1	4,005	4,005	4,008	4,006	4,009	4,015	4,015	4,013	16,076	8,020	8,030	8,030	8,027	0,482
12	F25_125_1225-2	4,028	4,030	4,030	4,029	4,015	4,008	4,010	4,011	16,162	8,030	8,035	8,030	8,032	0,482
13	F32_125_1225-1	4,015	4,018	4,025	4,019	4,010	4,030	4,025	4,022	16,164	7,993	7,992	7,990	7,992	0,480
14	F32_125_1225-2	4,025	4,040	4,035	4,033	3,997	3,995	4,010	4,001	16,136	8,005	8,005	7,989	8,000	0,480
15	F32_125_1350-1	3,984	3,993	3,990	3,989	4,010	4,019	4,019	4,016	16,020	7,995	7,994	7,995	7,995	0,480
16	F32_125_1350-2	3,990	3,994	3,995	3,992	4,023	4,023	4,017	4,021	16,052	7,983	7,995	7,995	7,991	0,479
17	F20_100_1225r-1	4,019	4,019	4,010	4,016	3,991	4,005	3,991	3,996	16,047	7,997	8,019	7,995	8,004	0,480
18	F20_100_1225r-2	3,982	3,986	3,994	3,987	4,046	4,047	4,032	4,042	16,115	7,993	8,017	8,016	8,009	0,481
19	F11_100_1350r	4,020	4,025	4,025	4,023	4,030	4,032	4,005	4,022	16,183	8,010	8,012	8,010	8,011	0,481

